

# **$^{19}\text{F}$ Dynamic Nuclear Polarisation**

Towards a novel method for studies of protein  
dynamics

by

**Antonio Gennaro**

Thesis submitted to the University of Nottingham  
for the degree of  
Doctor of Philosophy

June 2019

# Abstract

Nuclear Magnetic Resonance (NMR) spectroscopy is a powerful technique capable of reporting on the structure of molecules and has numerous applications in chemistry, biophysics and medicine. It is based on probing transitions between energy levels formed by non-zero spins placed in a static magnetic field.

Nuclei of  $^{19}\text{F}$ , due to their high natural abundance and large gyromagnetic ratio, are perfectly suitable for NMR spectroscopy, and they can be used for studying structure and dynamics of large and small biomolecules.

However, one of the NMR significant limitations is a relatively low sensitivity, that entails the need of large amounts of studied material, or the averaging of many experimental results, that compromises the time resolution of the experiment. For example, typical solution NMR samples require few millimolars of measured substance in 2 – 3 ml volume, which is a rather large amount of material. However, in many practical cases the amount available is much lower than that. In particular, in ligand binding experiments and studies of enzymatic reactions and other kinetic processes, tracking molecules at micromolar concentration could be required. For these reasons, significant efforts in the magnetic resonance community are directed towards solving this problem of sensitivity.

One of the approaches for increasing NMR signals is to use Dynamic Nuclear Polarisation (DNP), which is a process of transferring large polarisation of electron spins onto nearby nuclei via irradiation of electron energy transitions. Such a process is usually most effective at cryogenic temperatures, while NMR is most informative at ambient temperatures in solution. In their seminal work, Ardenkjaer-Larsen et al. [1] have demonstrated that after polarisation of nuclei at low temperatures the sample can be dissolved and measured in a conventional NMR system at room temperature. This approach leads to a rapid development of such dissolution DNP

systems primarily targeted towards studies of metabolites in living organisms, but also for studies of enzymatic and chemical reaction kinetics.

The overarching goal of this work is to develop a methodology for studies of protein folding kinetics using dissolution DNP when  $^{19}\text{F}$  labels are added to the protein.  $^{19}\text{F}$ -containing labels have previously been widely used for reporting on protein folding. The big advantages in using fluorinated compounds is the large  $^{19}\text{F}$  chemical shift dispersion, that leads to well-resolved peaks in the NMR spectra. Moreover, the absence of  $^{19}\text{F}$  background signals offers “clean” spectra compared to the ones obtained by observing at other nuclei like  $^1\text{H}$  or  $^{13}\text{C}$ . However, it remains difficult to perform dissolution DNP on  $^{19}\text{F}$  due to its short longitudinal relaxation time constant. In conventional dissolution DNP setups, the hyperpolarisation achieved would be lost between the dissolution and NMR acquisition processes, as the dead time in between these two processes is usually longer than the  $^{19}\text{F}$  relaxation time.

However, the dual iso-centre magnet at the University of Nottingham features a short dead time of 300 ms between the dissolution and sample transferring for NMR measurements. Such a short dead time opens an opportunity to explore the fast kinetic processes such as ligand binding and protein folding kinetics, allowing to acquire the hyperpolarised  $^{19}\text{F}$  NMR signal before it relaxes to thermal equilibrium.

Chapter 1 of this work presents an introduction to NMR spectroscopy, and the behaviour of spin 1/2 nuclei in presence of a static magnetic field is shown. An introduction to  $^{19}\text{F}$  NMR is also provided, showing what the main issues related to its sensitivity are, and how they can be overcome by means of dissolution DNP.

In Chapter 2 magnetic resonance relaxation is discussed, explaining why a perturbed spin ensemble in a magnetic field recovers its equilibrium status. Moreover, the main mechanisms responsible for relaxation are shown. The theory of these mechanisms is needed to understand some of the issues discussed in Chapters 5 and 6.

Chapter 3 presents the theory of DNP, and the main mechanisms that allow the polarisation transfer from electrons to nuclei are discussed, while in Chapter 4 brief introductions to the hardware and methodologies used for the experiments shown in this work are given. The spectrometers used for solid-state studies are presented, as well as the dual iso-centre magnet used for the dissolution DNP experiments. The main pulse sequences used to acquire the NMR spectra are also shown.

In Chapter 5, the feasibility of producing large  $^{19}\text{F}$  polarisation at cryogenic temperatures by means of DNP is investigated in order to optimise the DNP enhancement and to establish the optimal conditions and parameters which lead to the maximum enhancement of the  $^{19}\text{F}$  NMR signal. For these experiments, the free radical TEMPO has been used. In addition, a spontaneous polarisation transfer from hyperpolarised  $^1\text{H}$  nuclei to  $^{19}\text{F}$  under solid-state DNP conditions is observed and characterised. The experiments presented in this Chapter show the importance of the electrons in the transfer process.

In Chapter 6 the previously observed spontaneous polarisation transfer from  $^1\text{H}$  nuclei to  $^{19}\text{F}$  is studied in more detail. The free radical BDPA has been used in place of TEMPO to better understand the mechanisms that lead to this polarisation transfer. Results of DNP experiments are also shown where, alongside with the Solid Effect, a second DNP mechanism contributing for to the hyperpolarisation of  $^1\text{H}$  and  $^{19}\text{F}$  is observed. A quantum dynamical model is introduced to explain these results, and simulations are performed to validate the model.

Chapter 7 presents the conclusions of this work, where a methodology for studies of protein folding kinetics using dissolution DNP is developed. First, the longitudinal relaxation time constants of  $^{19}\text{F}$  containing compounds at room temperature are investigated, to show that  $^{19}\text{F}$  nuclei can retain the hyperpolarisation achieved through DNP during the dead time before the NMR acquisition in a dissolution DNP experiment.

Later in this Chapter, solid-state experiments are performed on simple fluorinated molecules, to optimise the  $^{19}\text{F}$  polarisation achieved through DNP. Finally, dissolution DNP experiments are performed on simple  $^{19}\text{F}$ -containing chemicals and, as a proof-of-principle, a dissolution DNP experiment is performed on a sample containing a fluorinated protein.

# Acknowledgements

I already knew that the “acknowledgements chapter” was going to be hard to write for me. Especially the start. So, I was wondering about a smart way to start them, maybe romantic. Eventually I stumbled on a clever idea: why not start with the time I took to complete this PhD? Almost four years is after all a life time for some animals. Maybe even a noble one, which was born the day I joined the University of Nottingham and died the day I submitted this thesis, after living a life full of adventure and discovery. A nice metaphor to describe my journey in the research world, I thought. Unfortunately, a quick search on the internet destroyed my enthusiasm, as the only result I found for a 4-year life span is the brown rat. So, the very same day I joined the “K-team”, a brown rat was born. Not very exciting. And as I was learning about superconducting magnets and four-spin quantum mechanics effects, this very same rat was, I don’t know, infesting a sewer, breeding, or whatever a brown rat does. It is not the good incipit I was hoping for, but still, it is one.

Anyway, back to the acknowledgements now. Starting from my supervisors Walter and Alexey, thanks for the guidance and help you gave throughout these years. Thanks to the early “K-team” mates: Ben, Sank, Adam, Ed, Dan, and Jamie, with whom I shared the first years of my PhD. Thanks also to the part of the team that accompanied me during the last years: I-can’t-be-bothered-Tommy, Subhradip (never say “break a leg” to wish him luck), Fed the flooder and Harry, the latest addition. Thanks to all the people in the SPMIC and thanks to the MSc fellows. And a big “thank you” to everyone else, lost or found, or that has always been there for me. Finally, a special thanks to mum and dad, who always loved and supported me (and still do).

# Contents

<b>1</b>	<b>Introduction</b>	<b>1</b>
1.1	Concepts in Nuclear Magnetic Resonance . . . . .	1
1.1.1	NMR spectroscopy . . . . .	2
1.1.2	Spin 1/2 particle in a static magnetic field . . . . .	2
1.1.3	Ensemble of spin 1/2 particles . . . . .	3
1.1.4	The density operator . . . . .	6
1.1.5	Radio frequency pulses . . . . .	7
1.2	$^{19}\text{F}$ NMR . . . . .	11
1.2.1	NMR sensitivity issue . . . . .	11
1.2.2	Dynamic Nuclear Polarisation . . . . .	12
1.2.3	Dissolution DNP . . . . .	13
1.2.4	$^{19}\text{F}$ hyperpolarisation . . . . .	14
1.2.5	Challenges in $^{19}\text{F}$ dissolution DNP . . . . .	14
<b>2</b>	<b>Relaxation in NMR</b>	<b>16</b>
2.1	Population and relaxation . . . . .	16
2.2	Origin of relaxation . . . . .	20
2.3	Spectral density function . . . . .	20
2.4	Mechanisms for relaxation . . . . .	22
2.5	Conclusion . . . . .	28
<b>3</b>	<b>Dynamic Nuclear Polarisation</b>	<b>29</b>
3.1	Principles of hyperpolarisation . . . . .	29
3.1.1	The Solid Effect . . . . .	30
3.1.2	The Cross Effect . . . . .	34

3.1.3	Thermal Mixing . . . . .	37
3.1.4	The Overhauser Effect . . . . .	38
<b>4</b>	<b>Hardware</b>	<b>40</b>
4.1	Solid state experiments . . . . .	40
4.1.1	Polariser . . . . .	40
4.1.2	Microwave source . . . . .	41
4.1.3	Probes . . . . .	41
4.1.4	Spectrometer for solid state measurement . . . . .	45
4.2	Dissolution DNP setup . . . . .	45
4.2.1	The dewar . . . . .	47
4.2.2	Quasi-optical microwave system . . . . .	48
4.2.3	Waveguide and sample cups . . . . .	49
4.2.4	Dissolution dock . . . . .	49
4.2.5	Line-broadening of the NMR line after dissolution . . . . .	51
4.3	Methodology for experiments performed in the polariser . . . . .	53
4.3.1	Frequency sweep experiments . . . . .	53
4.3.2	Saturation recovery . . . . .	54
4.3.3	Saturation recovery for cross-relaxation experiment . . . . .	55
4.3.4	Interleaved acquisition of $^1\text{H}$ and $^{19}\text{F}$ for cross-relaxation . . . . .	55
4.3.5	Saturation recovery with continuous $^1\text{H}$ saturation . . . . .	57
4.3.6	Temperature stability in the polariser . . . . .	58
<b>5</b>	<b><math>^{19}\text{F}</math> DNP optimisation and TEMPO-mediated <math>^1\text{H}</math>-<math>^{19}\text{F}</math> cross-relaxation at cryogenic temperatures</b>	<b>61</b>
5.1	Optimisation of $^{19}\text{F}$ DNP in solid state . . . . .	62
5.1.1	Samples . . . . .	63
5.1.2	Experiments and results . . . . .	64
5.1.3	Discussion . . . . .	70
5.2	$^1\text{H}$ - $^{19}\text{F}$ polarisation transfer under ss-DNP conditions . . . . .	75
5.2.1	Experimental evidence for polarisation transfer between $^1\text{H}$ and $^{19}\text{F}$ . . . . .	76
5.2.2	TEMPO concentration variation . . . . .	79

5.2.3	Transient polarisation in a sample without free radicals . . .	81
5.2.4	Cross-relaxation using the bi-radical TEKPol and narrow- linewidth free radical BDPA . . . . .	82
5.2.5	Characterisation of $^1\text{H}$ - $^{19}\text{F}$ cross-relaxation process for dif- ferent $^{19}\text{F}$ concentrations . . . . .	85
5.2.6	Discussion . . . . .	87
5.3	Conclusions . . . . .	95
<b>6</b>	<b>Cross-relaxation between <math>^1\text{H}</math> and <math>^{19}\text{F}</math> at cryogenic temperatures and DNP with the free radical BDPA</b>	<b>97</b>
6.1	$^{19}\text{F}$ - $^1\text{H}$ polarisation exchange at cryogenic temperatures without mi- crowave irradiation . . . . .	98
6.1.1	Sample preparation . . . . .	99
6.1.2	Saturation recovery experiments with and without continu- ous $^1\text{H}$ saturation in a sample free of paramagnetic centres .	100
6.1.3	Saturation recovery experiments with and without continu- ous $^1\text{H}$ saturation in samples with the free radical BDPA . .	102
6.1.4	Control experiment . . . . .	103
6.1.5	Discussion . . . . .	104
6.2	Enhancement by DNP . . . . .	110
6.2.1	Study of the DNP profile for samples with different BDPA concentrations . . . . .	114
6.3	Discussion . . . . .	117
6.4	Conclusions . . . . .	131
<b>7</b>	<b>Developing a methodology to study protein dynamics with <math>^{19}\text{F}</math> NMR after dissolution DNP</b>	<b>133</b>
7.1	Feasibility of $^{19}\text{F}$ dissolution DNP . . . . .	134
7.1.1	$T_1$ for different fluorinated chemicals . . . . .	134
7.1.2	$T_1$ for samples with different free radical concentration in liquid state . . . . .	138
7.1.3	Solid state DNP experiments . . . . .	139
7.1.4	Dissolution . . . . .	144

7.2	Hen egg-white Lysozyme . . . . .	147
7.2.1	<sup>19</sup> F labelling of lysozyme . . . . .	147
7.2.2	Labelled vs non-labelled protein . . . . .	150
7.2.3	DNP of labelled lysozyme in solid state . . . . .	150
7.3	Dissolution DNP of labelled lysozyme . . . . .	152
7.4	Conclusions . . . . .	154
<b>8</b>	<b>Conclusions</b>	<b>156</b>
8.1	Outlook . . . . .	156
8.2	Future works . . . . .	158

# List of Figures

1.1	Polarisation as a function of the temperature at 3.4 T . . . . .	5
1.2	Magnetisation in a magnetic field before and after a RF pulse . . .	9
1.3	Example of a simple pulse sequence . . . . .	10
2.1	Energy levels of a spin 1/2 nucleus in a magnetic field $B_0$ . . . . .	17
3.1	Solid Effect energy levels . . . . .	32
3.2	Cross Effect energy levels . . . . .	35
3.3	Schematic diagram of Thermal Mixing . . . . .	38
4.1	Picture and schematic representation of the “polariser” . . . . .	42
4.2	Circuit diagram for the tuning box for two frequencies . . . . .	44
4.3	Probes used for the solid-state experiments . . . . .	44
4.4	Scematic picture of the routing for the “polariser” . . . . .	45
4.5	Magnetic field profile and section of the dual iso-centre magnet . . .	48
4.6	Sample cups used with the dual iso-centre magnet . . . . .	50
4.7	The dissolution set-up . . . . .	51
4.8	Dual iso-centre magnet schematics . . . . .	52
4.9	Pulse sequence used in a frequency sweep experiment . . . . .	54
4.10	Pulse sequence used for saturation recovery experiments . . . . .	55
4.11	Pulse sequence used during experiments to study cross-relaxation .	56
4.12	Pulse sequence used in the multizg experiments for cross-relaxation	57
4.13	Pulse sequence used during experiments with $^1\text{H}$ saturation . . . . .	58
4.14	Temperature and helium level in the “polariser” . . . . .	59
5.1	Chemical structures of the fluorobenzene, toluene and TEMPO . . .	62
5.2	DNP enhancement profile for $^{19}\text{F}$ and $^1\text{H}$ in a sample with TEMPO	65

5.3	$^{19}\text{F}$ DNP build-up experiment in a sample with TEMPO . . . . .	66
5.4	Solid state $^{19}\text{F}$ spectra with different SNR . . . . .	68
5.5	$T_1$ , $\tau_{\text{DNP}}$ and enhancement for $^{19}\text{F}$ and $^1\text{H}$ . . . . .	71
5.6	$T_1$ as a function of the $^{19}\text{F}$ concentration . . . . .	73
5.7	Evidence of transient $^{19}\text{F}$ polarisation . . . . .	78
5.8	Double quasi-simultaneous acquisition experiments for the samples containing TEMPO . . . . .	80
5.9	$^{19}\text{F}$ saturation recovery with and without $^1\text{H}$ saturation . . . . .	81
5.10	Chemical structure of the TEKPol molecule . . . . .	83
5.11	DNP enhancement profile of $^{19}\text{F}$ for the sample containing TEKPol	83
5.12	Double quasi-simultaneous acquisition experiment for the sample containing TEKPol . . . . .	84
5.13	Double quasi-simultaneous acquisition experiment for the sample containing BDPA . . . . .	84
5.14	$^{19}\text{F}$ polarisation for the non deuterated samples containing TEMPO	85
5.15	$^{19}\text{F}$ polarisation for the deuterated samples containing TEMPO . .	86
5.16	Schematic diagram of two energy reservoirs . . . . .	89
5.17	Schematic diagram of the energy reservoirs with electrons . . . . .	89
6.1	Energy levels of a two spin system A and B. . . . .	98
6.2	Chemical structure of a BDPA molecule . . . . .	99
6.3	Saturation recovery with and without $^1\text{H}$ saturation . . . . .	101
6.4	Saturation recovery with and without $^1\text{H}$ in samples with BDPA . .	102
6.5	Control saturation recovery experiment . . . . .	104
6.6	DNP enhancement profile of $^{19}\text{F}$ and $^1\text{H}$ for the sample with BDPA	111
6.7	Positive Solid Effect DNP enhancement profile of $^{19}\text{F}$ . . . . .	112
6.8	Positive Solid Effect DNP enhancement profile of $^{19}\text{F}$ and $^1\text{H}$ . . . .	113
6.9	DNP enhancement profile for samples with different concentrations of BDPA . . . . .	114
6.10	$^{19}\text{F}$ DNP profile in the central region of the frequency spectrum . .	116
6.11	Energy levels of a three spin system . . . . .	119
6.12	Energy levels of a four spin system . . . . .	124

6.13	Saturation recovery with and without microwave irradiation at the frequency of heCE . . . . .	126
6.14	Simulated DNP spectra of the four spin system in the SE region . .	127
6.15	Simulated DNP spectra of the four spin system in the heCE region	128
6.16	Simulated DNP spectra of the four spin system in the heCE region (different coupling constants) . . . . .	129
6.17	Maximum $^{19}\text{F}$ enhancements shown in a colour map . . . . .	130
6.18	Maximum $^1\text{H}$ enhancements shown in a colour map . . . . .	130
6.19	Maximal steady-state $^{19}\text{F}$ polarisation . . . . .	131
7.1	$^{19}\text{F}$ spectrum before and after background removal . . . . .	137
7.2	Microwave allignment in the “x” direction . . . . .	140
7.3	Microwave allignment in the “y” direction . . . . .	141
7.4	DNP enhancement profile of $^{19}\text{F}$ . . . . .	142
7.5	$^{19}\text{F}$ DNP build-up experiment . . . . .	143
7.6	Dissolution DNP enhanced and thermal $^{19}\text{F}$ spectrum . . . . .	146
7.7	$^{19}\text{F}$ NMR spectrum of the labelled lysozyme . . . . .	148
7.8	Inversion recovery of $^{19}\text{F}$ in the lysozyme with TEMPOL . . . . .	150
7.9	DNP enhancement profile of $^{19}\text{F}$ in lysozyme . . . . .	151
7.10	Saturation recovery of $^{19}\text{F}$ in lysozyme during microwave irradiation	152
7.11	Chemical structure of 5-fluorouracil. . . . .	153
7.12	$^{19}\text{F}$ dissolution DNP enhanced spectrum . . . . .	153
7.13	$^{19}\text{F}$ dissolution DNP enhanced spectrum of labelled lysozyme . . . .	154

# List of Tables

5.1	Compositions of samples studied with different $^{19}\text{F}$ concentrations . . . . .	64
5.2	$T_1$ , $\tau_{\text{DNP}}$ and $\epsilon$ for the non deuterated samples with TEMPO . . . . .	67
5.3	$T_1$ , $\tau_{\text{DNP}}$ and $\epsilon$ for the deuterated samples with TEMPO . . . . .	67
5.4	$T_1$ , $\tau_{\text{DNP}}$ and $\epsilon$ for the samples with BDPA and TEKPol . . . . .	68
5.5	$T_1$ , $\epsilon$ and temperatures of the experiments performed using TEMPO	90
5.6	$T_1$ , $\epsilon$ and temperatures of the experiments performed using TEKPol and BDPA . . . . .	92
5.7	$^1\text{H}$ $T_1$ and $\sigma^{-1}$ for the samples containing TEMPO . . . . .	94
6.1	Samples used for the experiments described in this Chapter. . . . .	100
6.2	Build-up time constants and steady-state polarisation ratios . . . . .	103
6.3	Intrinsic $R_F$ and $\sigma$ . . . . .	106
6.4	Contribution of $T_1^{eF}$ to the intrinsic $T_1$ . . . . .	108
6.5	Contribution of $\sigma_{par}$ to the total $\sigma$ . . . . .	109
6.6	$T_1$ , $\tau_{\text{DNP}}$ and $\epsilon$ for the samples with BDPA . . . . .	115
6.7	$T_1$ , $\tau_{\text{DNP}}$ and $\epsilon$ at low microwave power . . . . .	116
7.1	$T_1$ values for the fluorinated samples in different solvent. . . . .	138
7.2	$^{19}\text{F}$ $T_1$ for different TEMPOL concentrations . . . . .	139
7.3	$\tau_{\text{DNP}}$ and integrals obtained by means of the saturation recovery . . . . .	143
7.4	Fluorinated samples used to test dissolution DNP. . . . .	144
7.5	Enhancements achieved after dissolution DNP . . . . .	145
7.6	Assignment of the labelled lysine amino acids . . . . .	149
7.7	Values for $^{19}\text{F}$ $T_1$ in the labelled protein . . . . .	149

# Chapter 1

## Introduction

In this Chapter, a brief introduction to concepts of Nuclear Magnetic Resonance (NMR) is provided. First, the behaviour of a single spin in a magnetic field is described. Then, an ensemble of spins is analysed, and its macroscopic properties as a function of temperature are shown. Finally, an introduction to fluorine nuclei is given, showing why  $^{19}\text{F}$  NMR is important, what the issues related to its sensitivity are, and how dissolution Dynamic Nuclear Polarisation (DNP) could be a useful tool to overcome these problems.

### 1.1 Concepts in Nuclear Magnetic Resonance

When a nucleus is placed in a magnetic field, its magnetic moment interacts with the external magnetic field, forming energy levels split by the Zeeman energy [2]. Nuclear Magnetic Resonance spectroscopy is an analytical technique that takes advantage of this nuclear behaviour to measure the energy transitions due to the Zeeman splitting. This technique allows investigation of the physical environment around the nucleus, and to study the interactions with other nuclei and electrons. Several properties related to NMR provide important information on the nuclei in a sample. For example, the electrons surrounding nuclei in a molecule shift their resonance frequency (this phenomenon is the so-called “chemical shift”). Also, the interaction between two or more nuclei gives rise to a splitting of the resonance lines, where the separation of the lines reflects the strength of the interaction, which in turn depends on the distances between the interacting nuclei.

### 1.1.1 NMR spectroscopy

Spin is an intrinsic property of a quantum particle. The spin of a particle is, among other things, responsible for its interaction with magnetic fields. It is possible to build an analogy with the angular momentum of a rotating object that interact with a gravitational field. A spin placed in a time-independent magnetic field precesses in the same way a spinning top's symmetry axis precesses about the gravitational field. The precession frequency of a spin in a magnetic field is called "Larmor Frequency", and it is defined as  $\omega_I = \gamma B_0$ , where  $B_0$  is the intensity of the field and  $\gamma$  is the "gyromagnetic ratio", a physical constant characteristic of particles or nuclei of given species.

Spin behaves like a pseudo-vector, and because of the laws of quantum mechanics, it can have only a well determined number of orientations. These orientations are conventionally taken as projections of the spin along the  $z$ -axis, parallel to the direction of the static magnetic field.

### 1.1.2 Spin 1/2 particle in a static magnetic field

All the information concerning the dynamics of a quantum particle is contained in the Hamiltonian operator, a physical quantity that can be related to the total energy of a particle.

For a single particle in a static magnetic field  $B_0$ , the Hamiltonian operator can be expressed by the equation

$$\mathcal{H}_{\text{total}} = \mathcal{H}_{\text{free}} + \mathcal{H}_{\text{spin}}, \quad (1.1)$$

where  $\mathcal{H}_{\text{free}}$  is a term related to the kinetic energy of the particle, and  $\mathcal{H}_{\text{spin}}$  describes the interaction of that particle with the magnetic field  $B_0$ . The particle state is represented by the wave function  $|\psi(t)_{\text{total}}\rangle$  which obeys the Schrödinger equation:

$$\frac{d}{dt} |\psi(t)_{\text{total}}\rangle = -\frac{i}{\hbar} \mathcal{H}_{\text{total}} |\psi(t)_{\text{total}}\rangle. \quad (1.2)$$

According to the so-called "spin Hamiltonian hypothesis" [3], it is possible to neglect all the terms of the Hamiltonian but the spin term, by assuming that

the spin behaviour is independent of the other terms affecting the dynamics of a particle.

For a single particle in a static magnetic field along the  $z$  direction ( $\vec{B} = B_0\hat{z}$ ),  $\mathcal{H}_{\text{spin}}$  can be written as

$$\mathcal{H}_{\text{spin}} = \mathcal{H}_0 = -\gamma\hat{I}_z\hbar B_0, \quad (1.3)$$

where  $\hat{I}_z$  is a quantum mechanical spin operator and  $\hbar$  is the reduced Planck constant.

According to the rules of quantum mechanics, a spin  $S$  particle can have  $2S + 1$  possible spin eigenvalues of the  $I_z$  spin operator, denoted by  $m_z$  ( $m_z = -S, -S + 1, \dots, S - 1, S$ ). Each one of these eigenvalues corresponds to a projection of the spin along the  $z$ -axis. For a  $1/2$  spin particle, only two opposite directions are possible, described by  $m_z = -1/2$  and  $m_z = +1/2$ . These two states are commonly known as the “spin down” state and “spin up” state respectively.

The energy of a particle related to the spin part of the Hamiltonian is therefore proportional to the spin projection  $m_z$ , the intensity of the magnetic field  $B_0$  and the gyromagnetic ratio  $\gamma$ :

$$E = -\gamma\hbar m_z B_0 = -m_z\hbar\omega_I. \quad (1.4)$$

Using Equation 1.4, it is easy to show that the difference in energy between two identical spin  $1/2$  particles with opposite spin is equal to

$$\Delta E = \gamma B_0\hbar = \hbar\omega_I. \quad (1.5)$$

### 1.1.3 Ensemble of spin 1/2 particles

Since for the works presented in this thesis all studied nuclei have spin  $S = 1/2$ , only this case will be considered.

An ensemble of spin  $1/2$  particles obeys the laws of thermodynamics, and the spin population is distributed in the energy levels according to the Boltzmann distribution:

$$\exp\left(-\frac{E}{k_B T}\right). \quad (1.6)$$

In this equation,  $k_B$  is the Boltzmann constant and  $T$  is the temperature of the system.

If  $N$  is the total number of spins in the sample, the number of spins which populate the  $\pm 1/2$  energy level are

$$\begin{aligned}
 N_\alpha &= N \frac{\exp\left(-\frac{\hbar\omega_I}{2k_B T}\right)}{\exp\left(\frac{\hbar\omega_I}{2k_B T}\right) + \exp\left(-\frac{\hbar\omega_I}{2k_B T}\right)} \\
 N_\beta &= N \frac{\exp\left(\frac{\hbar\omega_I}{2k_B T}\right)}{\exp\left(\frac{\hbar\omega_I}{2k_B T}\right) + \exp\left(-\frac{\hbar\omega_I}{2k_B T}\right)}.
 \end{aligned}
 \tag{1.7}$$

Since the exponents of Equations 1.7 are very small<sup>1</sup>, it is possible to perform a Taylor series expansion and take into account only the first order, obtaining the equation for the “high temperature approximation”:

$$\begin{aligned}
 N_\alpha &= \frac{N}{2} \left(1 - \frac{\hbar\omega_I}{2k_B T}\right) \\
 N_\beta &= \frac{N}{2} \left(1 + \frac{\hbar\omega_I}{2k_B T}\right),
 \end{aligned}
 \tag{1.8}$$

At room temperature both energy levels are almost equally populated, since the thermal energy is much larger than the energy term related to the magnetic field, with a small population excess in the lower energy state.

The polarisation of a spin ensemble is defined as the difference in the number of spins that populate the spin up and spin down energy levels over the total number of spins in the ensemble:

$$P = \frac{N_\alpha - N_\beta}{N} = \tanh\left(\frac{\hbar\omega_I}{2k_B T}\right) \simeq \frac{\hbar\omega_I}{2k_B T}.
 \tag{1.9}$$

The net polarisation of the ensemble is directly proportional to the magnetic field and indirectly proportional to the temperature. In Figure 1.1 the polarisations of  $^1\text{H}$ ,  $^{19}\text{F}$  and  $e^-$  ensembles as functions of the temperature in a static magnetic fields of 3.4 T are shown. The net polarisation of the electrons is  $\sim 660$  times the  $^1\text{H}$  one, since it is proportional to the ratio of the gyromagnetic constants.

---

<sup>1</sup>Even at a very low temperature ( $\sim 1.5$  K) in a magnetic field of 9.4 T for  $^1\text{H}$  nuclei, it is  $\sim 6.4 \cdot 10^{-3}$

The macroscopic quantity associated with the polarisation is the “magnetisation”.

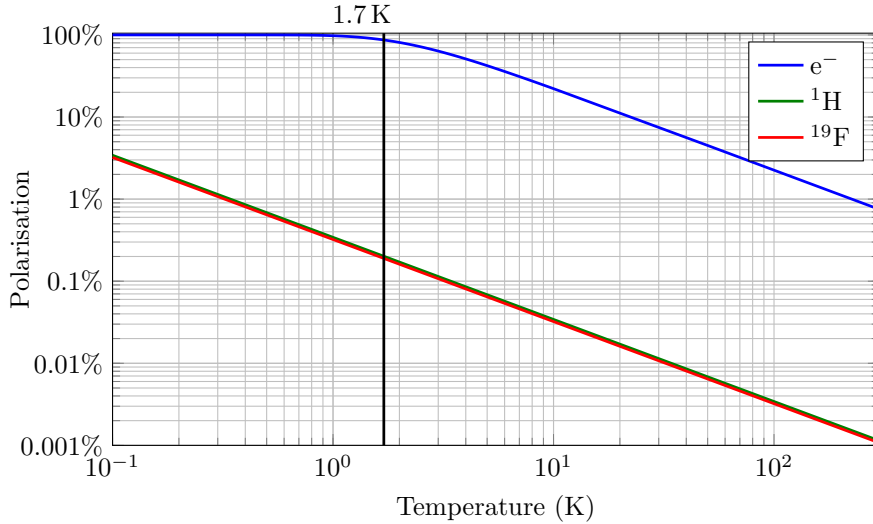


Figure 1.1: Temperature dependence of  $^1\text{H}$ ,  $^{19}\text{F}$  and  $e^-$  polarisations in a 3.4 T magnetic field. The “solid state” experiments described in Chapters 5 and 6 of this thesis are carried out at 1.7 K, marked by a vertical black line in the figure.

When the ensemble is at equilibrium, its magnetisation  $\vec{M}$  is defined as:

$$\vec{M} = \frac{1}{2}N\hbar\gamma P\hat{z}. \quad (1.10)$$

The magnetisation is therefore a vector parallel to the static magnetic field. If the magnetisation is perturbed from its equilibrium, it will return to the starting configuration according to the well-known Bloch Equations 1.11 [4], which describe its dynamics. In their differential form, this set of equations is written as

$$\begin{aligned} \frac{dM_x(t)}{dt} &= \gamma \left( \vec{M}(t) \times \vec{B}(t) \right)_x - \frac{M_x(t)}{T_2} \\ \frac{dM_y(t)}{dt} &= \gamma \left( \vec{M}(t) \times \vec{B}(t) \right)_y - \frac{M_y(t)}{T_2} \\ \frac{dM_z(t)}{dt} &= \gamma \left( \vec{M}(t) \times \vec{B}(t) \right)_z - \frac{M_z(t) - M_0}{T_1}. \end{aligned} \quad (1.11)$$

Equations 1.11 introduce relaxation as an important concept in NMR.  $T_1$ , known also as the longitudinal relaxation time constant, is the characteristic time for the recovery of the longitudinal magnetisation  $M_z$ .  $T_2$ , the transverse relaxation time, is the characteristic time of loss of magnetisation in the  $x - y$  plane.

It can be demonstrated [2] that when the magnetisation is perturbed in a state

$\vec{M} = M_0 \hat{x}$ , the solutions of 1.11 are given by:

$$\begin{aligned} M_x(t) &= M_0 \exp\left\{-\frac{t}{T_2}\right\} \cos(\omega_I t) \\ M_y(t) &= M_0 \exp\left\{-\frac{t}{T_2}\right\} \sin(\omega_I t) \\ M_z(t) &= M_0 \left[1 - \exp\left\{-\frac{t}{T_1}\right\}\right] \end{aligned} \quad (1.12)$$

These equations show that the transverse magnetisation rotates with frequency  $\omega_I$  around the magnetic field direction, and this frequency coincides with the Larmor frequency of the nuclei of the spin ensemble.

Although the concept of magnetisation represents a classical and intuitive approach to spin mechanics, it is not useful for the analysis of interacting nuclei. A formalism that describes the dynamics of an ensemble of spins in quantum mechanics is based on the use of the density operator. In the next section this approach is explained, since it can be used as a powerful tool to predict the spin ensemble behaviour in presence of the more complex interactions.

#### 1.1.4 The density operator

In quantum mechanics a single 1/2 spin particle is represented by the vector

$$|\psi\rangle = \begin{pmatrix} c_\alpha \\ c_\beta \end{pmatrix}. \quad (1.13)$$

$c_\alpha$  and  $c_\beta$  are coefficients such that  $|c_\alpha|^2$  and  $|c_\beta|^2$  are the probabilities of that particle to be in the eigenstate of  $I_Z$   $|\alpha\rangle = \begin{pmatrix} 1 \\ 0 \end{pmatrix}$  or  $|\beta\rangle = \begin{pmatrix} 0 \\ 1 \end{pmatrix}$  (the “spin up” or “spin down” states respectively). The density operator  $\rho$  is defined by the matrix

$$\rho = |\psi\rangle \langle\psi| = \begin{pmatrix} c_\alpha c_\alpha^* & c_\alpha c_\beta^* \\ c_\beta c_\alpha^* & c_\beta c_\beta^* \end{pmatrix}, \quad (1.14)$$

and it is used to describe a system made up from a large number of spins representing a spin ensemble. The diagonal terms  $c_\alpha c_\alpha^*$  and  $c_\beta c_\beta^*$  are the “populations” of the spin up and down states. At the equilibrium condition they are  $(c_\alpha c_\alpha^*)_{eq} = \frac{N_\alpha}{N}$

and  $(c_\beta c_\beta^*)_{eq} = \frac{N_\beta}{N}$ , defined in Section 1.1.3. The off-diagonal terms  $c_\alpha c_\beta^*$  and  $c_\beta c_\alpha^*$  represent “coherences”, related to the transverse magnetisation of the spin ensemble. At equilibrium there is no transverse magnetisation, and the system has no coherence. It can be shown [3] that the amplitude of the NMR signal is proportional to the modulus of the coherence:

$$A = 2i\rho_-(0) \exp(-i\Phi_{\text{rec}}) \quad (1.15)$$

where  $\rho_-(0) = c_\beta c_\alpha^*(0)$  is the value of the coherence at the beginning of the signal detection, while  $\Phi_{\text{rec}}$  is a phase introduced in the receiver in order to detect the signal. In other terms, whenever a coherence is present, an NMR signal can be detected.

The time evolution of the density operator is given by the Liouville-von Neumann equation, that describes how the Hamiltonian operator affects the density matrix. This equation can be written in the form:

$$\frac{d\rho}{dt} = -\frac{i}{\hbar}[\rho, \mathcal{H}_{\text{spin}}]. \quad (1.16)$$

This equation is particularly useful for more complex spin systems in which several types of quantum particles are interacting.

### 1.1.5 Radio frequency pulses

As stated in Section 1.1.3, at equilibrium the spin ensemble is described by the density operator

$$\rho_{eq} = \begin{pmatrix} \frac{N_\alpha}{N} & 0 \\ 0 & \frac{N_\beta}{N} \end{pmatrix} \simeq \frac{1}{2} \begin{pmatrix} 1 + \frac{\hbar\omega_I}{2k_B T} & 0 \\ 0 & 1 - \frac{\hbar\omega_I}{2k_B T} \end{pmatrix}. \quad (1.17)$$

It is useful to write the density operator in terms of spin operators:

$$\rho_{eq} = \frac{1}{2}\mathbb{1} + \frac{1}{4} \frac{\hbar\omega_I}{k_B T} I_z, \quad (1.18)$$

where  $\mathbb{1}$  is the  $2 \times 2$  identity matrix.

The following section describes how a spin ensemble can be driven away from

equilibrium by applying radio frequency (RF) pulses.

Consider a magnetic field  $\vec{B}_1$  with the following properties:

1. it is orthogonal to the static magnetic field along the  $z$ -axis;
2. it oscillates at a frequency  $\omega_{RF}$  close to the Larmor frequency of the spins in the ensemble, and has a phase  $\Phi$ .

Under these conditions, this new field can be written as:

$$\vec{B}_1(t) = \frac{1}{2}B_{RF} [\cos(\omega_{RF}t + \Phi)\hat{x} + \sin(\omega_{RF}t + \Phi)\hat{y}] \quad (1.19)$$

This radio frequency pulsed field introduces a new term in the spin Hamiltonian:

$$\mathcal{H}_{RF} \cong - \left| \frac{1}{2}\hbar\gamma B_{RF} \right| \left\{ \cos(\omega_{RF}t + \Phi)\hat{I}_x + \sin(\omega_{RF}t + \Phi)\hat{I}_y \right\}. \quad (1.20)$$

This new term is a sum of two components, one proportional to  $\hat{I}_x$  and the other to  $\hat{I}_y$ . Since  $\mathcal{H}_{RF}$  and  $\mathcal{H}_0$  do not commute, the spin system will be perturbed from its equilibrium state  $\rho_{eq}$ . The evolution of the density operator is

$$\rho(t + \Delta t) = \exp(-i\mathcal{H}_{spin}\Delta t)\rho(t)\exp(i\mathcal{H}_{spin}\Delta t). \quad (1.21)$$

In order to simplify the next steps, it is useful to move from the laboratory frame of reference to a frame of reference that rotates at a frequency  $\omega_{RF}$  around the  $z$ -axis. This is often referred to as the “rotating frame”. In this particular frame of reference, the Hamiltonian operator changes as shown in Equation 1.22:

$$\begin{aligned} \mathcal{H}_0 &\longmapsto (\omega_I - \omega_{RF})\hbar\hat{I}_z = \Omega_0\hbar\hat{I}_z \\ \mathcal{H}_{RF} &\longmapsto \left| \frac{1}{2}\hbar\gamma B_{RF} \right| \left\{ \cos(\Phi)\hat{I}_x + \sin(\Phi)\hat{I}_y \right\}. \end{aligned} \quad (1.22)$$

The quantity  $\left| \frac{1}{2}\gamma B_{RF} \right| = \omega_{nut}$  is the “nutaton frequency”, and is used to express the intensity of the radio-frequency field.

In the rotating frame, a frequency offset  $\Omega_0$  is therefore introduced, and the frequency detected will be the difference between the Larmor frequency of the nuclei in the sample and the frequency  $\omega_{RF}$  at which the frame rotates.

If  $B_{RF}$  acts for a time interval  $\Delta t$ , the corresponding Hamiltonian term behaves like a rotation operator, flipping the magnetisation around the direction in the  $x - y$  plane that forms an angle  $\Phi$  with the  $x$ -axis (a value  $\Phi = 0$  corresponds to the  $x$ -axis, while a value  $\Phi = \pi/2$  corresponds to the  $y$ -axis). This so-called “flip angle”  $\beta = \omega_{nut}\Delta t$  depends on the duration of the pulse and on the intensity of the pulsed magnetic field. Figure 1.2 shows the effect of a radio-frequency pulse on the magnetisation vector. Equation 1.21 becomes

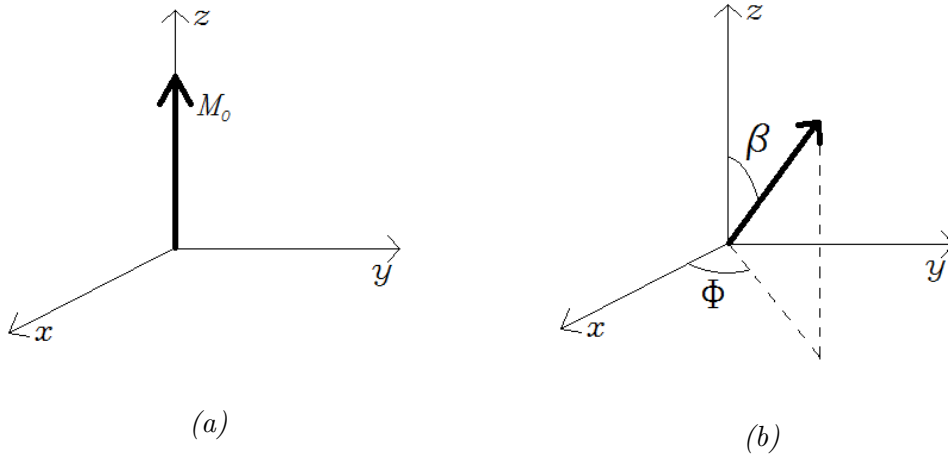


Figure 1.2: (a) Magnetisation  $M_0$  of a spin ensemble in a static magnetic field directed along the  $z$ -axis at thermal equilibrium. (b) The effect of a  $\beta$  flip angle pulse on the magnetisation.

$$\rho(t + \Delta t) = R_\Phi(\beta)\rho(t)R_\Phi(-\beta) \quad (1.23)$$

and the rotation operator can be written as

$$\begin{aligned} R_\Phi(\beta) &= \cos\left(\frac{\beta}{2}\right)\mathbb{1} - i\sin\left(\frac{\beta}{2}\right)\left(\cos(\Phi)\hat{I}_x + \sin(\Phi)\hat{I}_y\right) \\ &= \begin{pmatrix} \cos\left(\frac{\beta}{2}\right) & -i\sin\left(\frac{\beta}{2}\right)\exp(-i\Phi) \\ -i\sin\left(\frac{\beta}{2}\right)\exp(i\Phi) & \cos\left(\frac{\beta}{2}\right) \end{pmatrix}. \end{aligned} \quad (1.24)$$

It is easy to show that as the rotation operator  $R_\Phi(\beta)$  acts on the density operator, as shown in Equation 1.23, it generates off-diagonal terms in the density operator, which represent coherences and can be detected by the receiver to generate a NMR signal.

For example, suppose that a  $\beta$  flip angle pulse around the  $x$ -axis is applied to a sample of spin 1/2 particles initially at thermal equilibrium in a static magnetic field along the  $z$ -axis, as shown in Figure 1.3. Data acquisition begins after the pulse. Before the RF pulse, the density operator  $\rho_1$  is equal to  $\rho_{eq}$  (Equation 1.18),

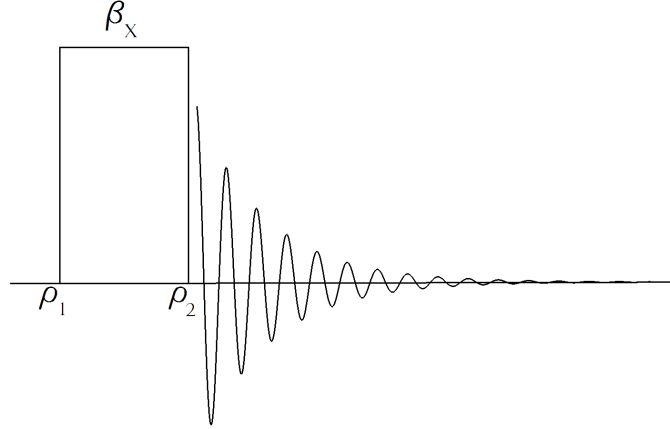


*Figure 1.3:* Schematic representation of a RF pulse sequence in which a NMR signal is acquired after a  $\beta$  flip angle pulse.  $\rho_1$  is the density operator before and  $\rho_2$  is the density operator after the RF pulse. The acquisition, illustrated with a Free Induction Decay (FID) in the figure, starts after the pulse ends.

since the ensemble is at thermal equilibrium. After the pulse, the density operator evolves according to Equation 1.23, becoming:

$$\begin{aligned}
 \rho_2 &= R_x(\beta)\rho_1R_x(-\beta) \\
 &= \frac{1}{2} \begin{pmatrix} \cos(\frac{\beta}{2}) & -i \sin(\frac{\beta}{2}) \\ -i \sin(\frac{\beta}{2}) & \cos(\frac{\beta}{2}) \end{pmatrix} \begin{pmatrix} 1 + \frac{\hbar\omega_I}{2k_B T} & 0 \\ 0 & 1 - \frac{\hbar\omega_I}{2k_B T} \end{pmatrix} \begin{pmatrix} \cos(\frac{\beta}{2}) & i \sin(\frac{\beta}{2}) \\ i \sin(\frac{\beta}{2}) & \cos(\frac{\beta}{2}) \end{pmatrix} \\
 &= \frac{1}{2} \begin{pmatrix} 1 + \frac{\hbar\omega_I}{2k_B T} \cos(\beta) & i \frac{\hbar\omega_I}{2k_B T} \sin(\beta) \\ -i \frac{\hbar\omega_I}{2k_B T} \sin(\beta) & 1 - \frac{\hbar\omega_I}{2k_B T} \cos(\beta) \end{pmatrix}.
 \end{aligned} \tag{1.25}$$

According to what was previously stated, the amplitude of the NMR signal generated after the pulse is proportional to the coherence  $-i \frac{\hbar\omega_I}{2k_B T} \sin(\beta)$ .

This is the simplest example for a RF pulse that generates coherences in a nuclear ensemble. Other pulse sequences, used in the experiments shown in this thesis,

will be described in Chapter 4.

## 1.2 $^{19}\text{F}$ NMR

Among the nuclei which have a spin quantum number, fluorine stands out for several reasons. Fluorine is the 9<sup>th</sup> element in the periodic table. Its nucleus has a spin quantum number of 1/2, and has a large gyromagnetic ratio (94% of  $^1\text{H}$ ) which makes its detection by NMR rather sensitive [5]. Moreover,  $^{19}\text{F}$  is the only stable isotope of fluorine, and therefore it has a 100% natural abundance.

In contrast to  $^1\text{H}$ ,  $^{19}\text{F}$  atoms contain 9 electrons, which cause a large chemical shielding and greater sensitivity to the local environment. For these reasons, fluorine NMR spectroscopy has a wide application range in chemistry and biochemistry. Among others applications, it can be used for drug analysis through ligand-binder interactions [6], as well as in studies of protein structure and dynamics [7]. In both cases, the lack of background signals is a big advantage compared to the crowded spectra of commonly used nuclei.

### 1.2.1 NMR sensitivity issue

Among other factors, the sensitivity of NMR experiments depends on the overall magnetisation of the sample. As shown in the previous section, the magnetisation of spin 1/2 nuclei in the high temperature approximation is given by:

$$|M| = \frac{N\hbar^2\gamma^2 B_0}{4k_B T}. \quad (1.26)$$

This equation shows that if the temperature and the magnetic field are fixed, the magnitude of the NMR signal is proportional to the number of nuclei in the sample. Also, the sensitivity depends on the square of the gyromagnetic ratio, so the lower its value, the more difficult the detection of the NMR signal [8].

The great natural abundance and sensitivity of  $^1\text{H}$  makes NMR a powerful analysis tool. However, sometimes the use of different nuclei is required: for example, the  $^{13}\text{C}$  isotope in pyruvate is used for in-vivo imaging because of its slow relaxation to detect and diagnose tumours in animals and humans [9].

Nonetheless, the small gyromagnetic ratio of  $^{13}\text{C}$  ( $\sim 1/4$  of the proton one) and natural abundance of this isotope ( $\simeq 1.1\%$ ) make the detection of such signals results difficult because of the low Signal-to-Noise Ratio (SNR). Although  $^{19}\text{F}$  has a gyromagnetic ratio similar to the  $^1\text{H}$  one and its natural abundance is 100%, other issues are related to the use of this nuclear specie in NMR. For example, in ligand binding experiments and studies of enzymatic reactions and other kinetic processes, tracking molecules at micromolar concentration could be required. This also causes a low SNR since the amplitude of the NMR signal depends also on the concentration of nuclei.

For these reasons, it is very important to overcome the sensitivity issue by enhancing the magnitude of the signal while keeping a low nuclear concentration.

In light of these considerations, there is a great potential if the NMR sensitivity could be improved, since it opens up possibilities to study systems that could not be studied otherwise. Dynamic Nuclear Polarisation (DNP) [10] is one of the approaches which increases significantly the NMR signals by transferring the large electron polarisation to nuclei under microwave irradiation.

## 1.2.2 Dynamic Nuclear Polarisation

In the high temperature approximation,  $^1\text{H}$  polarisation, as shown in Figure 1.1, is around 660 times less than that of the electrons. The difference in polarisation with electron spins is even larger for other nuclei with lower  $\gamma$ , such as  $^{13}\text{C}$ ,  $^{15}\text{N}$  and  $^{19}\text{F}$ .

The polarisation transfer through DNP is achieved by irradiating the sample with microwaves (MW) at a frequency near to the electron Larmor frequency, and the maximum theoretical enhancement can be calculated as  $\frac{\gamma_e}{\gamma_N}$ , where  $\gamma_e$  and  $\gamma_N$  are the gyromagnetic ratio of the electron and the nucleus respectively.

The theory of DNP will be discussed in detail in Chapter 3. During a DNP experiment, the system is driven into a new quasi-equilibrium state with a spin polarisation that is higher than the thermal one by several orders of magnitude. For example, typical values obtained for the  $^{13}\text{C}$  polarisation after DNP are in the range of 10 – 30% [11, 12].

### 1.2.3 Dissolution DNP

Equation 1.9 shows that nuclear polarisation increases by lowering the temperature. At  $\approx 1$  K and 3.4 T, the electron polarisation is  $\sim 100\%$ . Dissolution DNP is a technique which combines DNP with the temperature jump effect through a fast dissolution of the sample. In a dissolution DNP experiment, the sample is cooled down to cryogenic temperature, and polarised under microwave irradiation. Then, it is dissolved and brought to room temperature with a hot solvent, and transferred into another magnet where the NMR experiment is performed. With this technique it is possible to measure hyperpolarised NMR signals at room temperature, where usually biologically relevant processes take place.

Ardenkjaer-Larsen et al. [1] demonstrated in 2003 the feasibility of this technique. They polarised  $^{13}\text{C}$ -urea at 1.1 K in a 3.4 T magnet and acquired the NMR signal in a 9.4 T magnet after dissolution, achieving an enhancement in the magnitude of the NMR signal by a factor greater than 10 000.

However, a limitation of dissolution DNP experiments is given by the nuclear longitudinal relaxation time constant  $T_1$ . Since the equilibrium nuclear magnetisation is recovered according to the nuclear  $T_1$ , the dissolution procedure and the sample transfer into the NMR magnet must occur on a time scale shorter than  $T_1$ , so that no significant polarisation is lost during the process. This delay between dissolution and acquisition, usually of the order of few seconds, limits the use of dissolution DNP to nuclei with long longitudinal relaxation time constants. For this reason,  $^{13}\text{C}$  is commonly employed since, depending on the used chemical, it features long  $T_1$  time constants. For example,  $^{13}\text{C}$   $T_1$  in pyruvate ranges between  $\approx 45$  s and  $\approx 1$  min, depending on the magnetic field [13].

One of the main goals of the NMR scientific community is to perform in-vivo MRI to track hyperpolarised contrast agents [9], where nuclei with long relaxation times  $T_1$ , such as  $^{13}\text{C}$  and  $^{15}\text{N}$  are commonly used, and much effort has been dedicated to optimise the DNP mechanisms that drive their polarisation.

On the other hand, DNP of nuclei with short  $T_1$  relaxation time constants such as  $^1\text{H}$  and  $^{19}\text{F}$  prove themselves to be worthy of study: for example,  $^1\text{H}$  is currently used to cross-polarise  $^{13}\text{C}$ , to get an efficient enhancement in short times [14, 15].

Attempts are made to shorten the dissolution dead time, to allow to perform dissolution DNP on nuclei with short  $T_1$ . The best results have so far been achieved using a dual iso-centre dissolution DNP system [16]. Currently it features an overall dead time of 300 ms for dissolution, transfer and flow settling. This setup is described in Chapter 4, while experiments performed with it are discussed in Chapter 7.

### 1.2.4 $^{19}\text{F}$ hyperpolarisation

Although dissolution DNP has been widely used for different nuclei [1, 17, 18], literature concerning  $^{19}\text{F}$  DNP is very scarce and provides little insight into the experimental parameter optimisation and reproducibility of the experimental procedure.

Hilty and his group performed DNP experiments in 2012 [19] and 2015 [20] in order to study protein-ligand interactions for the characterisation and discovery of drugs. They overcame the sensitivity issue due to the need of a low ligands concentration and achieved an enhancement in the  $^{19}\text{F}$  signal of several thousand fold, making it possible to study ligands in slow exchange and to calculate the dissociation constant without any need of titration with a single scan CPMG experiment [21]. In their experiments, they hyperpolarised  $^{19}\text{F}$  in TFBC<sup>2</sup>, TFM CPP<sup>3</sup>, FMBC<sup>4</sup> and sodium trifluoroacetate, achieving a maximum enhancement factor of  $\approx 3000$  for the latter. These experiments were carried out in a HyperSense DNP polariser (Oxford Instruments, Tubney Woods, UK) at a temperature of 1.4 K.

However they only provide a brief description of the DNP setup, focussing on the application of this technique rather than a study of a fundamental approach to  $^{19}\text{F}$  DNP and the optimisation of the relevant experimental parameters.

### 1.2.5 Challenges in $^{19}\text{F}$ dissolution DNP

In order to study protein dynamics and protein-ligand interaction using dissolution DNP, the following questions need to be addressed:

---

<sup>2</sup>4-(trifluoromethyl)benzenecarboximida-mide hydrochloride

<sup>3</sup>4-(trifluoromethyl)-1,5,6,7-tetrahy-dro-2H-cyclopenta[b]pyridin-2-one

<sup>4</sup>3-fluoro-4-methylbenzenecarboximidamide hydrochloride

- How long is the life time of  $^{19}\text{F}$  magnetisation? Can  $^{19}\text{F}$  hyperpolarisation survive the transfer delay in a dissolution DNP experiment?
- Is it possible to hyperpolarise  $^{19}\text{F}$ ? Under which conditions will it polarise?
- What is the largest polarisation that can be achieved? What is the most effective mechanism for the polarisation transfer from the electrons?
- What is the time scale of the polarisation build-up process?

In the following Chapters of this work, answers to these questions will be sought. In Chapters 5 and 6 the DNP processes that drive  $^{19}\text{F}$  hyperpolarisation are studied. In Chapter 7, a study of the longitudinal relaxation time of some fluorinated compounds is performed, in order to determine whether its polarisation can survive the dissolution process, and dissolution DNP experiments of fluorinated compounds are performed. In particular, an application to a fluorinated protein as proof-of-principle is described. Experimental data are shown to demonstrate the feasibility of such applications.

# Chapter 2

## Relaxation in NMR

In Chapter 1, it was shown that the magnetic properties of a spin system in a static magnetic field are described by a macroscopic quantity called “magnetisation”. The magnetisation of a spin ensemble can be represented by a vector pointing in the direction of the magnetic field. Its intensity is proportional to the Boltzmann factor, and in stationary conditions it is in equilibrium with the lattice and does not change in time.

When the equilibrium state is perturbed, the system returns to the initial state. The time constants characteristic of the recovery are called longitudinal relaxation time  $T_1$  and transverse relaxation time  $T_2$ , whose values depend on the system considered.

This Chapter contains a short summary of the physics of the relaxation processes. After providing information on the empirical observation of spins recovering their equilibrium magnetisation, the relaxation process and its causes will be analysed. Finally, the principal mechanisms leading to relaxation are presented, focusing on the ones that are more relevant to the experiments shown in this work.

### 2.1 Population and relaxation

As explained in Chapter 1, an ensemble of spin 1/2 nuclei in a magnetic field  $B_0$  has two different energy levels, separated by an energy  $\Delta E = \gamma B_0 \hbar$  (see Figure 2.1). For a nucleus with positive gyromagnetic ratio, the state with lower energy corresponds to the case in which the nucleus is in the spin up ( $\alpha$ ) state. On the other

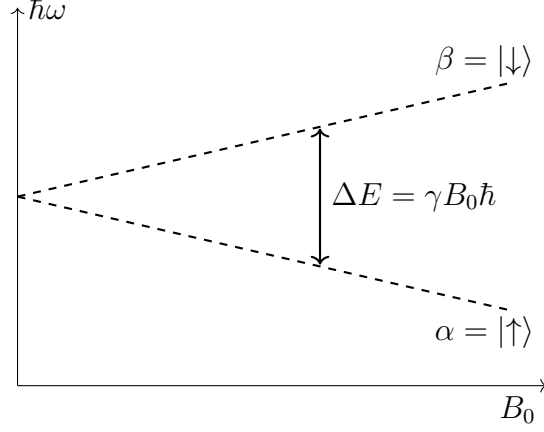


Figure 2.1: Energy levels of a spin 1/2 nucleus in a magnetic field  $B_0$ .

hand, the higher energy level ( $\beta$ ) corresponds to the spin down state. The spins populate the two energy levels with populations  $N_\alpha$  and  $N_\beta$  respectively. The application of radio frequency pulses changes the population distribution, moving nuclei from the  $\alpha$  to the  $\beta$  state and vice-versa. If  $P_{\alpha \rightarrow \beta}$  is the probability rate for a transition from  $\alpha$  to  $\beta$  induced by the radio frequency pulses, and  $P_{\beta \rightarrow \alpha}$  is the probability rate for the opposite transition  $\beta \rightarrow \alpha$ , the variation of population for the  $\alpha$  state is:

$$\frac{dN_\alpha}{dt} = P_{\beta \rightarrow \alpha} N_\beta - P_{\alpha \rightarrow \beta} N_\alpha. \quad (2.1)$$

In the following paragraph it is demonstrated using the concepts of quantum mechanics that the probability transitions are equal  $P_{\alpha \rightarrow \beta} = P_{\beta \rightarrow \alpha} = P$  [22, 23].

In fact, by using the Hamiltonian description, the radio frequency pulses introduce a time dependent term in the spin Hamiltonian, which is

$$\mathcal{H}_1(t) = -\gamma \hbar \vec{I} \cdot \vec{B}_1, \quad (2.2)$$

where  $\vec{I} = \hat{I}_x \vec{i} + \hat{I}_y \vec{j} + \hat{I}_z \vec{k}$  is the spin operator and  $\vec{B}_1 = B_1 \cos(\omega t) \vec{i} + B_1 \sin(\omega t) \vec{j} = B_x \vec{i} + B_y \vec{j}$  is the oscillating magnetic field. By defining the raising and lowering

operators  $\hat{I}_+ = \frac{\hat{I}_x + \hat{I}_y}{2}$  and  $\hat{I}_- = \frac{\hat{I}_x - \hat{I}_y}{2i}$ , Equation 2.2 becomes

$$\begin{aligned}
\mathcal{H}_1(t) &= -\gamma\hbar(\hat{I}_x B_x + \hat{I}_y B_y) = \\
&= -\gamma\hbar B_1 \left( \frac{\hat{I}_+ + \hat{I}_-}{2} \cos(\omega t) + \frac{\hat{I}_+ - \hat{I}_-}{2i} \sin(\omega t) \right) = \\
&= -\gamma\hbar B_1 \left( \hat{I}_+ \frac{\cos(\omega t) - i \sin(\omega t)}{2} + \hat{I}_- \frac{\cos(\omega t) + i \sin(\omega t)}{2} \right) = \\
&= -\gamma\hbar B_1 \left( \hat{I}_+ e^{-i\omega t} + \hat{I}_- e^{i\omega t} \right).
\end{aligned} \tag{2.3}$$

According to the Fermi's Golden Rule [24], the transition probability of a jump from the  $\alpha$  to the  $\beta$  state is given by the matrix element

$$P_{\alpha \rightarrow \beta} = \frac{1}{2\pi\hbar} |\langle \beta | \mathcal{H}_1 | \alpha \rangle|^2 \delta(E_\alpha - E_\beta - \hbar\omega), \tag{2.4}$$

where  $\delta(E_\alpha - E_\beta - \hbar\omega)$  is the Dirac delta function, which is non-zero only when the exact amount of energy  $\hbar\omega = E_\alpha - E_\beta$  is absorbed by the system. Since the state  $\alpha$  corresponds to the spin up state, and state  $\beta$  to the spin down state, the matrix element  $|\langle \beta | \mathcal{H}_1 | \alpha \rangle|$  is

$$\begin{aligned}
|\langle \beta | \mathcal{H}_1 | \alpha \rangle|^2 &= (\gamma\hbar H_1)^2 \left| \langle \beta | \left( \hat{I}_+ e^{-i\omega t} + \hat{I}_- e^{i\omega t} \right) | \alpha \rangle \right|^2 = \\
&= (\gamma\hbar H_1)^2 \left| \langle \beta | \hat{I}_- | \alpha \rangle \right|^2 = (\gamma\hbar H_1)^2 |\langle \beta | \beta \rangle|^2 = (\gamma\hbar H_1)^2.
\end{aligned} \tag{2.5}$$

On the other hand, with similar arguments, it can be easily proven that to the opposite transition  $P_{\beta \rightarrow \alpha}$  is associated the matrix element  $|\langle \alpha | \mathcal{H}_1 | \beta \rangle|^2 = |\langle \beta | \mathcal{H}_1 | \alpha \rangle|^2$ , hence demonstrating that the two probability transitions have the same value.

By defining the population difference  $n = N_\alpha - N_\beta$ , Equation 2.1 can be re-written as:

$$\frac{dn}{dt} = -2Pn. \tag{2.6}$$

Its solution

$$n(t) = n(0)e^{-2Pt} \tag{2.7}$$

indicates that the population difference disappears because of the radio frequency pulse. If instead no radio frequency pulse is applied, the population difference re-

mains constant. This argument is in disagreement with experimental observation, where the non-equilibrium polarisation is observed to change in time to reach the steady-state polarisation. In fact, transitions between the two states take place until the ratio between the equilibrium populations  $N_\beta^0$  and  $N_\alpha^0$  is

$$\frac{N_\beta^0}{N_\alpha^0} = \exp\left(-\frac{\gamma\hbar B_0}{k_B T}\right). \quad (2.8)$$

The natural conclusion to this observation is that there exists another mechanism that generates transitions between the two energy levels. In absence of radio frequency pulses, the equation governing the evolution of the population  $\alpha$  is:

$$\frac{dN_\alpha}{dt} = W_{\beta\rightarrow\alpha}N_\beta - W_{\alpha\rightarrow\beta}N_\alpha. \quad (2.9)$$

Unlike for the radio frequency pulses, the transition rates  $W_{\beta\rightarrow\alpha}$  and  $W_{\alpha\rightarrow\beta}$  are not equal, and from the equilibrium conditions for the populations (Equation 2.8) and Equation 2.9 the relation

$$\frac{W_{\beta\rightarrow\alpha}}{W_{\alpha\rightarrow\beta}} = \frac{N_\alpha^0}{N_\beta^0} \quad (2.10)$$

is obtained. At thermal equilibrium  $N_\beta^0 < N_\alpha^0$ , since the  $\alpha$  state is at lower energy. It follows that  $W_{\beta\rightarrow\alpha} > W_{\alpha\rightarrow\beta}$ . Therefore, the probability of a spin going from the higher energy state to the lower one is higher than the opposite probability.

By defining the total number of spins  $N = N_\beta + N_\alpha$ , Equation 2.9 can be re-written as

$$\frac{dn}{dt} = (W_{\beta\rightarrow\alpha} - W_{\alpha\rightarrow\beta})N - (W_{\beta\rightarrow\alpha} + W_{\alpha\rightarrow\beta})n. \quad (2.11)$$

The solution to this equation is given by:

$$n(t) = n_0 + Ae^{-t/T_1}, \quad (2.12)$$

where  $n_0 = N \frac{W_{\beta\rightarrow\alpha} - W_{\alpha\rightarrow\beta}}{W_{\beta\rightarrow\alpha} + W_{\alpha\rightarrow\beta}}$  is the population difference at thermal equilibrium,  $A$  is an integration constant and  $T_1 = (W_{\beta\rightarrow\alpha} + W_{\alpha\rightarrow\beta})^{-1}$  is the characteristic time associated with the evolution of the populations towards thermal equilibrium, the ‘‘longitudinal relaxation time constant’’.

Experimental observations of spins relaxing to an equilibrium state lead to the conclusion that there must be an oscillating field that matches the Larmor frequency of the nuclear spin. This field brings the ensemble to its thermal equilibrium state after it is perturbed. However, in the above described theory, the origin and nature of these fields was not defined. In the next section the origins of these oscillating fields are explained and later in this Chapter the main mechanisms that lead to relaxation will be presented.

## 2.2 Origin of relaxation

Motions in the sample can drive the magnetisation of a sample back to its equilibrium value after it is perturbed. The reason for this is the variation of the local magnetic field acting on a nuclear spin.

A single spin of a nucleus in a molecule is considered in the following analysis. As theory predicts, the other spins in the molecule generate a local magnetic field, that interacts with the first spin. As the molecule tumbles in the sample, the local field will change as well, becoming time-dependent. It can be demonstrated that if the resulting magnetic field has fluctuations with a frequency component that matches the nuclear Larmor frequency, it can drive transitions between the energy levels of the nuclear spin [25]. When many spins are considered, these transitions bring the spin system to its lower energy state, which is the thermal equilibrium, as stated by the Boltzmann equation (Equation 2.8).

The longitudinal relaxation process arises from fluctuations of the local field in the transverse  $x$ - $y$  plane. Fluctuations along all directions lead to a loss of phase coherence and thus cause transverse relaxation.

## 2.3 Spectral density function

In the previous sections it was discussed the fact that fluctuating magnetic fields can drive a perturbed spin system back to its equilibrium state. In this section, the properties of such fields are analysed, using the “spectral density function”.

Two spins close to each other interact, with a characteristic interaction constant. If the two spins randomly move, i.e. due to vibrations of the molecule they belong to, the interaction becomes time dependent. The distance fluctuation, as well as the change in orientation of the vector connecting the two spins with respect to the external magnetic field, introduce a time dependence in the interaction between the two spins. For the sake of simplicity, a single spin 1/2 nucleus in a molecule is considered with a time dependent magnetic field arising from paramagnetic centres. As the molecule tumbles, the magnetic field  $F_1(t)$  generated by the paramagnetic centre on the nucleus varies, becoming a random function of time. A second nucleus in the sample, in a different location, will sense a different magnetic field  $F_2(t)$ . The  $i$ -th nucleus in the sample experiences another magnetic field  $F_i(t)$ . By adding all these fields, one obtains the average magnetic field on the ensemble  $\overline{F(t)} = \sum_i F_i(t)$ . Since these magnetic fields are randomly distributed around zero, the average value will be zero as well.

The coherence of a random field can be evaluated by means of the *autocorrelation function* [2], defined as:

$$G(t, \tau) = \sum_i F_i(t) F_i^*(t + \tau), \quad (2.13)$$

with  $\tau > 0$ . The autocorrelation function  $G(t, \tau)$  assumes a large value if  $\tau$  is very short, since  $F_i(t)$  and  $F_i^*(t + \tau)$  will not differ much one from the other. Moreover, their product will be positive. As  $\tau$  increases, the correlation between  $F_i(t)$  and  $F_i^*(t + \tau)$  becomes smaller, the two fields will differ more, and their product is not necessarily positive anymore. Therefore, in the first case, the terms of the sum of  $G(t, \tau)$  are positive, and it will assume a large value. For large  $\tau$  instead, the members of the sum are values randomly distributed around zero, and  $G(t, \tau)$  approaches zero. Since the fields are independent of time  $t$ , the autocorrelation function is simply written as  $G(\tau)$ . The autocorrelation function is therefore related to the “memory” of the system, assuming a decreasing value as  $\tau$  increases. It can be shown [23] that  $G(\tau)$  can be frequently written in the form:

$$G(\tau) = G(0)e^{-\tau/\tau_c}, \quad (2.14)$$

where the characteristic time  $\tau_c$  is the “correlation time” and  $G(0) = \overline{F^2}$  is the square of the mean fluctuating magnetic field. If the fields  $F_i(t)$  fluctuate slowly, the correlation time  $\tau_c$  of the autocorrelation function is big. If  $F_i(t)$  oscillate quickly,  $\tau_c$  will be small.

By performing the Fourier Transform of the autocorrelation function, the spectral density function  $J(\omega)$  is obtained. If the autocorrelation function is in the form of Equation 2.14, the spectral density function is:

$$J(\omega) = 2 \int_0^\infty G(\tau) e^{-i\omega\tau} d\tau = 2\overline{F^2} \frac{\tau_c}{1 + \omega^2\tau_c^2} = 2\overline{F^2} \mathcal{J}(\omega), \quad (2.15)$$

where  $\mathcal{J}(\omega)$  is the “normalised spectral density function”. It can be demonstrated [23] that the probability of a transitions induced by a random field in Equation 2.9 in the high temperature approximation can be written as

$$\begin{aligned} W_{\beta \rightarrow \alpha} &= W \left(1 - \frac{1}{2} \mathcal{B}\right) \\ W_{\alpha \rightarrow \beta} &= W \left(1 + \frac{1}{2} \mathcal{B}\right), \end{aligned} \quad (2.16)$$

with

$$W = \frac{1}{2} \gamma^2 \overline{F^2} \mathcal{J}(\omega) \quad (2.17)$$

and  $\mathcal{B}$  the Boltzmann factor, defined as  $\mathcal{B} = \frac{\hbar\gamma B_0}{k_B T}$ . Since  $\mathcal{B}$  is always positive, it follows that the transitions that drive the spins to the lower energy state  $\alpha$  occur more frequently than the opposite transitions.

## 2.4 Mechanisms for relaxation

As Equation 2.17 shows, the transition probability that leads to the relaxation depends on the spectral density function and on the strength of the fluctuating magnetic fields. While the spectral density function describes the fluctuating nature of these fields, their intensity is related to the interaction of the nuclear spin with the surrounding spins.

According to the Hamiltonian description of Section 1.1.2, every term in the spin Hamiltonian that does not commute with the Zeeman Hamiltonian  $\mathcal{H}_Z$  generates terms that lead to relaxation. The principal processes that are responsible for

relaxation are:

- The nuclear dipole-dipole interaction;
- The hyperfine interaction between electrons and nuclei;
- Electric quadrupole interaction;
- The chemical shift anisotropy;
- The scalar coupling interactions, or J-coupling interaction;
- Spin-rotation interactions.

Only the first two mechanisms are relevant to understand the results that will be presented in the next Chapters of this thesis, and therefore a more in depth description of these two relaxation pathways will be provided. However, for the sake of completeness, all pathways will be briefly mentioned.

### Dipole-dipole relaxation

Two 1/2 spin nuclei can directly interact with each other. The first nucleus, possessing a magnetic moment, generates a magnetic field that interacts with the magnetic dipole of the second spin and vice versa. The interaction that arises is called “direct dipole-dipole interaction”. Like two magnetic dipoles interact in electrodynamics, an analogous mechanism takes place when two spin are close to each other. The Hamiltonian term that is associated with the dipole-dipole interaction of two spins  $I_1$  and  $I_2$  can be written as

$$\mathcal{H}_{II} = d_{II} \left[ 3 \left( \hat{I}_{z1} \cdot \hat{e}_{II} \right) \left( \hat{I}_{z2} \cdot \hat{e}_{II} \right) - \vec{I}_1 \cdot \vec{I}_2 \right], \quad (2.18)$$

where  $\hat{e}_{II}$  is the unit vector connecting the two spins, while

$$d_{II} = -\frac{\mu_0 \gamma_{I1} \gamma_{I2} \hbar}{4\pi |r_{II}|^3} \quad (2.19)$$

is the dipolar interaction strength constant. It is important to note that the interaction strength is proportional to the product of the gyromagnetic ratios of the nuclei involved. This means that for nuclei like  $^1\text{H}$  and  $^{19}\text{F}$  this mechanism will

affect the relaxation more than it would influence the relaxation of nuclei like  $^{13}\text{C}$  or  $^{15}\text{N}$ , which have a lower gyromagnetic ratio. Moreover, the interaction strength depends on the third power of the inverse of the distance between the two spins  $r_{II}$ . In fact, due to the  $r_{II}^{-3}$  dependency, the interaction strength already drops of a factor of 8 for nuclei distant twice the closest nucleus. Therefore, predominantly the closest neighbouring nuclei will contribute to the relaxation. Also the angular distribution plays an important role. The interaction strength is in fact the largest when the two nuclei lie on the same plane perpendicular to the external magnetic field, while it is zero when  $\hat{e}_{II}$  forms an angle of  $\Theta_{II} \approx 54.74^\circ$  (the magic angle) with the external magnetic field.

It can be shown that in presence of high magnetic fields the non-secular terms of the Hamiltonian can be neglected, leaving only the secular Hamiltonian

$$\mathcal{H}_{II} = \frac{d_{II}}{2} \left( 3\hat{I}_{z1}\hat{I}_{z2} - \vec{I}_1 \cdot \vec{I}_2 \right) (3 \cos^2 \Theta_{II} - 1). \quad (2.20)$$

As the molecules containing spins tumble in the sample, the angular dependence, as well as the distance between the two nuclei, changes. Therefore, the magnetic field experienced by the nuclei becomes time-dependent, giving rise to relaxation. It can be demonstrated [23] that the relaxation time of spin  $I_1$  associated with the dipole-dipole interaction with spin  $I_2$  in liquid state is given by

$$\frac{1}{T_1} = \frac{3\mu_0^2}{64\pi^2} \frac{\gamma_{I1}^2 \gamma_{I2}^2 \hbar^2}{|r_{II}|^6} \left[ \frac{1}{12} \mathcal{J}^{(0)}(\omega_{I1} - \omega_{I2}) + \frac{3}{2} \mathcal{J}^{(1)}(\omega_{I1}) + \frac{3}{4} \mathcal{J}^{(2)}(\omega_{I1} + \omega_{I2}) \right] \quad (2.21)$$

in the heteronuclear case, while it is

$$\frac{1}{T_1} = \frac{9\mu_0^2}{128\pi^2} \frac{\gamma_I^4 \hbar^2}{|r_{II}|^6} \left[ \mathcal{J}^{(1)}(\omega_I) + \mathcal{J}^{(2)}(2\omega_I) \right] \quad (2.22)$$

between nuclei of the same species. In these equations, the functions  $\mathcal{J}^{(i)}$  (with  $i = 0, 1, 2$ ) represent the random nature of the magnetic fields associated with the spherical harmonics  $Y_2^i(\theta, \varphi)$  (see Abragam [23] for more detail). Although these equations are derived for samples in liquid state, the longitudinal relaxation time constant retains its spatial dependence for samples in solid state.

Therefore, a strong dependence of the longitudinal relaxation time on the distance

between nuclei is predicted. The more nuclei in the sample, the more packed they are, and the shorter the distance between them.

### Paramagnetic relaxation

In the previous section, the interaction between two nuclear spin was considered to study the dipole-dipole mechanism that leads to relaxation. If an electron is considered instead of the second nucleus, “paramagnetic relaxation” is instead observed. Paramagnetic relaxation can be considered as a special case of the dipole-dipole interaction, where one of the nuclei is replaced by an electron. The interaction between a nucleus and an electron is called the “hyperfine interaction”, and the Hamiltonian is written in the same way as the dipole-dipole Hamiltonian. Since the gyromagnetic ratio of the electron is much larger than that of any nucleus (it is in fact  $\approx 660$  times larger than the  $^1\text{H}$  one), it is easy to understand how a small number of paramagnetic centres in the sample can drastically affect the longitudinal relaxation time constant of nuclei close to the electron.

There are two main reasons to consider the effect of paramagnetic centres in a sample. The first is the presence of dissolved oxygen in the sample. When preparing a liquid sample, it is inevitable that  $\text{O}_2$  molecules dissolve in the sample. The  $\text{O}_2$  molecule is paramagnetic, and unless the sample undergoes a degassing process, it can be found in both organic and inorganic solvents at relatively high concentration. Electrons in the  $\text{O}_2$  molecule arrange in such a way that in the  $\pi$  orbital there are two unpaired electrons, that behave like free radicals in the sample, interacting with the neighbouring nuclei.

Another way to introduce electrons in the sample, is to intentionally mix it with free radicals. As it will be discussed in Chapter 3, free radicals are needed to achieve DNP hyperpolarisation, since this technique relies on the polarisation transfer from the electrons in the free radicals to the nuclei.

When considering paramagnetic relaxation, a few changes to Equation 2.21 must be taken into account. In fact, in the interaction between a nucleus and an electron, it is not necessarily the coupling constant that changes in time, but the value of the electronic  $\hat{S}$  operator itself. This time dependence is due to the electron relaxation, that typically takes place on a much shorter timescales compared to the nuclear

relaxation.

In a solid sample, molecules are “frozen” in space. The full dipolar Hamiltonian (Equation 2.18) can be written as

$$\mathcal{H}_{IS} = d_{IS} [A + B + C + D + E + F], \quad (2.23)$$

where the terms in square brackets are:

$$\begin{aligned} A &= (1 - 3 \cos^2 \theta) \hat{S}_z \hat{I}_z \\ B &= -\frac{1}{4} (1 - 3 \cos^2 \theta) (\hat{S}_- \hat{I}_+ + \hat{S}_+ \hat{I}_-) \\ C &= -\frac{3}{2} \sin \theta \cos \theta e^{-i\varphi} (\hat{S}_z \hat{I}_+ + \hat{S}_+ \hat{I}_z) \\ D &= -\frac{3}{2} \sin \theta \cos \theta e^{i\varphi} (\hat{S}_z \hat{I}_- + \hat{S}_- \hat{I}_z) \\ E &= -\frac{3}{4} \sin^2 \theta e^{-i2\varphi} \hat{S}_+ \hat{I}_+ \\ F &= -\frac{3}{4} \sin^2 \theta e^{i2\varphi} \hat{S}_- \hat{I}_-. \end{aligned} \quad (2.24)$$

The operator  $A$ , that commutes with the Zeeman Hamiltonian, is the “secular terms”. The other operators are instead the “non-secular terms”.

The operators  $C$  and  $D$  contain terms that introduce a nuclear flip, leaving the electron unchanged. The energy necessary for this flip is therefore equal to the Zeeman splitting.

It can be shown [23] that the nuclear longitudinal relaxation time constant related to this process can be written as

$$\frac{1}{T_1} = \frac{6\mu_0^2}{160\pi^2} \frac{\gamma_I^2 \gamma_S^2 \hbar^2}{|r_{IS}|^6} \frac{\tau_c}{1 + \omega_I^2 \tau_c^2}, \quad (2.25)$$

In solid state, the correlation time  $\tau_c$  is related to the electronic relaxation. This parameter can be approximated reasonably well by the electronic  $T_1$  relaxation time constant [26] or with the electron-electron spin diffusion time constant [27]. Like the dipole-dipole relaxation depends on the concentration of nuclei in the sample, this relaxation pathway is strongly dependent on the amount of paramagnetic centres dissolved in the sample. In fact, the more the free electrons, the shorter the distance between them and the nuclei, and the faster the nuclear

relaxation.

### **Quadrupole relaxation**

This relaxation pathway takes place when nuclei with spin  $I > 1/2$  are involved. This mechanism represents the interaction between the nuclear spin and the electric field gradient at the position of the nucleus. Since  $I > 1/2$  spin nuclei have not been used in the experiments described in this thesis, no further information is provided.

### **CSA relaxation**

As mentioned in Chapter 1, the magnetic field experienced by a nucleus is influenced by the surrounding electronic cloud. The local field is not necessarily symmetric, and its effect is represented by the “chemical shift tensor” in the Hamiltonian. In the case in which the chemical shift tensor is anisotropic, the generated magnetic field is dependent on the orientation of the molecule in the sample. As the molecule moves, this magnetic field fluctuates, and can generate relaxation in the nuclei of the molecule. The magnitude of the effect of the CSA in the relaxation of a nucleus depends on the degree of anisotropy of the tensor.

### **Scalar relaxation**

The interaction of two spins can be mediated by the electronic clouds that surround and bond the nuclei in a molecule. The scalar relaxation is a relaxation mechanism deriving from intramolecular interaction due to a simultaneous Fermi contact of both nuclei with each bond electron. This interaction depends on the molecular orientation with respect to the external magnetic field.

### **Spin-rotation relaxation**

The last relaxation mechanism is related to the magnetic fields that are generated at the location of a nucleus by the motion of a molecular magnetic moment arising from the electron distribution in a molecule. In fact the electron, rotating with the molecule, generate a current that induce a magnetic field. This effect, related

to the rotation of the molecule, can be ignored at cryogenic temperature since the degree of freedom associated with the rotation of molecules is frozen.

## 2.5 Conclusion

In this Chapter the principal mechanisms that lead to relaxation have been discussed. It is important, for the purpose of this thesis, to divide the aforementioned mechanisms in two main groups. To the first group belong the dipole-dipole and paramagnetic relaxation mechanisms. These two mechanisms are dependent on the average distance between the spins involved, whether nuclei or electrons. The strong dependence on the distance implies that as the concentration of the used chemicals<sup>1</sup> changes, the contribution of these mechanisms to the global nuclear longitudinal relaxation time constant  $T_1$  varies.

To the second group instead belong all the other mechanisms. Since the changes in the studied samples do not change the nature and characteristic of the mechanisms belonging to the latter group, it is assumed that the contribution to the relaxation time constants do not change and it is the same for all analysed samples.

Since the total longitudinal relaxation rate can be expressed as the sum of all the aforementioned contribution, it is possible to write the total longitudinal relaxation time constant as

$$\frac{1}{T_1} = \frac{1}{T_1^{dd}} + \frac{1}{T_1^{par}} + \frac{1}{T_1^{rest}}, \quad (2.26)$$

where  $T_1^{dd}$  indicates the contribution from the dipole-dipole mechanism,  $T_1^{par}$  indicates the paramagnetic relaxation contribution and  $T_1^{rest}$  indicates the contribution of all the other mechanisms. The latter is assumed to be independent of the composition of the samples used for the experiments shown in this thesis.

---

<sup>1</sup>Either the molecules containing the spin nuclei, or the free radicals containing unpaired electrons.

# Chapter 3

## Dynamic Nuclear Polarisation

A problem that often occurs when performing a NMR experiment is related to the poor signal-to-noise ratio, that may arise for many reasons. For example, nuclei with low gyromagnetic ratio can prove challenging for the NMR acquisition. In fact, their NMR peak, whose intensity is proportional to the gyromagnetic ratio cubed, can be hidden in the noise of the spectrum. Another reason that leads to poor signal-to-noise ratio is the low abundance of spin nuclei in the sample. If, for one hand,  $^1\text{H}$  and  $^{19}\text{F}$  are the most abundant isotopes of their species, for other spin nuclei, like  $^{13}\text{C}$  or  $^{15}\text{N}$ , further issues can occur due to their poor natural abundance. On top of this, NMR analysis often require low concentration of nuclei in the sample to preserve biological properties.

Dynamic Nuclear Polarisation (DNP) is a technique that helps overcoming these issues, enhancing the signal-to-noise ratio by up to four orders of magnitude. In this chapter the DNP theory is presented, and the principal mechanisms that lead to hyperpolarisation are discussed.

### 3.1 Principles of hyperpolarisation

Among the known techniques that allow to hyperpolarise a nuclear ensemble, together with spin-exchange optical pumping [28], Para Hydrogen Induced Polarised (PHIP) [29] and Signal Amplification By Reversible Exchange (SABRE) [30], DNP is one of the most used ones. DNP was first predicted by Overhauser for nuclei conducting materials [31] in the 50s, and confirmed in the same year by the ex-

periments conducted by Slichter and Carver [32]. Later Abragam and Goldman studied similar processes in other solids [10]. Initially abandoned due to hardware limitations, DNP regained popularity in the last decades thanks to the ability to build instruments that allow to perform DNP in high magnetic fields.

In recent years, DNP became a very popular technique due to Magic Angle Spinning (MAS) experiments [33], that allow to obtain a good resolution even at liquid nitrogen temperatures. MAS DNP is used nowadays to determine the structure of proteins and biologically relevant materials.

One of the most popular techniques in this field is dissolution DNP. Dissolution DNP [1] combines the hyperpolarisation achieved in solid state via DNP with the one obtained by a rapid temperature jump by melting the sample at room temperature to enhance the NMR signal.

Through dissolution DNP, in principle, it is possible to achieve an enhancement proportional to the DNP enhancement in solid state and to the ratio of the temperatures, after and before the melting of the sample.

The idea behind DNP is to transfer the polarisation from the electrons in the sample to the nuclei. As shown in Section 1.1.3, due to their high gyromagnetic ratio, under given magnetic field and temperature, the polarisation of electrons is much higher than any nucleus. In the next sections of this Chapter, the main mechanisms that allow transfer of the electron polarisation in solid state are presented.

### 3.1.1 The Solid Effect

The simplest mechanism that allows transfer of the electron polarisation to the surrounding nuclei is the Solid Effect [34]. The theory of Solid Effect can be reduced to the analysis of a nucleus coupled with an electron.

The Hamiltonian operator for one spin nucleus interacting with an electron can be written as

$$\mathcal{H} = \mathcal{H}_{S_z} + \mathcal{H}_{I_z} + \mathcal{H}_{IS} = \hbar\omega_S \hat{S}_z + \hbar\omega_I \hat{I}_z + A_z \hat{S}_z \hat{I}_z + \frac{1}{2}(A^+ \hat{S}_z \hat{I}^+ + A^- \hat{S}_z \hat{I}^-), \quad (3.1)$$

where  $\mathcal{H}_{S_z} = \hbar\omega_S\hat{S}_z$  is the Zeeman Hamiltonian for the electron,  $\mathcal{H}_{I_z} = \hbar\omega_I\hat{I}_z$  is the nuclear Zeeman Hamiltonian and the remaining term  $\mathcal{H}_{IS} = A_z\hat{S}_z\hat{I}_z + \frac{1}{2}(A^+\hat{S}_z\hat{I}^+ + A^-\hat{S}_z\hat{I}^-)$  represents the hyperfine interaction.  $A$  and  $A^\pm$  are the secular and pseudo-secular hyperfine interaction constants.

The pseudo-secular component of the hyperfine interaction introduces a mixing between states. The eigenstates of the Hamiltonian presented in Equation 3.1 are in fact

$$\begin{aligned}
|\alpha\rangle' &= c_b |\downarrow_S\uparrow_I\rangle + s_b |\downarrow_S\downarrow_I\rangle \\
|\beta\rangle' &= c_b |\downarrow_S\downarrow_I\rangle - s_b |\downarrow_S\uparrow_I\rangle \\
|\gamma\rangle' &= c_a |\uparrow_S\uparrow_I\rangle + s_a |\uparrow_S\downarrow_I\rangle \\
|\delta\rangle' &= c_a |\uparrow_S\downarrow_I\rangle - s_a |\uparrow_S\uparrow_I\rangle.
\end{aligned} \tag{3.2}$$

In these equations, the coefficients  $c_{a,b} = \cos\left(\frac{\eta_{a,b}}{2}\right)$  and  $s_{a,b} = \sin\left(\frac{\eta_{a,b}}{2}\right)$ , with  $\eta_{a,b} = \arctan\left(-\frac{A^+ + A^-}{4\omega_I \pm A_z}\right)$ , are the mixing coefficients.

The energy levels of a system composed of one electron and one nucleus are shown in Figure 3.1. According to conventions, since the electron has negative gyromagnetic ratio, in the lowest energy level it is in the “spin down” state. On the other hand, the nucleus considered has positive gyromagnetic ratio, and the “spin down” state corresponds to higher energy. The transitions between the energy levels are also shown in the figure. They correspond to single-quantum transitions ( $W_I$  and  $W_S$ ), zero-quantum transition ( $W_{ZQ}$ ) and double-quantum transition ( $W_{DQ}$ ). The single-quantum transitions represent the flipping of the nuclear or electronic spin, and they are analogous to the transitions observed in NMR experiments. In the zero-quantum transition, the two spins undergo a flip-flop, exchanging their spin values. In the double-quantum transitions both spins, with the same orientation, change simultaneously.

Of the aforementioned transitions, only the single quantum transitions are allowed by the laws of quantum mechanics. Double-quantum and zero-quantum transitions are instead “forbidden transitions”, since in absence of the hyperfine interaction there is no term in the Hamiltonian operator that links the involved states.

The Solid Effect relies on this mixing to allow the forbidden transitions and to

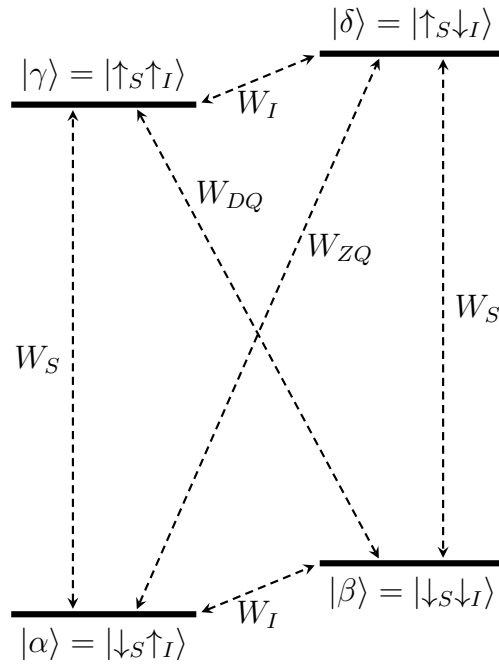


*Figure 3.1:* Energy levels and transitions for a system of an electron “S” and a spin nucleus “I”. Shown in the diagram are the states of the uncoupled spins, eigenstates of the total Zeeman Hamiltonian. When the hyperfine interaction is included, the new resulting eigenstates are obtained by a linear combination of the previous ones. Following the mixing, the double and zero-quantum transitions, forbidden for the unmixed states, become allowed upon microwave irradiation.

drive a large polarisation transfer on the nuclei. At low temperatures, electrons almost fully populate their lowest energy levels,  $|\alpha\rangle'$  and  $|\beta\rangle'$ . When the system is irradiated with energy  $\hbar\omega = \hbar(\omega_S - \omega_I)$ , the populations of the states  $|\delta\rangle'$  and  $|\beta\rangle'$  are equalised. The electron  $T_1$ , fast compared to the nuclear one, quickly induces relaxation from the state  $|\delta\rangle'$  to the state  $|\alpha\rangle'$ . The process produces an imbalance of populations, leading to a new equilibrium state different from the thermal one during microwave irradiation. Starting from the states  $|\alpha\rangle'$  and  $|\beta\rangle'$  almost equally populated, in the final picture the state  $|\alpha\rangle'$  has a population greater than the state  $|\beta\rangle'$ . In terms of nuclear spin, the Solid Effect transfers the population from the spin down to the spin up state.

If the transition induced by the energy externally supplied is faster than the nuclear  $T_1$ , the population of the state  $|\alpha\rangle'$  will increase while the population of  $|\beta\rangle'$  is depleted, producing a positive nuclear hyperpolarisation. A negative enhancement is instead obtained if the sample is irradiated to stimulate the zero-quantum transition at  $\hbar\omega = \hbar(\omega_S + \omega_I)$ .

To achieve an effective Solid Effect, the EPR line width of the electron must be narrower than the nuclear Larmor frequency [35]. Should this requirement not be satisfied, the irradiation of the system would drive both zero and double-quantum transition simultaneously, cancelling the effect.

The Solid Effect is efficient for low electron concentrations to reduce the effect of the dipolar electron-electron interactions [34], and the produced DNP enhancement scales with the static magnetic field with a  $B_0^{-2}$  dependence.

In order to carry out DNP hyperpolarisation, the Solid Effect, as well as the other DNP mechanism, requires the presence of free electrons in the sample. Free electrons are added to the sample in form of free radicals, molecules that carry an unpaired electron in their structure.

For the Solid Effect, low concentrations of free radicals with narrow EPR line are needed. Two of the most commonly used free radicals for the Solid Effect are Trityl [36] and BDPA [37, 38] (for example, a polarisation of  $\approx 42\%$  for  $^{13}\text{C}$  has been achieved by Ardenkjaer-Larsen et al. at 1.35 K in a 5 T magnetic field in a sample containing Trityl [39]).

### 3.1.2 The Cross Effect

Another mechanism that can drive DNP is the Cross Effect [40]. The Cross Effect requires an additional electron to the minimal model used for the Solid Effect. This mechanism is efficient when the electron EPR line is inhomogeneously broadened, and typically the concentration of electrons in the sample is higher than for the Solid Effect.

In such circumstances, the EPR line is made of many narrow electronic resonances, that add up to form the electron spectrum. An important requirement is that there exist two electron resonances in the EPR line that have a difference in Larmor frequency that matches the nuclear Larmor frequency [41]. The energy levels associated with the three spin system is shown in Figure 3.2.

The Hamiltonian representing this three-spin system is

$$\mathcal{H} = \mathcal{H}_Z + \mathcal{H}_{IS} + \mathcal{H}_{SS}. \quad (3.3)$$

The first term of the sum represents the Zeeman Hamiltonian:

$$\mathcal{H}_Z = \mathcal{H}_I + \mathcal{H}_{S_1} + \mathcal{H}_{S_2} = \omega_I \hat{I}_z + (\omega_{s1} - \omega_{\text{MW}}) \hat{S}_{1z} + (\omega_{s2} - \omega_{\text{MW}}) \hat{S}_{2z}. \quad (3.4)$$

The second term of the Hamiltonian represents the hyperfine interaction:

$$\mathcal{H}_{IS} = \sum_{i=1,2} [A_{z,i} \hat{S}_{iz} \hat{I}_z + \frac{1}{2} (A_i^+ \hat{S}_{iz} \hat{I}^+ + A_i^- \hat{S}_{iz} \hat{I}^-)] \quad (3.5)$$

This term takes into account the interaction of each electron with the nucleus.  $A_{z,i}$  and  $A_i^\pm$  (where  $i = 1, 2$  is the electron index) are the secular and pseudo-secular coefficient of the dipolar hyperfine interaction. The electron-electron dipolar interaction Hamiltonian terms is:

$$\mathcal{H}_{SS} = D_{12} \left( 3\hat{S}_{1z} \hat{S}_{2z} - \bar{S}_1 \cdot \bar{S}_2 \right), \quad (3.6)$$

where  $D_{12}$  is the dipolar coupling constant, representing the strength of the interaction between the two electrons.

When microwaves irradiate the sample, one last operator is introduced. If mi-

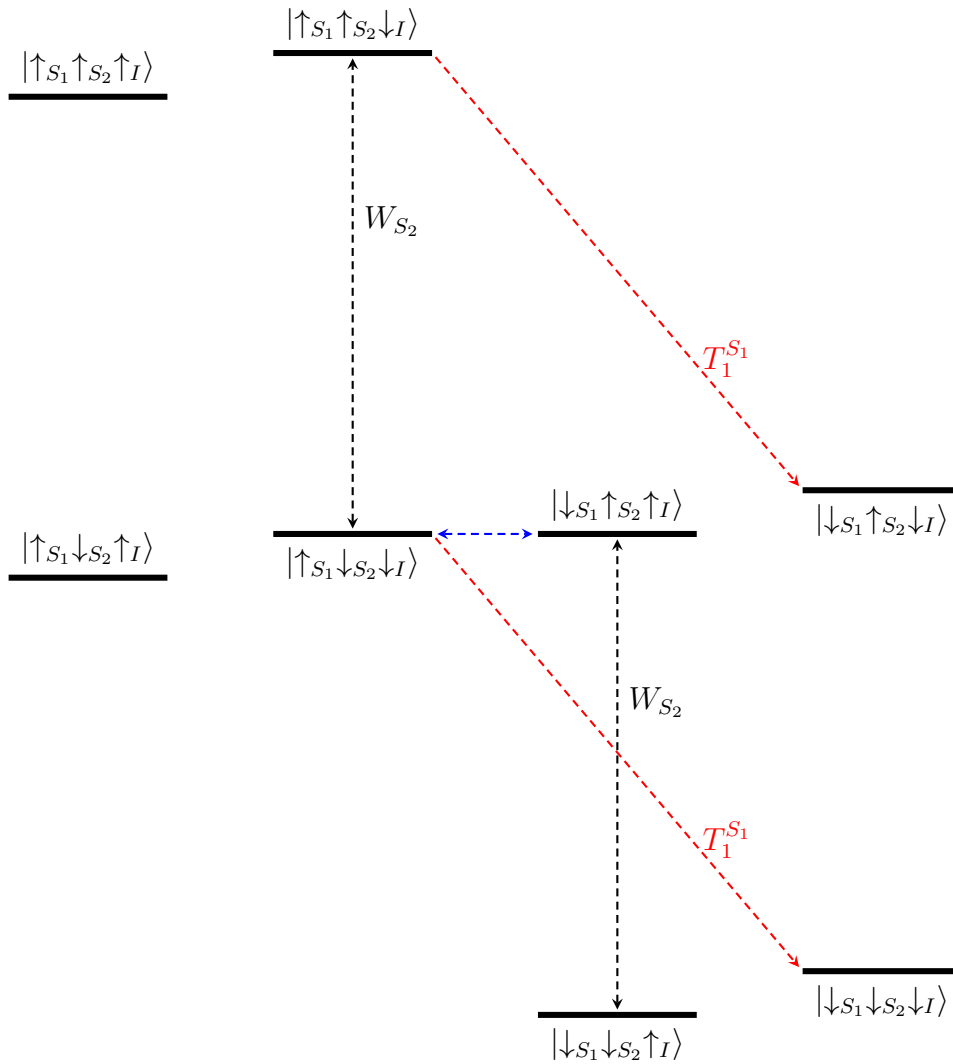


*Figure 3.2:* Energy levels and transitions for a system of two electrons (“ $S_1$ ” and “ $S_2$ ”) and a spin nucleus (“ $I$ ”). In the figure the energy levels and some of the transitions are shown. The black dotted lines represent the transition induced by the microwave irradiation on resonance with the Larmor frequency of the second electron. The blue one connects the degenerate energy levels, while the red line shows the relaxation path of the first electron.

crowaves are on resonance with the second electron, this term commutes with the x-projection of its angular momentum, and is written as:

$$\mathcal{H}_{mw} = \omega_{mw} \hat{S}_{2x}. \quad (3.7)$$

When the condition  $|\omega_{S_1} - \omega_{S_2}| = \omega_I$  is met, the levels  $|\downarrow_{S_1} \uparrow_{S_2} \uparrow_I\rangle$  and  $|\uparrow_{S_1} \downarrow_{S_2} \downarrow_I\rangle$  become degenerate. When the system is irradiated with microwaves at energy corresponding to the Larmor frequency of the second electron, the populations associated with the energy states of its single-quantum transition are equalised. In the figure only the transitions  $|\downarrow_{S_1} \downarrow_{S_2} \uparrow_I\rangle \leftrightarrow |\downarrow_{S_1} \uparrow_{S_2} \uparrow_I\rangle$  and  $|\uparrow_{S_1} \downarrow_{S_2} \downarrow_I\rangle \leftrightarrow |\uparrow_{S_1} \uparrow_{S_2} \downarrow_I\rangle$  are shown ( $W_{S_2}$ ), but microwave irradiation equalises the populations of each state with the one of the state directly above it. Then, due to the mixing of the degenerate energy levels  $|\uparrow_{S_1} \downarrow_{S_2} \downarrow_I\rangle$  and  $|\downarrow_{S_1} \uparrow_{S_2} \uparrow_I\rangle$ , an efficient polarisation transfer occurs between the two states [42]. Finally, the fast longitudinal relaxation of the first electron drives an increase of population on the states with  $\downarrow_I$ , which corresponds to a negative hyperpolarisation for the nuclear spins. A positive nuclear enhancement is instead achieved when the irradiation is on resonance with the Larmor frequency of the first electron.

The maximum nuclear hyperpolarisation that can be achieved is proportional to the difference in polarisation of the two electrons, according to the equation:

$$P_I = \frac{P_{S_1} - P_{S_2}}{1 - P_{S_1} P_{S_2}}, \quad (3.8)$$

valid when  $\omega_{S_1} > \omega_{S_2}$  [43] (for example, a polarisation of 61% for  $^1\text{H}$  has been achieved by Siaw et al. at 4 K in a 7 T magnetic field [44]).

The Cross Effect enhancements scale as  $\omega_I^{-1}$  because the number of spin packets that satisfy the Cross Effect matching condition  $|\omega_{S_1} - \omega_{S_2}| = \omega_I$ , decreases linearly with  $\omega_I$ . For this reason, the Cross Effect is more efficient than the Solid Effect at higher magnetic fields [45].

The Cross Effect requires free radicals with large and inhomogeneously broadened EPR line, in relatively high concentrations. A family of radicals used to achieve the Cross Effect is the nitroxide radical family. Nitroxide radicals are a species containing the  $\text{R}_2\text{N}-\text{O}\cdot$  functional group, and they are persistent radi-

cals. (2,2,6,6-Tetramethylpiperidin-1-yl)oxyl (known as TEMPO) and 4-hydroxy-TEMPO (known as TEMPOL) are used with concentrations  $> 30$  mM to polarise the surrounding nuclei through the Cross Effect. Alternatively, bi-radicals are used particularly in DNP MAS spectroscopy.

### 3.1.3 Thermal Mixing

The Thermal Mixing [46] is a DNP mechanism that describes a spin system made of many strongly coupled electrons interacting with neighbouring nuclei. Due to the complex nature of this mechanism, a thermodynamic approach is commonly used to describe it, although in recent times, attempts to describe Thermal Mixing with quantum mechanics have been made [47].

In the thermodynamic picture, Thermal Mixing makes use of the “spin temperature” concept [48], according to which each spin ensemble has an associated temperature value. The spin temperature is equal to the lattice temperature when the system is at equilibrium. When a polarisation greater than the equilibrium one is achieved, the spin bath is said to be colder than the lattice, while it is hotter if its polarisation is smaller than the equilibrium value. It is possible to write the spin temperature as a function of the polarisation  $P$  according to the Boltzmann equation, and in the high temperature limit (valid for the conditions of the experiments presented in this thesis), it can be written as

$$T_N = \frac{\hbar\gamma_N B_0}{2k_B P}. \quad (3.9)$$

Therefore, when a nuclear ensemble is polarised via Thermal Mixing, its spin temperature decreases with respect to the lattice temperature. The energy exchange between the electronic and nuclear ensembles can be illustrated by using thermal reservoirs, shown in Figure 3.3. There are three ensembles involved in the Thermal Mixing process. The nuclear Zeeman ensemble is related to the energy that arises from the interaction of the nuclear spins with the external magnetic field. The Zeeman electron ensemble is analogous to the nuclear one. Finally, the electron dipolar ensemble is related to the dipole-dipole interactions occurring between the electrons. When the sample is irradiated with microwaves that

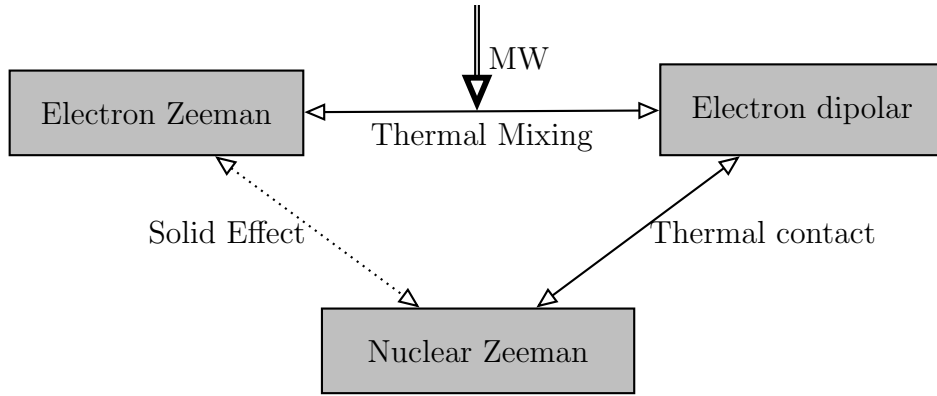


*Figure 3.3:* Schematic diagram of Thermal Mixing. When the sample is irradiated with microwaves, the dipolar reservoir is cooled down. The electron dipolar reservoir is also in thermal contact with the nuclear Zeeman reservoir via three spin flips. Therefore, microwave irradiation indirectly puts in contact the electron and nuclear Zeeman reservoirs. The polarisation transfer path given by the Solid Effect during microwave irradiation is also shown in the diagram.

saturate the EPR line, the electron Zeeman reservoir is put in “thermal contact” with the electron dipolar ensemble. At this point, the dipolar ensemble is cooled down to the electron spin temperature, and exchanges energy with the nuclear reservoir, that becomes cooler as well [49], via three spin flips process. The overall process therefore results in a increase in polarisation of the nuclear spin ensemble (for example, Lumata et al. achieved a maximum polarisation of  $\approx 6\%$  for  $^{13}\text{C}$  at 1.4 K in a 3.35 T magnetic field with Thermal Mixing [50]).

An important requirement for Thermal Mixing to be efficient is the large presence of free radicals with homogeneously broadened EPR linewidth. Moreover, the EPR line has to be larger than the nuclear Larmor frequency, to ease the polarisation transfer via three spin flips.

### 3.1.4 The Overhauser Effect

The only DNP mechanism that works in liquid state is the Overhauser Effect [31], as molecular motions in a liquid facilitate this mechanism. Since the Overhauser Effect is not studied in this thesis, this mechanism is briefly presented in this section. For the Overhauser Effect, The polarisation transfer from electrons occurs via cross-relaxation processes with neighbouring nuclei. In this framework, one electron is coupled with a nucleus via the hyperfine interaction. The energy level

diagram for the Overhauser Effect is analogous to the one illustrated in Figure 3.1 for the Solid Effect.

Microwave irradiation saturates the levels connected by the single-quantum transition. Once the microwave are switched off, the system relaxes according to the transition probabilities of zero ( $W_{ZQ}$ ), single ( $W_S$  and  $W_I$ ) and double-quantum ( $W_{DQ}$ ) transitions. Solomon equations [51] can be used to show that cross-relaxation builds up a nuclear polarisation above its thermal equilibrium value.

It can be demonstrated [52] that the theoretical enhancement factor  $\epsilon$  predicted for the Overhauser Effect is

$$\epsilon = \xi f s \frac{\gamma_S}{\gamma_I}. \quad (3.10)$$

In this equation,  $\xi$  is the coupling factor, and its value depends on the nature of the coupling.  $f$  is the leakage factor, and takes into account the losses of nuclear polarisation due to processes that are not associated to the electron spin. Finally,  $s$  is the saturation factor, that reflects the effect of the microwave irradiation on the spin system. If only dipolar relaxation occurs between nuclei and electrons, the maximum enhancement achievable for  $^1\text{H}$  nuclei is  $\approx 330$  [53].

# Chapter 4

## Hardware

NMR spectroscopy is a powerful technique that allows us to study the structure, as well as dynamic processes, of proteins and molecules. The main pieces of equipment in a NMR lab are a magnet, that provides a static magnetic field, and a probe, that contains the sample, and includes a coil that can transmit RF pulses to the sample and acquire induced NMR signals. These pulses are transmitted by a spectrometer, interfaced with a computer. For DNP, a microwave source is also needed.

In this Chapter the hardware used for the experiments in this thesis will be presented in more detail. The two different setups are described in two sections, while the final section, some of the recurring pulse sequences used for the experiments are also described.

### 4.1 Solid state experiments

Experiments described in Chapters 5 and 6 have been performed at cryogenic temperatures with the system here described.

#### 4.1.1 Polariser

The magnet, referred to as “polariser”, is a  $\approx 3.34$  T shielded magnet produced by Oxford Instruments. Its magnetic field is created by a superconducting coil cooled down to 4.2 K by a liquid helium bath. A further liquid nitrogen jacket surrounds it to decrease the temperature jump between the coil environment and

the external one and reduce He boil off.

Figure 4.1a shows a picture of the polariser, while a schematic view of the inner part of the magnet is shown in Figure 4.1b. The helium jacket has an outlet into a vacuum dewar containing the NMR probe with a sample (A) and a microwave delivery system (E). The microwave delivery system consists of an overmoded waveguide that connects the sample space to the microwave source placed outside of the magnet barrel. The flow of helium from the magnet jacket into the sample space is controlled by a needle valve (C). A capacitor consisting of two concentric tubes (D) in the sample space allows measurements of the level of helium in the sample space. The capacitance changes depending on the amount of helium between the two tubes of the capacitor in the bore, and a LabVIEW (National Instruments - Austin, TX, USA) programme converts the voltage across the capacitor into values for the helium level, reported in percentage. A pressure sensor is also present in the bore.

This bore is connected to a rotary vane pump (Trivac D 65 B HE3, Oerlikon Leybold Vacuum), that lowers the pressure and, therefore, the helium boiling temperature. This allows to cool down the sample to  $\sim 1.7$  K.

### **4.1.2 Microwave source**

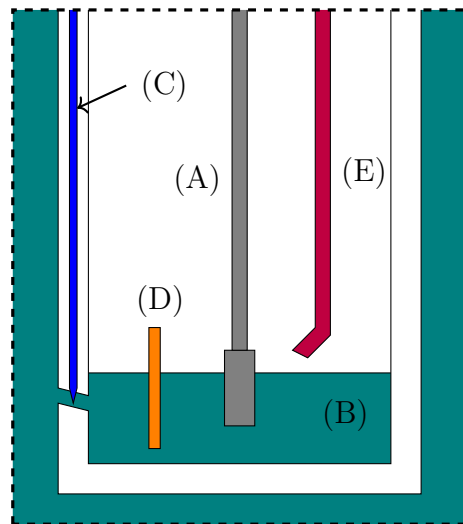
Microwave irradiation is supplied by a microwave solid state source (ELVA-1 - St. Petersburg, Russia), which covers a frequency range from 93.75 GHz to 94.25 GHz, up to a power of 400 mW. The microwave source is controlled by a LabVIEW programme, that controls the microwave frequency and power with high precision, and is connected to the spectrometer to allow the use of Transistor-Transistor Logic (TTL) signals as triggers during the NMR acquisition process.

### **4.1.3 Probes**

For the solid state experiments performed in the polariser two different custom designed probes have been used.



(a)



(b)

*Figure 4.1:* Figure 4.1a shows a photograph of the magnet, while Figure 4.1b shows a schematic representation of the cryostat. The sample sits at the bottom of the probe (A), which is embedded in liquid helium (B). The flow of helium into the sample space is regulated by a needle valve (C), while voltage readings at the ends of a capacitor (D) provide measurements of the level of liquid helium. Microwaves are radiated into the sample space through a waveguide (E).

## **$^{19}\text{F}$ detection**

The first probe is designed for the  $^{19}\text{F}$  NMR signal acquisition. It is shown in Figure 4.3a. The probehead is made of DELRIN, a plastic material which does not contain  $^{19}\text{F}$  atoms, so it does not provide background signals. Moreover, this material is microwave-transparent, so the sample holder does not shield the sample when irradiation is provided during the DNP experiments. The sample holder has a cylindrical shape, and its axis is oriented along a direction perpendicular to the static magnetic field. A solenoidal 5-turn coil wound around the sample holder is tuned and matched to the  $^{19}\text{F}$  frequency, which at the polariser magnetic field corresponds to  $\nu_F \approx 134.2$  MHz. The tuning is achieved through the use of ceramic capacitors placed close to the coil, and through variable capacitors in a tuning box outside of the magnet. The sample holder can contain  $\sim 50 \mu\text{L}$  of sample.

## **$^{19}\text{F}$ and $^1\text{H}$ acquisition**

The second probe is also a custom designed one, shown in Figure 4.3b. It has been designed and produced in a second stage of this project, when the need to monitor  $^1\text{H}$  NMR signal together with the  $^{19}\text{F}$  one had arisen. The probehead is made of brass, and the RF pulses are transmitted to the sample through a 2-loop saddle coil, sitting around a 4 mm quartz tube with a length of  $\approx 2$  cm that can contain  $\approx 100 \mu\text{L}$  of sample.  $^1\text{H}$  and  $^{19}\text{F}$  free materials have been carefully chosen so that they do not give rise to any background signals during the experiments. Connected to the probe outside from the magnet, a tuning box allows tuning and matching of the coil to  $^1\text{H}$  and  $^{19}\text{F}$  Larmor frequencies simultaneously, at 142.7 and 134.2 MHz respectively. Figure 4.2 shows the circuit designed to double-tune the coil to both frequencies.

The geometry of the coil, even though less efficient in transmitting the RF pulse with respect to the solenoid coil, was constrained due to the choice of  $^{19}\text{F}$ -free materials used for the probehead and sample tube.

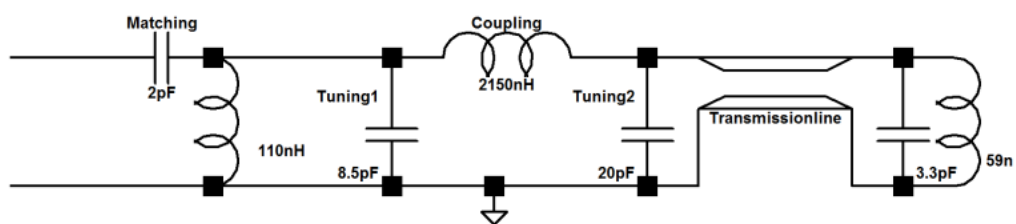
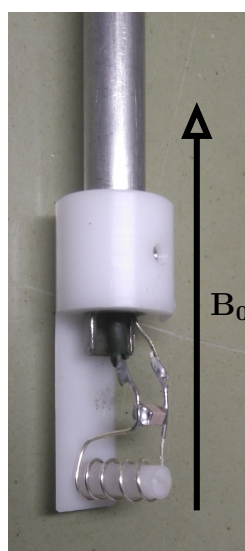
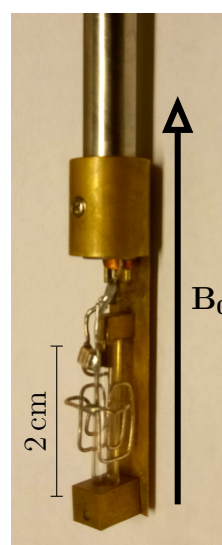


Figure 4.2: Circuit showing the components to tune the coil to  $^1\text{H}$  and  $^{19}\text{F}$  frequencies in a 3.4 T magnetic field. It has been designed by using the software LTSpice, that allows to simulate the circuit response to RF pulses.



(a)



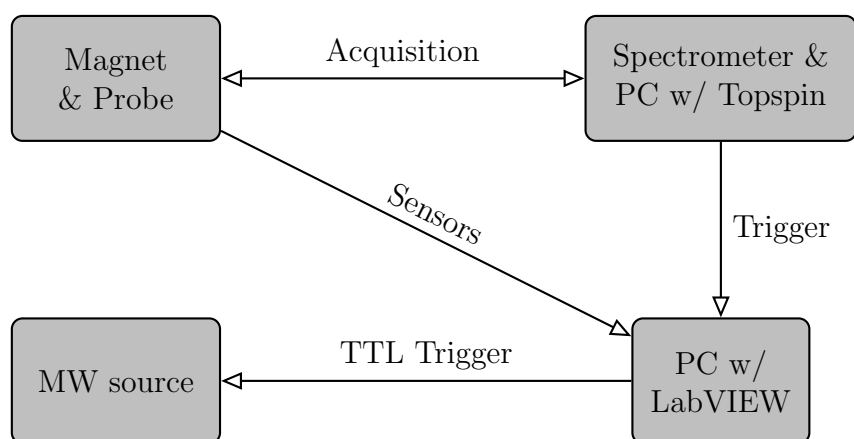
(b)

Figure 4.3: In Figure 4.3a a photograph of the DELRIN probe used in  $^{19}\text{F}$  DNP experiments is shown. Figure 4.3b shows the brass probe used for both  $^{19}\text{F}$  and  $^1\text{H}$  acquisitions. The direction of the static magnetic field  $B_0$  is also shown in the pictures.

#### 4.1.4 Spectrometer for solid state measurement

The NMR spectrometer used during the solid state experiments is a Bruker Avance DSX 400 console, interfaced to a computer running the software Topspin 1.3 (Bruker GmbH - Karlsruhe, Germany). A broad band amplifier is connected to the probe through a XBB preamplifier. Notice that since the spectrometer is meant to be used with a 9.4 T magnet (400 MHz), it was necessary to use the configuration of nuclei with lower gyromagnetic ratios for the NMR acquisition of  $^{19}\text{F}$  and  $^1\text{H}$  signals.

A TTL output from the spectrometer is connected to a DAQ card (National Instruments - Austin, TX, USA) connected to the computer where the same LabVIEW programme used to control the microwave source is running. Figure 4.4 shows a schematic picture of the used configuration.



*Figure 4.4:* The sensors in the magnet are connected through a DAQ card to a PC running the LabVIEW software, that shows the temperature and pressure readings. The probe is connected to the spectrometer that is connected to a PC running Topspin for NMR data acquisition. A trigger from the spectrometer to the other computer, through the DAQ card, allows control of the MW source, connected to the PC using LabVIEW.

## 4.2 Dissolution DNP setup

Among the techniques used to hyperpolarise a sample, dissolution DNP is nowadays one of the most efficient ones, achieving enhancements factors over 10000 [1]. It combines the DNP mechanism at low temperatures and a temperature jump

from cryogenic temperatures up to room temperature.

Dissolution DNP experiments take advantage of two different magnets. In a conventional setup, one of them is used to hyperpolarise the sample at low temperatures (below 2 K), and conventionally 3.4 T or 6.7 T magnets are used for this purpose. After the desired enhancement is achieved, the sample is dissolved by a hot solvent, that brings it to the liquid state at room temperature, and it is quickly transferred to a second magnet. This magnet could be a high resolution magnet, generally of 9.4 T, used to acquire the NMR signal from the sample that finishes in an NMR tube inside a standard NMR probe. Alternatively, a MRI scanner is used, where the sample can be injected in a patient prior to NMR acquisition [54]. The dissolution DNP process is limited by the longitudinal relaxation time constants of the hyperpolarised nuclei. Once the sample is dissolved, the polarisation achieved through DNP decays to its thermal equilibrium value according to an exponential decay characterised by  $T_1$ . However, the transfer time in between the dissolution process and the acquisition for a conventional dissolution DNP setup is of the order of few seconds [39, 55]. One of the limiting factors for the transfer time is the distance between the two magnets, since they are in separate locations, usually a few metres one from the other. Moreover, two separate magnets need a magnetic transfer tube to avoid loss of hyperpolarisation due to the absence of a magnetic field during transfer [56], as in absence of magnetic field there would be no the Zeeman splitting. Dissolution DNP is therefore suitable for nuclei with long longitudinal relaxation time constants such as  $^{13}\text{C}$  and  $^{15}\text{N}$ , but it penalises nuclei with short  $T_1$  like  $^1\text{H}$  or  $^{19}\text{F}$ , whose values can be of the same order of magnitude as the transfer time.

A new approach to dissolution DNP that overcomes the “long” dead time issue is used for the dissolution experiments presented in this work. For this scheme the two magnets sit in the same dewar, one on top of the other, minimising therefore the space between the two. In the following sections the parts composing this setup are described. A detailed description of the setup can be found here [16].

### 4.2.1 The dewar

Inside the dewar, two superconducting magnets are stacked vertically. The iso-centre of the top one, that generates a 3.4 T magnetic field, is 85 cm above the iso-centre of the bottom magnet, of 9.4 T. Such a distance is the minimum spacing that ensures a good homogeneity of both the magnetic fields at the iso-centres. A profile of the magnetic field as function of the distance relative to the iso-centre of the 3.4 T magnet is shown in Figure 4.5a, together with a drawing of the magnet (Figure 4.5b). Notice that the minimum magnetic field between the two iso-centre is 0.2 T: by keeping the sample in a magnetic field while it is moved from one magnet to the other ensures that the spin up and spin down states of the nuclei never become degenerate, so the polarisation is not lost during the transfer.

The bottom magnet is a 400 MHz (9.4 T) high resolution NMR magnet. Its bore can accommodate a standard NMR probe.

The top magnet is dedicated to the hyperpolarisation of the sample. The bore hosts a continuous flow cryostat (VTI - IceOxford - Abingdon, UK), that allows the sample to be cooled down by using liquid helium provided by an external helium dewar. The liquid helium is collected in a chamber in the cryostat, and a needle valve allows it to be driven to the sample space via a thin capillary. Then the liquid helium, sprayed into the sample, creates a thin film around it, and is evaporated by a vacuum pump (Pfeiffer TC-400 - Asstar, Germany) that quickly expands it, bringing the sample to a temperature of around 1.7 K, lower than the helium boiling point. At the bottom of the cryostat sits the “dissolution dock”, that is described in the next section.

#### Cool down procedure

Prior to loading the sample into the sample cup, the Variable Temperature Insert (VTI) is cooled down by means of liquid helium, supplied by an external helium dewar attached to the cryostat of the magnet. When the temperature reaches  $\approx 100$  K, the sample under investigation is loaded into the sample cup, and the waveguide is inserted in the cryostat. A couple of hours is needed for the cryostat to cool down to the target temperature of 1.7 K. The microwave source is then aligned with the top part of the waveguide, and turned on to start the microwave

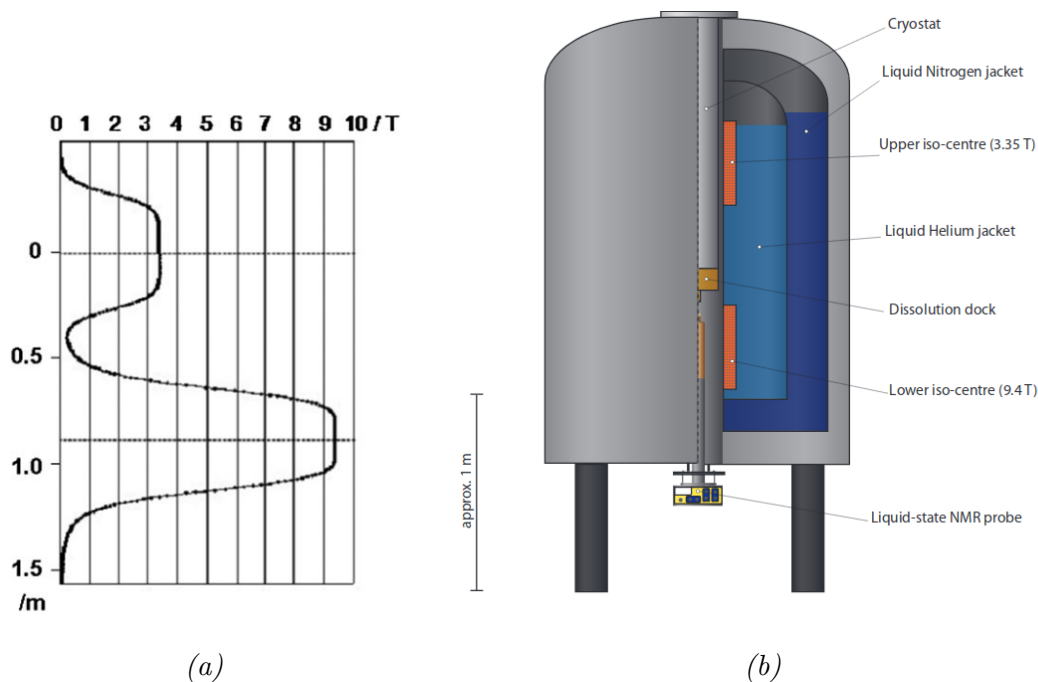


Figure 4.5: (a) Magnetic field at different height. The zero point was chosen to be at the iso-centre of the polarising magnet (Figure adapted from [16]). (b) Section of the dual iso-centre magnet, showing the position of the two superconducting coils, the cryostat and the dissolution dock (Figure adapted from [57]).

irradiation of the sample.

The bottom of the cryostat is sealed by a couple of valves, that allow hot solvent to reach the sample, and the sample to reach the high resolution NMR magnet during the dissolution process. In order to cool down the sample, liquid helium is sprayed directly onto the sample cup from capillaries. It creates a thin film surrounding the sample, that evaporates quickly thanks to the vacuum pumps connected to the cryostat. The process that allows to cool down the sample in this manner is the Joule-Kelvin expansion [58]. With the available vacuum pumps, the minimum reached temperature shown by the sensors is 1.7 K.

## 4.2.2 Quasi-optical microwave system

The same microwave source described in Section 4.1.2 is used for the experiments performed with the dual iso-centre magnet<sup>1</sup>. The microwave source sits on top of a quasi optic table, where the microwaves exiting the source are first converted into a Gaussian beam, passed through a series of polarising lenses and mirrors and

<sup>1</sup>This is a modification of the system with respect to previous works [16].

finally are directed into the waveguide.

### 4.2.3 Waveguide and sample cups

A hollow stainless steel tube hosts a corrugated waveguide. The tube,  $\approx 2$  m long, is vacuum-sealed from the top with a rexolite cap, that allows microwaves to enter the corrugated waveguide. The incoming Gaussian beam is converted by the waveguide into a  $HE_{11}$  field, and it is transmitted to the sample.

The waveguide is attached to a mechanical actuator (FESTO - Esslingen am Neckar, Germany), that can slide it up and down. The actuator is controlled by LabVIEW, and it is used in different phases of the experiments, as discussed in Chapter 7.

At the bottom of the waveguide it is possible to attach the sample cup. Two sample cups have been used in the dual iso-centre magnet. In the first one, shown in Figure 4.6a, a saddle coil surrounds the sample space. The coil can be connected to the spectrometer to monitor and study the hyperpolarisation process. This sample cup is mainly used to acquire DNP enhancement profiles via frequency sweep experiments, and to determine the DNP build-up time.

The second sample cup is shown in Figure 4.6b, and is designed to fit into the dissolution dock during a dissolution DNP experiment. It can contain up to  $50 \mu\text{L}$  of sample, which can be placed into the inverted sample cup.

### 4.2.4 Dissolution dock

The dissolution dock is shown in Figure 4.7. The dissolution dock (b) is designed so that the dissolution sample cup (a) tightly fits inside the cavity and creates a seal between the sample and the dock itself. There are two holes that connect the dock to the bottom of the cryostat: the tilted one is connected to a pneumatically controlled valve (Takasago Fluidic Systems - Nagoya, Japan) (d), connected to a tube that hosts pressurised hot solvent (c). The same tube is located inside another tube where hot oil is continuously flowing to warm up the solvent, that is loaded into the reservoir (f) prior to dissolution. The vertical hole is connected to another pneumatically controlled valve (i) that is connected to the NMR tube in the NMR probe (k) through an adapter (j). The two valves are triggered by

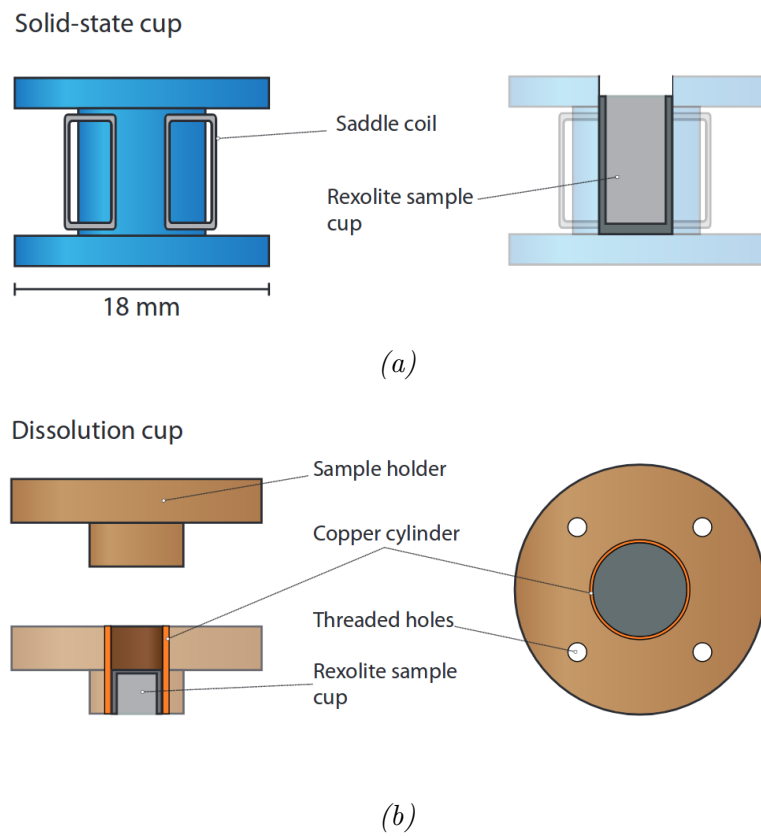
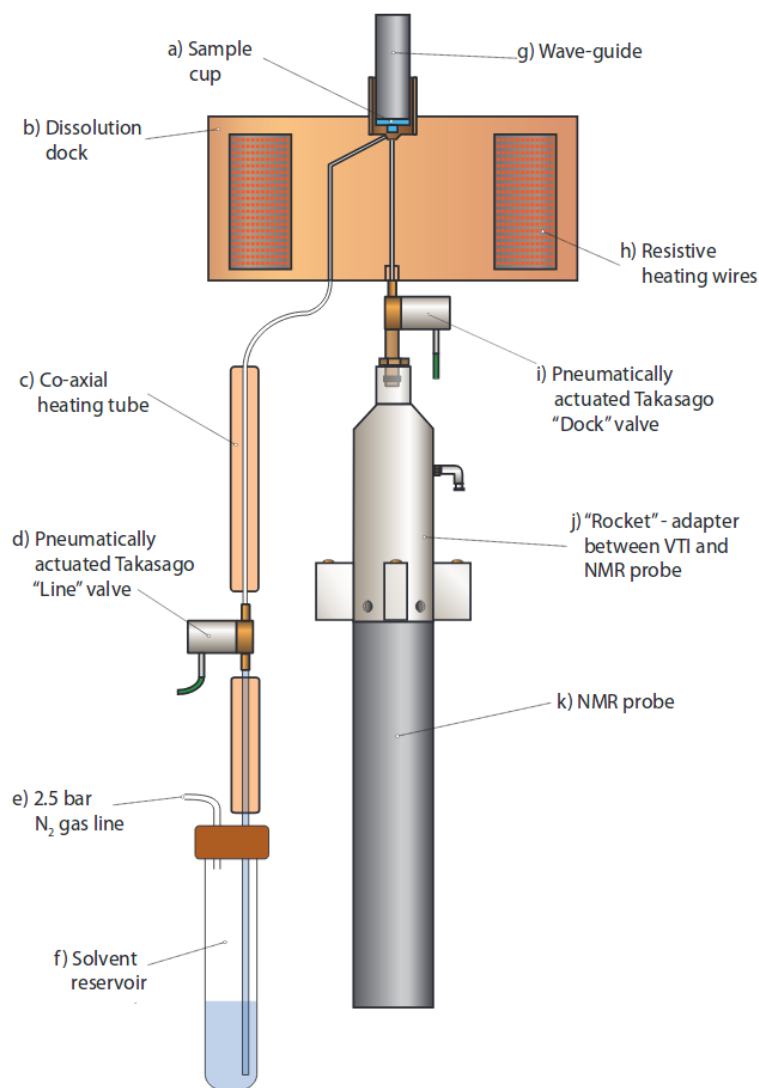


Figure 4.6: Schematic of the sample cup used for solid state experiments (a) and dissolution (b) (Figures adapted from [57]).

LabVIEW during the dissolution procedure, as described in Chapter 7, to allow the hot solvent to reach the sample and then to drive the dissolved sample into the NMR tube.

Finally, Figure 4.8 shows the schematic of the system as initially designed.



*Figure 4.7:* Schematic of the dissolution system where all the main components are shown (Figure adapted from [57]).

#### 4.2.5 Line-broadening of the NMR line after dissolution

The main issue incurred during dissolution experiments is the broadening of the NMR line after the dissolution. This broadening is caused by micro-bubbles that form in the hot solvent during the dissolution procedure, generating a susceptibility mismatch that distorts the local magnetic field in their vicinity. Once the sample

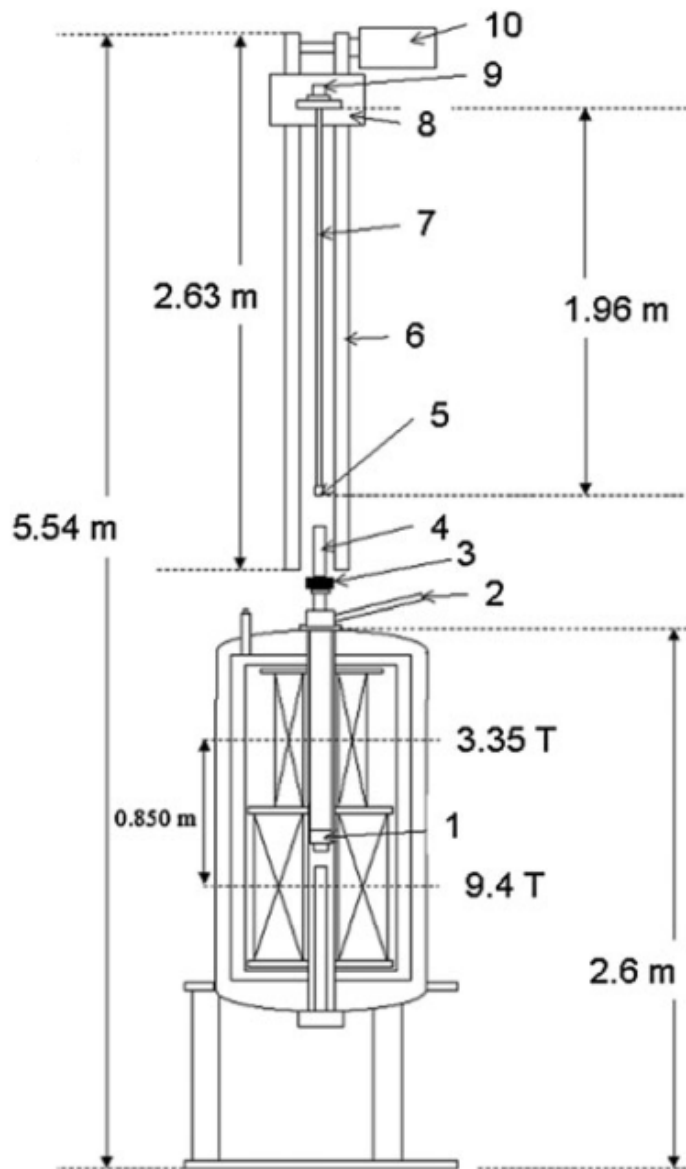


*Figure 4.8:* Dual iso-centre magnet schematics. (1) dissolution dock, (2) helium inlet for cryoinsert, (3) vacuum valve, (4) air lock, (5) sample cup, (6) actuator, (7) waveguide, (8) carriage, (9) Rexolite vacuum cap, (10) stepper motor for actuator control (Figure adapted from [16]).

is dissolved and reaches the NMR tube, bubbles move towards the upper surface of the sample. The effect of bubbles can be seen in the time-dependence of the width of the NMR line, that gets narrower as time passes. The NMR line reaches a steady-state value after  $\approx 1$  s that the sample settles in the tube.

A slight vacuum is applied to speed-up the settling process. The presence and effect of bubbles in a dissolution DNP experiment with the dual iso-centre magnet has been already studied in previous works [57, 59].

### 4.3 Methodology for experiments performed in the polariser

Experiments discussed in Chapter 5 and 6 are performed in the polariser magnet previously described. For the experiments where only  $^{19}\text{F}$  NMR signals are recorded, the DELRIN probe has been used. For the experiments where also  $^1\text{H}$  NMR signals are acquired, the brass probe was used instead.

In this section the methodology and issues related to the solid state experiments performed in the polariser are explained.

#### 4.3.1 Frequency sweep experiments

One of the most common experiments performed for the work described in the next chapters concerns the determination of the microwave frequency  $\nu_{MW}$  that creates the maximum DNP enhancement.

To determine  $\nu_{MW}$ ,  $N$  NMR spectra of the analysed nucleus are acquired while irradiating the sample with microwaves at a certain frequency. At the beginning of each experiment, the nuclear polarisation is saturated to ensure identical initial conditions. The saturation is achieved by using a train of  $n = 256$   $\pi/2$  pulses with alternating phases (x, y), and spaced by intervals of  $50 \mu\text{s}$ . The efficiency of the saturation was tested by acquiring a spectrum just after the last pulse in the train and checking that the integral of the signal intensity was negligibly small.

After saturation, the nuclear polarisation builds up during a certain delay  $T_{MW}$ . Then, a FID is acquired following a  $\pi/2$  pulse. After each acquisition, the mi-

crowave frequency is increased.

Figure 4.9 shows the pulse sequence used for frequency sweep experiments.

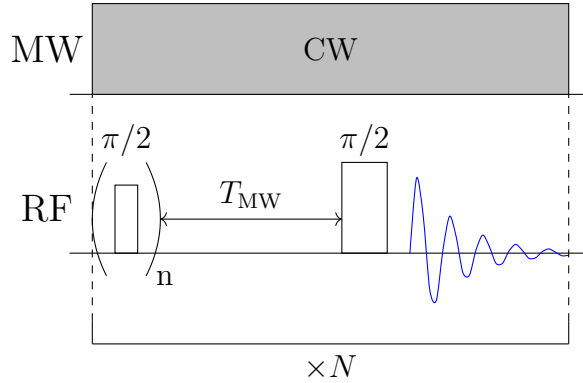


*Figure 4.9:* Pulse sequence used in a frequency sweep experiment. The polarisation is initially saturated by a  $\pi/2$  pulses train. Then hyperpolarisation builds up for a time  $T_{MW}$ . Following this delay, the FID is acquired after another  $\pi/2$  pulse. This sequence is repeated, and the microwave frequency is increased each time.

### 4.3.2 Saturation recovery

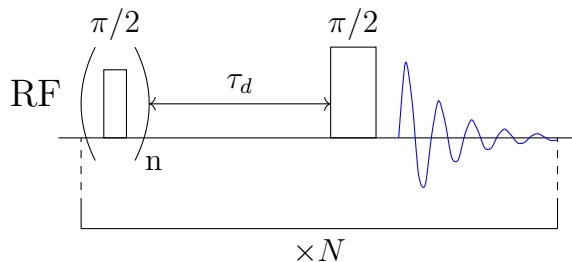
Another common pulse sequence used in the experiments described in this work is “saturation recovery”. This pulse sequence is usually performed to obtain the longitudinal relaxation build-up time constant  $T_1$  of a nuclear spin system. However, it also allows us to determine the nuclear DNP build-up time  $\tau_{DNP}$  if the sample is irradiated with microwaves throughout the duration of the experiment. During a saturation recovery experiment, a train of pulses, like the one described for the frequency sweep experiment, saturates the nuclear polarisation. A FID is acquired following a variable delay  $\tau_d$  and a  $\pi/2$  pulse. The experiment is repeated  $N$  times, incrementing  $\tau_d$  with increasing steps for each experiment, in order to show the time dependence of the nuclear signal.

Figure 4.10 shows the pulse sequence for a saturation recovery experiment.

Data from the experiments have been fitted with the empirical function:

$$I(t) = I_0 (1 - \exp\{-Rt\}) , \quad (4.1)$$

where  $I(t)$  is the signal integral of each NMR spectrum at time  $t$  after saturation,  $I_0$  is the value of the integral at thermal equilibrium or the steady-state signal under



*Figure 4.10:* Pulse sequence used for saturation recovery experiments. The polarisation is initially saturated by a  $\pi/2$  pulse train. Then the spin ensemble recovers its polarisation for a time  $\tau_d$ . Following this delay, that increases each time this sequence is repeated, the FID is acquired following another  $\pi/2$  pulse.

microwave irradiation, and the rate  $R$  is the inverse of the longitudinal relaxation time constant (or DNP build-up time constant  $\tau_{\text{DNP}}$  if the sample is irradiated with microwaves during the experiment). The ratios between  $I_0$  under microwave irradiation and  $I_0$  with MW off have been calculated in order to estimate the DNP enhancement achieved.

### 4.3.3 Saturation recovery for cross-relaxation experiment

To show the transient  $^{19}\text{F}$  polarisation that builds up in some experiments of Chapter 5, the saturation recovery pulse sequence shown in the previous section was modified.

For these experiments, the sample is irradiated with microwaves at the frequency corresponding to the maximum DNP enhancement for  $^{19}\text{F}$  for an interval  $T_{\text{MW}}$ , so the sample is hyperpolarised. After the microwaves are turned off, a train of pulses saturates the  $^{19}\text{F}$  polarisation, and a FID is acquired following a delay  $\tau_d$ , like in a standard saturation recovery experiment. As for the saturation recovery pulse sequence, the experiment is repeated  $N$  times and the delay  $\tau_d$  is incremented each time. The pulse sequence is shown in Figure 4.11.

### 4.3.4 Interleaved acquisition of $^1\text{H}$ and $^{19}\text{F}$ for cross-relaxation

In Chapter 5, some of the experiments are performed by acquiring quasi-simultaneously the  $^1\text{H}$  and  $^{19}\text{F}$  NMR signals. These experiments are required to improve the data

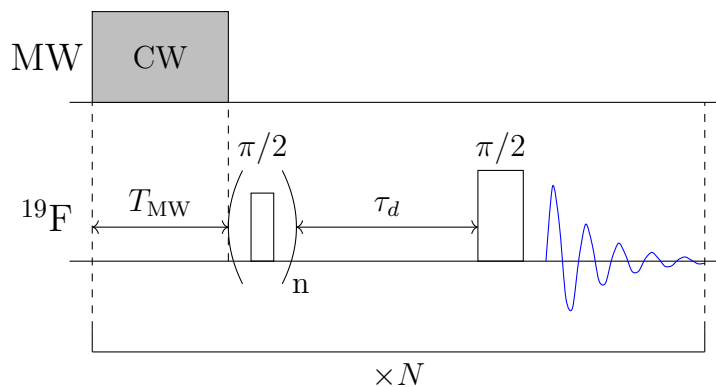


Figure 4.11: Pulse sequence used during experiments to study cross-relaxation. For a time  $T_{\text{MW}}$  the spin ensemble is hyperpolarised by microwave irradiation. After this time, the microwave irradiation is interrupted, and the rest of the pulse sequence is identical to the saturation recovery pulse sequence, shown in Figure 4.10.

quality and avoid bias of data by temperature variation, discussed later in this Chapter. Experiments with double acquisition were performed by using the double tuned brass probe.

By using this pulse sequence,  $^1\text{H}$  and  $^{19}\text{F}$  signals were consecutively acquired in the same experiment. The pulse sequence used to acquire the data is shown in Fig. 4.12. This pulse sequence is the same as the one in Fig. 4.11, with the addition of a pulse and acquisition on the frequency corresponding to the  $^1\text{H}$  Larmor frequency just after  $^{19}\text{F}$  acquisition. The time difference between  $^{19}\text{F}$  and  $^1\text{H}$  acquisition is  $\Delta t \ll 1\text{ s}$ , which is the shortest time interval that has been used, and therefore has been ignored when fitting  $^1\text{H}$  decay data.

Each spectrum is acquired in a separate experiment on Topspin 1.5 software. A *multizg* acquisition linked the experiments together, allowing one experiment to start after the previous one has just finished. The first experiment, as well as all the odd-numbered experiments, contains the pulse programme related to the pulses on the  $^{19}\text{F}$  channel. It also controls the trigger that turns on and off the microwave source. For each experiment, the delay  $\tau_d$  was increased as in a standard saturation recovery experiment. The microwave source, controlled by a TTL signal from the console, was turned on for period  $T_{\text{MW}}$  prior to every experiment to allow a full  $^1\text{H}$  DNP build-up. The second experiment, as well as the remaining even-numbered

ones, contains a single pulse and acquisition with reference frequency close to the  $^1\text{H}$  Larmor frequency (third line of the pulse sequence in Fig. 4.12).

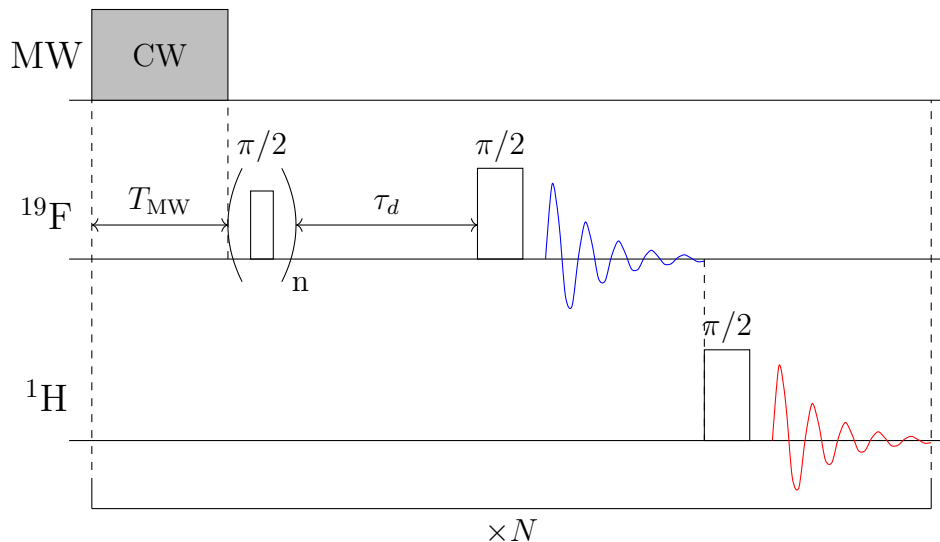


*Figure 4.12:* Pulse sequence used in the multizg experiments for cross-relaxation. This pulse sequence is identical to the pulse sequence used to study cross-relaxation (Figure 4.11). However, after the  $^{19}\text{F}$  FID acquisition, the carrier frequency, initially set to match the  $^{19}\text{F}$  Larmor frequency, is changed to the  $^1\text{H}$  Larmor frequency. Then a pulse excites the  $^1\text{H}$  ensemble and the  $^1\text{H}$  FID is acquired.

### 4.3.5 Saturation recovery with continuous $^1\text{H}$ saturation

In Chapters 5 and 6 experiments are performed to show how the presence of the presence of  $^1\text{H}$  nuclei in the sample affects the  $^{19}\text{F}$  polarisation. In these experiments, the  $^1\text{H}$  magnetisation is continuously saturated, while a saturation recovery experiment is performed on the  $^{19}\text{F}$  nuclei.

The used pulse sequence is shown in Figure 4.13. The  $^1\text{H}$  saturation is achieved by using a series of  $\pi/2$  pulses every 250 ms on resonance with the  $^1\text{H}$  Larmor frequency during the recovery time  $\tau_d$  between the saturation of  $^{19}\text{F}$  polarisation and FID acquisition. Therefore, during the delay between the  $^{19}\text{F}$  saturation and the FID acquisition, four pulses per second are sent to the  $^1\text{H}$  channel.

To check the efficiency of the saturation,  $^1\text{H}$  FIDs have been acquired in place of  $^{19}\text{F}$  signals by using the same pulse sequence, and it was observed that their signal-to-noise ratios were  $S/N < 1$  for each spectrum.

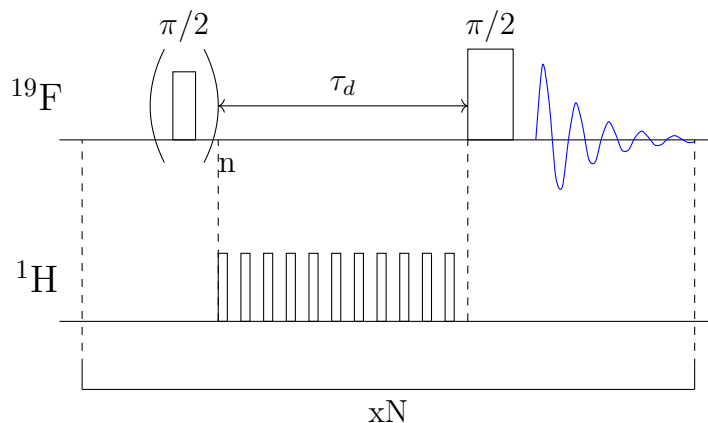


Figure 4.13: Pulse sequence used during experiments to study the evolution of  $^{19}\text{F}$  while  $^1\text{H}$  is continuously saturated. The pulse sequence is identical to the saturation recovery pulse sequence, shown in Figure 4.10, with the addition of pulses to saturate the  $^1\text{H}$  magnetisation.

### 4.3.6 Temperature stability in the polariser

Temperature data during experiments in the polariser are collected by a pressure sensor which is connected to the cryostat of the magnet. Sensor calibration allows conversion of collected pressure measurements into temperatures. It is also possible to measure the level of liquid helium inside the bore by means of the capacitor placed in the sample space.

To cool down the sample, the needle valve that connects the helium reservoir of the magnet and the bore is opened. However, it is extremely challenging to stabilise the flow of helium through the needle valve. Moreover, it was noticed that the helium flow dropped slowly down to zero, and it was necessary to further open the needle valve to re-establish the helium flow. As a result, the pressure and temperature conditions slightly changed for every experiment, since a small difference in the valve opening entailed a different helium flux through the valve, and therefore a change in temperature. The observed temperature variation was  $\pm \approx 0.1\text{ K}$ .

Variations in relaxation rates were in fact recorded when the same experiment was repeated. For example, the results for  $^{19}\text{F}$   $T_1$  from saturation recovery experiments in a sample containing 75% toluene, 25% fluorobenzene and 40 mM TEMPO are:

$87 \pm 4\text{ s}$	$104.2 \pm 0.7\text{ s}$	$116.2 \pm 1.4\text{ s}$	$121.0 \pm 1.3\text{ s}$
---------------------	--------------------------	--------------------------	--------------------------

The errors in each measurement are based on the fit results, since the errors associated with the spectra integrals are negligibly small. The fact that these errors are small compared to the  $T_1$  values indicates that the temperature variation is negligible within a single experiment. In fact  $^{19}\text{F}$  polarisation recovers its equilibrium value according to the expected saturation recovery function, without drifting away from the expected pattern.

However, a notable variation in time constants was observed when experiments were repeated with the same sample, with a difference of  $\approx 33\text{ s}$  between the shortest and longest recorded values.

Based on these four  $T_1$  values, it is possible to calculate the mean value  $\bar{T}_1 = 107 \pm 13\text{ s}$ , where the error is given by their standard deviation.

According to this calculation, the relative error on the relaxation time constant is  $\approx 12\%$  of its value.

However, the number of readings is too small, and many more measurements would be needed for a better estimation of the error.

The temperature and helium level variation can be observed in Figure 4.14, where these values are recorded during two different cross-relaxation experiments.

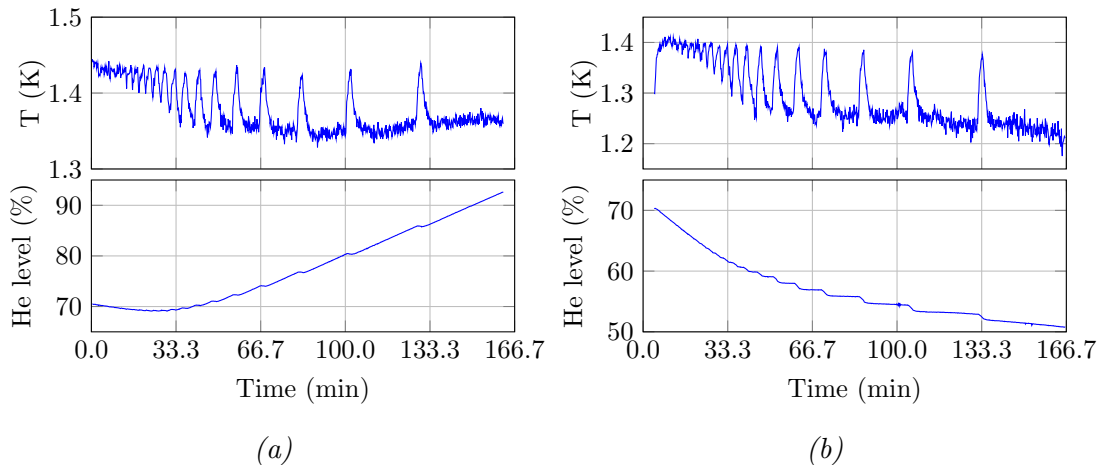


Figure 4.14: Temperature and helium level recorded during two different experiments where the same pulse sequence was used.

It is important to note that despite the effort in keeping the temperature at the same value, the physical conditions change between the two experiments: the

temperature is in fact higher in the first case (Figure 4.14a) than in the second (Figure 4.14b).

The spikes in the temperature figures are caused by a momentary increase in temperature when microwaves are applied to the sample ( $T_{\text{MW}} = 2$  min for both experiments), returning to its equilibrium value just after. The temperature increase is caused by the liquid helium that boils off, due to the microwave irradiation that heats up the helium in the sample space. For the first minutes of the experiments, when the recovery delays  $\tau_d$  are too short, the decay of temperature to equilibrium is negated by the incoming microwaves which warm up the sample again before it returns to its equilibrium value.

Moreover, the sensor is not calibrated and presents an offset in the read temperature, which is  $\approx 0.4$  K lower than the real one, measured by using a calibrated sensor in place of the probe. This temperature offset has therefore been considered when temperature readings are provided in Chapters 5 and 6.

## Chapter 5

# $^{19}\text{F}$ DNP optimisation and TEMPO-mediated $^1\text{H}$ - $^{19}\text{F}$ cross-relaxation at cryogenic temperatures

In this Chapter the feasibility of producing large  $^{19}\text{F}$  polarisation at cryogenic temperatures by DNP is investigated.

As explained in Chapter 3, DNP requires the presence of unpaired electrons in the sample. Among the mechanisms that drive  $^{19}\text{F}$  DNP at low temperatures ( $\sim 1.6\text{ K}$ ) with mono radicals that possess a significant g-anisotropy like TEMPO, it was shown that the Cross Effect [40] and the Solid Effect [34] are the dominant ones [60, 61].

Polarisation is built-up in time with a characteristic time constant  $\tau_{\text{DNP}}$  which depends on several factors, such as the number of free electrons and the power of the irradiating microwaves, as well as the nuclear and electron relaxation time  $T_1$ . These parameters also determine the maximum amount of polarisation that is transferred from the electrons to the nuclei.

In this Chapter the signal enhancement produced by DNP for  $^{19}\text{F}$  is optimised, and factors influencing the enhancement, such as the concentration of the polarising agent, the  $^{19}\text{F}$  concentration, the sample deuteration, and DNP build-up time, are analysed at cryogenic temperatures.

Since  $^1\text{H}$  and  $^{19}\text{F}$  nuclei have gyromagnetic ratios whose values are close to each other [62], also their Larmor frequencies are similar ( $\nu_H - \nu_F \sim 8$  MHz in a 3.4 T magnetic field) compared to the broad TEMPO EPR spectrum, and they are simultaneously hyperpolarised during DNP. After the optimal DNP conditions for  $^{19}\text{F}$  are found, the effect produced by hyperpolarised  $^1\text{H}$  nuclei on  $^{19}\text{F}$  is also studied. Parameters like the dependence of this effect on the electron and  $^{19}\text{F}$  concentrations in the samples are analysed, as well as the type of free radical used for DNP.

## 5.1 Optimisation of $^{19}\text{F}$ DNP in solid state

Experiments on  $^{19}\text{F}$  and  $^1\text{H}$  solid state NMR have been performed in a strong magnetic field (3.37 T) at cryogenic temperatures in the “polariser” magnet with the double-tuned brass probe, both instruments described in Section 4.1. The samples were prepared by mixing fluorobenzene and toluene (Figures 5.1a and 5.1b). The free radical TEMPO (Figure 5.1c) was added to the sample to achieve hyperpolarisation of the spin nuclei in the sample via DNP. According to the Boltzmann distribution Equation 1.6 in Section 1.1.3, at 1.6 K, thermal polarisation of  $^{19}\text{F}$  and  $^1\text{H}$  is  $\approx 0.2\%$ , while for electrons it is around 89%. This means that while at such temperature electrons are almost fully polarised, nuclei have still a low polarisation level.

Through microwave irradiation of the sample at a defined frequency that induces

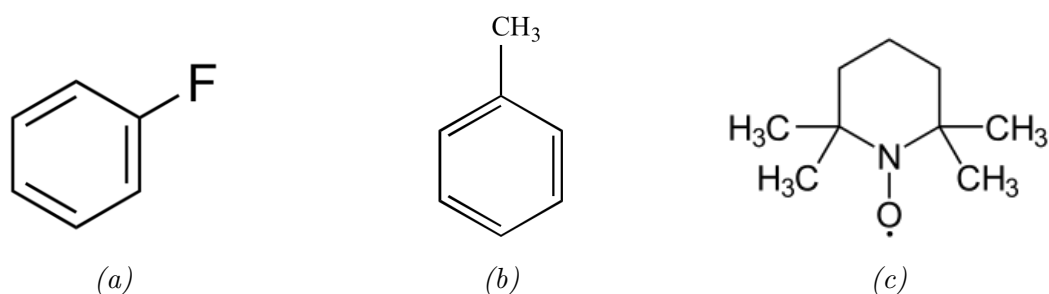


Figure 5.1: Chemical structures of the fluorobenzene (a), toluene (b) and TEMPO (c).

DNP hyperpolarisation<sup>1</sup>, the system is driven to a new equilibrium state, resulting

<sup>1</sup>As previously discussed on Chapter 3.

in an increase of the population difference of the nuclear spins in the lower energy level and producing an enhancement  $\epsilon$  of the NMR signal<sup>2</sup>. The time constant  $\tau_{DNP}$  characterising the build-up into the non-equilibrium state, ranges between  $\approx 20$  s and  $\approx 5$  min for  $^1\text{H}$  and  $^{19}\text{F}$ . When microwaves are turned off, the enhanced polarisation of the nuclei in the sample decays with the usual longitudinal relaxation time constant  $T_1$ .

The contribution of  $^{13}\text{C}$  nuclei, present in natural abundance in the used samples, is neglected during the analysis of the experimental data.

### 5.1.1 Samples

Several experiments have been performed to determine the optimal sample preparation that leads to an efficient  $^{19}\text{F}$  hyperpolarisation. Samples containing the free radical TEMPO in a matrix of organic solvent made of toluene, fluorobenzene and benzene have been prepared.

A glassy sample is needed to ensure that the free radicals added to the sample are uniformly distributed. In fact a solvent that freezes in a crystalline structure can cause phase separation between the polarising agent and the molecules, resulting in a strong reduction of the enhancements [63–65].

Mixtures containing different volume ratios of toluene and benzene have been cooled down in liquid nitrogen. Starting from a ratio of 50:50 (v/v), the benzene to toluene ratio was decreased in the tested samples until the frozen sample exhibited characteristics of a transparent solid. This transparency is characteristic of glasses. A final ratio of 25% benzene and 75% toluene has been selected. This ratio provides the mixture with the most benzene in the sample that still forms a glassy matrix at cryogenic temperature.

Samples have been prepared by combining benzene with fluorinated benzene to make up 25% of the sample. Deuterated benzene and deuterated toluene have been used for three of the samples. These samples have been prepared to study the dependency of  $^{19}\text{F}$  and  $^1\text{H}$  polarisation dynamics as a function of  $^1\text{H}$  concentration in the sample. In addition, one radical free sample has been used. Finally, two samples containing the free radicals TEKPol [66] and BDPA [37,38] have been

---

<sup>2</sup>More details of DNP have already been discussed in Chapter 3.

prepared. Table 5.1 shows the composition of samples used in the experiments described in this Chapter.

			25% (v/v)		75% (v/v)	
	[ <sup>19</sup> F] (mM)	[ <sup>1</sup> H] (mM)	C <sub>6</sub> H <sub>5</sub> F	C <sub>6</sub> H <sub>6</sub>	Toluene	TEMPO (mM)
<b>Sample 1a</b>	$2.7 \times 10^3$	$69.5 \times 10^3$	1	0	1	40
<b>Sample 2a</b>	660	$71.5 \times 10^3$	1/4	3/4	1	40
<b>Sample 3a</b>	161	$72 \times 10^3$	1/16	15/16	1	40
<b>Sample 4a</b>	54	$72 \times 10^3$	1/48	47/48	1	40
<b>Sample 5a</b>	0	$72.2 \times 10^3$	0	1	1	40
<b>Sample 6a</b>	$2.7 \times 10^3$	$69.5 \times 10^3$	1	0	1	0
<b>Sample 1b</b>	$2.7 \times 10^3$	$69.5 \times 10^3$	1	0	1	60
<b>Sample 1c</b>	$2.7 \times 10^3$	$69.5 \times 10^3$	1	0	1	20
	[ <sup>19</sup> F] (mM)	[ <sup>1</sup> H] (mM)	C <sub>6</sub> H <sub>5</sub> F	C <sub>6</sub> H <sub>6</sub>	Toluene	TEKPol (mM)
<b>Sample 1e</b>	$2.7 \times 10^3$	$69.5 \times 10^3$	1	0	1	20
	[ <sup>19</sup> F] (mM)	[ <sup>1</sup> H] (mM)	C <sub>6</sub> H <sub>5</sub> F	C <sub>6</sub> H <sub>6</sub>	Toluene	BDPA (mM)
<b>Sample 1f</b>	$2.7 \times 10^3$	$69.5 \times 10^3$	1	0	1	40
	[ <sup>19</sup> F] (mM)	[ <sup>1</sup> H] (mM)	C <sub>6</sub> H <sub>5</sub> F	C <sub>6</sub> D <sub>6</sub>	Toluene-d <sub>8</sub>	TEMPO (mM)
<b>Sample 1d</b>	$2.7 \times 10^3$	$13.5 \times 10^3$	1	0	1	40
<b>Sample 2d</b>	660	$3.3 \times 10^3$	1/4	3/4	1	40
<b>Sample 3d</b>	54	270	1/48	47/48	1	40

Table 5.1: Compositions of samples studied with different <sup>19</sup>F concentrations, degree of deuteration and free radical concentrations.

## 5.1.2 Experiments and results

### Determination of microwave frequency and power for maximum enhancement

<sup>19</sup>F DNP frequency sweeps were recorded using Sample 1d to determine the microwave frequency that provides the largest DNP enhancement: Fig. 5.2 shows the integrals of <sup>19</sup>F and <sup>1</sup>H NMR signals acquired at different microwave frequencies, with an irradiation period of 60 s for <sup>19</sup>F and 30 s for <sup>1</sup>H. The microwave power transmitted by the source for these experiments was set to  $P_{\text{MW}} = 400$  mW. Integrals are normalised to the maximum positive value. The details of this experiment are presented in Section 4.3.1, where the DNP frequency sweep experiment is described.

As the figure shows, when the sample is irradiated with microwaves at  $\nu_{\text{MW}} \approx$

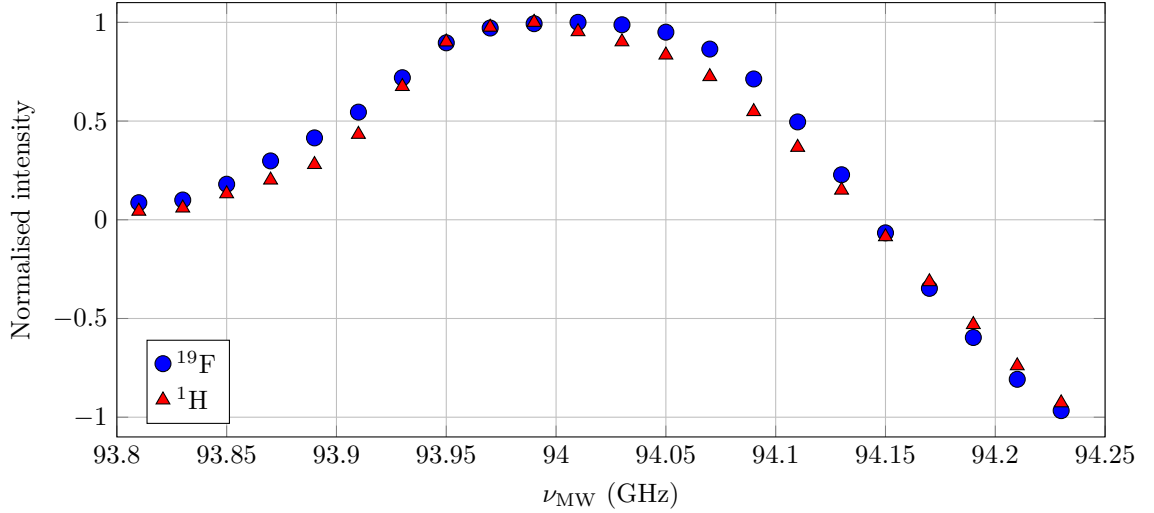


Figure 5.2: Normalised DNP enhancement profile of  $^{19}\text{F}$  and  $^1\text{H}$  NMR signals for Sample 1d as a function of microwave frequency after microwave irradiation at  $P_{\text{MW}} = 400$  mW. The curve is truncated due to the restricted sweep range of the microwave source.  $^{19}\text{F}$  polarisation period is  $T_{\text{MW}} = 60$  s, while  $^1\text{H}$  polarisation period is  $T_{\text{MW}} = 30$  s.

94 GHz, a maximum DNP enhancement can be observed for both  $^{19}\text{F}$  and  $^1\text{H}$ . Note that the curve is truncated for higher frequencies since the microwave source has only a sweep range of 500 MHz, which is smaller than the full DNP enhancement profile. Nonetheless, the behaviour of the intensity as a function of microwave frequency is consistent with other similar experiments in which the complete curve is shown [67, 68].

To determine the microwave power corresponding to the maximum DNP enhancement, build-up curves were recorded at various power levels.

Four different saturation recovery experiments (for details see Section 4.3.2), were performed on Sample 1d while irradiating the sample with microwaves at frequency 94 GHz. The power levels used for each experiment are 50, 100, 200 and 400 mW. The experimental data are shown in Figure 5.3.

As shown in the figure, the microwave power that provide the highest DNP enhancement and shortest build-up time  $\tau_{\text{DNP}}$  is  $P_{\text{MW}} = 400$  mW. For this reason, this value has been used for all the experiments presented in this Chapter.

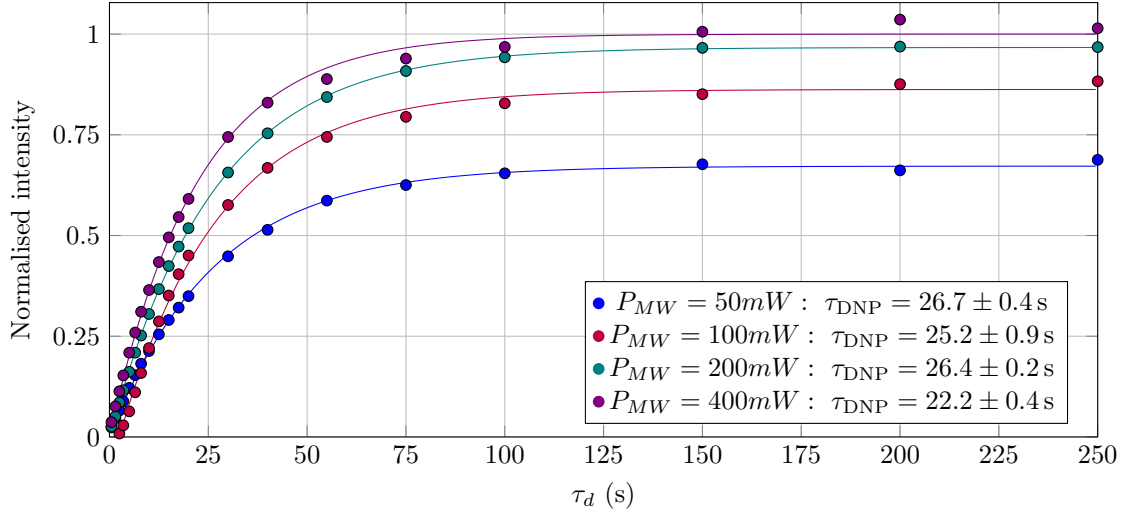


Figure 5.3:  $^{19}\text{F}$  DNP build-up experiment while irradiating the sample with microwaves at  $\nu_{MW} = 94$  GHz at four different powers. For these experiments Sample 1d has been used. The build-up time constants  $\tau_{DNP}$ , obtained by fitting the data with the saturation recovery function described in Section 4.3.2, are shown alongside the microwave power in the legend.

### Longitudinal relaxation and DNP build-up times

Saturation recovery experiments (see Section 4.3.2) have been performed for the samples in Tab. 5.1 to measure the longitudinal relaxation time constants  $T_1$ . The same pulse sequence was also used while irradiating the sample with microwaves at frequency  $\nu_{MW} = 94$  GHz and power  $P_{MW} = 400$  mW.  $\nu_{MW}$  and  $P_{MW}$ , determined in the previous section, allow to obtain the optimal DNP enhancement  $\epsilon$ , as well as the corresponding build-up time constants  $\tau_{DNP}$ . Enhancements have been calculated as  $\epsilon = I_{DNP}/I_{th}$ , where  $I_{DNP}$  and  $I_{th}$  are the integral of the hyperpolarised and thermal NMR spectra respectively.

Data from the experiments have been fitted with the empirical function:

$$I(t) = I_0 (1 - \exp\{-Rt\}), \quad (5.1)$$

described in the saturation recovery experiment (Section 4.3.2). Tab. 5.2 shows nuclear  $T_1$ ,  $\tau_{DNP}$  and DNP enhancement  $\epsilon$  for both  $^{19}\text{F}$  and  $^1\text{H}$  for each sample in Tab. 5.1.

	$^1\text{H}$			$^{19}\text{F}$		
	$T_1$ (s)	$\tau_{\text{DNP}}$ (s)	$\epsilon$	$T_1$ (s)	$\tau_{\text{DNP}}$ (s)	$\epsilon$
<b>Sample 1a</b>	$88.1 \pm 1.8$	$18.2 \pm 0.8$	$28.6 \pm 0.4$	$104.2 \pm 0.7$	$23.20 \pm 0.13$	$58.44 \pm 0.17$
<b>Sample 1b</b>	$85.1 \pm 1.5$	$20 \pm 3$	$70.0 \pm 0.5$	$80 \pm 30$	$26.4 \pm 1.0$	$101 \pm 14$
<b>Sample 1c</b>	$127.6 \pm 1.5$	$82 \pm 2$	$23.4 \pm 0.2$	$500 \pm 200$	$170 \pm 13$	$31 \pm 8$
<b>Sample 2a</b>	$91 \pm 3$	$24.8 \pm 0.9$	$43.1 \pm 0.7$	$191 \pm 4$	$67.1 \pm 1.1$	$65.1 \pm 0.6$
<b>Sample 3a</b>	$63.5 \pm 1.8$	$16.7 \pm 0.3$	$40.1 \pm 0.4$	$580 \pm 40$	$197 \pm 9$	$102 \pm 3$
<b>Sample 4a</b>	$141 \pm 8$	$47.6 \pm 1.0$	$50.3 \pm 1.0$	$600 \pm 130$	$330 \pm 30$	$90 \pm 7$
<b>Sample 5a</b>	$193 \pm 3$	$42.9 \pm 0.5$	$65.1 \pm 0.3$	–	–	–

*Table 5.2:* Time constants  $T_1$  and  $\tau_{\text{DNP}}$ , and DNP enhancement  $\epsilon$  for both  $^{19}\text{F}$  and  $^1\text{H}$  for the non deuterated samples 1a (2.7 M  $^{19}\text{F}$ , 40 mM TEMPO), 1b (2.7 M  $^{19}\text{F}$ , 60 mM TEMPO), 1c (2.7 M  $^{19}\text{F}$ , 20 mM TEMPO), 2a (660 mM  $^{19}\text{F}$ , 40 mM TEMPO), 3a (161 mM  $^{19}\text{F}$ , 40 mM TEMPO), 4a (54 mM  $^{19}\text{F}$ , 40 mM TEMPO) and 5a (no  $^{19}\text{F}$ , 40 mM TEMPO) in Tab. 5.1. Microwaves irradiation at frequency  $\nu_{\text{MW}} = 94$  GHz was used for the DNP experiments. The samples are arranged in decreasing order of the  $^{19}\text{F}$  concentration.

	$^1\text{H}$			$^{19}\text{F}$		
	$T_1$ (s)	$\tau_{\text{DNP}}$ (s)	$\epsilon$	$T_1$ (s)	$\tau_{\text{DNP}}$ (s)	$\epsilon$
<b>Sample 1d</b>	$174 \pm 4$	$19.1 \pm 0.4$	$110.3 \pm 1.2$	$144.0 \pm 1.9$	$23.6 \pm 0.3$	$80.5 \pm 0.5$
<b>Sample 2d</b>	$47.2 \pm 1.9$	$11.9 \pm 0.2$	$125.5 \pm 1.7$	$255 \pm 4$	$86.8 \pm 1.9$	$115.1 \pm 1.0$
<b>Sample 3d</b>	$63 \pm 4$	$22.1 \pm 1.7$	$\approx 160$	$700 \pm 300$	$250 \pm 20$	$\approx 200$

*Table 5.3:* Time constants  $T_1$  and  $\tau_{\text{DNP}}$ , and DNP enhancement  $\epsilon$  for both  $^{19}\text{F}$  and  $^1\text{H}$  for the deuterated Samples 1d (2.7 M  $^{19}\text{F}$ , 40 mM TEMPO), 2d (660 mM  $^{19}\text{F}$ , 40 mM TEMPO) and 3d (54 mM  $^{19}\text{F}$ , 40 mM TEMPO) in Tab. 5.1. Microwaves irradiation at frequency  $\nu_{\text{MW}} = 94$  GHz was used for the DNP experiments. The samples are arranged in decreasing order of the  $^{19}\text{F}$  concentration.

The errors associated with the measurements are the regression errors obtained while fitting the data. As discussed in Section 4.3.6, these errors represent a lower limit of the “true” error associated with the values. The experimental error, coming from differences in temperature between experiments, has been estimated to be  $\approx 12\%$  of each value. The error associated to the measurements is indicative of the “goodness” of the experiment, showing whether the results are self-consistent within each experiment. Assuming that the temperature does not change significantly within each experiment, the error based on the fit result depends on the signal-to-noise ratio of each spectrum. Wherever the error is large, the signal-to-noise ratio value was poor. On the other hand, small errors are associated to data with large signal-to-noise ratios. Figure 5.4 shows two example of spectra with large and poor signal-to-noise ratios.

	$^1\text{H}$			$^{19}\text{F}$		
	$T_1$ (s)	$\tau_{\text{DNP}}$ (s)	$\epsilon$	$T_1$ (s)	$\tau_{\text{DNP}}$ (s)	$\epsilon$
<b>Sample 1e</b>	$121 \pm 2$	$20.9 \pm 0.9$	$24.3 \pm 0.3$	$181 \pm 8$	$24 \pm 2$	$35.4 \pm 1.3$
<b>Sample 1f</b> ( $\nu_{\text{SE}}$ )	$130 \pm 17$	$130 \pm 7$	$13.3 \pm 0.7$	$225 \pm 7$	$240 \pm 20$	$9.1 \pm 0.3$
<b>Sample 1f</b> ( $\nu_{\text{heCE}}$ )	$130 \pm 17$	$81 \pm 9$	$1.82 \pm 0.12$	$225 \pm 7$	$167 \pm 7$	$3.53 \pm 0.06$

Table 5.4: Time constants  $T_1$  and  $\tau_{\text{DNP}}$ , and DNP enhancement  $\epsilon$  for both  $^{19}\text{F}$  and  $^1\text{H}$  for Samples 1e (2.7 M  $^{19}\text{F}$ , 20 mM TEKPol) and 1f (2.7 M  $^{19}\text{F}$ , 40 mM BDPA) in Tab. 5.1. Microwaves irradiation at frequency  $\nu_{\text{MW}} = 94$  GHz was used for the DNP experiments of Sample 1e. DNP experiments for Sample 1f were performed at  $\nu_{\text{MW}} = \nu_{\text{SE}} = 93.79$  GHz and  $\nu_{\text{MW}} = \nu_{\text{heCE}} = 93.9$  GHz.

The results in Table 5.2 show that for  $^1\text{H}$  the  $T_1$  and build-up time  $\tau_{\text{DNP}}$  con-

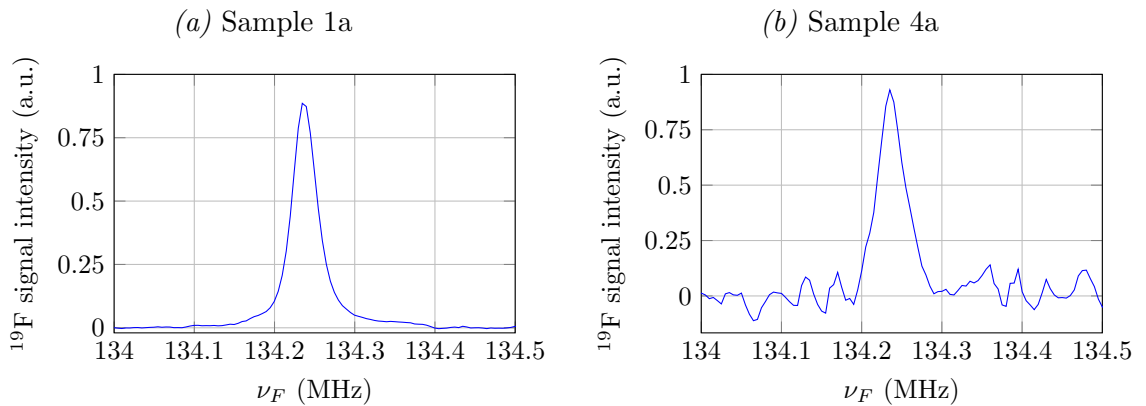


Figure 5.4:  $^{19}\text{F}$  spectra acquired at cryogenic temperatures. These spectra are acquired under microwave irradiation for Samples 1a and 4a (containing 2.7 M and 54 mM of  $^{19}\text{F}$  respectively). They are reported as examples of data with large and poor signal-to-noise ratios.

stants, as well as the enhancements, are of the same order of magnitude. However, values for  $^1\text{H}$   $T_1$  for Samples 4a and 5a differ from the others: this difference may arise from the different glass structure formed and rate of freezing of the sample when it is inserted into the cryostat. It has been observed that a sample can freeze in different ways, which affect the  $T_1$  and  $\tau_{\text{DNP}}$  time constants [69]. However, the dependence of  $T_1$  on the sample structure is not very well known at the temperatures these experiments are performed at. The  $^1\text{H}$  concentration of the samples listed in Tab. 5.2 does not change significantly and it is therefore reasonable to assume that the presence of  $^{19}\text{F}$  does not affect  $^1\text{H}$  polarisation and build-up. Data in Table 5.2 show that both longitudinal relaxation and DNP build-up time constants increase as the  $^{19}\text{F}$  concentration decreases.

On the other hand,  $^{19}\text{F}$  DNP enhancement increases by decreasing the  $^{19}\text{F}$  concentration.

For Sample 1b, where the TEMPO concentration is increased, the recorded time constants do not change significantly. On the other hand, the DNP enhancement of both nuclei is larger, proving a more efficient hyperpolarisation in the sample. When the TEMPO concentration in the sample is lowered, as shown from the results from Sample 1c, the DNP process loses efficiency. With less electrons in the sample in fact, for both  $^1\text{H}$  and  $^{19}\text{F}$ , the build-up time constant  $\tau_{\text{DNP}}$  gets longer and the  $^{19}\text{F}$  enhancement decreases. Also the  $^{19}\text{F}$   $T_1$  value increases, while  $^1\text{H}$   $T_1$  does not change significantly for Sample 1c.

For Sample 1e, where TEKPol was used, results for  $^1\text{H}$  do not differ significantly respect to Sample 1a (in these two samples, the quantity of free electrons is in fact the same).  $^{19}\text{F}$   $T_1$  instead increases, while the DNP enhancement is lower.

Two sets of data are provided for Sample 1f, since the DNP profile showed two sets of enhancement regions, centred at  $\nu_{\text{MW}} = \nu_{\text{SE}} = 93.79\text{ GHz}$  and  $\nu_{\text{MW}} = \nu_{\text{heCE}} = 93.9\text{ GHz}$ . These result will be discussed further in Chapter 6. However, it is important to point out that all of the enhancements achieved for this sample are much lower than the ones obtained for Sample 1a (which has the same chemical composition, with 40 mM of TEMPO changed with 40 mM BDPA), and are obtained with a longer build-up time.

$^{19}\text{F}$  and  $^1\text{H}$  DNP enhancements are higher if the sample is partially deuterated (see Table 5.3): this is observed also in other works [70–72], where it is demonstrated that deuteration provides higher enhancement when the sample is doped with TEMPO-like free radicals.

Moreover, for all the analysed samples, the DNP build-up time constants  $\tau_{\text{DNP}}$  of  $^1\text{H}$  and  $^{19}\text{F}$  nuclei are always shorter than the corresponding longitudinal relaxation time constants  $T_1$ .

Finally, it is important to notice that for deuterated samples  $\epsilon_H > \epsilon_F$ , while for non-deuterated samples  $\epsilon_H < \epsilon_F$ . This indicates that there is no fast exchange of polarisation between these two spin ensembles.

The results of these experiments are summarised in Figure 5.5, where  $^1\text{H}$  and

$^{19}\text{F}$   $T_1$ ,  $\tau_{\text{DNP}}$  and enhancements are plotted as a function of the  $^{19}\text{F}$  concentration. The conclusion of these experiments is that the sample that provides the best  $^{19}\text{F}$  enhancement (a factor of  $\approx 200$ ), regardless of the time required, is the one that contains the smallest  $^{19}\text{F}$  concentration when the sample is deuterated (Sample 3d). The enhancement corresponds to a  $^{19}\text{F}$  polarisation of  $\approx 40\%$ . The polarisation build-up time, of the order of 700 s, although longer than the one for samples with more  $^{19}\text{F}$  nuclei, is still shorter compared to the build-up time of most commonly used  $^{13}\text{C}$  labelled compounds in DNP experiments [13].

### 5.1.3 Discussion

Saturation recovery experiments have been performed in all samples listed in Table 5.1 to obtain their  $T_1$  and  $\tau_{\text{DNP}}$  time constants, as well as the DNP enhancement  $\epsilon$ .

Data in Table 5.2 and 5.3 show how the  $^{19}\text{F}$  longitudinal relaxation time constant  $T_1$  increases when the  $^{19}\text{F}$  concentration in the sample decreases.

As shown in Section 2.5, it is possible to separate the contribution of  $^{19}\text{F}$  relaxation in paramagnetic relaxation contribution  $T_1^{\text{par}}$ , dipole-dipole relaxation contribution  $T_1^{\text{dd}}$ , plus remaining contributions gathered under the term  $T_1^{\text{rest}}$ . The latter is supposed to be constant for all samples.

In this instance, the polarisation exchange between the  $^1\text{H}$  and  $^{19}\text{F}$  ensembles mediated by free electrons is ignored. However, as it will be shown later in this chapter, this process plays an important role in the evolution of  $^{19}\text{F}$  polarisation. Moreover, the DNP Cross Effect may manifest as  $T_1$ , regardless of the presence or absence of microwave irradiation [27]. For sake of simplicity, the Cross Effect is also ignored for this study when there is no microwave irradiation. Another assumption to further simplify the discussion of relaxation is a fast spin diffusion process, and the spin diffusion barrier is not taken into account for its complex nature [26, 35, 42].

The measured  $T_1$ s can therefore be expressed by the equation:

$$\frac{1}{T_1} = \frac{1}{T_1^{\text{par}}} + \frac{1}{T_1^{\text{dd}}} + \frac{1}{T_1^{\text{rest}}}. \quad (5.2)$$

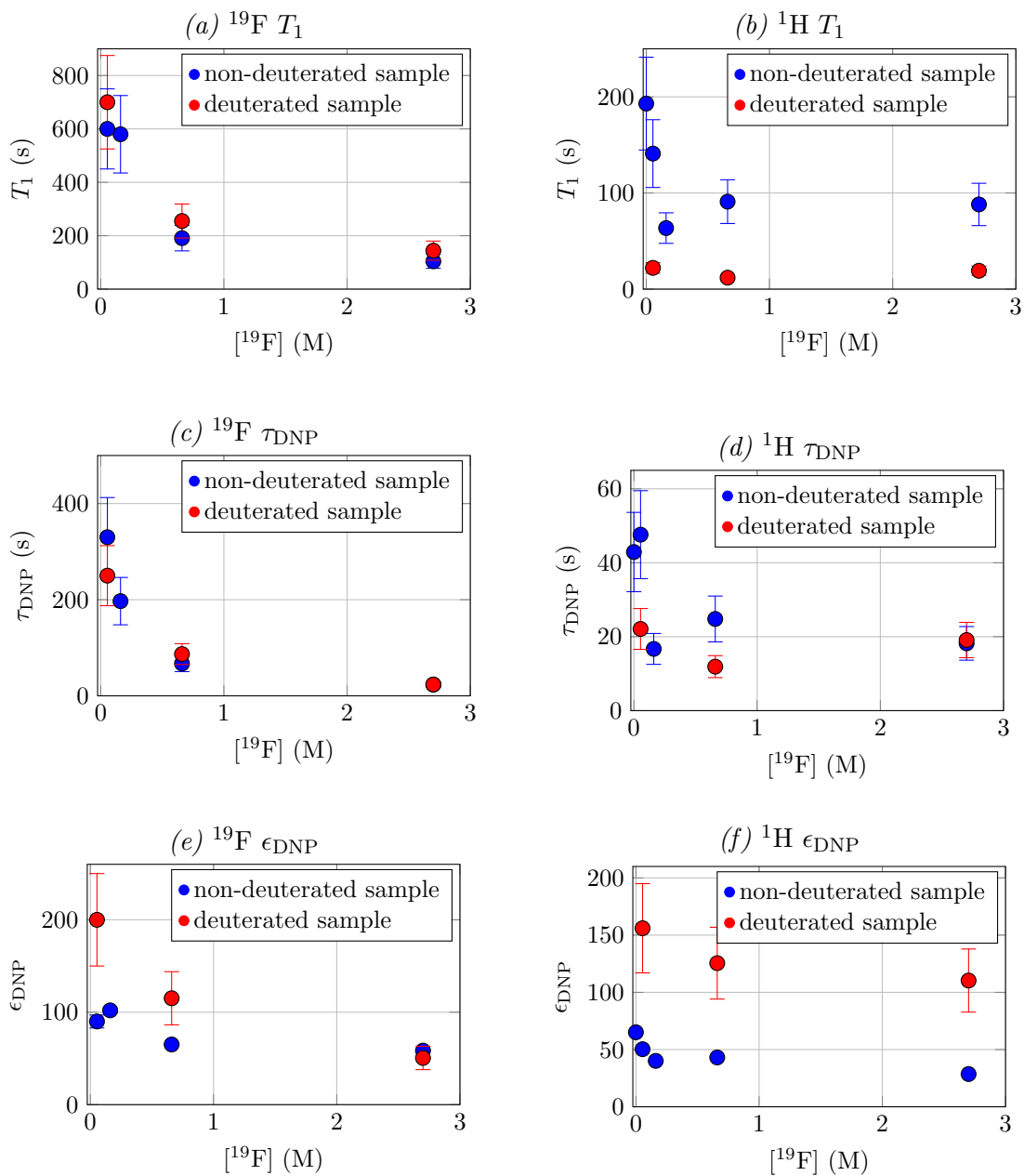


Figure 5.5: Longitudinal relaxation time, DNP build-up time and DNP enhancement for both non-deuterated and deuterated samples for  $^{19}\text{F}$  and  $^1\text{H}$  nuclei as a function of the  $^{19}\text{F}$  concentration in the sample. Errors in the figure are 12% of the values.

A further assumption, related to the dipole-dipole relaxation mechanism, is also made. The  $^1\text{H}$  nuclei closest to the  $^{19}\text{F}$  nuclei are the ones belonging to the same fluorobenzene molecule. The distance of the  $^{19}\text{F}$  nucleus from the closest  $^1\text{H}$  in fluorobenzene, measured to be  $\approx 2.58 \text{ \AA}$  at room temperature [73], is shorter than the distance with any other intermolecular  $^1\text{H}$  nuclei. Therefore, the dipolar interaction between  $^{19}\text{F}$  and  $^1\text{H}$  can be assumed to be constant for all samples used, and the factor  $1/T_1^{\text{dd}}$  can be incorporated in  $1/T_1^{\text{rest}}$ , so that Equation 5.2 can be re-written as

$$\frac{1}{T_1} = \frac{1}{T_1^{\text{par}}} + \frac{1}{T_1^{\text{rest}}}. \quad (5.3)$$

It was shown in Section 2.4 that the  $^{19}\text{F}$  paramagnetic relaxation rate depends on the distance between the nuclei and the paramagnetic centres. In fact, the hyperfine interaction between  $^{19}\text{F}$  nuclei and electrons in the sample generates a coupling constant  $B$  proportional to  $r_{eF}^{-3}$ , where  $r_{eF}$  is the distance between the two spins. According to this theory, the relaxation rate  $R_F^{\text{par}}$  can be written as

$$R_F^{\text{par}} = \frac{1}{T_1^{\text{par}}} \propto \frac{B^2 \tau_c}{1 + \omega_F^2 \tau_c^2}, \quad (5.4)$$

where  $\tau_c$  is the correlation time, related to the electronic relaxation as discussed in Section 2.4.

The quadratic dependency of the rate  $R_F^{\text{par}}$  on the coupling constant  $B$  implies a dependency of  $R_F^{\text{par}}$  on the distance  $r_{eF}$  of  $r_{eF}^{-6}$ .

The effect of the hyperfine interaction becomes less intense when the two interacting particles get too far away from each other.

Figure 5.6 shows the plot of the  $^{19}\text{F}$  longitudinal relaxation time constant  $T_1$  as a function of the sixth power of the distance between the  $^{19}\text{F}$  nuclei and the electrons for Samples 1a to 4a (in red) and Samples 1d to 3d (in blue). The used distance is given by the minimum distance between electrons and  $^{19}\text{F}$ , and it has been calculated in the following way.

All  $^{19}\text{F}$  nuclei are equally displaced in an imaginary three dimensional grid. The distance between the closest nuclei is fixed, and can be estimated starting from

the molar concentration of  $^{19}\text{F}$  in the samples, so that

$$d_{\min} = \sqrt[3]{\frac{N_A}{[^{19}\text{F}]}}, \quad (5.5)$$

where  $N_A$  is the Avogadro Number, while  $[^{19}\text{F}]$  is the  $^{19}\text{F}$  molar concentration.

When a low concentration of electrons is used in the sample, the same amount of  $^{19}\text{F}$  nuclei are replaced by electrons in the grid, in such a way that they are uniformly distributed in the grid. Therefore, the minimum distance between electrons and  $^{19}\text{F}$  is equal to the minimum separation between  $^{19}\text{F}$  nuclei.

As Figure 5.6 shows, a linear dependency of the rate on the sixth power of the distance is not observed. This result indicates that for high  $^{19}\text{F}$  concentrations, and hence for short  $r_{eF}$ , the interaction with the electrons dominates the relaxation process. As the distance between electrons and  $^{19}\text{F}$  decreases, the rate decreases and reaches a plateau. At this point the relaxation mechanism is dominated by the other relaxation pathways contained in  $T_1^{\text{rest}}$ .

In fact, by fitting the data with the function  $T_1 = (1/T_1^{\text{rest}} + B/r^6)^{-1}$ , a good

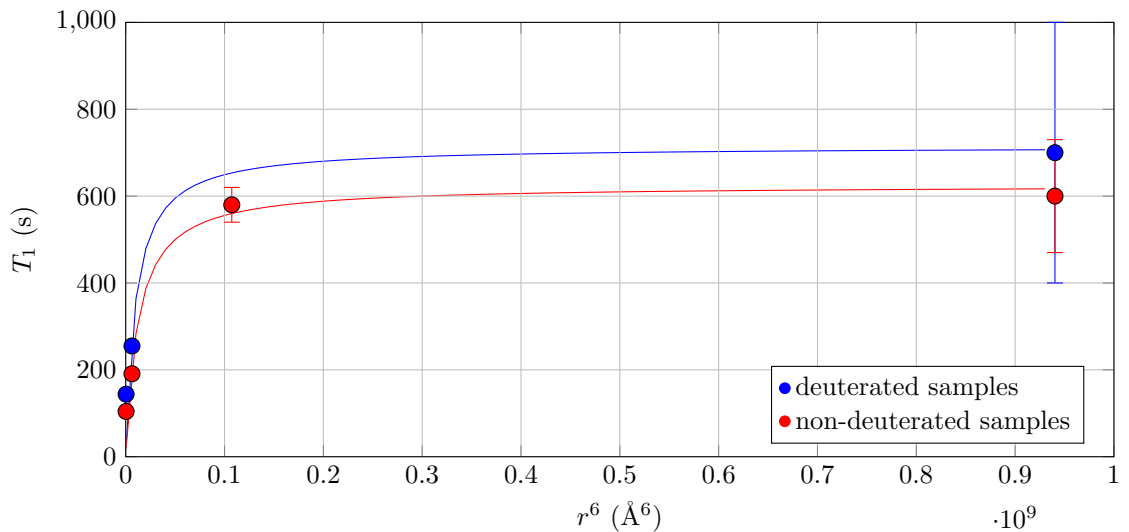


Figure 5.6: Experimental longitudinal relaxation times as function of the  $^{19}\text{F}$  concentration in the sample, for deuterated (in blue) and non-deuterated samples (red). Data have been fitted with the function  $T_1 = (1/T_1^{\text{rest}} + B/r^6)^{-1}$ .

accordance between theory and experimental results is achieved. It is also possible to obtain the value of  $T_1^{\text{rest}}$ , constant for all samples. This value corresponds to  $T_1^{\text{rest}} = 710 \pm 100$  s for the deuterated samples, and  $T_1^{\text{rest}} = 630 \pm 50$  s for the

non-deuterated ones.

Even though the fit shows a good agreement with the data, the number of used points is not high enough to draw more accurate conclusions, other than showing a trend for the data. More data are in fact needed for samples with low  $^{19}\text{F}$  concentrations to enhance the statistical meaning of the fit.

An increase of  $T_1$  due to paramagnetic relaxation is also expected for  $^1\text{H}$  in the deuterated Samples 1d, 2d and 3d. However, as Table 5.3 shows,  $^1\text{H}$   $T_1$  time constants do not change significantly by decreasing the  $^1\text{H}$  concentration in the sample. This result can be explained by the geometrical arrangement of the  $^1\text{H}$  nuclei in the sample. Since the  $^1\text{H}$  nuclei in the sample are only present in the fluorobenzene molecules, it means that they are “packed” together in groups of five. The  $^1\text{H}$ - $^1\text{H}$  dipolar interaction dominates the relaxation mechanism, since its largest contribution is dominated by the interaction of the  $^1\text{H}$  nuclei within the same molecule.

By comparing the results shown in Table 5.2 and 5.3, it is possible to notice that DNP enhancements are higher if the sample is partially deuterated. The main reason for this observation is that an increase of the nuclear  $T_1$  will lead to the preservation of a higher nuclear polarisation since the leakage of non-thermal polarisation is reduced.

For all the analysed samples, the DNP build-up time constants  $\tau_{\text{DNP}}$  of  $^1\text{H}$  and  $^{19}\text{F}$  nuclei are always shorter than the corresponding longitudinal relaxation time constants  $T_1$ . While for Cross Effect DNP  $\tau_{\text{DNP}}$  is expected to be close to the nuclear  $T_1$  [27], the DNP build-up time for the Solid Effect is shorter than the nuclear  $T_1$  [74]. The experimental results for  $\tau_{\text{DNP}}$  and  $T_1$  obtained in this work indicate that the Solid Effect contributes to the nuclear hyperpolarisation build-up. On the other hand, the DNP profiles shown in Figure 5.2 are characteristic of the Cross Effect. Therefore it is possible to conclude that the hyperpolarisation of the analysed samples is generated by a mixture of the Solid and the Cross Effect. For deuterated samples  $\epsilon_H > \epsilon_F$ , while for non-deuterated samples  $\epsilon_H < \epsilon_F$ . This indicates that there is no fast exchange of polarisation between these two spin

ensembles. The enhancements of the two nuclei would in fact have been the same if there was fast exchange, with both nuclear ensemble reaching the same polarisation value.

These results are of particular interest when designing the experiments described in Chapter 7, where a sample containing a  $^{19}\text{F}$ -labelled protein will be brought to ambient temperature and used in liquid state NMR experiments.

Finally, the fact that the DNP enhancements for Samples 1b, 1a and 1c (with 60,40 and 20 mM TEMPO respectively) increases with the free radical concentration is in accordance with theoretical studies on Cross Effect [40].

It was also shown that the DNP build-up time decreases as the TEMPO concentration increases. This behaviour was expected since, as shown in another work, this time constant roughly scales as the inverse square of the hyperfine coupling [75], whose average value increases with the electron concentration.

## 5.2 $^1\text{H}$ - $^{19}\text{F}$ polarisation transfer under ss-DNP conditions

As discussed in Section 2.4, two interacting spins can undergo a relaxation process caused by the dipole-dipole mechanism. In experimental terms, this means that a spin affects the way other neighbour spins relax. The Solomon equations describe how the dipole-dipole interaction can transfer the polarisation from one spin to the other [51, 76]. Many experimental techniques take advantage of this process to study the structure of proteins and molecules in liquid and solid state (e.g. the NOE [31]).

Cross-relaxation is usually intended as the process for which two nuclear ensemble can exchange their polarisation by means of dipole-dipole interaction. Its effect, first described by Solomon [51], has been widely observed in NMR experiments and many results can be found in literature [77–80].

In the context of this Chapter, the term cross-relaxation is used to describe a non-coherent process representing a polarisation transfer between  $^1\text{H}$  and  $^{19}\text{F}$ .

Cross-relaxation evidences can be found even at cryogenic temperatures in heteronuclear spin systems, for free radical-doped samples, where the Larmor frequen-

cies difference of the two nuclei is smaller than the EPR linewidth [10,46,78,81–94]. Kaminker et al. [95] observed cross-relaxation between  $^1\text{H}$  and  $^2\text{H}$  nuclei in solid state at 6 K in a sample containing 40 mM of TEMPOL radical. They concluded that the source of polarisation transfer from hydrogen to deuterium takes place at distinct sites in the samples and the polarisation exchange is mediated by the electrons of the free radical.

Guarin et al. [96] used the Thermal Mixing DNP mechanism to explain the polarisation exchange between  $^1\text{H}$  and  $^{13}\text{C}$  at high magnetic field ( $B_0 = 6.7\text{ T}$ ) and low temperatures ( $T = 4\text{ K}$ ) in samples with nitroxide radicals.

In the rest of the chapter, an attempt to characterise the cross-relaxation mechanism under DNP conditions is made. The experimental approach used by Cox et al. [84] will be followed. In their work, DNP experiments were performed in a sample containing lithium fluoride on  $^7\text{Li}$  and  $^{19}\text{F}$ . To analyse the polarisation exchange,  $^7\text{Li}$  polarisation was monitored after  $^{19}\text{F}$  was hyperpolarised.

It is important to point out that this polarisation transfer is different to the one theorised and observed by Vega et al. [97], in which the polarisation is due to a three spin solid effect-like conditions, where an enhancement of carbon NMR signal is observed when the sample containing free radical was irradiated with microwaves at  $\omega_{MW} = \omega_e \pm (\omega_H \pm \omega_C)$ . In fact, in that case, the enhancement was driven by microwave irradiation, while in the experiments on the rest of this chapter the polarisation transfer is observed without microwave irradiation.

Low-field thermal mixing [98] has been ruled out as a possible mechanisms responsible for the cross-relaxation since it takes place at much lower magnetic field strength.

### 5.2.1 Experimental evidence for polarisation transfer between $^1\text{H}$ and $^{19}\text{F}$

By performing preliminary  $^{19}\text{F}$  DNP experiments, a transient polarisation increase above the thermal equilibrium value was observed after the microwave irradiation was turned off.

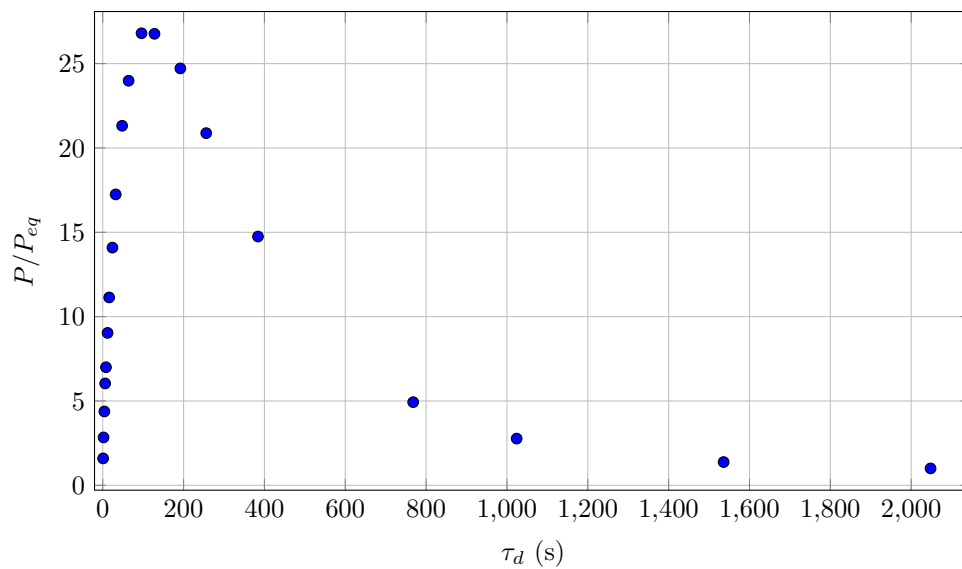
In order to show this effect, the following experiment on Sample 1a has been performed in the “polariser” at  $\approx 1.6\text{ K}$ . The pulse sequence used is the “saturation

recovery for cross-relaxation” (see Section 4.3.3). The parameters used during the microwave irradiation of the sample are  $\nu_{\text{MW}} = 94$  GHz and  $P_{\text{MW}} = 400$  mW, frequency and power corresponding to the maximum DNP enhancement. The microwave irradiation period is  $T_{\text{MW}} = 2$  min. Figure 5.7a shows the integrals of the recorded signals, plotted as function of time.

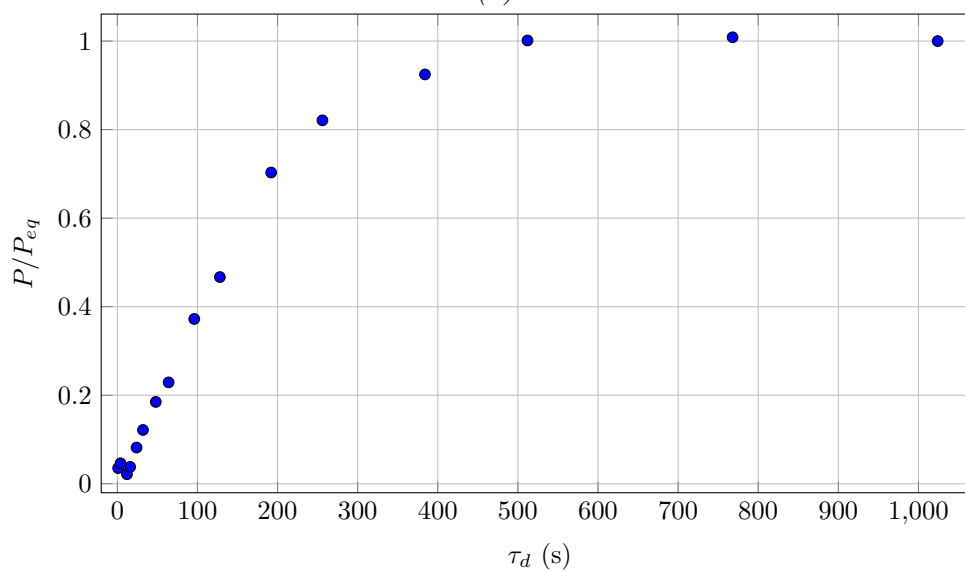
Integrals of the  $^{19}\text{F}$  signals have been normalised to the last value, which is reasonably assumed to be at the effective thermal equilibrium condition. The y-axis represents therefore the enhancement of  $^{19}\text{F}$  polarisation with respect to the thermal equilibrium one. As shown in the figure, instead of building up like in a standard saturation recovery experiment, a transient polarisation increase above the thermal equilibrium value is observed for time intervals  $t < 100$  s. For longer time intervals, an exponential decay in  $^{19}\text{F}$  polarisation is observed, until the polarisation reaches the thermal equilibrium value at  $t > 1000$  s.

It is at this point hypothesised that the transient polarisation is transferred from the  $^1\text{H}$  spin ensemble: in fact many  $^1\text{H}$  nuclei are present in the sample (eight in each toluene molecule, five in each fluorobenzene one), and since their gyromagnetic ratio is close to the  $^{19}\text{F}$ , it was shown in Fig. 5.2 that during microwave irradiation the  $^1\text{H}$  nuclear ensemble gets polarised as well as the  $^{19}\text{F}$  one. As the DNP frequency sweep figure shows, the maximum of  $^1\text{H}$  signal enhancement occurs at the same microwave irradiation frequency as the  $^{19}\text{F}$  one, and therefore the two spin ensembles are simultaneously polarised during microwave irradiation. In order to show that the transient polarisation is transferred from the  $^1\text{H}$  ensemble, the same experiment has been performed on the same sample, and a saturation pulse train simultaneous with  $^{19}\text{F}$  saturation was added on the  $^1\text{H}$  channel to destroy the  $^1\text{H}$  polarisation.

Results of this experiment (Figure 5.7b) show that no transient build-up of  $^{19}\text{F}$  polarisation is observed in this case. This provides strong evidence that the transient dynamic of the  $^{19}\text{F}$  polarisation arises from a transfer of non-thermal  $^1\text{H}$  polarisation.



(a)



(b)

Figure 5.7: (a) Experimental DNP recovery plot for Sample 1a where both  $^{19}\text{F}$  and  $^1\text{H}$  nuclei are polarised for  $T_{\text{MW}} = 2$  min, then  $^{19}\text{F}$  nuclei are saturated, and its polarisation is recorded after increasing delays. (b) Same experiment with  $^1\text{H}$  saturated after the polarisation period.

## 5.2.2 TEMPO concentration variation

In this section the transient polarisation transfer has been studied as a function of the concentration of free electrons in the sample to analyse the effect the free radical concentration has on this process. The experiments have been performed using three different samples containing toluene and monofluorobenzene with 75:25 (v/v) and either 40, 60 or 20 mM of TEMPO (respectively Samples 1a, 1b and 1c in Table 5.2).

For these experiments,  $^1\text{H}$  and  $^{19}\text{F}$  signals were acquired by using the technique explained in the “interleaved acquisition of  $^1\text{H}$  and  $^{19}\text{F}$  for cross-relaxation” discussed in Section 4.3.4 to improve the data quality and avoid bias of data by temperature variation. The polarisation time used is  $T_{\text{MW}} = 2$  min, and during this time the sample was irradiated with microwaves at frequency  $\nu_{\text{MW}} = 94$  GHz and power  $P_{\text{MW}} = 400$  mW, corresponding to maximum  $^1\text{H}$  and  $^{19}\text{F}$  DNP enhancements.

Figure 5.8 shows the graphs and fitted data for these experiments, together with the temperatures registered during the experiments and the level of helium in the sample space. As the figures show, all experimental results for all the samples exhibit a transient  $^{19}\text{F}$  polarisation that increase above the thermal equilibrium value and decreases afterwards. As the  $^1\text{H}$  signal decays from the hyperpolarised state at  $\tau_d = 0$ , its polarisation is transferred to the  $^{19}\text{F}$  in the sample. The  $^1\text{H}$  enhancements depends directly on the free radical concentration, with low radicals concentration causing a smaller enhancement. It is also possible to note that the  $^{19}\text{F}$  polarisation build-up time is longer when less free electrons are present in the sample.

The behaviour of the temperature shown in Figure 5.8 has already been discussed in Section 4.3.6.

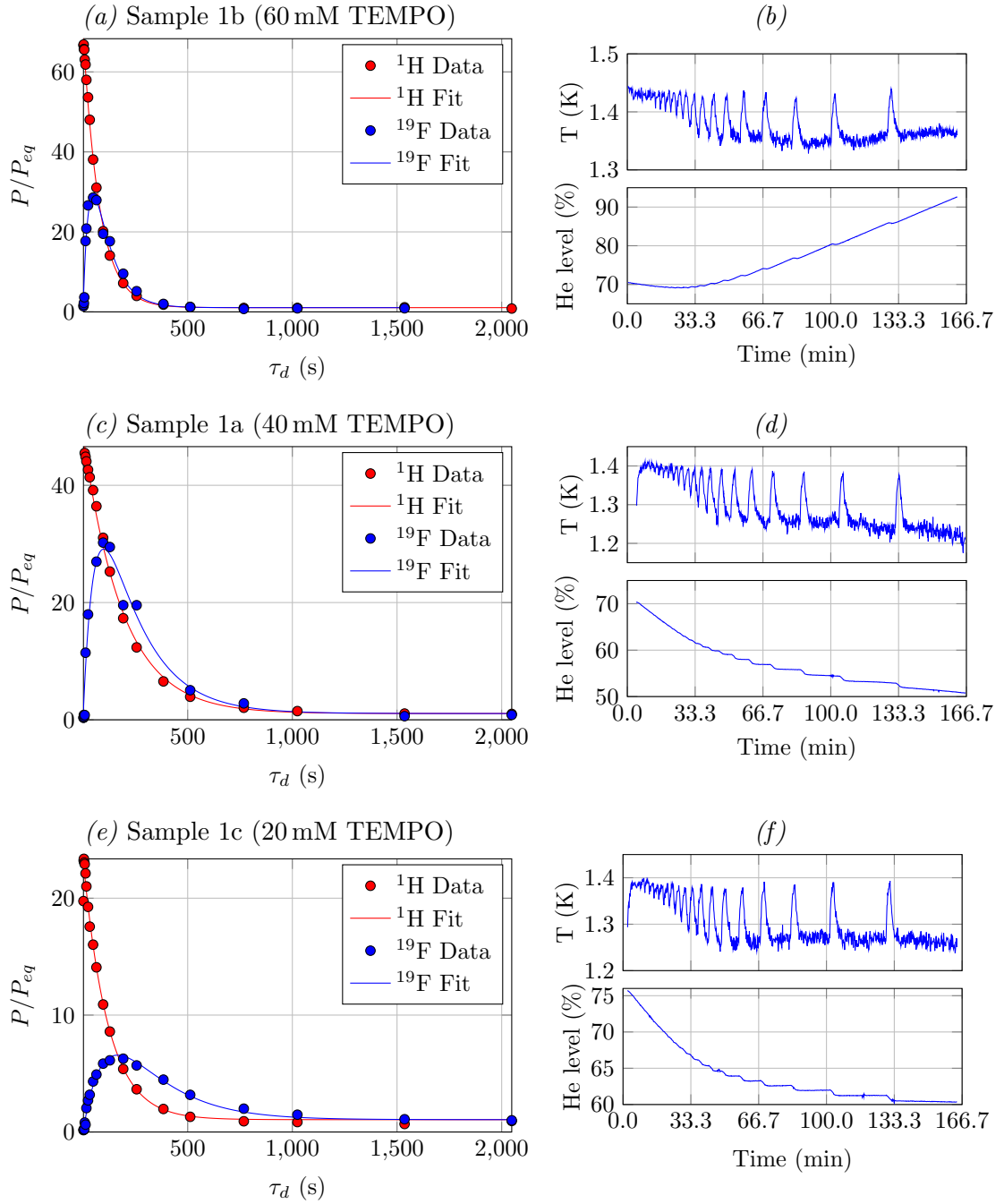


Figure 5.8: (a,c,e) Data and fitting curve of the double quasi-simultaneous acquisition experiments. (b,d,f) Temperature data (top) and helium level in the sample space data (bottom) collected during the experiment.

### 5.2.3 Transient polarisation in a sample without free radicals

Although experiments in Figure 5.8 show that the paramagnetic centres in the sample change the way the transient polarisation behaves, they are not the only cause of this mechanism at low temperatures. To demonstrate this, results of a standard saturation recovery experiment for  $^{19}\text{F}$  in Sample 6a (that does not contain free radical) of Table 5.1 have been compared with the results of a similar experiment where  $^1\text{H}$  nuclei are continuously saturated. The pulse sequence is shown in Section 4.3.5.

In this sample, the same longitudinal relaxation time constant and thermal equilibrium polarisation would be expected for  $^{19}\text{F}$  in both the experiments. If there is no polarisation exchange between  $^{19}\text{F}$  and  $^1\text{H}$  due to the absence of free electrons in the sample,  $^{19}\text{F}$  polarisation should evolve independently on the  $^1\text{H}$  one. Results of this experiment are presented in Figure 5.9, showing the results of the standard saturation recovery (“std” in the legend) and the one with continuous  $^1\text{H}$  saturation (“Hsat” in the legend). As the figure shows, the  $^{19}\text{F}$  build-up time

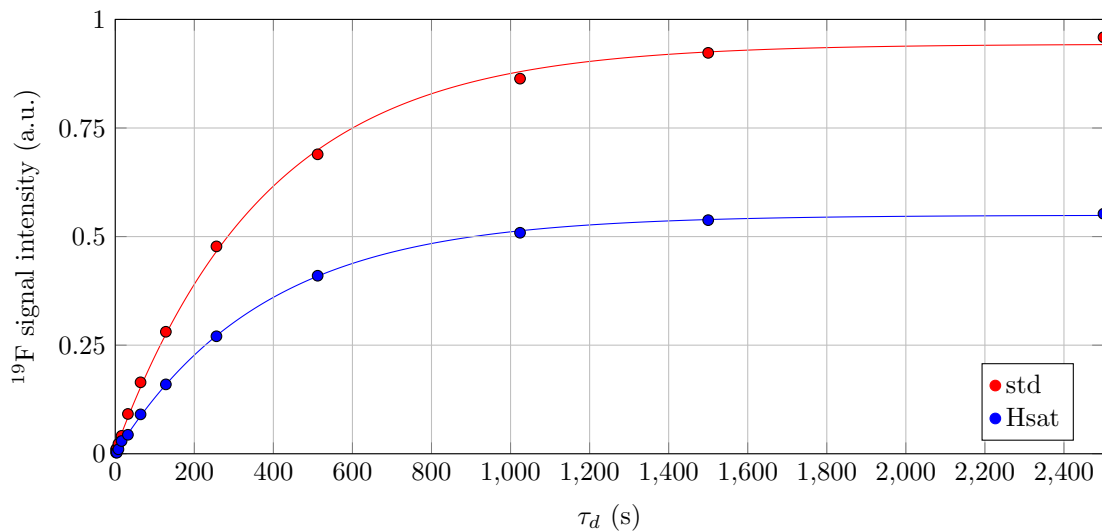


Figure 5.9: Results of  $^{19}\text{F}$  saturation recovery with (*Hsat*) and without (*std*)  $^1\text{H}$  continuous saturation.

constant  $T_{\text{bu}}$  does not change (from  $T_{\text{bu}} \approx 381 \pm 11$  s to  $T_{\text{bu}} \approx 376 \pm 6$  s when  $^1\text{H}$  is continuously saturated), while the steady-state polarisation changes dramatically. This result is predicted by Equation 6.5, discussed in the next chapter. In fact

according to this equation, when a standard saturation recovery experiment is performed while  $^1\text{H}$  nuclei are at thermal equilibrium, the build-up time constant is the same as in the case in which  $^1\text{H}$  are continuously saturated. However, the difference in steady-state polarisation shows that there is a polarisation exchange between the two nuclear ensembles. This observation shows that electrons are not the only responsible source of polarisation exchange between the two nuclei. This result will be examined in depth in Chapter 6.

#### 5.2.4 Cross-relaxation using the bi-radical TEKPol and narrow-linewidth free radical BDPA

In the previous section it was shown that the dynamics of the transient polarisation depends on the concentration when a radical like TEMPO, with a broad linewidth, is present in the sample.

To understand whether the distribution of free electrons in the sample affect the observed transient polarisation dynamics, experiments were carried out with the bi-radical TEKPol [66].

This free radical (Figure 5.10) consists in two TEMPO molecules rigidly linked, thus creating two paramagnetic centres kept at a well defined distance of  $\approx 13 \text{ \AA}$  [99]. By using 20 mM of TEKPol it is therefore possible to obtain the equivalent free electron concentration used in Sample 1a. However, instead of having a uniform distribution of electrons, pairs of equidistant electrons are distributed within the sample. The sample used for the experiments in this section is Sample 1e in Table 5.1.

The  $^{19}\text{F}$  DNP profile is shown in Figure 5.11, for a microwave power of 400 mW. Non-thermal polarisation was built up for 1 min through microwave irradiation before the acquisition of the signal. The integrals of the NMR peaks are shown in Figure 5.11 as a function of the microwave irradiation frequency. As Figure 5.11 shows, the maximum DNP enhancement is found at  $\nu_{\text{MW}} = 93.95 \text{ GHz}$ , very close to the microwave frequency that provided the maximum enhancement in samples with 40 mM of the free radical TEMPO (in Figure 5.2).

Figure 5.12 shows the result of the double quasi-simultaneous acquisition experiment discussed in the “interleaved acquisition of  $^1\text{H}$  and  $^{19}\text{F}$  for cross-relaxation”

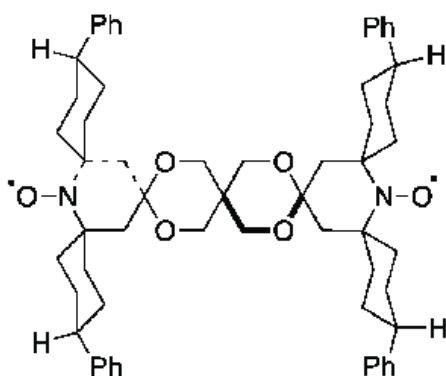


Figure 5.10: Chemical structure of the TEKPol molecule. The two dots close to the external oxygen nuclei represent the position of the two electrons in the molecule.

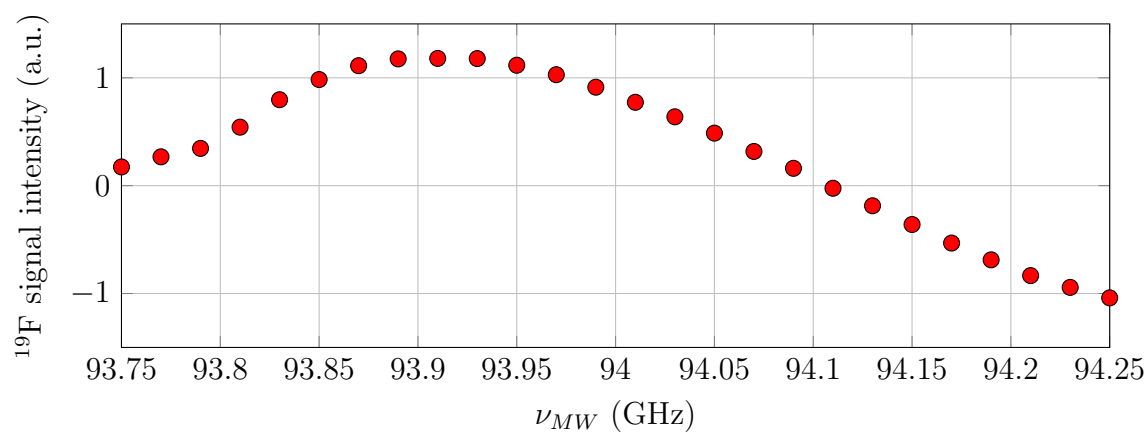


Figure 5.11: DNP enhancement profile of  $^{19}\text{F}$  NMR signals for Sample 1e, containing 20 mM TEKPol free radical.

section in Section 4.3.4 for both  $^1\text{H}$  and  $^{19}\text{F}$ .

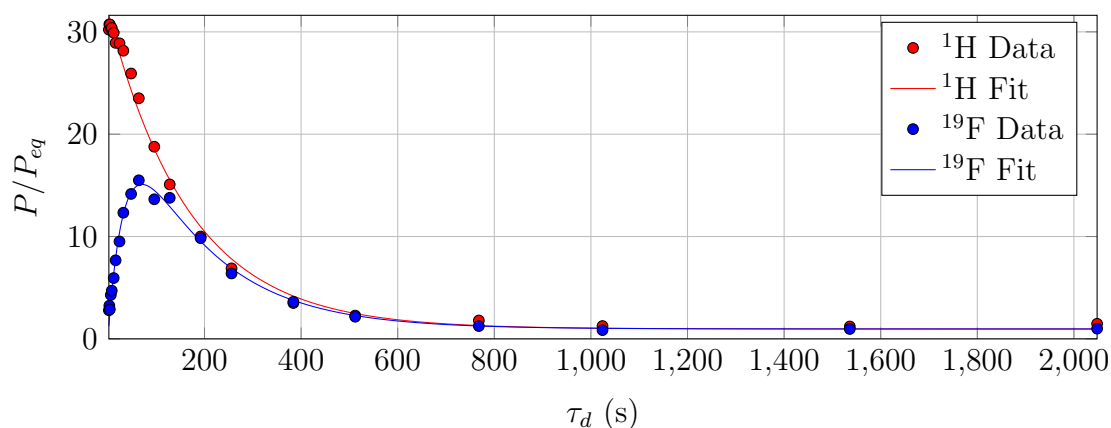


Figure 5.12: Data and fitting curve of the double quasi-simultaneous acquisition experiment performed on Sample 1e, containing 20 mM TEKPol free radical.

A similar experiment was repeated for a sample containing 40 mM of BDPA (Sample 1f in Table 5.1), a free radical with a small EPR linewidth ( $\approx 30$  MHz [38]), and results are shown in Figure 5.13. For this experiment, the microwave frequency corresponding to the maximum enhancement has been determined in a frequency sweep experiment shown in Section 6.2, where an in depth analysis of cross-relaxation between  $^{19}\text{F}$  and  $^1\text{H}$  is performed for samples containing BDPA.

Both Samples 1e and 1f exhibit the feature characteristic of the transient polari-

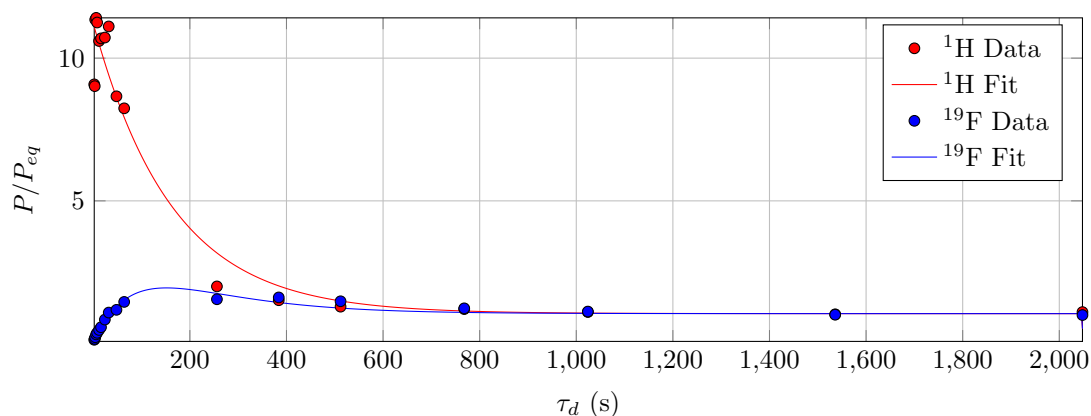


Figure 5.13: Data and fitting curve of the double quasi-simultaneous acquisition experiment performed on Sample 1f, containing 40 mM BDPA free radical.

sation in the performed experiments. However, it is possible to notice that, while for Sample 1e such a feature is similar to the one observed in samples with the free radical TEMPO, for Sample 1f the peak in the  $^{19}\text{F}$  curve is barely observable.

## 5.2.5 Characterisation of $^1\text{H}$ - $^{19}\text{F}$ cross-relaxation process for different $^{19}\text{F}$ concentrations

In this section the polarisation exchange mechanism between  $^1\text{H}$ - $^{19}\text{F}$  is studied, by analysing its dependence by varying the  $^{19}\text{F}$  concentration in the sample as well as its deuteration.

For Samples 1a, 2a, 3a and 4a in Tab. 5.1 experiments have been performed by using the pulse sequence described in Section 4.3.3 to study the behaviour of  $^{19}\text{F}$  polarisation after  $^1\text{H}$  have been hyperpolarised for 2 minutes. Results are shown in Figure 5.14, while Figure 5.15 shows the results for deuterated samples 1d, 2d and 3d.

As can be seen in Figure 5.14 and Figure 5.15, as the concentration of  $^{19}\text{F}$

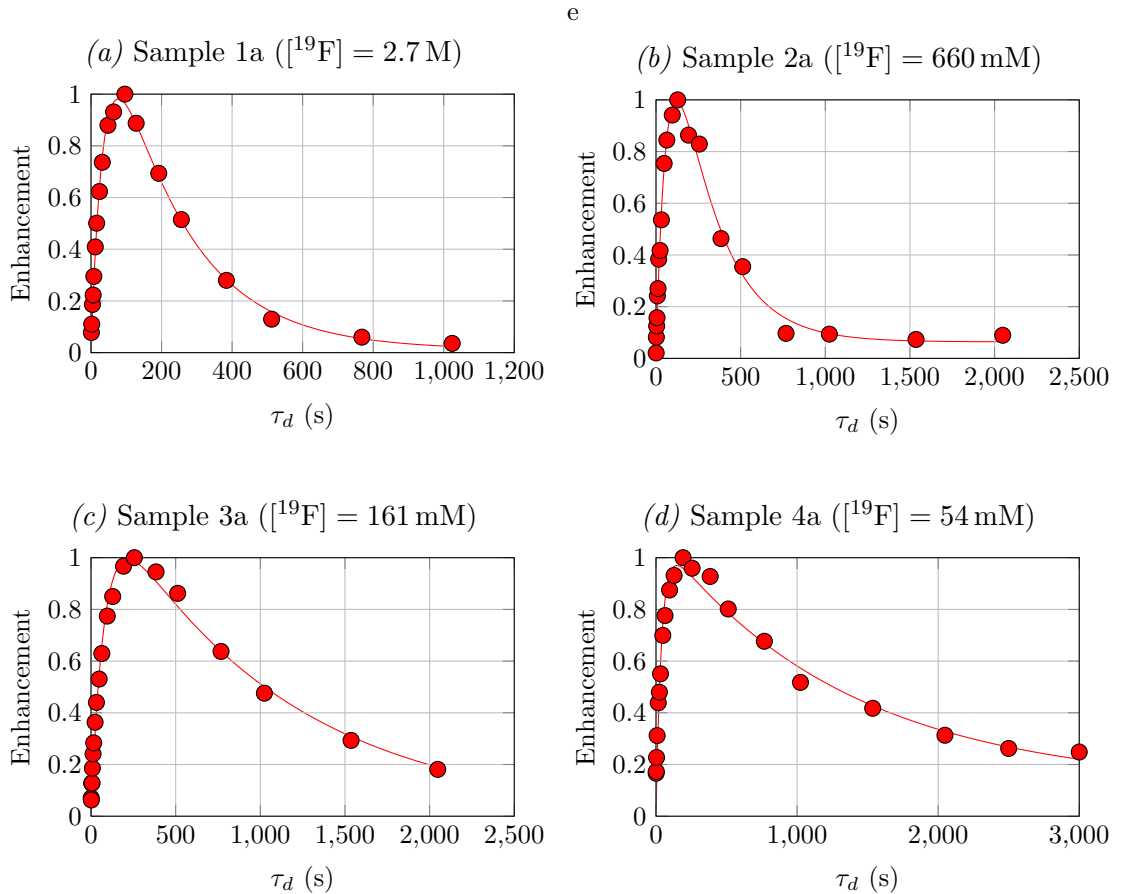
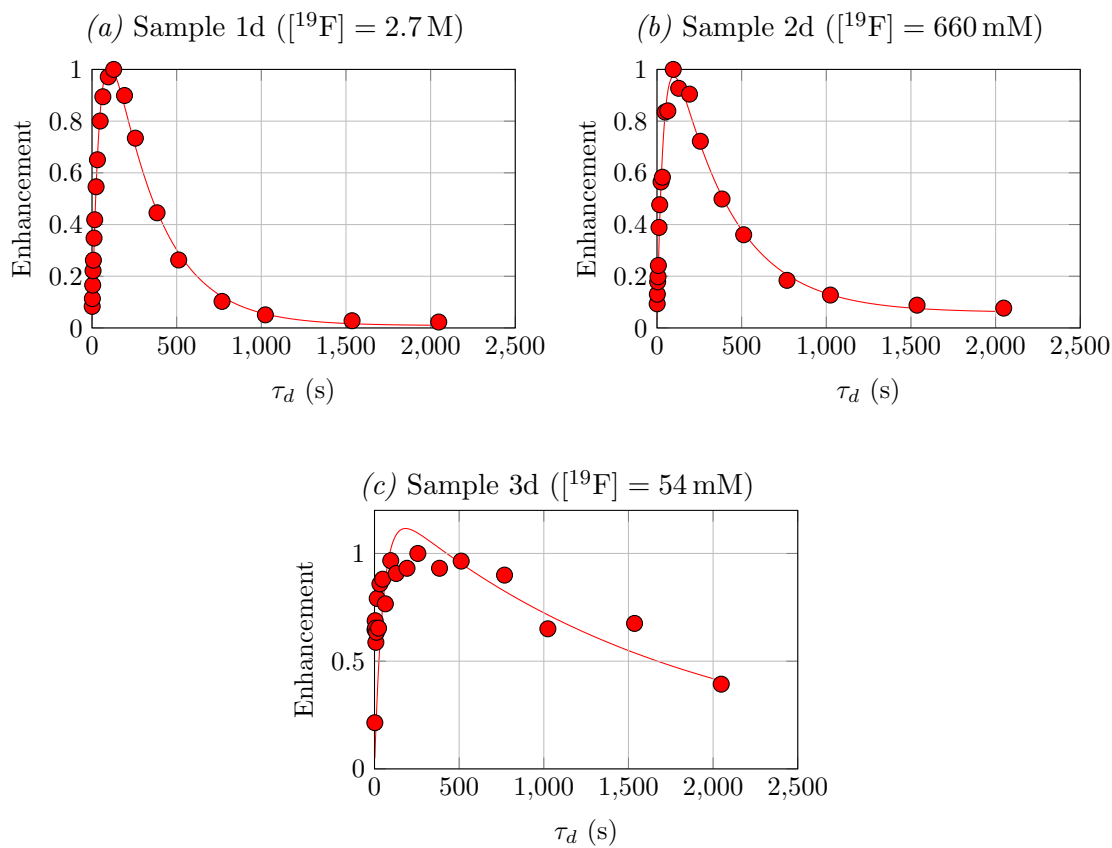


Figure 5.14:  $^{19}\text{F}$  saturation recovery plot for non-deuterated samples containing the free radical TEMPO (Samples 1a, 2a, 3a and 4a), where microwave irradiation hyperpolarised  $^1\text{H}$  nuclei before the  $^{19}\text{F}$  saturation. These experiments show the behaviour of the cross-relaxation process as a function of the  $^{19}\text{F}$  concentration.



*Figure 5.15:*  $^{19}\text{F}$  saturation recovery plot for deuterated samples containing the free radical TEMPO (Samples 1d, 2d and 3d), where microwave irradiation hyperpolarised  $^1\text{H}$  nuclei before the  $^{19}\text{F}$  saturation. These experiments show the behaviour of the cross-relaxation process as a function of the  $^{19}\text{F}$  concentration in deuterated samples.

decreases, the intensity of the peaks decreases as well. Also, the position of the maxima slightly change, reaching a maximum at  $t \approx 200$  s.

## 5.2.6 Discussion

### Empirical modelling of polarisation transfer dynamics

In order to describe the  $^{19}\text{F}$  transient polarisation in the aforementioned experiments, a system of two different nuclear species (A and B) with spin 1/2 embedded in a magnetic field is considered. The Solomon equations [51, 76] describe how the population of each species changes as the population of the other species evolves in time, relaxing to thermal equilibrium with its characteristic longitudinal relaxation time constant. These equations can be written in the differential form:

$$\begin{cases} \frac{dP_A(t)}{dt} = -R_A[P_A(t) - P_A^{eq}] - \sigma_{AB}[P_B(t) - P_A(t)] \\ \frac{dP_B(t)}{dt} = -R_B[P_B(t) - P_B^{eq}] - \sigma_{BA}[P_A(t) - P_B(t)] \end{cases} \quad (5.6)$$

In this set of equations,  $P_A$  and  $P_B$  represent the populations of the two species,  $R_A$  and  $R_B$  are the longitudinal relaxation rates, while  $\sigma_{AB}$  and  $\sigma_{BA}$  are the rates describing the exchange of polarisation between the two species. In this theoretical framework, the cross-relaxation mechanism is associated with the dipolar coupling between the two species.

In DNP experiments, when microwaves irradiate the sample, a contact between  $^1\text{H}$  (or  $^{19}\text{F}$ ) nuclei and the free radicals in the sample is induced, and polarisation exchange from electrons to the nuclei takes place with the characteristic DNP build-up rate constants  $R_H^{\text{DNP}}$  and  $R_F^{\text{DNP}}$ .

The set of equations that describe the evolution of  $^{19}\text{F}$  and  $^1\text{H}$  polarisation for this system are

$$\begin{cases} \frac{dP_F(t)}{dt} = -R_F^{\text{DNP}}[P_F(t) - P_{\text{DNP}}^F] - R_F[P_F(t) - P_{\text{eq}}] - \sigma_{FH}[P_F(t) - P_H(t)] \\ \frac{dP_H(t)}{dt} = -R_H^{\text{DNP}}[P_H(t) - P_{\text{DNP}}^H] - R_H[P_H(t) - P_{\text{eq}}] \end{cases} \quad (5.7)$$

where the following assumptions have been made:

- since  $\gamma_H \simeq \gamma_F$ , the polarisations of  $^1\text{H}$  and  $^{19}\text{F}$  at thermal equilibrium are

assumed to be equal ( $P_{\text{eq}}^F \simeq P_{\text{eq}}^H = P_{\text{eq}}$ );

- the number of  $^{19}\text{F}$  nuclei in the samples used in this work is smaller than the number of  $^1\text{H}$  (1  $^{19}\text{F}$  nucleus for every 30  $^1\text{H}$  in Sample 1a, where  $[^{19}\text{F}] = 2.7\text{M}$ , which is the highest  $^{19}\text{F}$  concentration used in this work), therefore it is assumed that the  $^1\text{H}$  polarisation is not influenced by the  $^{19}\text{F}$  one. According to this assumption, it results that  $\sigma_{HF} = 0$ .

When there is no microwave irradiation on the sample, both  $^{19}\text{F}$  and  $^1\text{H}$  recover their equilibrium polarisation corresponding to the equilibrium temperature of the lattice, and  $R_F^{\text{DNP}} = R_H^{\text{DNP}} = 0\text{s}^{-1}$ . If  $^{19}\text{F}$  polarisation is initially saturated ( $P_F(0) = 0$ ), as it happens in the experiment performed to study the polarisation transfer, the solutions of Equations 5.7 are:

$$\begin{cases} P_F(t) = P_{\text{eq}} [1 - e^{(-R_F - \sigma_{FH})t}] - \frac{\sigma_{FH}(P_H(0) - P_{\text{eq}})}{R_F - R_H + \sigma_{FH}} [e^{(-R_F - \sigma_{FH})t} - e^{-R_H t}] \\ P_H(t) = [P_H(0) - P_{\text{eq}}]e^{-R_H t} + P_{\text{eq}} \end{cases} \quad (5.8)$$

Moreover, when  $R_F \ll \sigma_{FH}$ , Eq. 5.8 become:

$$\begin{cases} P_F(t) = P_{\text{eq}} [1 - e^{-\sigma_{FH}t}] - \frac{\sigma_{FH}(P_H(0) - P_{\text{eq}})}{-R_H + \sigma_{FH}} [e^{-\sigma_{FH}t} - e^{-R_H t}] \\ P_H(t) = [P_H(0) - P_{\text{eq}}]e^{-R_H t} + P_{\text{eq}} \end{cases} \quad (5.9)$$

This assumption will be justified later in this chapter.

The presented model describes interacting nuclear ensembles that can exchange polarisation with each other with a rate  $\sigma$  and relax to their equilibrium value with the characteristic longitudinal relaxation time constants.

Equations 6.6 can be explained with a thermal mechanic model analogy, that is depicted by the diagram in Figure 5.16. In this model, the spin populations are associated with thermal baths, that are in contact with each other and with an infinite thermal capacity bath provided by the lattice.

If electrons are present in the sample, the modification introduced in the Solomon equations, written in Equations 5.7, slightly change the interpretation of the aforementioned thermal model.

In this case, Figure 5.17 provides a schematic representation of the spin ensembles

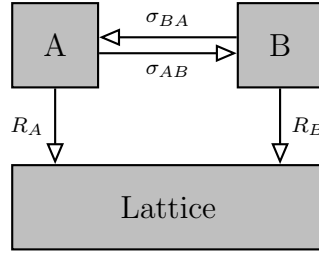


Figure 5.16: Schematic diagram of the two energy reservoirs A and B interacting with each other and with the lattice, which has infinite thermal capacity.

when electrons are added to the sample.

$^1\text{H}$ ,  $^{19}\text{F}$  and  $e^-$  ensembles are in contact with the lattice, and their longitudinal

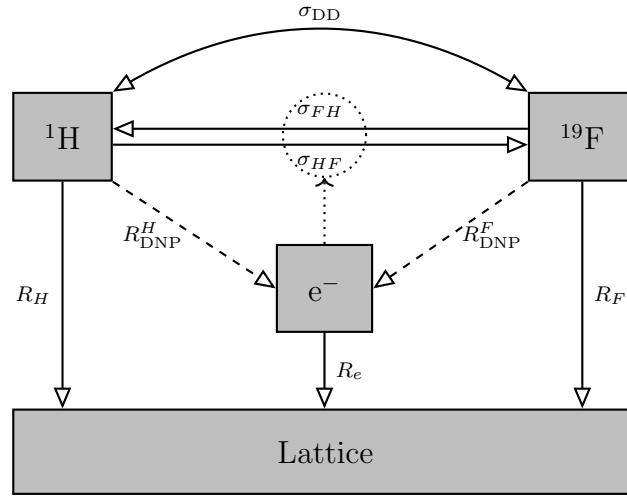


Figure 5.17: Schematic diagram of the energy reservoirs and the flows of energy between them. The dashed arrows represent microwave driven processes. The dotted arrow indicates that  $^1\text{H}$ - $^{19}\text{F}$  cross-relaxation is influenced by the presence of the electrons in this model.

relaxation rate constants are  $R_H$ ,  $R_F$  and  $R_e$  respectively.  $\sigma_{DD}$  is the rate constant of the polarisation exchange process between  $^{19}\text{F}$  and  $^1\text{H}$  due to their dipolar coupling. However, as the experimental results in Section 5.2.2 (Figure 5.9) have shown, there is another polarisation exchange pathway that depends on the free paramagnetic centres in the sample. This process, that mediates a polarisation exchange from  $^1\text{H}$  to  $^{19}\text{F}$  nuclei, is characterised by the rate constant  $\sigma_{HF}$  (while the opposite process is characterised by  $\sigma_{FH}$ ). The dependence of these rates on the free radical concentration, demonstrated by the experiments in Section 5.2.2, will be discussed later in this section.

According to this model, an interpretation of the results obtained for the experiments on the transient polarisation dynamics of  $^{19}\text{F}$  nuclei can be given. Experiments shown in Figures 5.7a and 5.7b point out that the observed polarisation transfer dynamics observed for  $^{19}\text{F}$  nuclei is generated by  $^1\text{H}$  nuclei in the sample.

Since the parameter  $\sigma_{HF}$  is neglected in the rest of this thesis, the only remaining rate constant  $\sigma_{FH}$  will be simply referred to as  $\sigma$ .

### Discussion on TEMPO concentration variation

Results of the experiments shown in Figures 5.8 have been studied by using the empirical model presented in Section 5.2.6.

Spectra have been integrated and normalised to their equilibrium values, and have been fitted with Equations 5.8.  $^{19}\text{F}$  and  $^1\text{H}$  data have been combined for each sample, and the resulting data sets were fitted together with Equations 5.8. This allowed to better constrain some parameters that, being present in both Equations 5.8, would assume different values if the fitting was performed separately for  $^{19}\text{F}$  and  $^1\text{H}$ .

Results of the fits are shown in Table 5.5, together with the average temperature  $\bar{T}$  shown by the sensors during the experiments. The  $^1\text{H}$  relaxation rate was ex-

	<b>Sample 1b</b> (60 mM TEMPO)	<b>Sample 1a</b> (40 mM TEMPO)	<b>Sample 1c</b> (20 mM TEMPO)
$\mathbf{R}_F$ (1/s)	$0.0081 \pm 0.0012$	$0 \pm 0.0006$	$0 \pm 0.0004$
$\mathbf{R}_H$ (1/s)	$0.0127 \pm 0.0003$	$0.0053 \pm 0.0002$	$0.0085 \pm 0.0003$
$\sigma$ (1/s)	$-0.0240 \pm 0.0010$	$-0.0175 \pm 0.0010$	$-0.0048 \pm 0.0003$
$\epsilon_H$	$70.0 \pm 0.5$	$48.6 \pm 0.7$	$23.4 \pm 0.2$
$\bar{T}$ (K)	$1.76 \pm 0.10$	$1.65 \pm 0.10$	$1.66 \pm 0.10$

*Table 5.5:* Results for relaxation time constants, enhancements and average temperatures of the experiments for the samples containing the free radical TEMPO.

pected to decrease by decreasing free electrons concentration. By lowering the number of paramagnetic centres the hyperfine interaction between electrons and  $^1\text{H}$  becomes weaker, decreasing the relaxation rate, as discussed in Section 2.4. However, the fitted parameter is inconsistent with this hypothesis, since its value for the intermediate TEMPO concentration is the lowest among the measured val-

ues and does not comply with the expected decreasing trend. On the other hand, the differences in temperature and pressure inside the bore during the experiments make it impossible to estimate the physical mechanisms behind such behaviour. Previous studies [80,100] showed that  $^1\text{H}$   $T_1$  dramatically increases by decreasing the temperatures. Therefore, if Sample 1b had been at the same temperature as samples 1a and 1c during the experiment,  $^1\text{H}$  and  $^{19}\text{F}$   $T_1$ s would have been longer than the values registered for sample 1a.

For Samples 1a and 1c, the  $^{19}\text{F}$  relaxation rate is shorter than the associated error. Therefore, the reported value is zero. This means that  $^{19}\text{F}$   $T_1$  is so long that its effect is exceeded by the cross-relaxation rate  $\sigma$ . In the equation used to fit the data, the parameter  $R_F$  always appears in a sum with the parameter  $\sigma$ . Since from the result of the fits  $R_F$  is always smaller than the parameter  $\sigma$  for each experiment performed, it will be neglected in future fits. By eliminating this parameter from the fitting equations, it is assumed that the build-up of  $^{19}\text{F}$  polarisation takes place with the rate constant  $\sigma$ , that dominates over any losses due to longitudinal relaxation.

Moreover, since the more electrons in the sample, the more efficient the polarisation transfer, it is possible to hypothesise that the cross-relaxation effect is influenced by the presence of free radicals in the sample, and that more than one electron is involved in the process.

### **Discussion and comparison of cross-relaxation in samples with different free radicals types**

Figure 5.12 shows the behaviour of  $^{19}\text{F}$  and  $^1\text{H}$  polarisation under conditions of the experiment to study the transient polarisation with TEKPol in the sample. Results of the fits for Sample 1e are shown in Table 5.6. For this sample,  $^{19}\text{F}$  relaxation rate  $R_F$  significantly increases with respect to Sample 1a, since the average distance between  $^{19}\text{F}$  nuclei and electron increase hence decreasing the dipolar interaction between them. An increase in  $R_H$  is also observed, though it is not significant and can be caused by the different temperature condition during the experiment.

Finally, since the parameter  $\sigma$  is of the same order of magnitude as in Sample 1a,

it is possible to conclude that the distribution of free electrons in the sample does not affect the cross-relaxation process from  $^1\text{H}$  to  $^{19}\text{F}$ .

Results for the same experiment for Sample 1f (see Figure 5.13) are also shown in Table 5.6. The  $\sigma$  parameter, indicative of the intensity of the cross-relaxation process, is smaller than the one obtained for the other samples. Therefore cross-relaxation, although present even in this sample, plays a minor role in the dynamics of  $^{19}\text{F}$  polarisation. An in-depth study of this effect is presented in Chapter 6.

	<b>Sample 1e</b> (20 mM of TEKPol)	<b>Sample 1f</b> (40 mM of BDPA)
$\mathbf{R}_F$ (1/s)	$0.0089 \pm 0.0013$	$0.009 \pm 0.009$
$\mathbf{R}_H$ (1/s)	$0.0059 \pm 0.0002$	$0.006 \pm 0.001$
$\sigma$ (1/s)	$-0.0200 \pm 0.0011$	$-0.0026 \pm 0.0011$
$\epsilon_H$	$32 \pm 10$	$11 \pm 3$
$\mathbf{T}$ (K)	1.67	1.66

*Table 5.6:* Results for relaxation time constants, enhancements and average temperatures of the performed experiments for the samples containing the free radicals TEKPol and BDPA.

By comparing these data with the ones obtained from Sample 1a (the one with 40 mM TEMPO) a few conclusions can be drawn. In the previous section it was discussed how the presence of the transient polarisation becomes more relevant as the free electrons concentration in the sample increases, suggesting that such a process is mediated by at least two electrons. With the experiments discussed in this section, it was shown that the EPR linewidth of the used free radical plays an important role in the polarisation transfer. The process is more efficient for free radicals with a large linewidth. This result is in agreement with theory and observations by Guarin et al. [96]. In their work, focused on the polarisation transfer between  $^1\text{H}$  and  $^{13}\text{C}$  in samples with TEMPOL, they showed that for high TEMPOL concentrations, a good thermal contact between the nuclear spin reservoirs is mediated by the electron non-Zeeman ensemble, allowing a fast paced polarisation exchange between the nuclei.

Another reasonable hypothesis that explains the polarisation exchange, is the one that involves flip-flops between two electrons that mediate the polarisation transfer between the two nuclei. For this to be applicable for the analysed samples,

the electron ensemble must not be fully polarised, and the two electrons involved in the process must have an energy difference  $\hbar(\omega_H - \omega_F)$ , corresponding to the Larmor frequency difference between  $^1\text{H}$  and  $^{19}\text{F}$ .

The assumption of non-completely polarised electrons is satisfied by the experimental conditions, since in a  $\approx 3.4\text{ T}$  magnetic field, at  $\approx 1.6\text{ K}$ , the electron polarisation is  $\approx 89\%$ . It serves the purpose to acknowledge the existence of continuous fluctuations of the electron spins, taking place on the timescale of the electronic  $T_1$ , much shorter than the nuclear ones.

When a flip-flop of two electron spins with energy difference  $\hbar(\omega_H - \omega_F)$  takes place, it mediates a flip-flop of the  $^1\text{H}$  and  $^{19}\text{F}$  nuclear spins.

Observations from the experiments above described fully support this hypothesis. Moreover, since the polarisation transfer rate  $\sigma$  is similar for Samples 1a and 1e (containing TEMPO and TEKPol free radicals respectively), it is possible to conclude that the position of the electrons is not a key element in the process. In fact, while in Sample 1a electrons can be considered uniformly distributed in the sample, for Sample 1e the uniform distribution is related to pairs of electrons, each pair being formed by electrons at a fixed distance.

### **Discussion on $^{19}\text{F}$ concentration dependence of the cross-relaxation process**

In Section 5.2.5, experiments where the  $^{19}\text{F}$  concentration and sample deuteration have been described.

Following the results of Section 5.2.2, it was concluded that the inverse  $^{19}\text{F}$  relaxation time  $1/T_1^F = R_F$  in Equations 5.9 can be neglected for the fittings of the experimental data. From the fit, values for  $\sigma$  and  $R_H$  are obtained, and their corresponding time constants are summarised in Table 5.7.

Results show that the  $^1\text{H}$  longitudinal relaxation time  $T_1^H$  are of the same order of magnitude for all samples, independently of the concentration of  $^{19}\text{F}$  nuclei in the sample.  $T_1^H$  in fact assumes values that vary between 37 and 80s, excluding the results for Sample 3d that will be commented later.

The interesting result is that through this experiments it is possible to estimate a value for  $T_1^H$  from an experiment where only  $^{19}\text{F}$  data are acquired, and results

	$T_1^H$ (s)	$\sigma^{-1}$ (s)
Sample 1a	$37 \pm 2$	$210 \pm 20$
Sample 2a	$67 \pm 8$	$240 \pm 40$
Sample 3a	$80 \pm 7$	$1040 \pm 120$
Sample 4a	$39 \pm 5$	$1300 \pm 500$
Sample 1d	$49 \pm 4$	$280 \pm 30$
Sample 2d	$40 \pm 4$	$340 \pm 50$
Sample 3d	$20 \pm 10$	$2000 \pm 3000$

*Table 5.7:* Results for  $^1\text{H}$  relaxation time constants and  $\sigma^{-1}$  of the performed experiments.

are comparable with the ones obtained in Section 5.1.3, where the same parameter was obtained by means of standard saturation recovery experiments on  $^1\text{H}$ .

The only exception to the general trend is given by Sample 3d, that presents an overall shorter  $T_1^H$ . However, due to the poor signal-to-noise ratios of the  $^{19}\text{F}$  data, from the errors associated to the parameters it is clear that the fit is not necessarily representative of the behaviour of  $^{19}\text{F}$  polarisation, therefore it will henceforth no longer be considered.

As for the inverse of the cross-relaxation parameter  $\sigma$ , it is possible to notice that as the  $^{19}\text{F}$  concentration decreases, its value becomes longer.

To understand the role of the parameter  $\sigma$  in this case, consider Equation 5.9, representing the evolution of the  $^{19}\text{F}$  polarisation when  $^1\text{H}$  nuclei are also present. The second term of the equation is the one that contains the parameters related to  $^1\text{H}$ , such as its initial polarisation and its longitudinal relaxation time constant. If the  $^1\text{H}$  polarisation is not perturbed during a  $^{19}\text{F}$  saturation recovery experiment, the second term of Equation 5.9 is null (in fact the initial value for  $^1\text{H}$  polarisation is equal to the thermal polarisation), and it can be rewritten as

$$P_F(t) = P_{\text{eq}} (1 - e^{-\sigma t}). \quad (5.10)$$

This equation has the same form of the saturation recovery equation used to fit the results of Section 5.1.3, where the build-up time of  $^{19}\text{F}$  was obtained. However, the parameter  $\sigma$  of the experiments in this section assumes the same role as the longitudinal relaxation time  $T_1^F$  in Section 5.1.3. By comparing those values to the build-up time  $T_1^F$  obtained in Section 5.1.3, it shows that  $\sigma^{-1}$  is longer than  $T_1^F$ , with this discrepancy increasing as the concentration of  $^{19}\text{F}$  decreases. This

discrepancy is probably caused by the too simplistic model used to fit the data. In order to get a better fit for these data, it would be in fact needed not to neglect the parameter  $R_F$  from Equation 5.8 and to take into account the polarisation exchange from  $^{19}\text{F}$  nuclei to  $^1\text{H}$  nuclei as well. Moreover, the polarisations, assumed to be the same for both  $^{19}\text{F}$  and  $^1\text{H}$ , should be considered different. However, the addition of these parameters in the fitting functions make it impossible to obtain values, since the correlation between them is too large.

In fact, even the used model has already too many parameters. Depending on the initial values for the parameters used in the fitting function, different values are obtained. The values shown in Table 5.7 have been obtained by bounding the  $T_1^H$  parameter to values close to the ones obtained in Section 5.1.3.

Finally it is important to note that even in the deuterated samples (Samples 1d, 2d and 3d) the transient polarisation dynamics can be observed, and the cross-relaxation parameter  $\sigma$  assumes values consistent with the ones obtained in non-deuterated samples. This means that, unlike in the experiment presented by Daube et al. [78], cross-relaxation cannot be induced by the rotation of the methyl group in toluene.

### 5.3 Conclusions

In this Chapter experiments have been discussed with the intention to determine the optimal sample composition for  $^{19}\text{F}$  DNP. NMR analysis was performed in samples containing fluorinated benzene, benzene and toluene with the free radical TEMPO at  $\approx 1.6\text{ K}$  in a  $3.4\text{ T}$  static magnetic field, by using a custom designed probe which made it possible to double tune the resonant coil to both  $^1\text{H}$  and  $^{19}\text{F}$  Larmor frequencies.

According to the results of the experiments, the best DNP enhancement for  $^{19}\text{F}$  is achieved for low concentrations of  $^{19}\text{F}$ . Moreover, sample deuteration boosts the enhancement, with a concomitant increase in polarisation build-up time  $\tau_{DNP}$  as the amount of deuterated chemicals increases. The highest enhancement was reached for the sample with  $\approx 50\text{ mM}$  of  $^{19}\text{F}$  and complete deuteration of toluene

and benzene, with a polarisation of  $\approx 40\%$ .

Additionally, the  $^{19}\text{F}$  longitudinal relaxation time constant component independent on the free radicals has been found.

Cross-relaxation experiments have been performed by varying the TEMPO concentration in the sample. It has been shown that the amount of free radicals in the sample determine the intensity of the cross-relaxation process from  $^1\text{H}$  to  $^{19}\text{F}$  nuclei: the lower the TEMPO concentration, the smaller the cross-relaxation rate.

It has also been shown that free electrons are not the only source of cross-relaxation, since evidence of cross-relaxation has been observed in a sample without free radicals.

It was also observed that by using the same amount of free electrons with large EPR linewidth added in the sample with 20 mM TEKPol or 40 mM TEMPO, the cross-relaxation process does not change. However, by using the same amount of electrons but from a narrow EPR linewidth free radical like BDPA, this mechanism becomes weaker. This shows that a prerequisite for the observed effect is the wide electron linewidth. It also highlights the possibility that the g-anisotropy of the electrons is important to provide electron pairs with appropriate shifts in Larmor frequency so that nuclear spin flip-flops between  $^1\text{H}$  and  $^{19}\text{F}$  can be mediated. Following the analysis of the experimental data, it was also concluded that the process that mediates the cross-relaxation involves the two nuclei as well as at least two electrons.

Finally, spontaneous cross-relaxation has been studied in samples with different  $^{19}\text{F}$  concentration, ranging from  $\approx 0.05$  to  $\approx 3$  M, as well as for different deuteration degrees. A strong dependence of cross-relaxation on  $^{19}\text{F}$  concentration has been observed. Also it was shown that, for  $^{19}\text{F}$  concentrations ranging from  $\approx 50$  mM up to  $\approx 3$  M, the  $^1\text{H}$  polarisation dynamics is unaffected by  $^{19}\text{F}$  nuclei.

## Chapter 6

# Cross-relaxation between $^1\text{H}$ and $^{19}\text{F}$ at cryogenic temperatures and DNP with the free radical BDPA

In Chapter 5, a transient polarisation transfer from  $^1\text{H}$  to  $^{19}\text{F}$  was discussed when paramagnetic radicals were added to the sample. Moreover, it was shown that the transfer rate increases as the concentration of the paramagnetic centre increases. To study this phenomenon, samples at cryogenic temperatures were hyperpolarised under microwave irradiation. In this Chapter, polarisation exchange is initially studied in a sample without free radicals. An experimental methodology that does not rely on microwaves has been developed to characterise the strength of this effect. The same methodology has later been used to study samples containing also the free radicals BDPA and TEMPO.

Experiments with microwave irradiation have also been performed, to study the performance of DNP for samples containing the free radical BDPA. As the experimental data show, alongside with the Solid Effect, another DNP mechanism contributes to the hyperpolarisation of  $^1\text{H}$  to  $^{19}\text{F}$  in the samples, as evidenced by the appearance of additional features in the DNP enhancement profile. This effect is observed at microwave frequencies different to the Solid Effect. A four spin model is formulated to explain this effect, and spin dynamics simulations are

carried out to validate the model.

## 6.1 $^{19}\text{F}$ - $^1\text{H}$ polarisation exchange at cryogenic temperatures without microwave irradiation

In a two spin system in a static magnetic field, as the one shown in Figure 6.1, the polarisation transfer between the two spins A and B occurs via the zero-quantum transition between energy levels separated by an energy difference  $\hbar\omega_{ZQ} = \hbar(\omega_A - \omega_B)$ . In principle, if there is no additional external source of energy, this transition is forbidden by the energy conservation law, since the two levels are not degenerate. However, in a real sample, dipolar interactions between spins, as well as hyperfine interaction with paramagnetic impurities, can generate fluctuating magnetic fields. These fields, when fluctuating at frequencies close to the transition frequencies, induce transitions between energy levels, and hence relaxation (or cross-relaxation for spins coupled by dipole-dipole interaction).

Usually in the liquid state the motion of the molecules in the sample at ambient

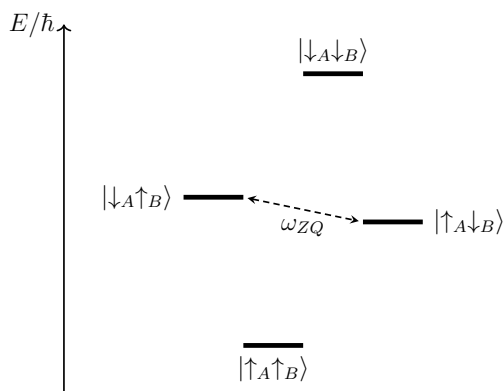


Figure 6.1: Energy levels of a two spin system A and B.

temperature is sufficient to stimulate the relaxation processes. This motion can even be responsible for the cross-relaxation between different species, as already observed [77–80].

However, when the sample is at cryogenic temperatures (e.g.  $T < 2\text{ K}$ ) molecular motion that involves vibrational, translational and rotational modes are frozen out [101] and in principle cross-relaxation should become a negligible process affecting the nuclear spin dynamics. In this Section this process will be studied when the

sample is under solid state DNP condition, demonstrating that the presence of free radicals can stimulate cross-relaxation even for temperatures below 2 K. All experiments in this Section have been performed without irradiating the samples with microwaves.

### 6.1.1 Sample preparation

#### Glassy matrix

The experiments presented in this Chapter are performed on the same organic sample as used for the experiments in Chapter 5, made of 75% toluene ( $C_7H_8$ ) and 25% monofluorobenzene ( $C_6H_5F$ ) (v:v). This sample forms a glassy matrix at cryogenic temperatures.

The  $^1H$  concentration in this sample is 69.5 M and the  $^{19}F$  concentration is 2.7 M.  $^{13}C$  nuclei are present in natural abundance at a concentration of 0.7 M concentration, and it is assumed that their presence does not affect the results of the experiments described in this Chapter.

#### The free radical BDPA

Three samples have been prepared by adding to the toluene-fluorobenzene mixture different concentrations of the free radical  $\alpha,\gamma$ -Bisdiphenylene- $\beta$ -phenylallyl (BDPA), at a final concentration of 20, 30 and 40 mM of BDPA (its chemical structure is shown in Figure 6.2).

BDPA has a narrow EPR linewidth compared to the nitroxide radicals, and it is

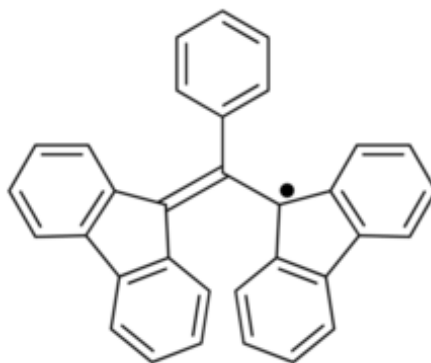


*Figure 6.2:* Chemical structure of a BDPA molecule. The black dot represents the most likely position of the free electron in the molecule.

soluble in the organic matrix. In fact its linewidth is of the order of 30 MHz in a 3.34 T magnetic field [38], compared to  $> 500$  MHz for nitroxide radicals [102]. The BDPA EPR linewidth is less than the Larmor frequency of  $^1\text{H}$  and  $^{19}\text{F}$  ( $\approx 142$  MHz and  $\approx 134$  MHz respectively) and therefore, as explained in Chapter 3, the dominating DNP process for these nuclei is the Solid Effect. BDPA was used to differentiate between the various DNP mechanisms, as will be explained later in this Chapter. Table 6.1 shows the samples used for the experiments in this Chapter. Alongside the samples with BDPA, a sample without free radical has been used, as well as a degassed sample without any BDPA. Also, a sample containing 40 mM TEMPO has been studied.

Degassing of Sample B was achieved by using a Schlenk line [103]. Three degassing cycles were performed on the sample, each of them consisting of three stages. First, the sample was frozen in liquid nitrogen. Once the sample was completely frozen, a vacuum pump was connected to the sample space, to remove the air. Finally, nitrogen gas was introduced in the sample space, and the sample was slowly warmed up to ambient temperature.

<b>Sample A</b>	75% toluene + 25% fluorobenzene
<b>Sample B</b>	75% toluene + 25% fluorobenzene, degassed
<b>Sample C</b>	75% toluene + 25% fluorobenzene, 40 mM BDPA
<b>Sample D</b>	75% toluene + 25% fluorobenzene, 30 mM BDPA
<b>Sample E</b>	75% toluene + 25% fluorobenzene, 20 mM BDPA
<b>Sample F</b>	75% toluene + 25% fluorobenzene, 40 mM TEMPO

*Table 6.1:* Samples used for the experiments described in this Chapter.

### 6.1.2 Saturation recovery experiments with and without continuous $^1\text{H}$ saturation in a sample free of paramagnetic centres

The experiments described in this Chapter are performed in a 3.34 T magnetic field at  $\approx 1.7$  K in the polariser magnet, by using the dual tuned brass probe. Spectrometer and probe are described in Section 4.1.

The results of two different experiments have been compared by using Sample A

of Table 6.1. The first is a standard saturation recovery experiment (described in Section 4.3.2). Results for this experiment are labelled “*std*”. For the second experiment, a saturation recovery has been performed on the  $^{19}\text{F}$  signal while  $^1\text{H}$  nuclei were continuously saturated. The used pulse sequence is described in details in Section 4.3.5, and results for this experiment are labelled “*Hsat*”.

Figure 6.3a shows the integrals of the  $^{19}\text{F}$  spectra obtained with the saturation recovery experiment (in red), as well as those obtained with the experiment with continuous  $^1\text{H}$  saturation (shown in blue). Both data sets have been fitted with the function

$$I(t) = I_0 \left( 1 - \exp\left\{-\frac{t}{T}\right\} \right) \quad (6.1)$$

described in Section 4.3.2.

The same two experiments have been performed for the degassed Sample B in Table 6.1, and the results are shown in Figure 6.3b.

The two figures show that for both samples, the build-up time constants do not

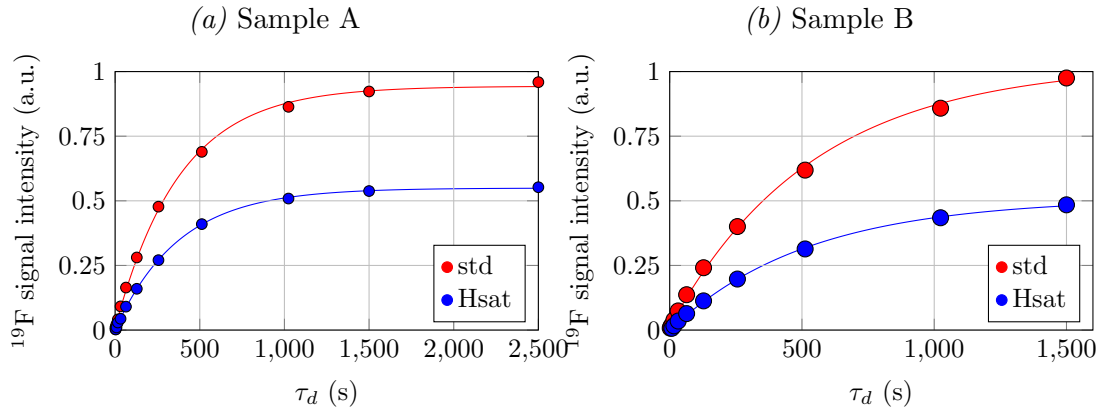


Figure 6.3: Results of the saturation recovery experiments with (blue) and without (red)  $^1\text{H}$  saturation. Samples are made of 75% of toluene and 25% of fluorobenzene, with Sample A and B prepared without and with degassing.

change by saturating the  $^1\text{H}$  spin ensemble. Their values are  $T^{std} = 381 \pm 11$  s and  $T^{Hsat} = 376 \pm 6$  s for Sample A without and with  $^1\text{H}$  saturation respectively, and  $T^{std} = 540 \pm 20$  s and  $T^{Hsat} = 520 \pm 20$  s for Sample B. A difference in steady-state polarisation on the other hand is observed in both cases, where the polarisations during  $^1\text{H}$  saturation are 58% and 50% of the standard saturation recovery case for sample A and B, respectively.

### 6.1.3 Saturation recovery experiments with and without continuous $^1\text{H}$ saturation in samples with the free radical BDPA

The same set of experiments has been performed for the remaining samples described in Table 6.1. These experiments were performed to analyse the dependency of the build-up time constant and difference in polarisation as a function of the concentration of free radicals in the sample. Figure 6.4 shows the results of these experiments.

Table 6.2 summarises the build-up time constants  $T$ . It also shows the ratio of

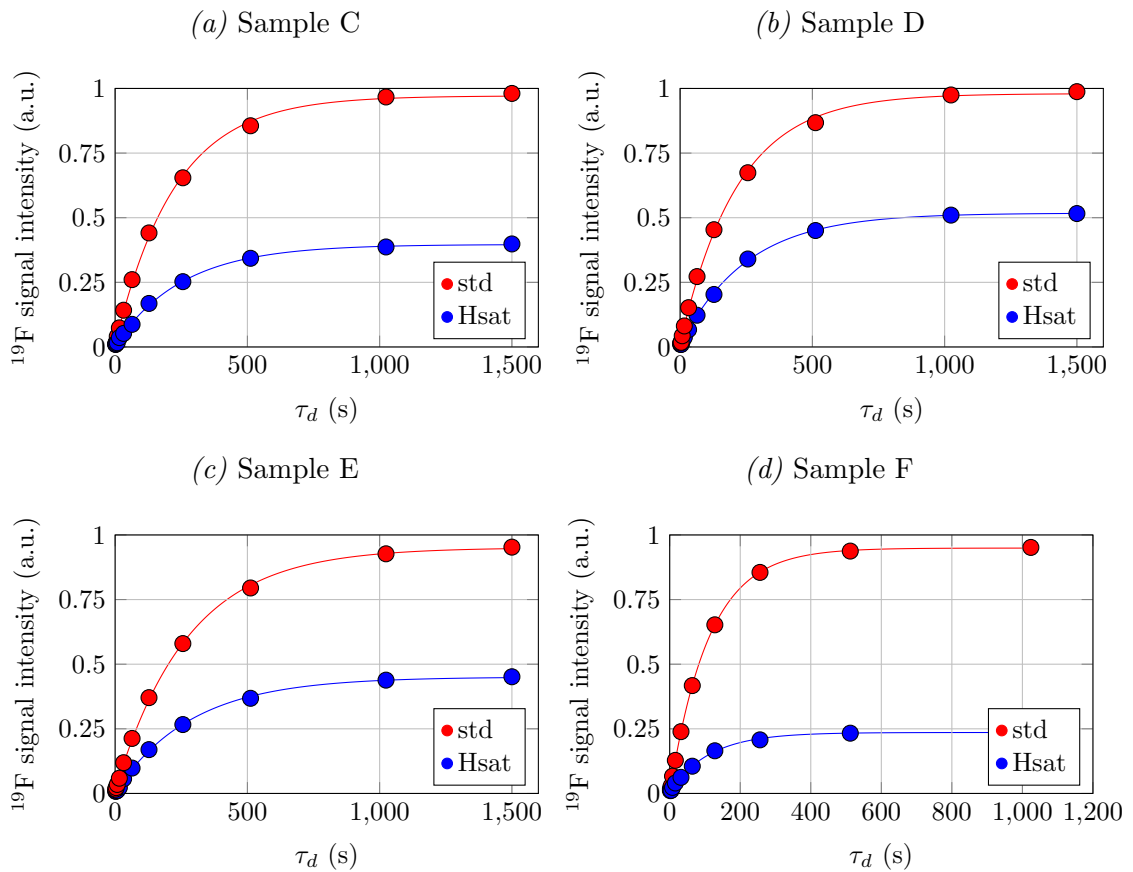


Figure 6.4: (a) Results of the experiments with (blue) and without (red)  $^1\text{H}$  saturation for samples with different concentrations of BDPA (40, 30, 20 mM - Samples C, D, E respectively) and 40 mM TEMPO (Sample F).

the steady-state polarisation obtained from the experiments with continuous  $^1\text{H}$  saturation and the steady-state polarisation of the standard saturation recovery, for all samples listed in Table 6.1.

As Table 6.2 shows, for samples C, D and E, the values of the build-up time

	Sample A	Sample B degassed	Sample C 40 mM BDPA	Sample D 30 mM BDPA	Sample E 20 mM BDPA	Sample F 40 mM TEMPO
$T_F^{\text{Hsat}}$ (s)	$376 \pm 6$	$520 \pm 20$	$255 \pm 7$	$249 \pm 5$	$287 \pm 8$	$113 \pm 4$
$T_F^{\text{std}}$ (s)	$381 \pm 11$	$540 \pm 20$	$225 \pm 7$	$217 \pm 7$	$274 \pm 5$	$110.2 \pm 0.7$
$\frac{P_F^{\text{Hsat}}}{P_F^{\text{std}}} \times 10^2$	$58.3 \pm 0.4$	$50.2 \pm 1.1$	$40.4 \pm 0.5$	$53.0 \pm 0.6$	$47.5 \pm 0.5$	$24.7 \pm 0.4$

*Table 6.2:* Results for the build-up time constants and steady-state polarisation ratios obtained by means of standard saturation recovery experiments and saturation recovery experiment with continuous  $^1\text{H}$  saturation for all samples in Table 6.1.

constants change slightly between the two performed experiments. However, each value falls within the confidence interval of the other experiments if the error associated with the temperature stability (see Section 4.3.6) is taken into account. This error, estimated to be  $\approx 12\%$  of the time constant values, matches the time constants of the two experiments for each sample.

### 6.1.4 Control experiment

A control experiment has been performed on Sample B to demonstrate that the difference in steady-state polarisation is not generated by artefacts related to the high power pulses used for continuous  $^1\text{H}$  saturation. Results of saturation recovery experiments without and with continuous  $^1\text{H}$  polarisation saturation are compared. For the latter, instead of pulsing on resonance with the  $^1\text{H}$  Larmor frequency, an arbitrary offset frequency of  $\approx 139$  MHz has been used. This frequency is off resonant to any nuclear Larmor frequency, while being within the tuning range of the capacitors in the tuning box. The probe has also been tuned to this frequency instead of  $^1\text{H}$  Larmor frequency. Results of this control experiment are shown in Figure 6.5.

As shown in the legend of the figure, the values of the fitting functions parameters do not differ significantly. Their difference is within the error generated by the temperature stability, discussed in Section 4.3.6. Furthermore, the steady-state polarisation ratio, equal to  $\approx 0.94$ , is almost twice than that observed for Sample B, for which the  $^1\text{H}$  Larmor frequency was used for  $^1\text{H}$  saturation.

This experiment provides strong evidence that the high power RF pulses on the  $^1\text{H}$  channel are not responsible for the observed lowering of the  $^{19}\text{F}$  polarisation

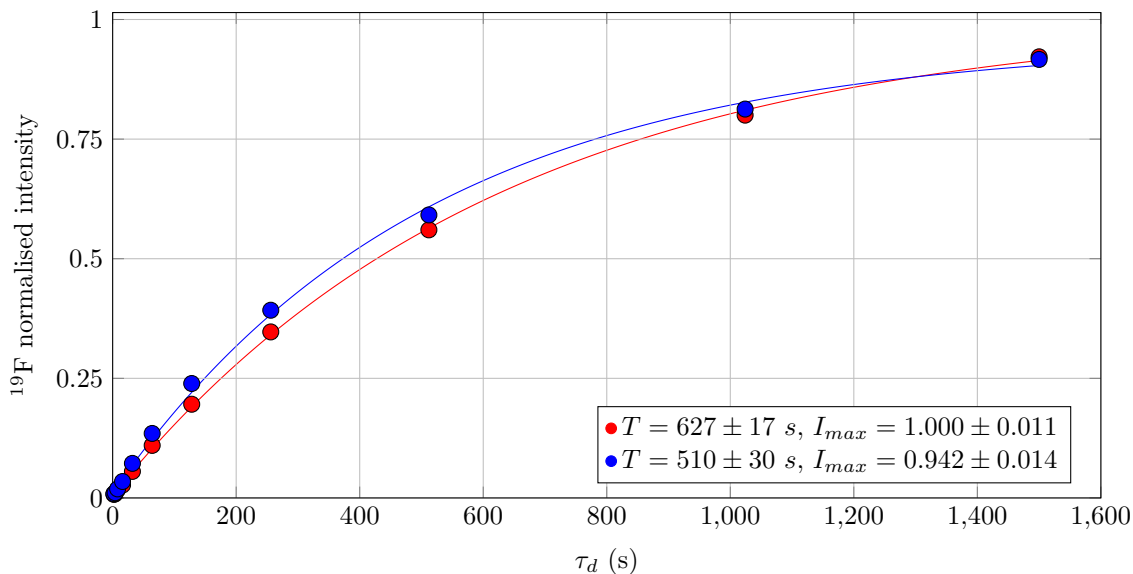


Figure 6.5: Result for the control saturation recovery experiment. The blue curve represents the experiment with off resonant pulses at frequency  $\approx 139$  MHz, while the red one is the standard saturation recovery. Build-up time constant  $T$  and steady-state intensity  $I_{max}$  are also shown in the legend for the two curves.

in the previous experiments, and that the observed phenomenon is related to the interaction of the two nuclear ensembles.

### 6.1.5 Discussion

Data shown in Figure 6.3 show saturation recovery experiments with and without continuous  $^1\text{H}$  saturation, performed on samples without free radicals. The results show that there is a significant difference in the dynamics of  $^{19}\text{F}$  nuclei that recover their polarisation after saturation. For both experiments,  $^{19}\text{F}$  nuclei recover a steady-state polarisation with the same build-up time constant  $T$ , but there is a difference in steady-state polarisation even without paramagnetic centres.

In Chapter 5 it was shown that  $^1\text{H}$  and  $^{19}\text{F}$  nuclei can interact if paramagnetic centres are added to the sample, exchanging polarisation. However, results of experiments presented in this Chapter show that the two nuclear ensembles interact with each other even if there are no paramagnetic centres in the sample. In fact, experiments were performed on the degassed Sample B in order to remove paramagnetic oxygen dissolved in the sample, and to show that cross-relaxation is still observed.

Using the Equations 5.7 introduced in Chapter 5 a solution that describes the polarisation  $P_F(t)$  dynamics in a standard saturation recovery experiment can be found:

$$P_F(t) = P_{\text{eq}} [1 - e^{(-R_F - \sigma)t}] - \frac{\sigma(P_H(0) - P_{\text{eq}})}{R_F - R_H + \sigma} [e^{(-R_F - \sigma)t} - e^{-R_H t}], \quad (6.2)$$

where  $P_H(0)$  is the initial polarisation of the  $^1\text{H}$  ensemble. Since  $^1\text{H}$  nuclei are at thermal equilibrium at the beginning of the experiment,  $P_H(0) = P_{\text{eq}}$  and Equation 6.2 can be written as

$$P_F^{\text{std}}(t) = P_{\text{eq}} [1 - e^{(-R_F - \sigma)t}]. \quad (6.3)$$

According to this equation, following a saturation recovery experiment,  $^{19}\text{F}$  polarisation builds up to the thermal equilibrium value  $P_F^{\text{std}}(\infty) = P_{\text{eq}}$  with a time constant  $T^{\text{std}} = \frac{1}{R_F + \sigma}$ .

On the other hand, when  $^1\text{H}$  polarisation is constantly saturated, the condition  $P_H(t) = 0$  is satisfied throughout the duration of the experiment. The  $^{19}\text{F}$  polarisation therefore evolves according to the differential equation

$$\begin{aligned} \frac{dP_F^{\text{Hsat}}(t)}{dt} &= R_F(P_{\text{eq}} - P_F^{\text{Hsat}}) + \sigma(P_H(t) - P_F^{\text{Hsat}}) \\ &= R_F(P_{\text{eq}} - P_F^{\text{Hsat}}) - \sigma P_F^{\text{Hsat}}, \end{aligned} \quad (6.4)$$

with solution

$$P_F^{\text{Hsat}}(t) = \frac{R_F}{R_F + \sigma} P_{\text{eq}} (1 - e^{-(\sigma + R_F)t}). \quad (6.5)$$

This equation shows that, after the  $^{19}\text{F}$  polarisation is initially saturated by a train of pulses, it builds up with a single exponential with time constant  $T^{\text{Hsat}} = \frac{1}{R_F + \sigma}$  and an equilibrium value  $P_F^{\text{Hsat}}(\infty) = \frac{R_F}{R_F + \sigma} P_{\text{eq}}$ .

It is possible to remove the  $P_{\text{eq}}$  dependency from these equations by calculating the ratio between the two steady-state polarisations, obtaining

$$\frac{P_F^{\text{Hsat}}(\infty)}{P_F^{\text{std}}(\infty)} = \frac{R_F}{R_F + \sigma} \quad (6.6)$$

Both the ratio  $\frac{P_F^{\text{Hsat}}(\infty)}{P_F^{\text{std}}(\infty)}$  and the build-up time constants  $T^{\text{std}} = T^{\text{Hsat}} = \frac{1}{R_F + \sigma}$  were experimentally calculated and are shown in Table 6.2. Using these data it is possible to calculate both the longitudinal relaxation time constant  $T_1 = 1/R_F$  for  $^{19}\text{F}$  nuclei, as well as the exchange parameter  $\sigma$ .

Table 6.3 shows the values for  $\sigma$  and  $R_F$  and their associated time constants for the samples analysed.

Before discussing the results of the experiments, it is important to point out

	$R_F \cdot 10^{-5}$ (1/s)	$T_1$ (s)	$\sigma \cdot 10^{-5}$ (1/s)	$\frac{1}{\sigma}$ (s)
Sample A	$156 \pm 3$	$641 \pm 12$	$110 \pm 3$	$910 \pm 20$
Sample B (degassed)	$96 \pm 6$	$1040 \pm 60$	$101 \pm 8$	$990 \pm 80$
Sample C (40 mM BDPA)	$158 \pm 5$	$630 \pm 20$	$233 \pm 9$	$429 \pm 17$
Sample D (30 mM BDPA)	$213 \pm 9$	$469 \pm 11$	$189 \pm 7$	$530 \pm 20$
Sample E (20 mM BDPA)	$165 \pm 5$	$606 \pm 18$	$183 \pm 7$	$550 \pm 20$
Sample F (40 mM TEMPO)	$214 \pm 8$	$467 \pm 17$	$666 \pm 9$	$150 \pm 2$

Table 6.3: Values for intrinsic relaxation rate  $R_F$  and exchange rate  $\sigma$ , and corresponding time constant.

that even if the  $^1\text{H}$  nuclei are always saturated, they are not decoupled from the  $^{19}\text{F}$  nuclei. The delay  $\Delta T$  between the saturation pulses is in fact much longer than the dipolar interaction between the two nuclear species, therefore the coupling between  $^1\text{H}$  and  $^{19}\text{F}$  is not averaged out by the pulses on the  $^1\text{H}$  channel. The time characteristic of the dipolar interaction strength between  $^1\text{H}$  and  $^{19}\text{F}$  is estimated to be  $\frac{1}{d_{HF}} \approx 30 \mu\text{s}$ . The dipolar coupling constant has been calculated using the formula

$$d_{HF} = \frac{\mu_0 \gamma_F \gamma_H \hbar}{r_{HF}^3}, \quad (6.7)$$

where  $\mu_0$  is the vacuum permeability,  $\gamma_H$  and  $\gamma_F$  are the gyromagnetic ratios of  $^1\text{H}$  and  $^{19}\text{F}$  respectively,  $\hbar$  is the reduced Planck constant and  $r_{HF}$  is the minimum distance between  $^1\text{H}$  and  $^{19}\text{F}$  in the sample. This distance has been estimated by assuming a uniform distribution of nuclei in the sample.

## The $^{19}\text{F}$ longitudinal relaxation time constant $T_1$

As the results in Table 6.3 show, the value of the longitudinal relaxation times  $T_1$  for  $^{19}\text{F}$  are consistent with each other within the experimental error<sup>1</sup>. The only exception is Sample B.

For Sample B, the lack of paramagnetic impurities has a big impact in the longitudinal relaxation time constant  $T_1$ , which becomes  $\approx 160\%$  the non-degassed value.

This dramatic change in intrinsic  $T_1$  is expected, since the paramagnetic impurities in the sample have a strong coupling with the spin nuclei. Sato et al. [104] calculated the maximum molar fraction of  $\text{O}_2$  at room temperature and pressure that can be dissolved in toluene and benzene to be  $x \approx 9 \times 10^{-4}$ , corresponding to a maximum concentration of  $\approx 10$  mM.

These paramagnetic impurities are also present in Samples C, D, E and F, in quantities which are of the same order of magnitude of the used free radical concentrations. It is therefore not surprising that the intrinsic  $T_1$  for the non-degassed samples does not change significantly for these samples.

The  $T_1$  time constant can be separated in two main components:

$$\frac{1}{T_1} = \frac{1}{T_1^{eF}} + \frac{1}{T_1^{rest}}, \quad (6.8)$$

where  $T_1^{eF}$  is related to the paramagnetic relaxation, caused by the interaction of  $^{19}\text{F}$  nuclei with the paramagnetic centres in the sample, while  $T_1^{rest}$  takes into account all the other contributions, as discussed in Section 2.5.

Since in Sample B there are no paramagnetic impurities or free radicals, the  $T_1^{eF}$  contribution to the intrinsic  $T_1$  is zero, and therefore  $T_1 = T_1^{rest}$ . It is assumed that this contribution is the same for all the other samples as well, and it is therefore possible to calculate the contribution to  $T_1^{eF}$  for all samples (shown in Table 6.4).

The specific mechanism that generates relaxation at such low temperatures is unknown. It is however reasonable to hypothesise that a small vibration of fluorobenzene molecules causes a non-vanishing spectral density function at the frequency of  $^{19}\text{F}$  and  $^1\text{H}$  nuclei (see Section 2.3).

---

<sup>1</sup>12% of the value, as calculated in Section 4.3.6

Sample	A	B	C	D	E	F
$T_1^{eF}$ (s)	$1670 \pm 190$	0	$1610 \pm 190$	$860 \pm 90$	$1450 \pm 170$	$850 \pm 70$

*Table 6.4:* Contribution of  $T_1^{eF}$  to the intrinsic  $T_1$  for the sample without BDPA (Sample A), the degassed one (Sample B), the samples with BDPA (40, 30, 20 mM BDPA - Samples C, D, E respectively), and the Sample with 40 mM TEMPO (Sample F).

Moreover, for samples containing BDPA, it was observed that at cryogenic temperatures, the rearrangement of the double and single bonds connecting the central carbon to either of the two fluorene moieties in BDPA can generate the electronic  $T_1$  relaxation [105].

For these samples, a simultaneous flip of one electron and one nucleus can therefore be the mechanism responsible of  $^{19}\text{F}$  relaxation.

### The exchange parameter $\sigma$

If there is no free radical in the sample, a difference in the steady-state polarisation is still observed, and therefore a non-zero value for  $\sigma$  is calculated. However, the value of  $\sigma$  is in this case lower than for the samples containing free radicals. The experiment without free radicals has been also repeated for the degassed Sample B.

The parameter  $\sigma$  represents the exchange rate of polarisation between the two nuclear ensembles. Its value is proportional to the intensity of the interactions that mediate the transfer. As the results in Table 6.3 show, the largest observed value is obtained for the sample with the free radical TEMPO. For samples containing BDPA, the intensity of  $\sigma$  decreases with the free radical concentration. These results confirm those obtained in Chapter 5 for samples containing TEMPO, where it was shown that polarisation transfer is positively correlated with the concentration of paramagnetic centres.

The fact that  $^1\text{H}$  polarisation affects the  $^{19}\text{F}$  polarisation also for the degassed sample leads to the conclusion that the cross-relaxation process is not mediated only by paramagnetic centres in the samples. In fact, in the non-degassed sample without free radicals, paramagnetic impurities are still present in the form of oxygen dissolved in the sample. Moreover, the intensity of  $\sigma$  is the same for both

Samples A and B, meaning that paramagnetic impurities do not influence the cross-relaxation mechanism. As already discussed for the longitudinal relaxation, it is unknown what may cause the cross-relaxation in the absence of free radicals or other paramagnetic impurities.

At this point, it is hypothesised that two main mechanisms contribute to the  $^1\text{H}$ - $^{19}\text{F}$  interaction, like it was done for the longitudinal relaxation time constant. One of them is related to the paramagnetic centres in the sample, while the other is related to a mechanism that does not depend on them. The parameter  $\sigma$  can therefore be expressed as a sum of two contributions:

$$\sigma = \sigma_{par} + \sigma_{HF}, \quad (6.9)$$

where  $\sigma_{par}$  represents the contribution due to the presence of paramagnetic centres, while  $\sigma_{HF}$  is related to the interaction that occurs independently of them, but requires a dipolar interaction between  $^{19}\text{F}$  and  $^1\text{H}$ .

By assuming that the contribution made by  $\sigma_{HF}$  is the same for all samples, it is possible to calculate  $\sigma_{par}$ . Results are shown in Table 6.5.

It is interesting to compare the intensity of the  $\sigma$  parameter for the sample with

Sample	A	B	C	D	E	F
$\sigma_{par} \times 10^{-5}$ (1/s)	$9 \pm 8$	0	$132 \pm 12$	$88 \pm 10$	$82 \pm 10$	$565 \pm 12$

*Table 6.5:* Contribution of  $\sigma_{par}$  to the total  $\sigma$  for the sample without BDPA (Sample A), the degassed one (Sample B), the samples with BDPA (40, 30, 20 mM BDPA - Samples C, D, E respectively), and the Sample with 40 mM TEMPO (Sample F).

40 mM TEMPO and the one with the same BDPA concentration. The parameter  $\sigma$  for the sample containing TEMPO is almost three times larger than the one obtained from the sample with BDPA, and therefore the cross-relaxation process is more efficient. This means that not only the concentration, but also the properties of the free radical are important in the process. In particular, this suggests that the cross-relaxation process is mediated by more than one electron. It is reasonable to hypothesise that when the difference in Larmor frequency of the two electrons  $|\nu_{e1} - \nu_{e2}| = \nu_H - \nu_F$ , non-coherent flip-flops of the electrons could generate a flip-flop of the two coupled nuclei, mediating the cross-relaxation process.

It should be noted that the values obtained for  $\sigma$  in the experiment with 40 mM TEMPO do not match the value obtained in Section 5.2.6 for the same parameter. This mismatch is attributed to different experimental conditions during the experiments. In fact, in the experiment performed in the previous Chapter, microwaves were irradiating the sample. During microwave irradiation, an increase of  $\approx 1$  K is observed, as already discussed in Section 4.3.6. As a consequence, the rates obtained in the experiment described in Section 5.2.6 differ from the ones described in this section.

To increase the quality of the analysis, more repetitions of the presented experiments would be needed, to obtain more precise results and reduce the impact of the experimental errors on the data.

## 6.2 Enhancement by DNP

$^{19}\text{F}$  and  $^1\text{H}$  spectra have been acquired for different microwave frequencies, covering the whole range available from the microwave source (93.75 GHz to 94.25 GHz), with a power of 400 mW at  $\approx 1.7$  K and a frequency step of 10 MHz. As an experimental protocol, the “Frequency sweep experiment” described in Section 4.3.1 was used. For these experiments, a 30 s DNP build-up time was chosen before each FID is acquired. Although the recovery time is not sufficient for the nuclei to reach the steady-state polarisation, such an experiment provides a picture of the DNP enhancements for  $^{19}\text{F}$  and  $^1\text{H}$  nuclei in the sample, showing their corresponding microwave frequencies. Therefore, the ratios of the enhancements do not represent the ratio of the steady-state polarisations since the corresponding build-up times can have a microwave frequency dependence. Figure 6.6 shows the integrals of the acquired spectra, normalised to the maximum enhancements, for  $^1\text{H}$  (red) and  $^{19}\text{F}$  (blue) nuclei for Sample C of Table 6.1. On the x-axis the difference between the reference frequency and the microwave reference frequency  $\Delta\nu$  is shown. The reference frequency in the figure is chosen to be at half of the distance between the two  $^1\text{H}$  external peaks. The intensity of the NMR signals are normalised to the maximum value.

The far left and far right peaks for both  $^{19}\text{F}$  and  $^1\text{H}$  are related to the Solid

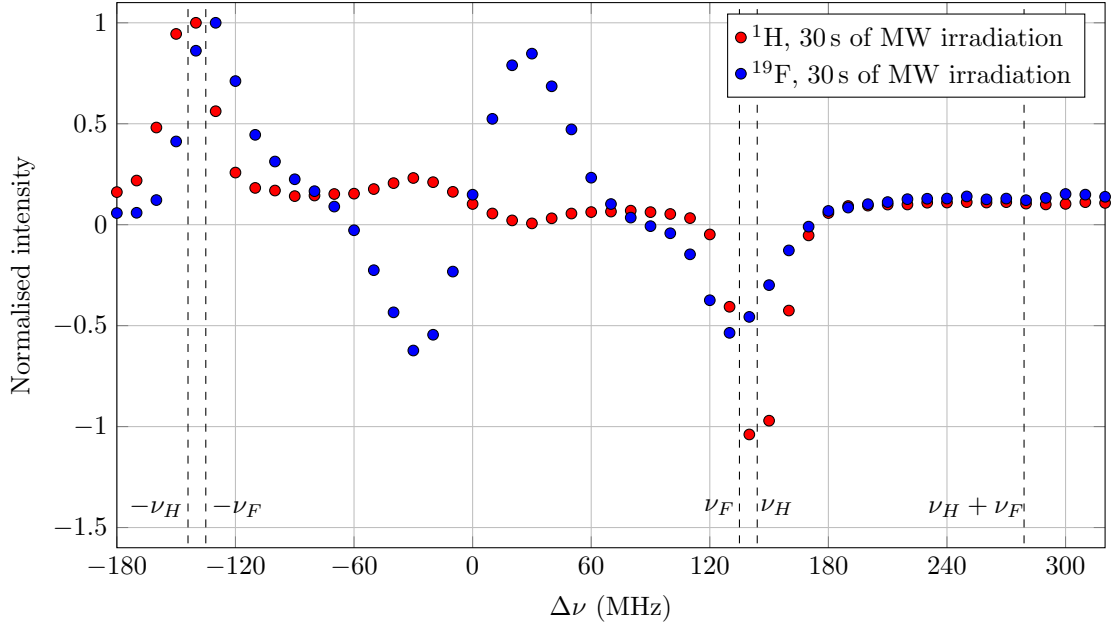


Figure 6.6: DNP enhancement profile of  $^{19}\text{F}$  and  $^1\text{H}$  NMR signals for Sample C (the sample with 40 mM BDPA), acquired with microwave power of 400 mW and 30 s of build-up time. Intensities are normalised to the maximum values for each of the DNP profiles. Dashed vertical lines mark the position of  $^{19}\text{F}$  and  $^1\text{H}$  Larmor frequencies as well as the sum of the two.

Effect. These two peaks are observed at the frequencies  $\nu_e \pm \nu_N$ , and in fact their separation is twice the Larmor frequency of the nuclei, as the Solid Effect theory predicts [10, 34]. In the frequency region between  $-60$  MHz and  $60$  MHz in the figure, a “secondary” enhancement region appears. These enhancements are antisymmetric with respect to the reference frequency, have opposite signs for the two nuclei, and their linewidth is larger than the one of the Solid Effect DNP lines. The opposite sign of  $^{19}\text{F}$  and  $^1\text{H}$  enhancements excludes the possibility that “regular” Cross Effect and Thermal Mixing could be responsible for them since, as shown in Figure 5.2 in the previous Chapter, the sign for the enhancements is the same for both nuclei in that case.

Another frequency sweep experiment was also performed to investigate one spectral region of the Solid Effect in more detail (Figure 6.6). In this experiment,  $^{19}\text{F}$  signals were acquired while irradiating the sample with microwaves with frequency ranging from  $-178$  to  $-78$  MHz. The microwave frequency was

incremented in smaller steps (2 MHz) to increase the resolution of the peak. Figure 6.7 shows the  $^{19}\text{F}$  DNP profile. The Larmor frequencies of the two different nuclei are also shown in the figure.

As the figure shows, the width at half maximum of the  $^{19}\text{F}$  Solid Effect peak is

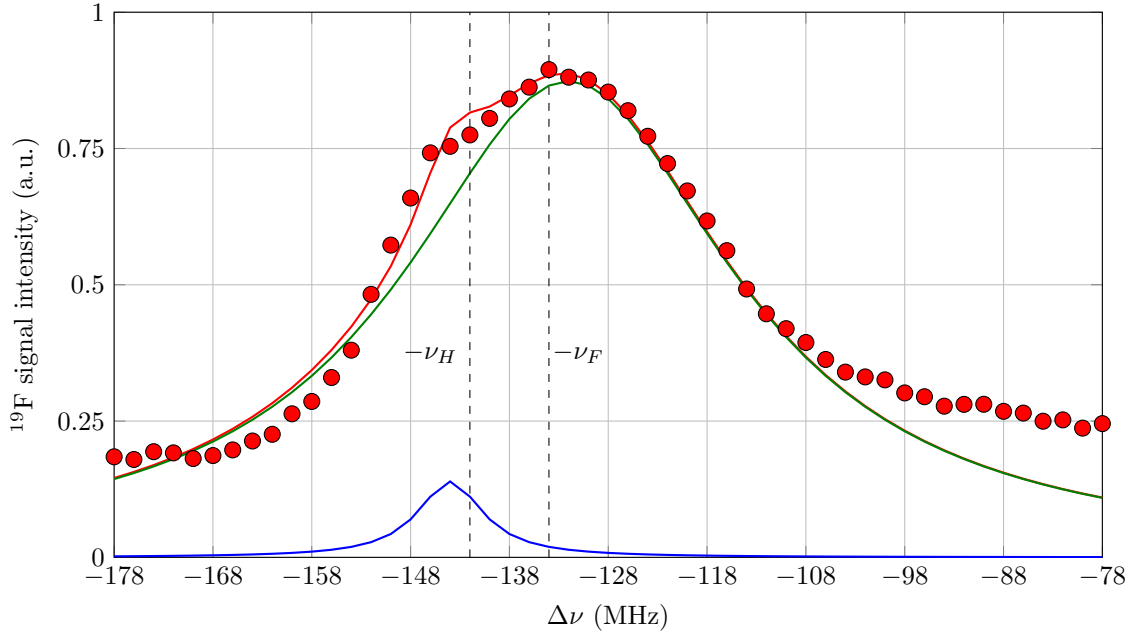


*Figure 6.7:* Positive Solid Effect DNP enhancement profile of  $^{19}\text{F}$  NMR signals for the sample with 40 mM BDPA (Sample C), acquired with microwave power of 400 mW and 30 s of build-up time. Dashed vertical lines mark the position of  $^{19}\text{F}$  and  $^1\text{H}$  Larmor frequencies. The data have been fitted with two Lorentzian functions. The red solid line is the sum of the two, the green curve is given by a Lorentzian centred at the  $^{19}\text{F}$  Larmor frequency, while the blue one is close to the  $^1\text{H}$  Larmor frequency.

$\approx 40$  MHz broad (same linewidth as the free radical BDPA). The figure also shows the presence of a “shoulder”, appearing on the left of the main peak. The experimental curve was fit with two Lorentzian functions. The Lorentzian function is defined as

$$L(x) = A \frac{\Gamma}{(x - x_0)^2 + \Gamma^2}, \quad (6.10)$$

where  $A$  is the normalisation value,  $x_0$  is the position of the maximum and  $\Gamma$  is the half-width at half-maximum. It is hypothesised that the green curve represents the  $^{19}\text{F}$  enhancement due to the Solid Effect. The position of the shoulder, indicated by the Lorentzian in blue in the figure, coincides with the position of the

positive  $^1\text{H}$  Solid Effect peak (indicated in the figure by a vertical dashed line). The quality of the fitting is not perfect since the integrals present a non-zero value outside of the Solid Effect region due to the  $^{19}\text{F}$  thermal equilibrium value. However, this shoulder presents evidence that cross-relaxation occurs between  $^1\text{H}$  and  $^{19}\text{F}$ . The  $^1\text{H}$  ensemble that gets hyperpolarised at  $\Delta\nu = -\nu_H = -142\text{ MHz}$  with the Solid Effect DNP mechanism as shown in Figure 6.6, cross-relaxes with the  $^{19}\text{F}$  nuclei resulting in a visible contribution to the enhancement of the  $^{19}\text{F}$  ensemble.

Figure 6.8 shows the positive Solid Effect DNP enhancement profile of  $^{19}\text{F}$  and  $^1\text{H}$  NMR signals.

The DNP profile for  $^1\text{H}$  nuclei lacks signal enhancement at the  $^{19}\text{F}$  Larmor fre-

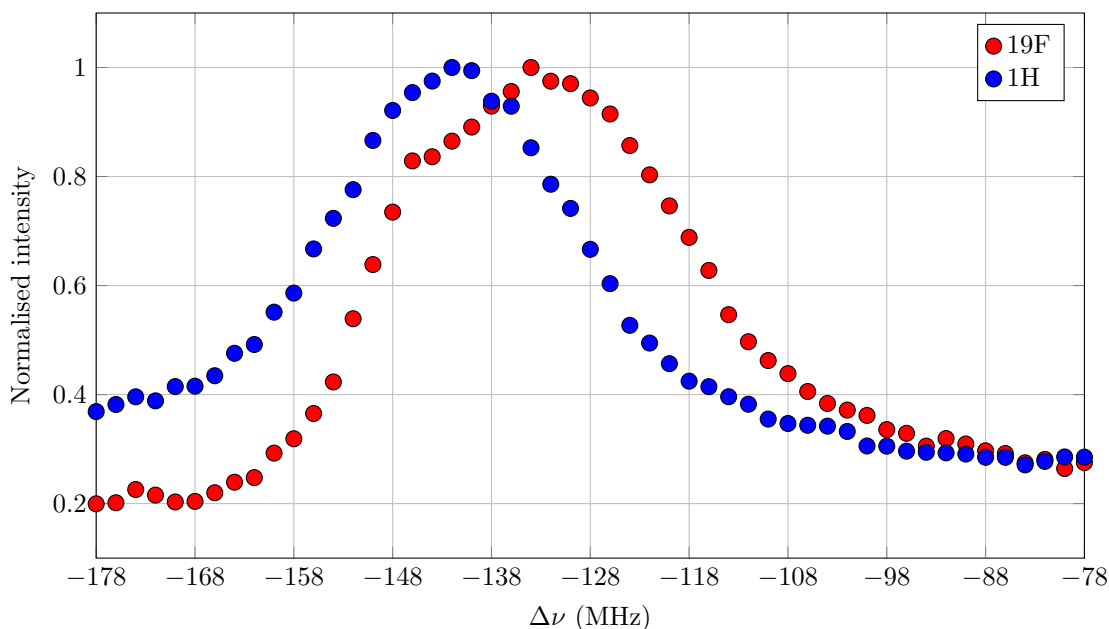


*Figure 6.8:* Positive Solid Effect DNP enhancement profile of  $^{19}\text{F}$  and  $^1\text{H}$  NMR signals for Sample C, normalised to the maximum value of  $^{19}\text{F}$  and  $^1\text{H}$  respectively. Each FID is acquired with microwave power of 400 mW and 30 s of build-up time.

quency above the standard Solid State profile, showing an asymmetric behaviour compared to the  $^{19}\text{F}$  profile. The absence of this enhancement can be interpreted as an inefficient cross-relaxation for transferring polarisation from the hyperpolarised  $^{19}\text{F}$  nuclei to the  $^1\text{H}$  ensemble. This result strengthens the assumption made in Chapter 5, where it was assumed that the evolution of the  $^1\text{H}$  polarisation in the sample is not significantly affected by the  $^{19}\text{F}$  nuclei, present in the

sample in lower quantity compared to the  $^1\text{H}$  nuclei.

### 6.2.1 Study of the DNP profile for samples with different BDPA concentrations

Frequency sweep experiments for  $^{19}\text{F}$  nuclei have been performed also for Samples D and E. Figure 6.9 shows the results of the experiments in the microwave frequency region that includes the positive Solid Effect peak and the negative secondary enhancement.

The position of the Solid Effect enhancement is the same for all samples analysed,

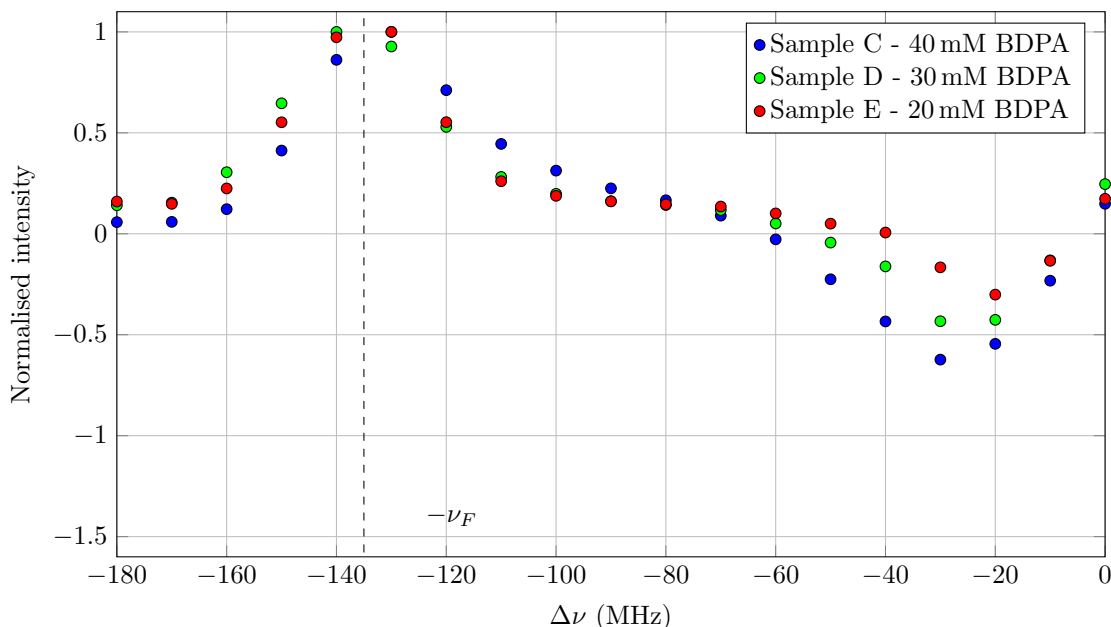


Figure 6.9: DNP enhancement profile of  $^{19}\text{F}$  NMR signals for samples with different concentrations of BDPA (40, 30, 20 mM - Samples C, D, E respectively) in the microwave frequency region that includes the positive Solid Effect peak and the negative secondary enhancement. Intensities are normalised to the maximum values for each of the DNP profiles. The dashed vertical line marks the position of  $^{19}\text{F}$  Larmor frequency in respect to  $\nu_e$ .

while the secondary enhancement shifts to higher frequencies as the concentration of BDPA decreases. Moreover, the peak of the secondary enhancement gets narrower for low BDPA concentration.

The enhancements  $\epsilon$  and DNP build-up times  $\tau_{DNP}$  have been collected for Samples B, C and D, and are summarised in Table 6.6.

As the table shows, the enhancement values for the Solid Effect are always higher

<sup>19</sup> F					
		Solid Effect		Secondary enhancement	
	$T_1$ (s)	$\tau_{DNP}$ (s)	$\epsilon$	$\tau_{DNP}$ (s)	$\epsilon$
Sample C (40 mM BDPA)	$225 \pm 7$	$240 \pm 20$	$9.1 \pm 0.3$	$167 \pm 7$	$3.58 \pm 0.06$
Sample D (20 mM BDPA)	$262 \pm 4$	$217 \pm 18$	$8.1 \pm 0.2$	$245 \pm 8$	$2.91 \pm 0.04$
Sample E (20 mM BDPA)	$274 \pm 5$	$318 \pm 10$	$6.19 \pm 0.08$	$440 \pm 20$	$1.82 \pm 0.03$
<sup>1</sup> H					
		Solid Effect		Secondary enhancement	
	$T_1$ (s)	$\tau_{DNP}$ (s)	$\epsilon$	$\tau_{DNP}$ (s)	$\epsilon$
Sample C (40 mM BDPA)	$130 \pm 17$	$130 \pm 7$	$12.1 \pm 0.6$	$81 \pm 9$	$1.75 \pm 0.09$
Sample D (30 mM BDPA)	$66 \pm 5$	$92 \pm 10$	$5.7 \pm 0.3$	—	—

*Table 6.6:* Longitudinal relaxation time constants, DNP build-up time constants and enhancements for the samples with 40, 30 and 20 mM BDPA (Samples C, D and E respectively), obtained while irradiating the sample with microwaves at the frequencies corresponding to Solid Effect enhancement and to the secondary enhancement. In the sample with 20 mM of BDPA (Sample E) there is no secondary enhancement for <sup>1</sup>H. The microwave power used during the experiments is 400 mW.

than for the secondary enhancement.

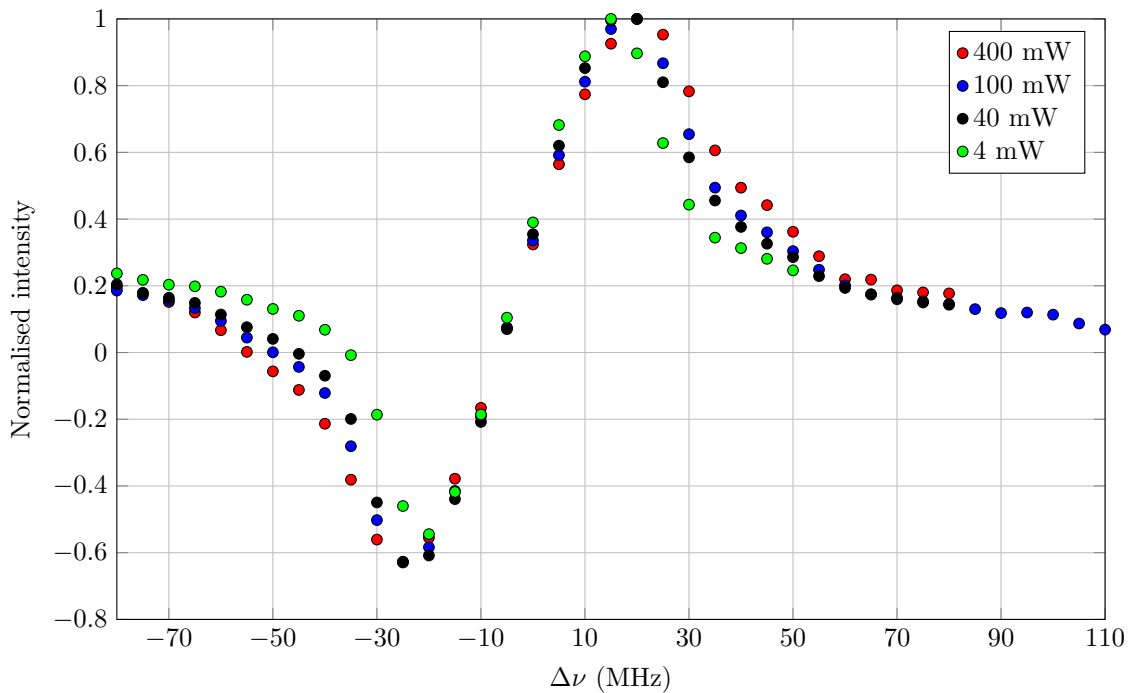
Data for the secondary enhancements for <sup>1</sup>H for Samples D and E are not shown since it is not possible to distinguish such features in the <sup>1</sup>H DNP profile due to the poor signal-to-noise ratios of the spectra.

Figure 6.10 shows the central region of the DNP profile of <sup>19</sup>F acquired for four different microwave powers, ranging from 4 to 400 mW, for the Sample D. The data in this figure demonstrate that by lowering the microwave power, the difference in frequency for the maximum and minimum becomes smaller. Note that the intensities of the signals are normalised to the signal with maximum intensity for each microwave power, obtained after 100 s of polarisation. In fact, since the spectra did not reach the steady-state hyperpolarisation during the experiment, a comparison between the intensities would have been pointless.

$^{19}\text{F}$					
		Solid Effect		Secondary enhancement	
	$T_1$ (s)	$\tau_{DNP}$ (s)	$\epsilon$	$\tau_{DNP}$ (s)	$\epsilon$
Sample D (30 mM BDPA)	$262 \pm 4$	$225 \pm 4$	$3.76 \pm 0.03$	$196 \pm 3$	$3.46 \pm 0.03$

*Table 6.7:* Longitudinal relaxation time constants, DNP build-up time constants and enhancements for Sample D, obtained while irradiating the sample with microwaves at the frequencies corresponding to Solid Effect enhancement and to the secondary enhancement. The used microwave power is 100 mW.

As the figure shows, by increasing the microwave power, the DNP spectrum is



*Figure 6.10:*  $^{19}\text{F}$  DNP profile in the central region of the frequency for four different microwave powers, after a DNP build-up of 100 s. Values are normalised to the maximum integral of each experiment.

broadened. This effect is caused by a broadening of the excitation bandwidth during microwave irradiation. Hovav et al. [106] observed a similar behaviour in simulations of a spin system composed by a nucleus surrounded by seven electrons. They also observed a maximal polarisation that initially increases with the microwave power, and then decays for higher values.

## 6.3 Discussion

To explain the presence of the secondary enhancements in Figure 6.6, two simple models will now be discussed. These two models take into account the interaction of one  $^{19}\text{F}$  and one  $^1\text{H}$  nuclei with one or two electrons respectively.

### e-F-H

The first model involves one  $^{19}\text{F}$  nucleus, one  $^1\text{H}$  nucleus and one electron, coupled with the two nuclei via the hyperfine interaction. This model relies only on the interactions of these three spins. The Hamiltonian describing this system is similar to the one introduced in Equation 3.1 for the Solid Effect DNP, with additional terms related to the second nuclear spin. It can be written as:

$$\mathcal{H} = \mathcal{H}_Z + \mathcal{H}_{IS} + \mathcal{H}_{II}. \quad (6.11)$$

The first term of the sum represents the Zeeman Hamiltonian:

$$\mathcal{H}_Z = \mathcal{H}_H + \mathcal{H}_F + \mathcal{H}_S = \omega_H \hat{H}_z + \omega_F \hat{F}_z + (\omega_S - \omega_{\text{MW}}) \hat{S}_z. \quad (6.12)$$

In this equation,  $\hat{F}_z$  and  $\hat{H}_z$  are the quantum mechanical spin operators for  $^{19}\text{F}$  and  $^1\text{H}$  respectively. Each term in the equation represents the interaction of each spin with the external magnetic field, and generates an energy splitting proportional to their Larmor frequencies.

The second term in the total Hamiltonian is related to the hyperfine interaction:

$$\begin{aligned} \mathcal{H}_{IS} = [ & A_{z,H} \hat{S}_z \hat{H}_z + \frac{1}{2} \left( A_H^+ \hat{S}_z \hat{H}^+ + A_H^- \hat{S}_z \hat{H}^- \right) \\ & A_{z,F} \hat{S}_z \hat{F}_z + \frac{1}{2} \left( A_F^+ \hat{S}_z \hat{F}^+ + A_F^- \hat{S}_z \hat{F}^- \right) ] \end{aligned} \quad (6.13)$$

This term takes into account the interaction of the electron with each of the two nuclei.  $A_{z,N}$  and  $A_N^\pm$  (where  $N = H, F$ ) are the secular and pseudo-secular coefficients of the dipolar hyperfine interaction. The Hamiltonian term related to

the  $^1\text{H}$ - $^{19}\text{F}$  interaction is expressed in the dipolar Hamiltonian:

$$\mathcal{H}_{HF} = d_{HF} \left( 3\hat{H}_z\hat{F}_z - \bar{H} \cdot \bar{F} \right), \quad (6.14)$$

where  $d_{HF}$  is the dipolar coupling constant for the two nuclei.

The last term of Equation 6.11 represents the effect of the microwave irradiation. This term commutes with the x-projection of the angular momenta of the electron, and can be simply written as:

$$\mathcal{H}_{MW} = \omega_1 \hat{S}_x, \quad (6.15)$$

where  $\omega_1$  is the strength of the microwave irradiation.

The energy levels associated with this three spin system are shown in Figure 6.11.

In such a system a double Solid Effect can take place. This effect was observed experimentally by De Boer et al. [82, 83] in a spin system made of one electron, one  $^1\text{H}$  and one  $^2\text{H}$  nucleus. The energy transition shown in blue corresponds to the triple quantum transition driven by microwave irradiation at a frequency  $\omega_{MW} = \omega_e - \omega_H + \omega_F$ . On the frequency axis of the DNP profile in Figure 6.6, this transition frequency is located on the left of the reference frequency ( $\Delta\nu = 0$ ). During the microwave irradiation, after the populations of the two energy levels are equalised, the state  $|\uparrow_H\downarrow_F\uparrow_e\rangle$  decays to the lower energy level given by  $|\uparrow_H\downarrow_F\downarrow_e\rangle$  due to the short electronic relaxation time, making it the “most” populated state. A population enhancement of this state corresponds to a positive enhancement for  $^1\text{H}$  and a negative one for the  $^{19}\text{F}$  spin. Microwave irradiation at  $\omega_{MW} = \omega_e + \omega_H - \omega_F$  would instead provide a negative enhancement for  $^1\text{H}$  and a positive one for  $^{19}\text{F}$ , with  $|\downarrow_H\uparrow_F\downarrow_e\rangle$  being the most populated state after the electron longitudinal relaxation.

However, the predictions of such a model are not consistent with the experimental observations for the  $^1\text{H} - ^{19}\text{F}$  system:

- The maximum enhancement in the region of the non-standard Solid Effect enhancement has an offset of 30 MHz to the electron Larmor frequency, in-

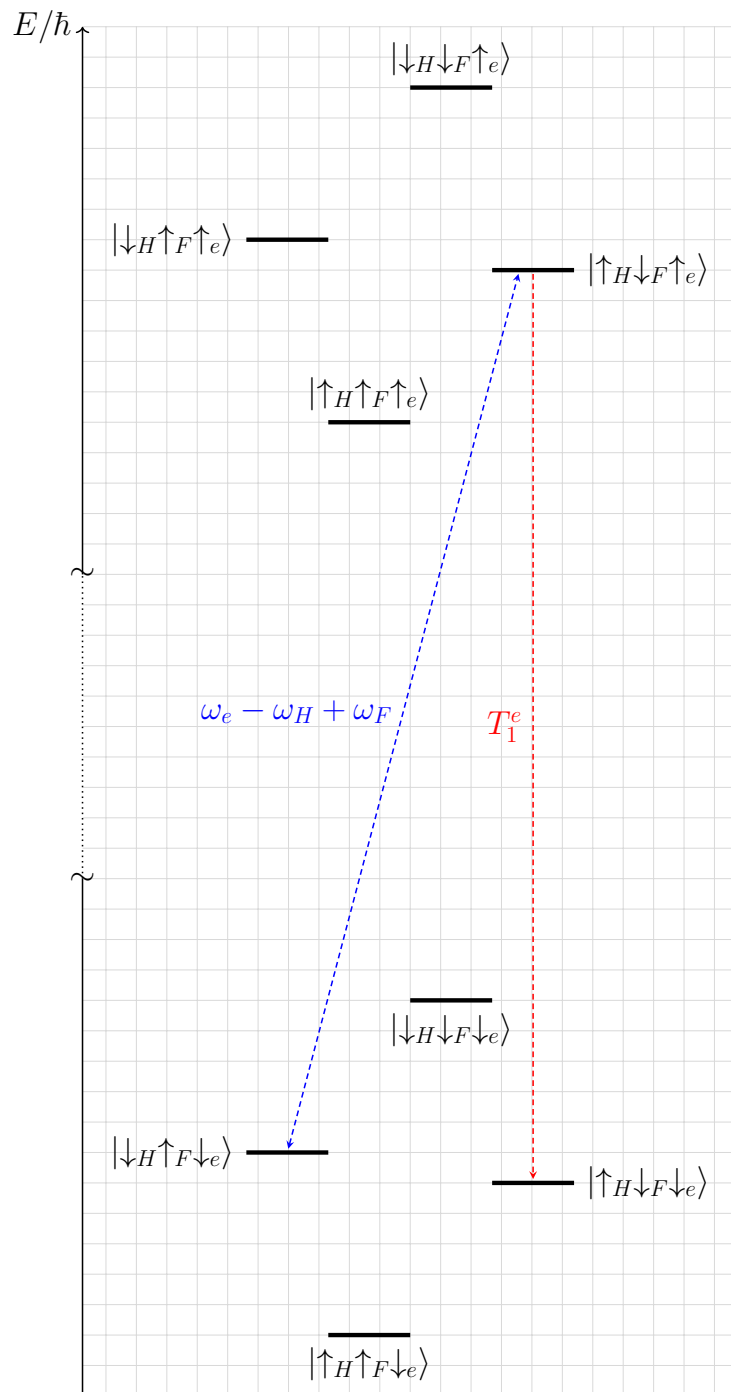


Figure 6.11: Energy levels of a three spin system with microwave irradiation at  $\omega_{MW} = \omega_e - \omega_H + \omega_F$  (blue dashed line). The red dashed line indicates one of the possible  $T_1^e$  relaxation pathways.

stead of the expected  $|\nu_{MW} - \nu_e| = |\nu_H - \nu_F| = 8 \text{ MHz}$ ;

- The double Solid Effect that takes place is a high order Solid Effect process, that results in narrow lines in the DNP spectrum with weaker enhancements compared to the standard Solid Effect [97], contrarily to what experimentally observed;
- As Figure 6.6 shows, there is no enhanced signal at  $\nu_H + \nu_F$ , the frequency corresponding to the triple spin flip  $|\uparrow_H \uparrow_F \downarrow_e\rangle \rightarrow |\downarrow_H \downarrow_F \uparrow_e\rangle$ . Enhanced signals in that frequency range for  $^1\text{H}$  and  $^{19}\text{F}$  would be expected since this transition, predicted by the double Solid Effect DNP, is driven by the same mechanism as the transition  $|\downarrow_H \uparrow_F \downarrow_e\rangle \rightarrow |\uparrow_H \downarrow_F \uparrow_e\rangle$ .

The polarisation transfer from the electron to the two nuclei is represented by the rate

$$C = -\frac{\omega_1}{4(\omega_H - \omega_F)} \left[ \frac{A_H^- A_F^+ \Delta}{\omega_H \omega_F} + \frac{2d_{HF}}{(\omega_H - \omega_F)} (A_{z,H} - A_{z,F}) \right], \quad (6.16)$$

where  $\Delta$  is the microwave frequency when one of the double Solid Effect conditions is met. According to this equation<sup>2</sup>, the transition rate is proportional to the microwave power  $\omega_1$ . Therefore, it is reasonable to conclude that the reason why the double Solid Effect is not observed in the experiments is the low microwave power that can reach the sample.

### **e-e-H-F**

Another model involves two electrons coupled with the two nuclei. This effect was predicted by Shimon et al. [97] and partially observed for  $^1\text{H}$  and  $^2\text{H}$  [95], and is called heteronuclear Cross Effect.

A detailed description of this model is provided in this section, and the Hamiltonian of four interacting spin system is discussed.

The Hamiltonian describing two coupled electrons interacting with one  $^1\text{H}$  and one  $^{19}\text{F}$  nuclei in the microwave rotating frame is the same as the one described

---

<sup>2</sup>Provided by W. Köckenberger and A. Karabanov

before (Equation 6.11), with few additions that take into account the second electron. It can be written as:

$$\mathcal{H} = \mathcal{H}_Z + \mathcal{H}_{IS} + \mathcal{H}_{SS} + \mathcal{H}_{II}. \quad (6.17)$$

In this case, the Zeeman Hamiltonian also includes the term related to the second electron:

$$\mathcal{H}_Z = \mathcal{H}_H + \mathcal{H}_F + \mathcal{H}_{S_1} + \mathcal{H}_{S_2}. \quad (6.18)$$

The hyperfine interaction term is written as

$$\begin{aligned} \mathcal{H}_{IS} = \sum_{i=1,2} [ & A_{z,iH} \hat{S}_{iz} \hat{H}_z + \frac{1}{2} (A_{iH}^+ \hat{S}_{iz} \hat{H}^+ + A_{iH}^- \hat{S}_{iz} \hat{H}^-) \\ & A_{z,iF} \hat{S}_{iz} \hat{F}_z + \frac{1}{2} (A_{iF}^+ \hat{S}_{iz} \hat{F}^+ + A_{iF}^- \hat{S}_{iz} \hat{F}^-) ], \end{aligned} \quad (6.19)$$

to take into account the interaction of both electron with each of the two nuclei. The electron-electron dipolar interaction Hamiltonian is also added to the total Hamiltonian:

$$\mathcal{H}_{SS} = D_{12} (3\hat{S}_{1z}\hat{S}_{2z} - \bar{S}_1 \cdot \bar{S}_2) \quad (6.20)$$

where  $D_{12}$  is the dipolar coupling constant for the two electrons.

Finally, to consider the addition of a second electron, the microwave irradiation term is written as:

$$\mathcal{H}_{MW} = \omega_1 (\hat{S}_{1x} + \hat{S}_{2x}). \quad (6.21)$$

In the described four spin system, Cross Effect conditions [40] can be satisfied depending on the energy difference between the two electrons, since energy levels may become degenerate. All the Cross Effect conditions that can be satisfied are related to couples of energy levels that have opposite electron spins  $|\uparrow_{e1}\downarrow_{e2}\rangle \leftrightarrow |\downarrow_{e1}\uparrow_{e2}\rangle$ . Since there are four possible nuclear states associated with the up-down or down-up electron state ( $|\uparrow_H\uparrow_F\rangle, |\uparrow_H\downarrow_F\rangle, |\downarrow_H\uparrow_F\rangle, |\downarrow_H\downarrow_F\rangle$ ), there are  $4^2 - 4 = 12$  different degeneracies between different nuclear states that can occur, depending on the difference  $\omega_{e1} - \omega_{e2}$ , with  $\omega_{e1} > \omega_{e2}$ <sup>3</sup>. Each degeneracy gives rise to a different DNP effect.

<sup>3</sup>If  $\omega_{e2} > \omega_{e1}$  instead, 12 degeneracies antisymmetric with respect to the previous cases occur.

When  $|\omega_{e1} - \omega_{e2}| \approx \omega_H$ , the  $^1\text{H}$  Cross Effect condition is satisfied. This condition corresponds to the degeneracy of the energy levels  $|\uparrow_{e1}\downarrow_{e2}\uparrow_H\downarrow_F\rangle \leftrightarrow |\downarrow_{e1}\uparrow_{e2}\downarrow_H\downarrow_F\rangle$  or  $|\uparrow_{e1}\downarrow_{e2}\uparrow_H\uparrow_F\rangle \leftrightarrow |\downarrow_{e1}\uparrow_{e2}\downarrow_H\uparrow_F\rangle$ . On the other hand, if the condition  $|\omega_{e1} - \omega_{e2}| \approx \omega_F$  is satisfied, the  $^{19}\text{F}$  Cross Effect occurs between the energy levels  $|\uparrow_{e1}\downarrow_{e2}\uparrow_H\uparrow_F\rangle \leftrightarrow |\downarrow_{e1}\uparrow_{e2}\uparrow_H\downarrow_F\rangle$  or  $|\uparrow_{e1}\downarrow_{e2}\downarrow_H\uparrow_F\rangle \leftrightarrow |\downarrow_{e1}\uparrow_{e2}\downarrow_H\downarrow_F\rangle$ . A higher level Cross Effect can be observed when the energy level crossing occurs between  $|\uparrow_{e1}\downarrow_{e2}\uparrow_H\uparrow_F\rangle \leftrightarrow |\downarrow_{e1}\uparrow_{e2}\downarrow_H\downarrow_F\rangle$  or  $|\uparrow_{e1}\downarrow_{e2}\downarrow_H\downarrow_F\rangle \leftrightarrow |\downarrow_{e1}\uparrow_{e2}\uparrow_H\uparrow_F\rangle$ , when  $|\omega_{e1} - \omega_{e2}| \approx \omega_H + \omega_F$ , or between  $|\uparrow_{e1}\downarrow_{e2}\uparrow_H\downarrow_F\rangle \leftrightarrow |\downarrow_{e1}\uparrow_{e2}\downarrow_H\uparrow_F\rangle$  or  $|\uparrow_{e1}\downarrow_{e2}\downarrow_H\uparrow_F\rangle \leftrightarrow |\downarrow_{e1}\uparrow_{e2}\uparrow_H\downarrow_F\rangle$ , when  $|\omega_{e1} - \omega_{e2}| \approx \omega_H - \omega_F$ . These cases, predicted by Shimon et al. [97], are known as heteronuclear Cross Effect (positive or negative depending on the sign of  $\omega_H \pm \omega_F$ ), and involve the simultaneous flip of all the four spins.

For the properties of the free radical used for the experiments described in this Chapter, the Cross Effect conditions for single nuclei are not satisfied, as well as the positive heteronuclear Cross Effect. In fact, the BDPA linewidth is  $\Gamma_{BDPA} \approx 30 \text{ MHz} \ll \omega_H \approx \omega_F$  [38]. Therefore the only observable mechanism is the negative heteronuclear Cross Effect, which will be discussed in details in the remaining sections.

The 16 energy levels describing the spin system are illustrated in Figure 6.12 for the assumption that the negative heteronuclear Cross Effect condition is fulfilled. In this case, the Larmor frequency difference of the two electrons matches the difference in Larmor frequency of the two nuclei, i.e.  $\omega_{e1}/2\pi - \omega_{e2}/2\pi = \omega_H/2\pi - \omega_F/2\pi = 8 \text{ MHz}$ .

Before microwaves irradiate the sample, the most populated energy states belong to group A in the figure, where both electrons are in the spin down state, as predicted by the Boltzmann distribution. When the system is irradiated with microwaves at the frequency corresponding to the Larmor frequency of one of the electrons (the second one, in the figure), saturation of the second electrons leads to the equalisation of the populations of the energy levels where  $\downarrow_{e1}\downarrow_{e2} \leftrightarrow \downarrow_{e1}\uparrow_{e2}$  and  $\uparrow_{e1}\downarrow_{e2} \leftrightarrow \uparrow_{e1}\uparrow_{e2}$ , with the nuclear spins not changing orientation. In the figure these transitions occur between each state of the groups  $A \leftrightarrow C$  and  $B \leftrightarrow D$  that does not involve a change the nuclear spin orientation.

In analogy to the Cross Effect theory, the equalisation of the populations in the states  $\alpha = |\uparrow_{e1}\downarrow_{e2}\uparrow_H\downarrow_F\rangle \leftrightarrow \beta = |\downarrow_{e1}\uparrow_{e2}\downarrow_H\uparrow_F\rangle$ , together with the longitudinal relaxation of the first electron, bring the system to a DNP equilibrium in which the state  $\gamma = |\downarrow_{e1}\downarrow_{e2}\uparrow_H\downarrow_F\rangle$  results the most populated one.

As in the previously discussed three spin model, the resulting enhancements for  $^{19}\text{F}$  and one  $^1\text{H}$  have opposite sign, in accordance to the sign of the enhancements experimentally observed.

If instead the frequency difference of the two electrons is  $\omega_{e1}/2\pi - \omega_{e2}/2\pi = \omega_H/2\pi - \omega_F/2\pi = 8\text{ MHz}$ , the two degenerate energy levels are  $|\uparrow_{e1}\downarrow_{e2}\downarrow_H\uparrow_F\rangle$  and  $|\downarrow_{e1}\uparrow_{e2}\uparrow_H\downarrow_F\rangle$ , and by irradiating the sample with microwaves at the frequency of the second electron, the corresponding DNP enhancements have opposite sign compared to the previous scenario.

The enhancements predicted by this model are in agreement with the ones observed in the  $^{19}\text{F}$  and  $^1\text{H}$  DNP profiles shown in Figures 6.6 and 6.9.

Unlike for the aforementioned e-H-F model for the double Solid Effect, the advantage of this model relies on the fact that all the transitions that take place during microwave irradiation are allowed single quantum transitions. Moreover, the distance between the positive and negative enhancements approaches the EPR linewidth of BDPA, since it depends on the pairs of electrons that fulfil the condition  $\nu_{e1} - \nu_{e2} = 8\text{ MHz}$  within the  $\approx 30\text{ MHz}$  linewidth of BDPA.

If only the interaction of the nuclei with the first electron is considered, the transition rate can be written as

$$C = -\frac{D_{12}}{8(\omega_H - \omega_F)} \left[ \frac{A_{1H}^- A_{1F}^+ \Delta}{\omega_H \omega_F} + \frac{2d_{HF}}{\omega_H - \omega_F} (A_{z,1H} - A_{z,1F}) \right], \quad (6.22)$$

where  $\Delta$  is the microwave irradiation frequency matching one of the heteronuclear Cross Effect conditions <sup>4</sup>. These terms correspond to the electron flip-flops with simultaneous nuclear flip-flop transitions that mediate the transfer of the difference of the electron polarisation onto the nuclear spin pair. The rate expression (Equation 6.22) is identical to the rate for the double Solid Effect (Equation 6.16),

---

<sup>4</sup>This rate was provided by W. Köckenberger and A. Karabanov

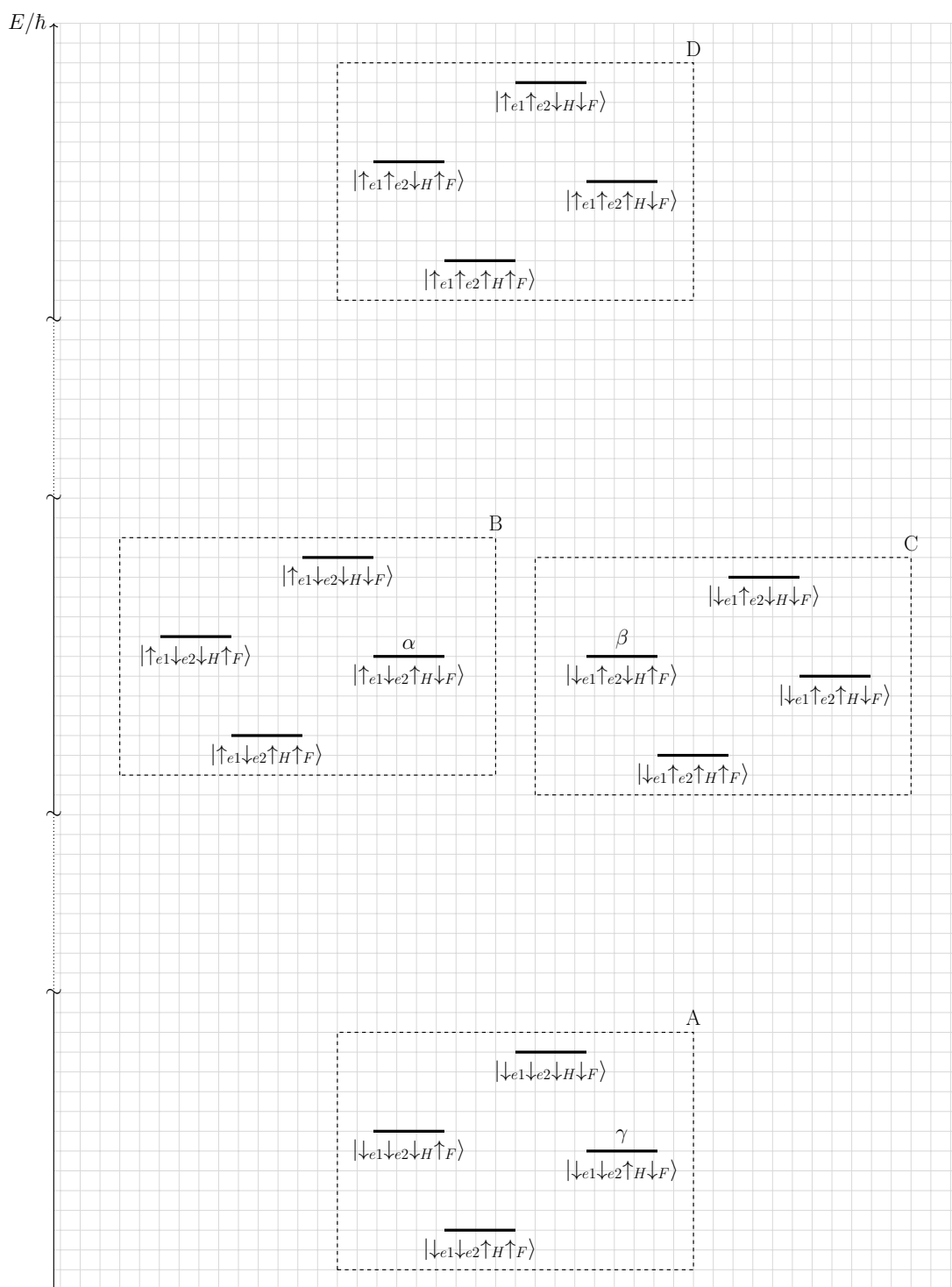


Figure 6.12: Energy levels of a four spin system in the negative heteronuclear Cross Effect condition, where the states  $\alpha$  and  $\beta$  are degenerate. The four blocks A, B, C and D represent the electronic states  $|\downarrow_{e1}\downarrow_{e2}\rangle$ ,  $|\uparrow_{e1}\downarrow_{e2}\rangle$ ,  $|\downarrow_{e1}\uparrow_{e2}\rangle$ ,  $|\uparrow_{e1}\uparrow_{e2}\rangle$  respectively. Within each block, the two spin system states for  $^1\text{H}$  and  $^{19}\text{F}$  are present.

apart from the factor  $D_{12}/2$  replacing the microwave field strength  $\omega_1$ .

The difference in intensity between  $^1\text{H}$  and  $^{19}\text{F}$  enhancements for  $\Delta\nu = \pm(\nu_H - \nu_F)$  can be explained according to the Cross Effect theory developed by Kessenikh et al. [107]. According to their theory, the polarisation  $P_N$  of a nuclear spin under Cross Effect conditions is proportional to the difference of the two electrons polarisation  $P_{e1}$  and  $P_{e2}$ , and can be written as

$$P_N = \frac{P_{e1} - P_{e2}}{1 - P_{e1}P_{e2}}. \quad (6.23)$$

In an analogous way, when the system is hyperpolarised with microwave irradiation at a frequency  $|\nu_{e1} - \nu_{e2}| = |\nu_H - \nu_F|$ , the relationship

$$P_H - P_F = \frac{P_{e1} - P_{e2}}{1 - P_{e1}P_{e2}} \quad (6.24)$$

is satisfied, and since the nuclear polarisations depend on their longitudinal relaxation time constants  $T_{1H}$  and  $T_{1F}$ , the two individual nuclear polarisations can be written as:

$$P_H = \frac{P_{e1} - P_{e2}}{(1 - P_{e1}P_{e2})(1 + \frac{T_{1F}}{T_{1H}})} = \frac{f(P_{e1}, P_{e2})}{1 + \frac{T_{1F}}{T_{1H}}} \quad (6.25)$$

and

$$P_F = -\frac{P_{e1} - P_{e2}}{(1 - P_{e1}P_{e2})(1 + \frac{T_{1H}}{T_{1F}})} = -\frac{f(P_{e1}, P_{e2})}{1 + \frac{T_{1H}}{T_{1F}}}. \quad (6.26)$$

Since these two quantities are proportional to the same function of the electron polarisations  $f(P_{e1}, P_{e2})$ , their ratio depends only on the longitudinal relaxation time constants, and can be written as

$$\frac{P_F}{P_H} = \frac{T_{1F}}{T_{1H}}. \quad (6.27)$$

To obtain experimental enhancement values for both  $^1\text{H}$  and  $^{19}\text{F}$ , saturation recovery experiments have been performed while the sample was irradiated with microwaves at the frequency corresponding to the secondary enhancement peak ( $\Delta\nu \approx -30$  MHz). Figure 6.13 shows the results of these experiments for  $^1\text{H}$  and  $^{19}\text{F}$  with and without microwave irradiation at the frequency corresponding to

$$\Delta\nu = -30 \text{ MHz.}$$

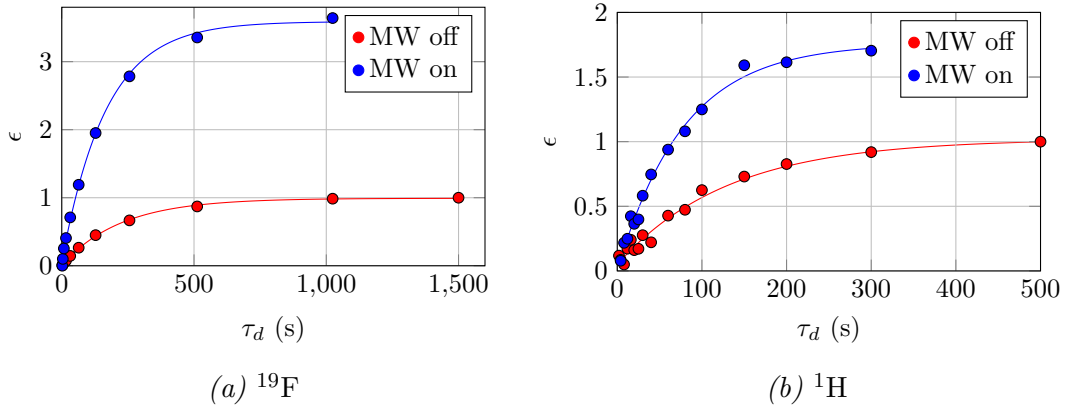


Figure 6.13: Saturation recovery results for  $^{19}\text{F}$  (a) and  $^1\text{H}$  (b) without microwave (red) and with microwave irradiation at the frequency of heCE (blue). Data have been normalised to their thermal equilibrium values.

The ratio  $\frac{P_F}{P_H}$  between  $^1\text{H}$  and  $^{19}\text{F}$  hyperpolarisation for these experiments is  $2.05 \pm 0.11$ , while the ratio between their relaxation times is  $1.7 \pm 0.2$ . These values are in good agreement with each other, thus providing further evidence in support of the heteronuclear Cross Effect theory.

### Numerical simulations of the heteronuclear Cross Effect

In order to validate the hypothesis of heteronuclear Cross Effect and to verify that the experimental results are in agreement with the theoretical prediction, the behaviour of the four spins system has been simulated.

The numerical simulations have been performed by evaluating the time evolution of the matrix elements of the spin density operator. The Hamiltonian used for the simulations is described by Equation 6.11, including the term  $\mathcal{H}_{MW} = \omega_1(\hat{S}_{1x} + \hat{S}_{2x})$  to consider the effect of microwaves. As the Hamiltonian describes the interaction of one  $^1\text{H}$  nucleus and one  $^{19}\text{F}$  nucleus with two electrons, this system has 16 energy levels, as shown in Figure 6.12. The methods of simulation are described in detail in [40, 108, 109].

For these simulations<sup>5</sup>, the coupling parameters are based on the interaction of each spin with the closest neighbours.

<sup>5</sup>Provided by W. Köckenberger

Figure 6.14 shows the results of the DNP profile when the microwaves are irradiated at frequencies in the Solid Effect region with positive enhancements, when the pseudosecular interaction terms  $A_{iF}^{\pm}$  and  $A_{iH}^{\pm}$  are the same. The enhancements in the figure have negative sign, due to the choice of the signs for the gyromagnetic ratios of the two nuclei.

For equal values of pseudosecular interaction terms ( $A_{iF}^{\pm} = A_{iH}^{\pm}$ ), an equal dis-

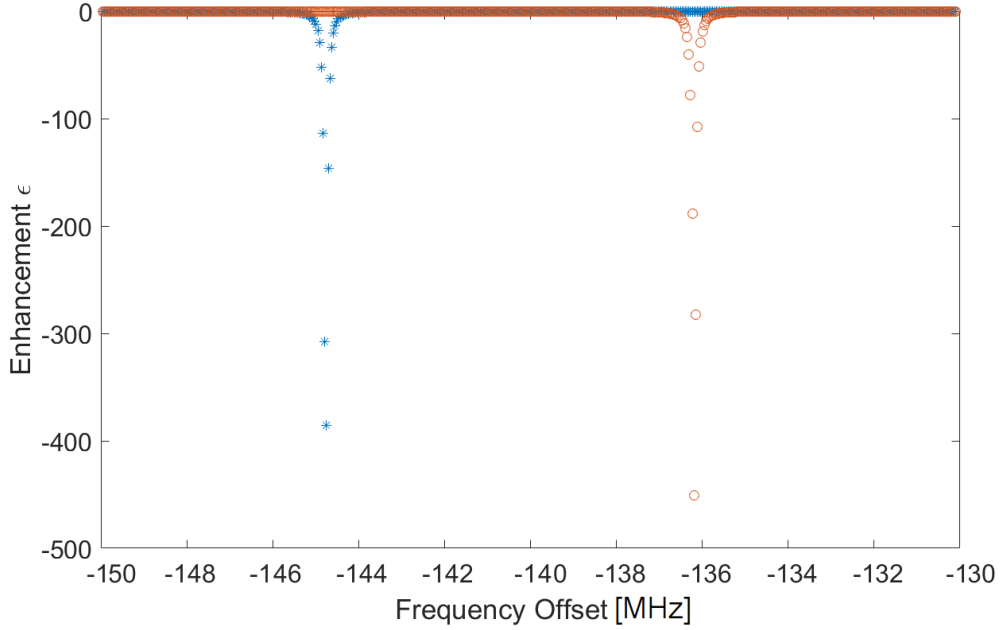


*Figure 6.14:* Simulated DNP spectra of the four spin system  $^1\text{H} - ^{19}\text{F} - e_1 - e_2$  in the Solid Effect region with positive enhancement. Plotted on the y-axis are the  $^1\text{H}$  (blue crosses) and  $^{19}\text{F}$  (red circles) polarisations with respect to the electron polarisation at thermal equilibrium in a 3.4 T magnetic field at  $T = 1.8$  K. The parameters used to simulate the DNP spectra are:  $d_{HF} = 0$ ,  $D_{12} = 1.64$  MHz,  $A_{z,iH} = A_{z,iF} = 0$ ,  $A_{iH}^{\pm} = A_{iF}^{\pm} = 2.15$  MHz,  $T_{1e} = 200$  ms,  $T_{2e} = 500$   $\mu\text{s}$ ,  $T_{1H} = T_{1F} = 300$  s,  $T_{2H} = T_{2F} = 10$  ms.

tribution of hyperpolarisation is obtained. This result is presented in Figure 6.15, that shows the simulated DNP profile in the heteronuclear Cross Effect region at the left of the reference frequency.

Notice that the sign of the enhancements for the  $^{19}\text{F}$  heteronuclear Cross Effect is opposite to the sign for the  $^1\text{H}$  heteronuclear Cross Effect enhancement. It has also opposite sign compared to the  $^{19}\text{F}$  Solid Effect, while both  $^1\text{H}$  Solid Effect and heteronuclear Cross Effect have the same sign. These results are in agreement with the experimental observations of Section 6.2.

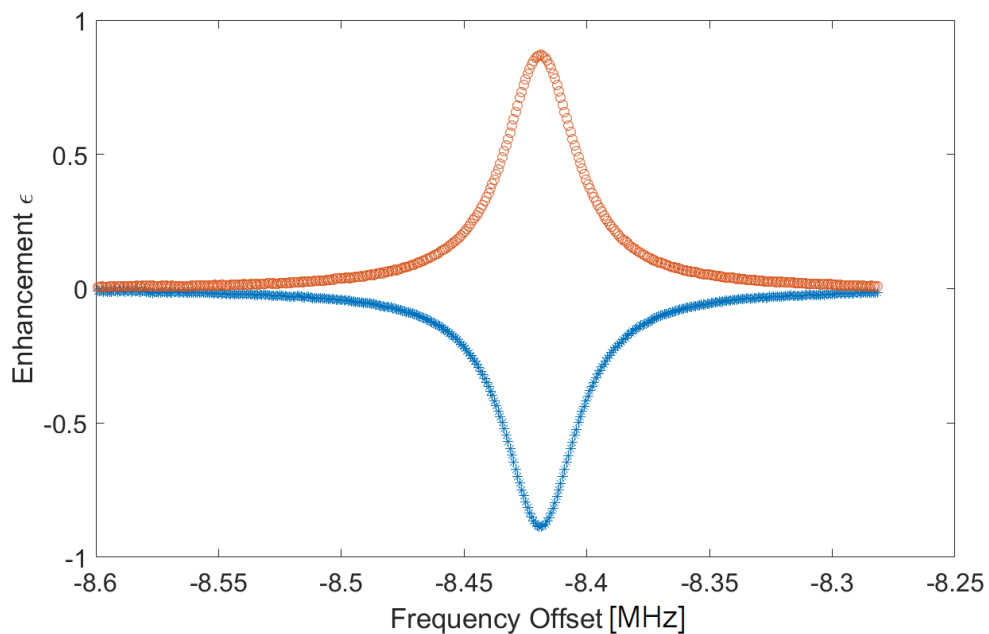


*Figure 6.15:* Simulated DNP spectra of the four spin system  $^1\text{H} - ^{19}\text{F} - e_1 - e_2$  in the heteronuclear Cross Effect region at the left of the reference frequency. Plotted on the y-axis are the  $^1\text{H}$  (blue crosses) and  $^{19}\text{F}$  (red circles) polarisations with respect to the electron polarisation at thermal equilibrium in a 3.4 T magnetic field at  $T = 1.8$  K. The parameters used to simulate the DNP spectra are the same of the ones listed in Figure 6.14.

In Figure 6.16 it is possible to notice how the uneven distribution of hyperpolarisation results from different hyperfine couplings. The stronger the coupling of the nuclei with the electrons, the lower the enhancement. This can be observed in the figure, where the  $^1\text{H}$  hyperfine coupling,  $\approx 13$  larger than the  $^{19}\text{F}$  hyperfine coupling, generate a  $^1\text{H}$  enhancement four times smaller than the  $^{19}\text{F}$  one.

Variation of both the electron dipolar interaction and  $^1\text{H}$  pseudosecular interac-

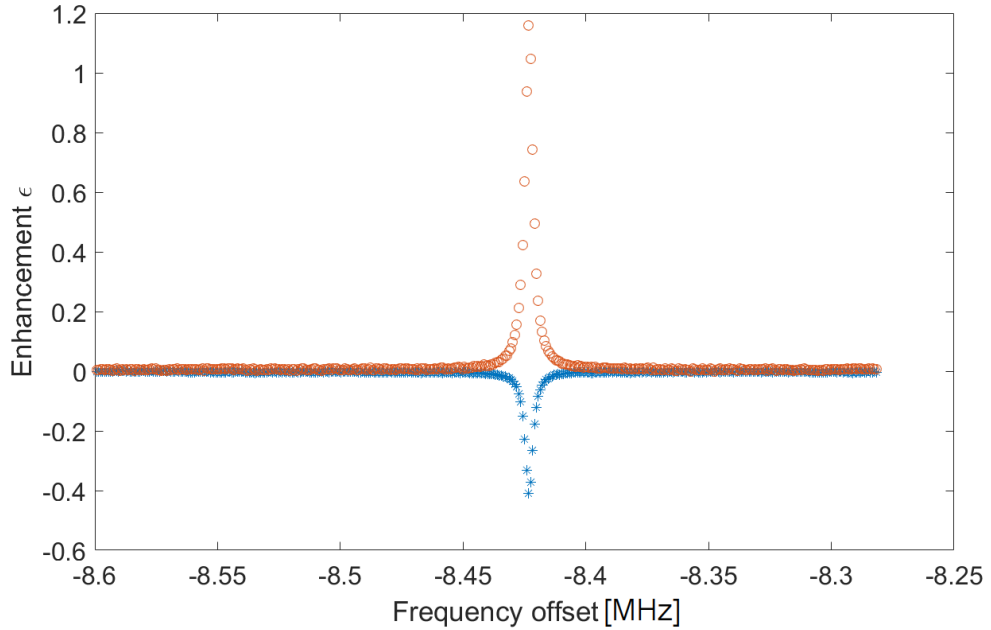


*Figure 6.16:* Simulated DNP spectra of the four spin system  $^1\text{H} - ^{19}\text{F} - e_1 - e_2$  in the heteronuclear Cross Effect region at the left of the reference frequency. Plotted on the y-axis are the  $^1\text{H}$  (blue crosses) and  $^{19}\text{F}$  (red circles) polarisations with respect to the electron polarisation at thermal equilibrium in a 3.4 T magnetic field at  $T = 1.8$  K. The parameters used to simulate the DNP spectra are:  $d_{HF} = 0$ ,  $D_{12} = 1.64$  MHz,  $A_{z,iH} = A_{z,iF} = 0$ ,  $A_{iH}^{\pm} = 2.15$  MHz,  $A_{iF}^{\pm} = 0.16$  MHz,  $T_{1e} = 200$  ms,  $T_{2e} = 500$   $\mu\text{s}$ ,  $T_{1H} = T_{1F} = 300$  s,  $T_{2H} = T_{2F} = 10$  ms.

tion (while keeping constant the  $^{19}\text{F}$  pseudosecular interaction) provides the 2D maps shown in Figures 6.17 (for  $^{19}\text{F}$  nuclei) and 6.18 (for  $^1\text{H}$  nuclei).

The numerical simulations shown in the figures present a scenario in which an asymmetry in heteronuclear Cross Effect can be seen, showing that the maximum enhancements for  $^1\text{H}$  and  $^{19}\text{F}$  can be achieved for different electron-electron dipolar interactions.

Another important results shown by the simulations is that the heteronuclear

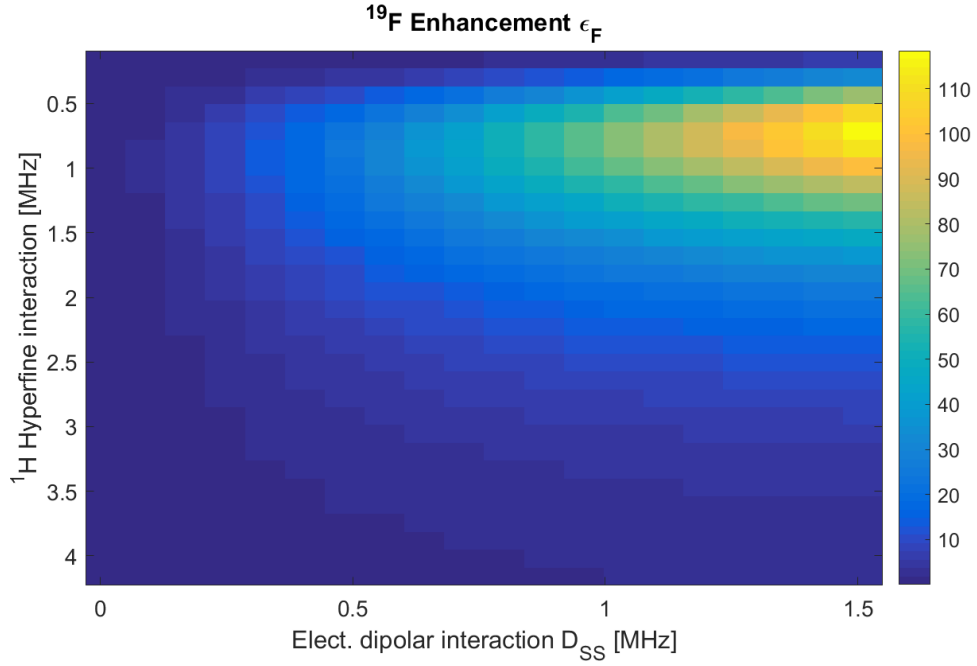


Figure 6.17: Maximum  $^{19}\text{F}$  enhancements shown in a colour map for different electron-electron dipolar interactions ( $D_{SS}$  in the figure) and  $^1\text{H}$  pseudosecular hyperfine interactions. In this simulation, the  $^{19}\text{F}$  pseudosecular hyperfine interaction is constant ( $A_{iF}^{\pm} = 0.16$  MHz).

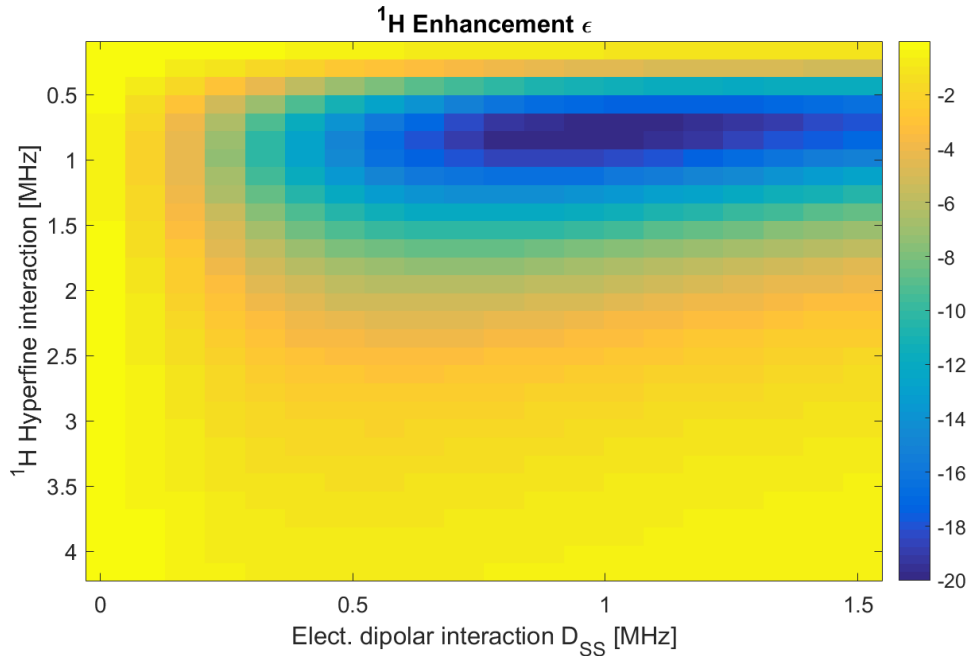
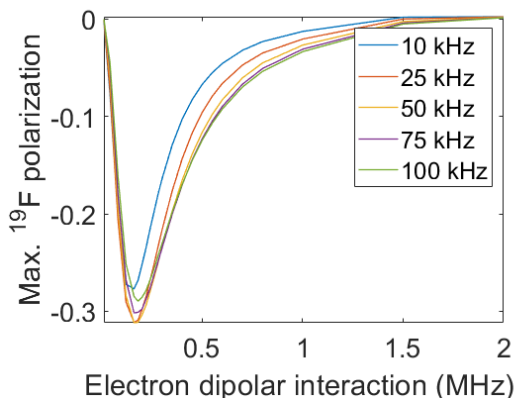


Figure 6.18: Maximum  $^1\text{H}$  enhancements shown in a colour map for different electron-electron dipolar interactions ( $D_{SS}$  in the figure) and  $^1\text{H}$  pseudosecular hyperfine interactions. In this simulation, the  $^{19}\text{F}$  pseudosecular hyperfine interaction is constant ( $A_{iF}^{\pm} = 0.16$  MHz).

Cross Effect takes place even if the two nuclei are only coupled to one of the two electrons. In this case, a value for the electron-electron dipolar coupling constant that provides the maximum  $^{19}\text{F}$  enhancement is found. For values lower than the optimal one, the heteronuclear Cross Effect does not operate efficiently. For higher values instead, the polarisation difference between the electrons becomes small and again the heteronuclear Cross Effect is not efficient (see Figure 6.19).

Finally, it is worth noting the differences in width of the enhancement profiles for



*Figure 6.19:* Maximal steady-state  $^{19}\text{F}$  polarisation depending on the electron dipolar coupling strength  $D_{12}$  for different microwave field strength  $\omega_1$ , set to the optimal frequency for the heteronuclear Cross Effect. For this simulations, the nuclei are coupled only to the first electron. Parameters for the simulations were  $A_{z,1F} = 3.0$  MHz,  $A_{z,1H} = 1.5$  MHz,  $A_{1H}^{\pm} = A_{1F}^{\pm} = 2.0$  MHz. Nuclear dipolar interaction  $d_{HF} = 5$  KHz.

the simulated data and the experimental results. This difference is due to the fact that the simulations consider a system made of only four spins, while the sample analysed during the experiments contains a large number of interacting nuclei and electrons.

## 6.4 Conclusions

In this Chapter, the cross-relaxation mechanism of samples containing the free radical BDPA is explored. The intensity of such effect has been calculated for samples with different BDPA concentrations, showing that the exchange rate increases as the free radical concentration increases. The build-up time constants for the  $^{19}\text{F}$  ensemble have been separated in two components, identified as the  $^{19}\text{F}$

intrinsic longitudinal relaxation time constants and the cross-relaxation rates. It was also confirmed the conclusion of Chapter 5, where it was hypothesised that the cross-relaxation process is mediated by more than one electron.

Experiments have also been performed while irradiating the samples with microwaves, to study the DNP mechanisms acting on the spin system. Alongside the Solid Effect, another DNP mechanism acting on both  $^1\text{H}$  and  $^{19}\text{F}$  has been observed. This mechanism has been identified as the predicted heteronuclear Cross Effect, and numerical simulations have been performed to validate this hypothesis.

Following the numerical simulations, it was demonstrated that it is possible to reproduce the experimental DNP profile for both  $^1\text{H}$  and  $^{19}\text{F}$  in presence of two coupled electrons, confirming that the observed effect is generated by the heteronuclear Cross Effect.

Moreover, it was shown that the difference in heteronuclear Cross Effect enhancements for the two nuclei is generated by different pseudosecular hyperfine interactions other than differences in longitudinal relaxation times of the two nuclei.

# Chapter 7

## Developing a methodology to study protein dynamics with $^{19}\text{F}$ NMR after dissolution DNP

NMR spectroscopy can be used as a powerful technique for investigating the structure of proteins and small molecules. However, one of its significant limitations is a relatively low sensitivity, requiring large amounts of studied material, which is why a big effort in the magnetic resonance community is directed towards solving this problem.

One approach for increasing NMR sensitivity is to use DNP to hyperpolarise nuclei by transferring polarisation from electron spins that, at cryogenic temperatures, have polarisation approaching unity. In their seminal work Ardenkjaer-Larsen et al. [1] demonstrated that after polarisation of nuclei at low temperatures the sample can be dissolved and signal measured in a conventional NMR spectrometer at room temperature. This approach led to a rapid development of such dissolution DNP systems primarily targeted towards studies of metabolites in living organisms, but also for studies of enzymatic and chemical reaction kinetics [110].

The dual iso-centre magnet, presented in Section 4.2, is a dissolution DNP system, featuring the shortest dead time of 300 ms between the dissolution and signal acquisition for NMR measurements. Such a short dead time opens an opportunity to explore fast kinetic processes such as ligand binding and protein folding.

The focus of this Chapter is to develop a methodology for studies of protein folding

kinetics using dissolution DNP.  $^{19}\text{F}$ -containing labels have previously been widely used for reporting on protein folding, due to the high gyromagnetic ratio of  $^{19}\text{F}$  and its high sensitivity to the chemical environment [62].

In the first section of this Chapter,  $^{19}\text{F}$ -labelled compounds will be tested at room temperature. These experiments are performed to check that  $^{19}\text{F}$  nuclei have a longitudinal relaxation time constant that is longer than the dead time of the dual iso-centre magnet, proving that  $^{19}\text{F}$  is suitable for dissolution experiment with the dual iso-centre magnet.

Later in this Chapter, solid state experiments in the polarising top magnet of the dual iso-centre system are discussed. Such experiments are performed on simple fluorinated molecules, and optimal DNP conditions are studied to obtain the maximum  $^{19}\text{F}$  polarisation achievable through DNP. At this stage, the DNP hyperpolarisation is studied as a function of the microwave frequency and power.

Dissolution DNP experiments are performed on simple  $^{19}\text{F}$ -containing chemicals and finally, as a proof-of-principle, a dissolution DNP experiment is performed on sample containing a fluorinated protein.

## 7.1 Feasibility of $^{19}\text{F}$ dissolution DNP

In Chapter 5 it was already shown that is possible to hyperpolarise  $^{19}\text{F}$  in simple molecules by means of DNP. In the stand-alone “polariser” magnet, DNP provided a high degree of enhancement, with a maximum  $\approx 40\%$  overall polarisation of  $^{19}\text{F}$  achieved in solid state. In the next section, experiments to obtain  $T_1$  time constants at room temperature of different fluorinated chemicals are discussed, to show that the longitudinal relaxation time constant is longer than the dead time of the dual iso-centre magnet.

### 7.1.1 $T_1$ for different fluorinated chemicals

Dissolution DNP produces large non-equilibrium nuclear polarisation. However, in order to carry out high sensitivity measurements, the hyperpolarisation produced at low temperature needs to be retained as much as possible during the dissolution step and the transfer to the high resolution NMR magnet. This pro-

cess usually takes place in few seconds [111,112], but only required 300 ms in the dual iso-centre magnet system.

Room temperature measurements of longitudinal relaxation times of small molecule  $^{19}\text{F}$ -containing compounds at a static magnetic field of 9.4 T are carried out. The small molecule compounds here studied serve as models for amino acids residues in proteins that are described later in this Chapter. Overall, these measurements help to establish the feasibility and limits of dissolution DNP measurements for fluorinated compounds.

The magnet used for room temperature experiments is an Oxford Instruments magnet with a static magnetic field of 9.4 T (corresponding to a  $^1\text{H}$  Larmor frequency of 400 MHz and a  $^{19}\text{F}$  Larmor frequency of 376 MHz) linked to a Bruker Avance 400 console. Due to the small difference in Larmor frequencies, a commercial  $^1\text{H}$  NMR probe (Bruker MIC 400MHz W4/S6 DIFF/30) has been re-tuned to match the  $^{19}\text{F}$  frequency.

## Samples

Since fluorinated proteins do not naturally occur, a fluorination process is needed in order to add  $^{19}\text{F}$  labels to the protein to be studied. For the study of a fluorinated protein, fluorinated analogues of aromatic amino acids are used, such as phenylalanine, tryptophane and tyrosine [5]. For this reason, aromatic compounds such as monofluorobenzene, hexafluorobenzene and fluoro-phenylalanine are used as a simplified version of the aforementioned amino acids. Another approach to labelling is a use of a fluorinated methyl group, attached to SH,  $\text{NH}_2$  or OH groups, a simple model of which is trifluoroacetic acid (TFA).

Both organic and inorganic solvents have been used. Water ( $\text{H}_2\text{O}$ ) and deuterium oxide ( $\text{D}_2\text{O}$ ) have been employed to investigate the effect of deuteration on the relaxation times. Benzene ( $\text{C}_6\text{H}_6$ ) and toluene ( $\text{C}_6\text{H}_5\text{CH}_3$ ) have been used for organic molecules such as monofluorobenzene ( $\text{C}_6\text{H}_5\text{F}$ ) and hexafluorobenzene ( $\text{C}_6\text{F}_6$ ). Table 7.1 shows the analysed chemicals and their concentrations in different solvents.

## Background removal

Before performing room temperature  $^{19}\text{F}$  experiments, a technique has been developed in order to remove the  $^{19}\text{F}$  background observed after many scans. The solid structure of the probe is in fact made of a polymeric material, designed for  $^1\text{H}$  acquisition. As a consequence, fluorinated materials are commonly employed since the probe is originally designed to acquire  $^1\text{H}$  NMR signals. This plastic, that sits close to the NMR coil, provides a  $^{19}\text{F}$  background signal with very broad linewidth compared to the liquid state  $^{19}\text{F}$  signals. The line broadening of the signal arising from the plastic is around 2 kHz, and becomes visible after the signal is averaged many times. For samples where  $^{19}\text{F}$  nuclei are present in low concentration, the signal arising from probehead material dominates the NMR signal from the sample. Figure 7.1 shows in blue the spectrum acquired signal averaging 216 times for a sample containing 2 mM TFA in water.

As the figure shows, the TFA signal, visible at  $\approx 77$  ppm in the spectrum, sits on top of the tail of the large background signal that dominates the spectrum. In order to remove the background signal, the processed spectrum has been divided in two different regions. The first region contains the peak of TFA, while the second is composed of the rest of the spectrum. The latter is fitted with a 9th degree polynomial function, and the obtained function is subtracted from the initial spectrum. Figure 7.1 shows in red the spectrum after the background subtraction.

## Measurement of the longitudinal relaxation time constant

After the flip angle calibration, longitudinal relaxation rates of  $^{19}\text{F}$  were obtained in inversion-recovery experiments [113].

In order to get  $T_1$  from each experiment, integrals of the NMR signals were fitted with the function:

$$I(t) = A(1 - 2e^{-Bt}) + C, \quad (7.1)$$

where the rate  $B$ , is the inverse of the relaxation time constant  $T_1$ ,  $A$  is the thermal polarisation, and  $C$  is a constant which takes into account the residual magnetisation of the sample.

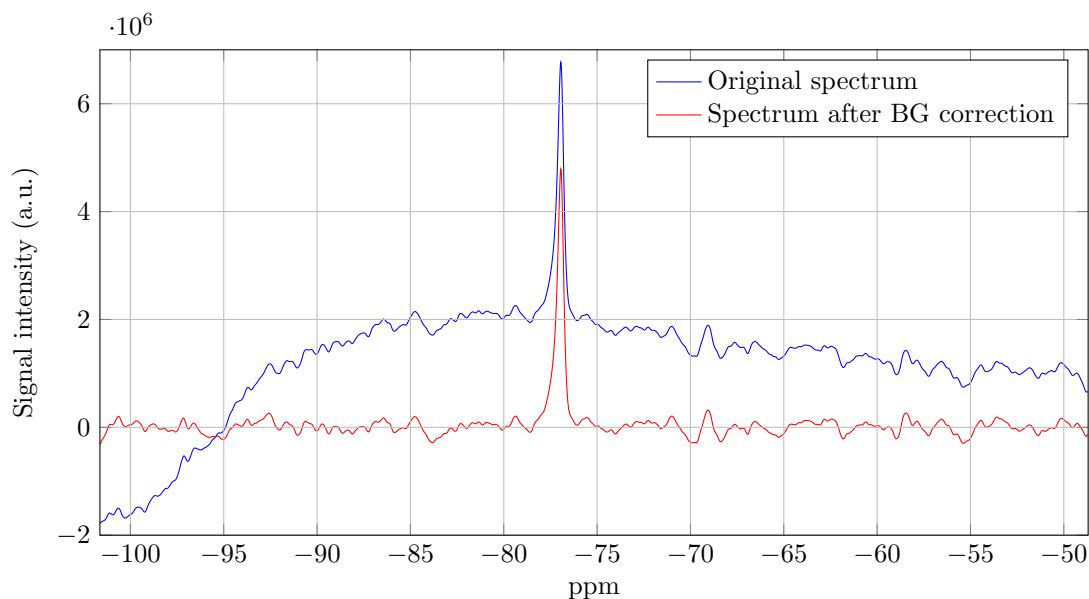


Figure 7.1:  $^{19}\text{F}$  spectrum of 2 mM TFA in water before (blue) and after (red) background removal. Signals averaged 216 times have been acquired in a 9.4 T magnet at room temperature.

Table 7.1 summarises the  $T_1$ 's measured for various compounds. It is important to point out that when the deuterated version of a solvent was used at equal chemical concentration (e.g. TFA in  $\text{H}_2\text{O}$  and  $\text{D}_2\text{O}$ ), the relaxation time of the fluorinated chemical in the deuterated sample was longer than the non-deuterated one. This is confirmed by the theory of relaxation discussed in Chapter 2 for dipolar interactions. By replacing  $^1\text{H}$  nuclei with  $^2\text{H}$ , the contribution of the dipole-dipole interaction to the longitudinal relaxation time decreases, since it is inversely proportional to the square of the product of the gyromagnetic ratios of the nuclei taken into account [114]. Since the  $^2\text{H}$  gyromagnetic ratio is 6 times less than the  $^1\text{H}$  one, the contribution of the dipole-dipole interaction causes  $T_1$  in the deuterated solvent to be larger than the value it assumes in the non-deuterated solvent.

Results range between 2 and 12 seconds, where the largest  $T_1$  values correspond to monofluorobenzene. Also, these values are greater than the typical dead times of many dissolution DNP setups, when the sample is warmed up and transferred to the NMR magnet. This proves that  $T_1$  times of  $^{19}\text{F}$ -containing chemicals are long enough for a dissolution DNP experiment, and that a significant amount of  $^{19}\text{F}$  hyperpolarisation can be retained until the NMR signal is acquired.

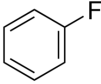
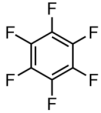
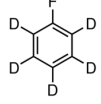
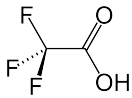
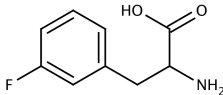
Chemical	Structure	Solvent	Concentration	$T_1$ (s)
Monofluorobenzene		H <sub>2</sub> O	18 mM	$8.0 \pm 1.8$
		D <sub>2</sub> O	18 mM	$11 \pm 2$
		Toluene	18 mM	$12 \pm 2$
		Benzene	18 mM	$5.2 \pm 1.2$
Hexafluorobenzene		D <sub>2</sub> O	13 mM	$2.85 \pm 0.07$
		Benzene	400 mM	$2.85 \pm 0.02$
Fluorobenzene-d <sub>5</sub>		H <sub>2</sub> O	16 mM	$7.1 \pm 0.3$
		D <sub>2</sub> O	16 mM	$11.2 \pm 0.7$
TFA		H <sub>2</sub> O	1 M	$2.57 \pm 0.04$
		D <sub>2</sub> O	1 M	$3.01 \pm 0.02$
<i>m</i> -fluoro-phenylalanine		H <sub>2</sub> O	50 mM	$2.10 \pm 0.06$
		D <sub>2</sub> O	50 mM	$2.46 \pm 0.11$

Table 7.1:  $T_1$  values for the fluorinated samples in different solvent.

### 7.1.2 $T_1$ for samples with different free radical concentration in liquid state

The nuclear longitudinal relaxation time constant strongly depends on the presence of free radicals in the sample. As discussed in Section 2.4, according to the paramagnetic relaxation theory, the higher the electronic concentration, the shorter the relaxation times are. Paramagnetic relaxation time is proportional to the sixth power of the inverse of the distance between the electron and nuclear spins.

In Chapter 3, it was explained why, in order to hyperpolarise the fluorinated protein, a sample containing free radicals is needed. In a typical DNP sample, up to 40 mM of free radical are used. However, the limiting factor during a dissolution experiment is the  $T_1$  of the nuclei in liquid state. During a dissolution experiment, the concentrated sample is melted by a hot solvent. Knowing the average dissolution factor after the dissolution process takes place, it is possible to estimate the concentration of free radicals in the final sample.

The final sample volume is  $\approx 800 \mu\text{L}$ , while the starting volume is  $20 \mu\text{L}$ . These

values correspond to a dissolution factor of  $\approx 30$ . The final sample therefore contain only 1/40 of the initial free radical concentration. According to this factor, a sample that in solid state contains 40 mM free radical ends up having 1 mM of free radical after dissolution.

In order to make sure that the hyperpolarisation is preserved in the liquid state sample after dissolution, the  $^{19}\text{F}$  longitudinal relaxation time constants for different samples containing up to 5 mM free radical have been measured.

Experiments have been performed to determine the longitudinal relaxation time constants through an inversion recovery pulse sequence. 2 mM TFA in water solution was analysed, by using free radicals in the form of 1, 2.5 and 5 mM TEMPOL. Considering the dissolution factor, these concentration correspond to 40, 100 and 200 mM before dissolution. Table 7.2 shows the measured  $T_1$  for the sample with TFA.

The results for TFA from the table show that, as expected, by increasing the con-

TFA	
[TEMPOL] (mM)	$T_1$ (s)
0	$2.5 \pm 0.4$
1	$2.1 \pm 0.4$
2.5	$1.12 \pm 0.15$
5	$0.9 \pm 0.2$

*Table 7.2:* Values for  $^{19}\text{F}$   $T_1$  for 2 mM TFA in  $\text{H}_2\text{O}$  for different TEMPOL concentrations.

centration of free radicals in the sample, the longitudinal relaxation time constant becomes shorter. However, below 2.5 mM, such time constants are longer than the dissolution dead time. This information will therefore be taken into account for the sample preparation for the dissolution sample.

### 7.1.3 Solid state DNP experiments

A sample cup with the saddle coil described in Section 4.2.3 has been used to perform solid state experiments on the sample, to find the microwave power and frequency that provide the best DNP enhancement. 100  $\mu\text{L}$  of 60% DMSO- $\text{d}_6$ , 30%  $\text{D}_2\text{O}$ , 10%  $\text{H}_2\text{O}$  with 100 mM TFA and 70 mM TEMPOL free radical have

been used.

### Microwave bench alignment

As shown in Section 4.2, the microwave source is not directly connected to the waveguide, to allow the latter to slide up or down into the cryostat. The microwave bench can therefore be moved on top of the waveguide once the waveguide is in position inside the magnet. It is therefore necessary to align the bench to the waveguide, to make sure that microwaves are transmitted to the sample cup with the least possible loss. Fine micro gauges allow to move the bench and measure its position in the directions perpendicular to the waveguide and to measure the displacement. A zero-biased detector is placed on top of the waveguide, aligned with its centre. The microwave alignment is performed by measuring the output of the zero-biased detector as function of the bench position, while the microwave source is turned on. Figures 7.2 and 7.3 show the voltage read by the detector while moving the bench in the two perpendicular directions “x” and “y”. The figures

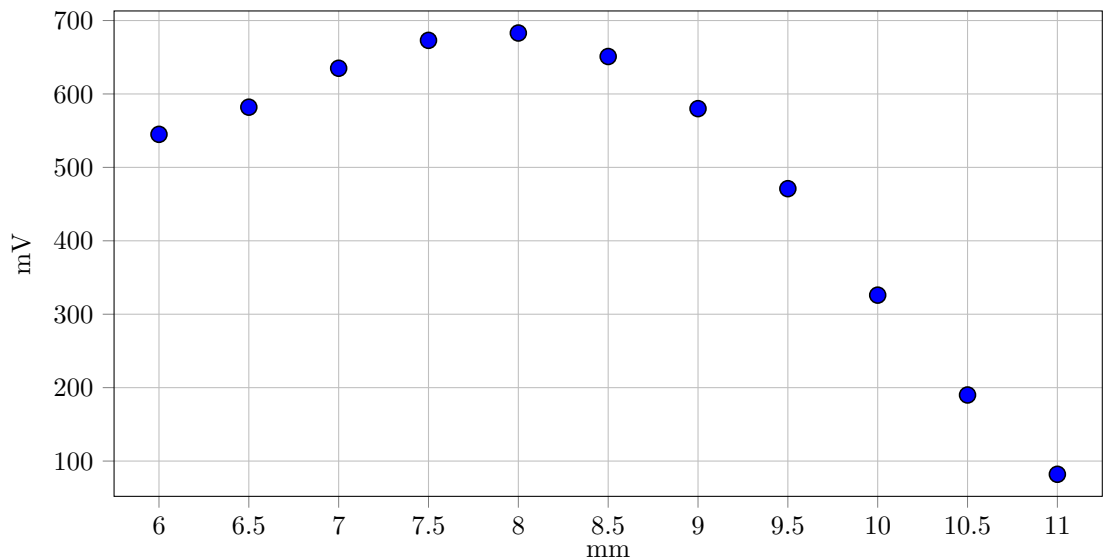


*Figure 7.2:* Allignment curve of the microwave bench in the “x” direction. The voltage is read in the voltmeter connected to the zero-biased detector as the microwave bench is moved along the “x” direction. The maximum voltage, proportional to the microwave intensity, is transmitted to the sample cup when the microwave bench is displaced 8 mm from its “zero” position in the “x” direction.

show that there is a well defined position in which there is a maximum microwave transmission to the waveguide. Moreover, as will be explained in section 7.1.3,

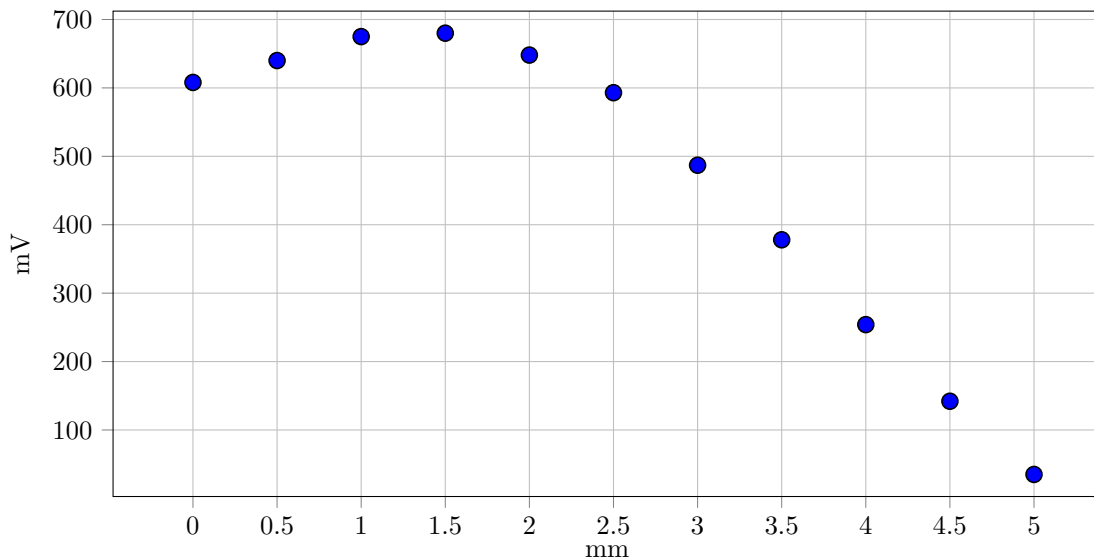


*Figure 7.3:* Allignment curve of the microwave bench in the “y” direction. The voltage is read in the voltmeter connected to the zero-biased detector as the microwave bench is moved along the “y” direction. The maximum voltage, proportional to the microwave intensity, is transmitted to the sample cup when the microwave bench is displaced 1.5 mm from its “zero” position in the “y” direction.

where solid state measurement are performed, a displacement of the microwave bench of a few millimetres around the optimal value does not change the DNP optimisation process.

### **DNP profile and DNP build-up time determination**

A coaxial cable, running along the waveguide, connects the saddle coil surrounding the sample cup, to the preamplifier unit.

To determine the microwave parameters that achieve the best DNP enhancement, experiments have been performed at 1.7 K in the top magnet of the dual iso-centre. The cool-down procedure is the one described in Section 4.2. DNP profile experiments have been collected for four different microwave powers. Figure 7.4 shows the results of the experiments. For each point,  $^{19}\text{F}$  magnetisation was saturated before letting the hyperpolarisation build-up for 30 s. These experiments clearly show that the microwave frequency corresponding to the maximum enhancement, which is the same for all the analysed microwave powers, is  $\nu_{MW} = 93.85$  GHz.

To confirm the results obtained in section 7.1.3, where the microwave bench was aligned with the waveguide, a control experiment was performed, measuring the

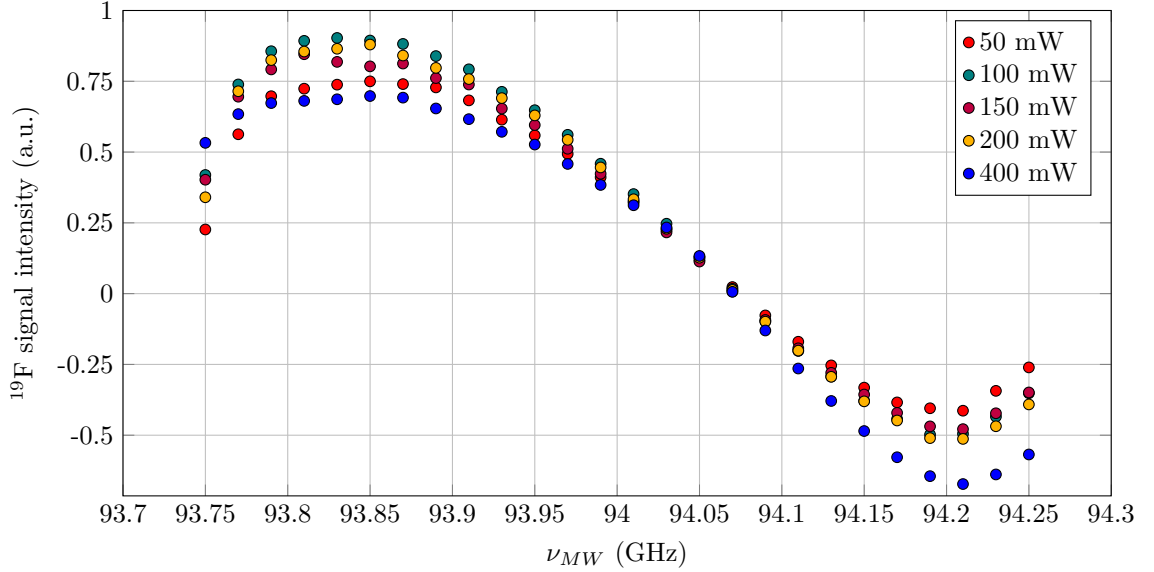


Figure 7.4: DNP enhancement profile of  $^{19}\text{F}$  as a function of microwave frequency after microwave irradiation at five different microwave powers, ranging from 50 mW to 400 mW output power for the microwave source.  $^{19}\text{F}$  polarisation period is  $T_{MW} = 30$  s. The shape of the DNP profile shows that the Cross Effect is one of the main DNP mechanisms contributing to the hyperpolarisation of  $^{19}\text{F}$  in the sample.

DNP enhancement at different positions of the microwave bench. The enhanced signals were acquired by using a pulse sequence in which the magnetisation was initially saturated, and then the FID was acquired after a 20 s delay during which the sample was hyperpolarised. Results showed that the intensity of the enhanced NMR signal is the same, independent of the bench position, provided the bench was displaced less than 3 mm from the position optimised in section 7.1.3.

Saturation recovery experiments were performed during microwave irradiation at different microwave powers to determine the DNP build-up time. The microwave irradiation frequency was set to the previously obtained value of 93.85 GHz. Figure 7.5 shows the experimental build-up curves, fitted with the function:

$$I(t) = I_{\text{DNP}} \left( 1 - \exp \left\{ -\frac{t}{\tau_{\text{DNP}}} \right\} \right). \quad (7.2)$$

Since it is not possible to acquire the thermal signal at low temperature, the integral values represent relative enhancements. Therefore, these values do not provide information on the absolute polarisation level achieved during the exper-

iments. The difficulty in measuring the thermal signal is linked to the fact that the thermal signal is invisible with a single scan. Many scans therefore need to be averaged for its acquisition, and for each of them a long recovery time would be needed. Table 7.3 summarises the parameters obtained by the fitting of the data. As the table shows, all the build-up times are of the same order of magnitude, and the largest enhancement corresponds to the experiment where a microwave power of  $P = 200 \text{ mW}$  was used. The hyperpolarisation of the samples for dissolution experiments will therefore be performed by using this power level.

Previous studies [64, 115] showed the relation between enhancement and mi-

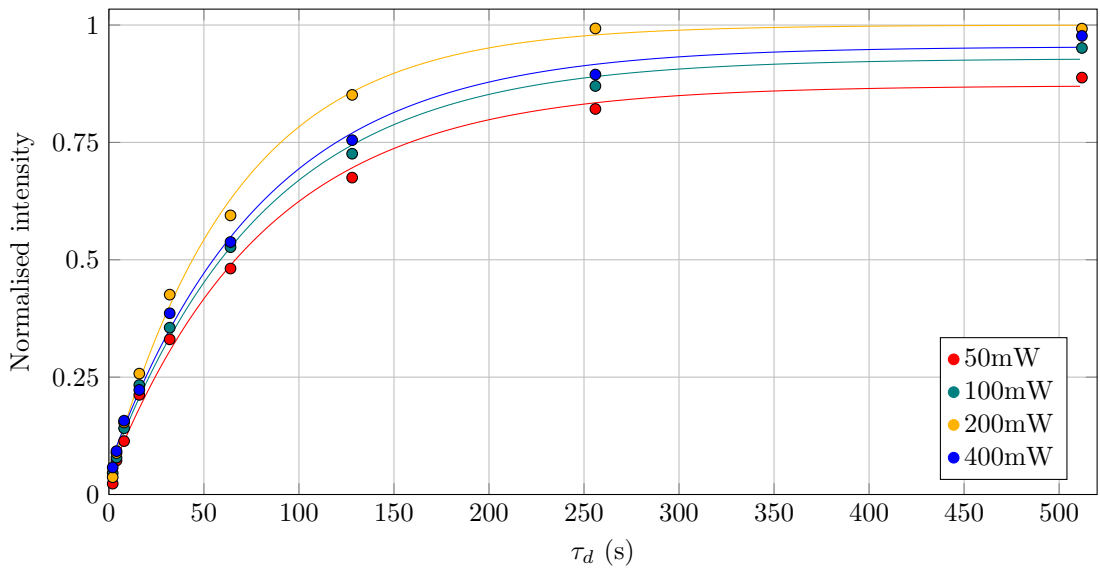


Figure 7.5:  $^{19}\text{F}$  DNP build-up experiment while irradiating the sample with microwaves at  $\nu_{MW} = 93.85\text{GHz}$  at four different powers. The intensities have been normalised to the value corresponding to the plateau of the data acquired when the used microwave power is 200 mW.

MW power	$\tau_{\text{DNP}}$ (s)	Normalised Intensity
50 mW	$82 \pm 7$	$0.87 \pm 0.03$
100 mW	$82 \pm 6$	$0.91 \pm 0.02$
200 mW	$67 \pm 4$	$1.00 \pm 0.02$
400 mW	$81 \pm 6$	$0.93 \pm 0.03$

Table 7.3: Results for build-up time constants and normalised intensities obtained by means of the saturation recovery experiment shown in Figure 7.5.

crowave power for the Cross Effect. They showed that the enhancement should

increase by increasing the microwave power, according to the equation

$$\frac{1}{\epsilon} = \frac{1}{\epsilon_{\infty}} \left( 1 + \frac{1}{aP_{\text{MW}}} \right), \quad (7.3)$$

where  $\epsilon_{\infty}$  is the enhancement with infinite microwave power and  $a$  is the saturation parameter.

However, the results obtained from the experiments above described show that the largest enhancement is achieved using 200 mW, a microwave power lower than the maximum available at the source. This is due to an increase in temperature of the sample for high microwave power. This corresponds to a decrease of electron polarisation, and hence of the polarisation transferred to the nuclei.

#### 7.1.4 Dissolution

Dissolution experiments have been performed on the samples shown in Table 7.4. Note that Samples C and D are taken from the same batch, to test the consistency

	Sample composition	Free radical
Sample A	60% DMSO-d <sub>6</sub> , 30% D <sub>2</sub> O, 10% H <sub>2</sub> O, 100 mM TFA	100 mM TEMPOL
Sample B	60% DMSO-d <sub>6</sub> , 30% D <sub>2</sub> O, 10% H <sub>2</sub> O, 100 mM TFA	70 mM TEMPOL
Sample C	60% DMSO-d <sub>6</sub> , 30% D <sub>2</sub> O, 10% H <sub>2</sub> O, 100 mM TFA	40 mM TEMPOL
Sample D	60% DMSO-d <sub>6</sub> , 30% D <sub>2</sub> O, 10% H <sub>2</sub> O, 100 mM TFA	40 mM TEMPOL

*Table 7.4:* Fluorinated samples used to test dissolution DNP.

of the experiment on the same sample. 20  $\mu$ L of each sample were used in the dissolution sample cup that was described in Section 4.2.3. Each of the samples was polarised at 1.7 K for  $\approx$  60 min. This time, much longer than  $5 \times \tau_{\text{DNP}}$ , was chosen to allow the sample to reach the base temperature. The hyperpolarisation is achieved by irradiating the sample with microwaves at frequency and power corresponding to the maximum enhancement obtained in the previous section.

For the dissolution, the waveguide is quickly shuttled to the bottom of the cryostat, between the two magnets, while the cryostat is filled with helium gas to increase the pressure. The high pressure in the cryostat is needed so that the hot solvent is not driven into the cryostat by the pressure difference. When the waveguide reaches the bottom of the cryostat, the sample cup sits in the dock, where

the magnetic field is 0.4 T. This non-zero magnetic field ensures that the hyperpolarised  $^{19}\text{F}$  nuclei retain their polarisation, instead of losing it due to the low field mixing. Water, preheated to  $100^\circ\text{C}$ , is injected into the sample cup, where it melts the sample and mixes with it. The new mixture of dissolved sample and solvent is driven into a NMR tube, sitting in a high resolution NMR probe in the iso-centre of the 9.4 T magnet. The NMR acquisition is triggered  $\approx 400$  ms after the sample reaches the NMR tube. The FID is induced by a  $\pi/2$  flip angle pulse, and then the signal is acquired.

After Fourier transformation, the integrals of the resonance lines were determined. The thermal signals of each dissolution sample have also been acquired, by averaging the signal of many scans, to achieve a signal-to-noise ratios comparable with the one of the enhanced spectra after the dissolution. Table 7.5 shows the enhancements obtained for the four studied samples, calculated as

$$\epsilon = \frac{I_{\text{DNP}} \cdot NS}{I_{\text{thermal}}}, \quad (7.4)$$

where  $I_{\text{DNP}}$  and  $I_{\text{thermal}}$  are the integrals of the dissolution DNP enhanced spectrum and the thermal spectrum respectively, while  $NS$  is the number of averages acquired for the thermal signal.

Figure 7.6 shows the enhanced and thermal signal acquired for Sample C, that

	$\epsilon$	NS
Sample A (100 mM)	150	592
Sample B (70 mM)	290	544
Sample C (40 mM)	780	424
Sample D (40 mM)	750	344

*Table 7.5:* Enhancement factors achieved for the samples of Table 7.4. The number of averaged signals NS acquired for each thermal acquisition is also shown in the table.

presents the highest enhancement. The largest enhancement is achieved for the samples C and D, containing 40 mM TEMPOL. The two samples present the same degree of enhancement, indicating that the dissolution process worked reliably for the experiments.

The enhancement decrease drastically by increasing the TEMPOL concentration.

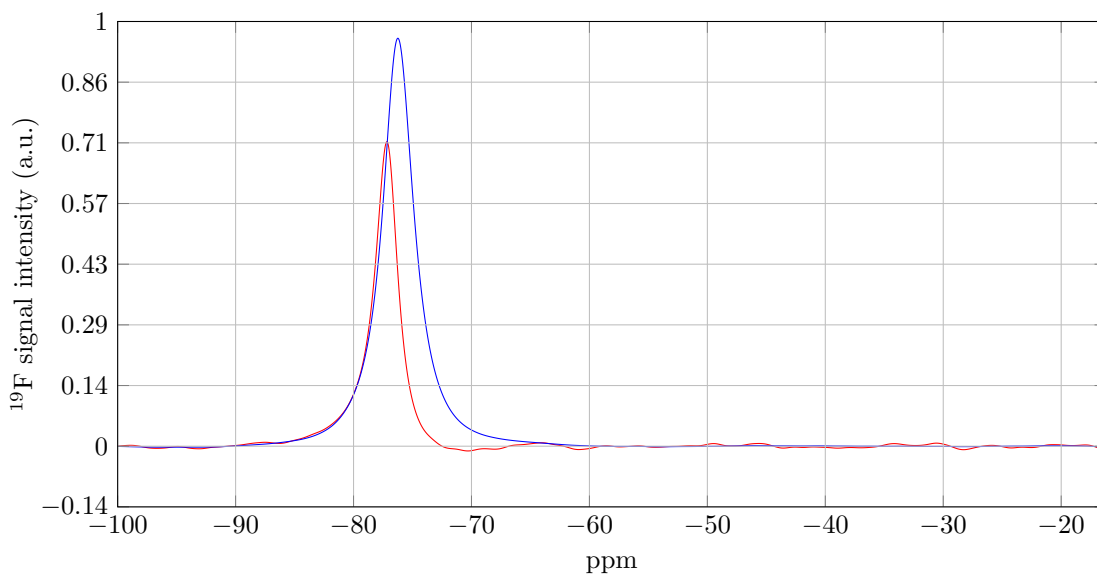


*Figure 7.6:* Single scan DNP enhanced  $^{19}\text{F}$  spectrum (blue) compared with the thermal spectrum (red) acquired after averaging 424 scans.

This fact is linked to the  $^{19}\text{F}$  longitudinal relaxation time constant in the presence of paramagnetic centres. As shown previously in Table 7.2,  $^{19}\text{F}$   $T_1$  decreases by increasing the free radical concentration. With 100 mM TEMPOL in the initial sample, and a dissolution factor of 40, the concentration of TEMPOL in the final sample is 2.5 mM, with a corresponding  $T_1$  of  $\approx 1$  s. On the other hand, by using 40 mM TEMPOL in the initial sample, its concentration after the dissolution process becomes 1 mM, and its  $T_1$  time constant is  $\approx 2$  s.

The line-width of the signal is broad, of  $\approx 50$  Hz for the dissolution DNP enhanced spectra. This line broadening results from the presence of micro bubbles in the sample after the injection in the NMR tube. Bubbles, as discussed in Section 4.2.5, disappear from the sample after  $\approx 1$  s, and the line width decreases drastically. However, while this additional delay would not affect the measurement of other DNP enhanced nuclei with long  $T_1$  like  $^{13}\text{C}$ , it is significantly deleterious for  $^{19}\text{F}$ . After 1 s  $^{19}\text{F}$  would in fact lose most of its hyperpolarisation due to its short  $T_1$ . For the purposes of this work, it has been chosen to sacrifice the resolution of the spectra in favour of the increased signal-to-noise ratio due to the larger hyperpolarisation.

## 7.2 Hen egg-white Lysozyme

After confirmation that a large dissolution DNP enhancement can be reached for  $^{19}\text{F}$  nuclei, efforts were directed to the development of a new methodology to study the dynamics of a fluorinated protein. The study of a fluorinated protein has been already proven to be worthy [116]. Lysozyme has been chosen as a benchmark for it is a widely studied protein. Lysozyme can be extracted from hen egg-white, and it is easily available commercially. According to the literature [117], lysozyme folding takes place in a time scale of few seconds, about the same as  $^{19}\text{F}$   $T_1$  in TFA.

By using the dual iso-centre magnet, it is therefore in principle possible to perform a fast dissolution DNP experiment, in which  $^{19}\text{F}$  nuclei attached to the protein are hyperpolarised. The dissolved sample can hence be analysed in the high resolution NMR magnet just 400 ms after the dissolution. Lysozyme temperature stability at high temperature has been shown by Venkataramani et al. [118].

### 7.2.1 $^{19}\text{F}$ labelling of lysozyme

Lysozyme from hen egg-white has 129 amino acid residues, that have been fully assigned by using a variety of different techniques [119]. Its molecular mass is of the order of 20 kDa, and it contains six lysine residues. Adriaensen et al. [120] successfully labelled the lysine residues in this protein with  $^{19}\text{F}$  labelled groups. They used S-ethyl trifluorothioacetate, since it labels each lysine with a fluorinated methyl group. To each of these groups, three equivalent  $^{19}\text{F}$  atoms are attached, therefore they provide a higher signal-to-noise ratio per residue compared to amino acids, where a single  $^{19}\text{F}$  atom is attached.

The trifluoroacetylation of the six lysine amino acid residues has been performed following the methodology discussed in Adriaensen's work. In this process, S-Ethyltrifluorothio-acetate was added to a lysozyme solution in  $\text{H}_2\text{O}$ , while the pH was maintained at 9.5-10 by addition of NaOH. After the base consumption ceased, the mixture was brought to pH 7 by using HCl, dialyzed and centrifuged. The pellet was dialyzed against water and freeze-dried. The freeze dried supernatant was then fractionated on a chromatography column, where different

fractions of labelled lysozyme were extracted and dialyzed. Each fraction was rechromatographed on the same column and eluted with the same gradient.

The labelled lysozyme is therefore studied in buffer solution in a high resolution NMR magnet. 0.3 mM of  $^{19}\text{F}$  labelled protein were dissolved in a pH 8.5 buffer. Figure 7.7 shows a labelled lysozyme spectrum, acquired after signal averaging 512 times. The spectrum shows six different resonances, corresponding to each trifluoroacetylated lysine residue. The spectrum has been fitted with six Lorentzian functions, all having the same linewidth. On the other hand, the intensities of each Lorentzian are left as free parameters during the fit, and they assume values different from each other. This is due to an uneven labelling of the lysine residues, since some of them are easier to label than others. Results of the fit are also shown in the figure.

The NMR spectral lines assignment was done according to the results shown in

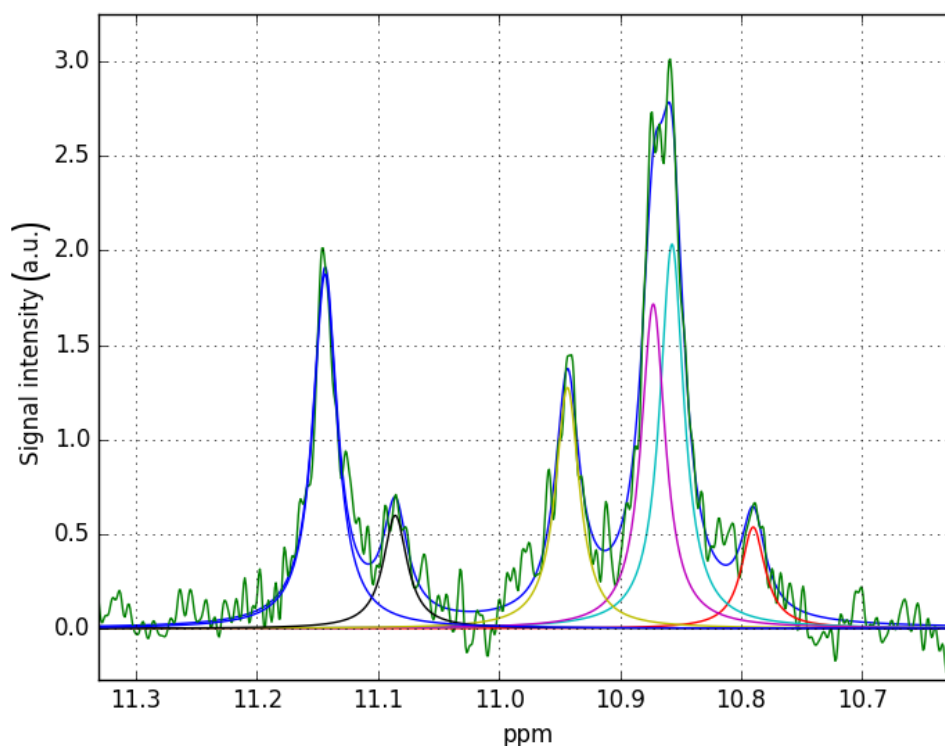


*Figure 7.7:*  $^{19}\text{F}$  NMR spectrum of the labelled lysozyme 0.3 mM acquired after signal averaging 512 times measured at 9.4 T. Six Lorentzian functions have been used to fit the data.

Adriaansen's work. Table 7.6 shows the amino acid residues corresponding to each

peak.

$^{19}\text{F}$   $T_1$  time constants were obtained by means of an inversion recovery experi-

Colour	Amino acid	Intensity	$T_1$ s
Blue	Lys-96	4	$0.91 \pm 0.04$
Black	Lys-13	1	$0.89 \pm 0.10$
Yellow	Lys-1	3	$0.98 \pm 0.04$
Purple	Lys-33	3.5	$1.03 \pm 0.14$
Light blue	Lys-11	4	$0.94 \pm 0.07$
Red	Lys-96	1	$1.18 \pm 0.17$

*Table 7.6:* Assignment of the labelled lysine amino acids performed according to Adriaensen's work. The colour scheme matches the fitting functions shown in Figure 7.7. The relative intensities and the  $T_1$  values are also shown for each peak.

ment. For each spectrum, the signal was averaged 2048 times. Background subtraction has been performed in order to remove the baseline generated by the  $^{19}\text{F}$  contained in the plastic close to the NMR coil. Moreover, longitudinal relaxation time constants were obtained for the same protein when 1 and 2 mM TEMPOL were added in the sample, to study the effect of free radicals on the  $^{19}\text{F}$   $T_1$  of the labelled lysozyme. These measurements are needed for the sample preparation of the dissolution DNP experiment. It is in fact important to take into account the lifetime of  $^{19}\text{F}$  polarisation after it undergoes the dissolution procedure. A too short  $T_1$  would in fact result in a loss of hyperpolarisation before the NMR acquisition. Figure 7.8 shows the results of the inversion recovery experiments for the aforementioned samples.

Results for  $T_1$  are shown in Table 7.7. In the concentration column, the numbers in parentheses represent the concentration of TEMPOL before the dissolution, assuming a dissolution factor of 40.

TEMPOL concentration	$T_1$
0 mM (0 mM)	$1.26 \pm 0.05$ s
1 mM (40 mM)	$0.94 \pm 0.04$ s
2 mM (80 mM)	$0.69 \pm 0.02$ s

*Table 7.7:* Values for  $^{19}\text{F}$   $T_1$  for the labelled protein obtained by an inversion recovery experiment shown in Figure 7.8. Next to the TEMPOL concentrations, in brackets, the free radical concentrations before dissolution are also shown.

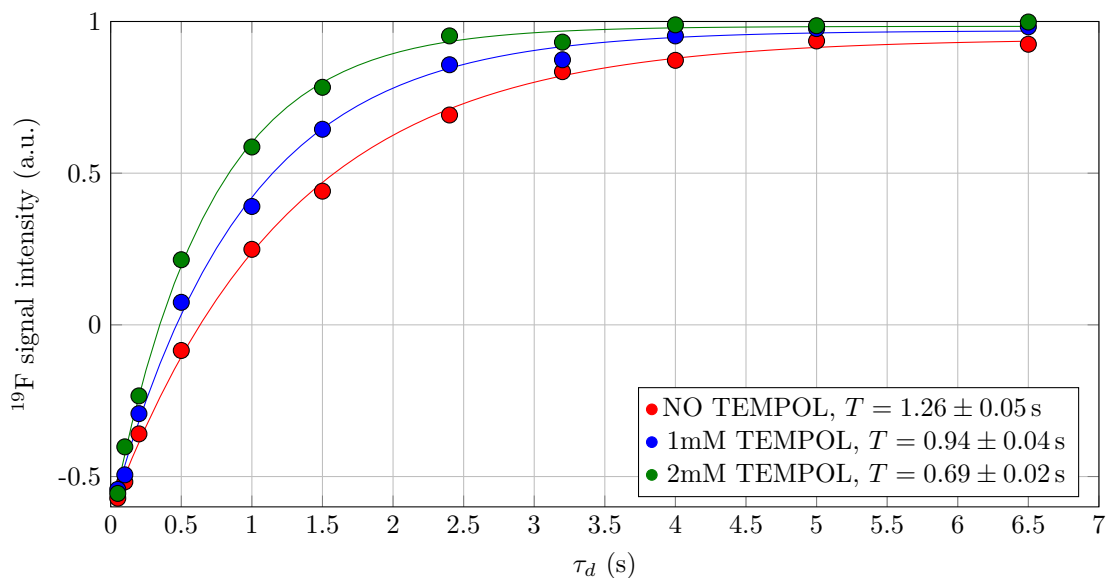


Figure 7.8: Inversion recovery experiments to measure the  $^{19}\text{F}$  longitudinal relaxation time for the labelled protein in presence of TEMPOL free radical.

## 7.2.2 Labelled vs non-labelled protein

In his work, Adriaensen et al. compared circular dichroism spectra of labelled and native protein. They demonstrated that the trifluoroacetylation of lysine induces only local conformational changes of some side chains, but no conformational change of the polypeptide backbone.

## 7.2.3 DNP of labelled lysozyme in solid state

In Chapter 5 it was shown that 40% of polarisation was achieved for  $^{19}\text{F}$  in monofluorobenzene by means of DNP in solid state. However, hyperpolarisation of  $^{19}\text{F}$  in a protein has never been performed to the author's knowledge. The difference in polarising a small molecule and a bulky protein like lysozyme is that in the protein, the nuclei to polarise can be surrounded by the rest of the protein, far away from the polarising agents. In order to demonstrate that it is possible to polarise  $^{19}\text{F}$  in the labelled lysozyme, a solid state experiment has been performed. Approximately 2 mM of labelled protein has been dissolved in a sample containing 60% DMSO- $d_6$ , 30%  $\text{D}_2\text{O}$ , 10%  $\text{H}_2\text{O}$  and 40 mM TEMPOL. 50  $\mu\text{L}$  of sample was put in the sample cup of the probe with the solenoid coil (described in Section 4.2.3), tuned at the  $^{19}\text{F}$  frequency. This sample was studied in the polariser magnet at

1.7 K.

In order to show that hyperpolarisation by DNP can be achieved, the sample was irradiated with microwaves during a saturation recovery experiment. The microwave frequency was set to 93.9 GHz following a frequency sweep experiment that shows the  $^{19}\text{F}$  DNP profile when the sample is irradiated with microwaves at different frequencies. For this experiment the microwave power was set to 400 mW, since the microwave delivery system is not as efficient as it is in the dual iso-centre magnet, in which experiments have been performed with microwaves at 200 mW. This profile is similar to the one obtained in the experiments previously performed on a sample containing monofluorobenzene with the free radical TEMPO, described in Section 5.1.2. Figure 7.9 shows the positive and negative enhancements obtained in this experiment.

The results of a saturation recovery with microwave irradiation for hyperpolarisation

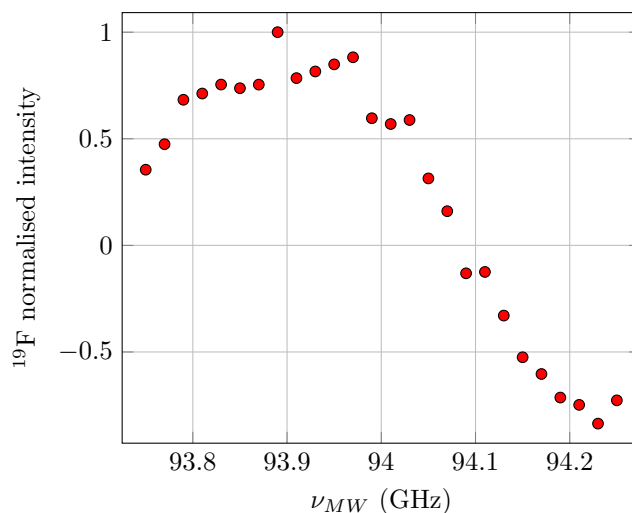


Figure 7.9: Normalised DNP enhancement profile of  $^{19}\text{F}$  in lysozyme as a function of microwave frequency after microwave irradiation at  $P_{MW} = 400$  mW. The  $^{19}\text{F}$  polarisation time is  $T_{MW} = 30$  s.

sation (Figure 7.10) shows that the steady-state DNP polarisation is achieved in  $\tau_{\text{DNP}} = 230 \pm 30$  s. However, due to the poor signal-to-noise ratio, it was impossible to measure the thermal signal, and therefore to estimate the DNP enhancement. Nonetheless, this experiment proves that it is possible to hyperpolarise  $^{19}\text{F}$ -labelled lysozyme.

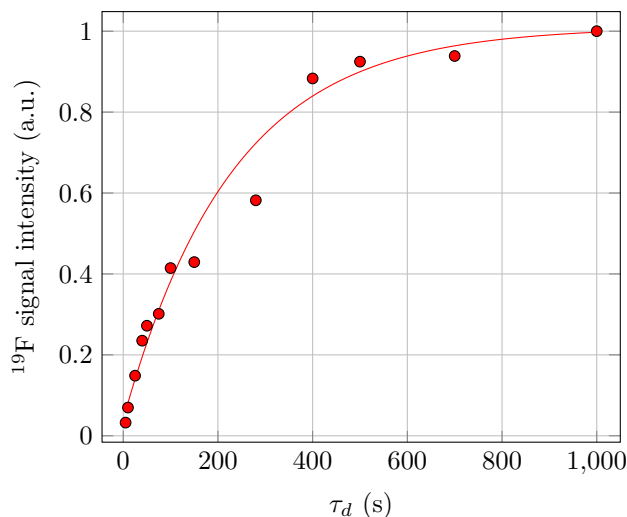


Figure 7.10: Saturation recovery of  $^{19}\text{F}$  in lysozyme during microwave irradiation at 1.7 K in the 3.4 T magnet. During this experiment, microwaves were irradiated on the sample at  $\approx 93.9$  GHz and 400 mW.

### 7.3 Dissolution DNP of labelled lysozyme

In this Chapter, it was shown that it is possible to perform dissolution DNP on simple fluorinated chemicals. It was also shown that  $^{19}\text{F}$  labelled lysozyme is suitable for dissolution DNP experiment.

A dissolution experiment has been performed on a sample containing  $\approx 5$  mM labelled protein. The protein was dissolved in  $30 \mu\text{L}$  of solvent, made of 60%  $\text{DMSO-}d_6$ , 30%  $\text{D}_2\text{O}$ , 10%  $\text{H}_2\text{O}$  and 40 mM TEMPOL. 100 mM 5-fluorouracil (Figure 7.11) were also dissolved in the matrix. This chemical has been used as reference signal for the high resolution NMR acquisition in liquid state after dissolution. It was not possible to use TFA (the similar chemical used for the previous dissolution experiments) since it resonates at the same chemical shift as the  $^{19}\text{F}$  in the labelled protein.

The sample was put in the sample cup at the bottom of the waveguide, and inserted into the cryostat during the cool down procedure. Once a temperature of  $\approx 1.7$  K was reached, the microwave source was switched on in order to hyperpolarise the sample. A microwave frequency of 93.85 GHz and power of 200 mW were chosen accordingly with the results obtained in section 7.1.3 of this Chapter. The sample was hyperpolarised for a time longer than  $5 \times \tau_{\text{DNP}}$ , where  $\tau_{\text{DNP}}$  was the time constant obtained in section 7.2.3. After this time, the polarisation of

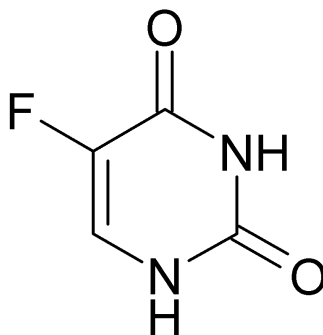


Figure 7.11: Chemical structure of 5-fluorouracil.

the  $^{19}\text{F}$  nuclei reaches a quasi steady-state.

The dissolution process has been carried out by using water to melt the sample, as explained for the dissolution experiment shown in section 7.1.4. The total volume of sample after dissolution was  $\approx 500\ \mu\text{L}$ . Figure 7.12 shows the spectrum acquired in the high resolution magnet after dissolution. The spectrum was acquired by using a single  $\pi/2$  flip angle pulse 400 ms after dissolution of the sample. The figure shows the enhanced labelled protein signal, at around 11 ppm,

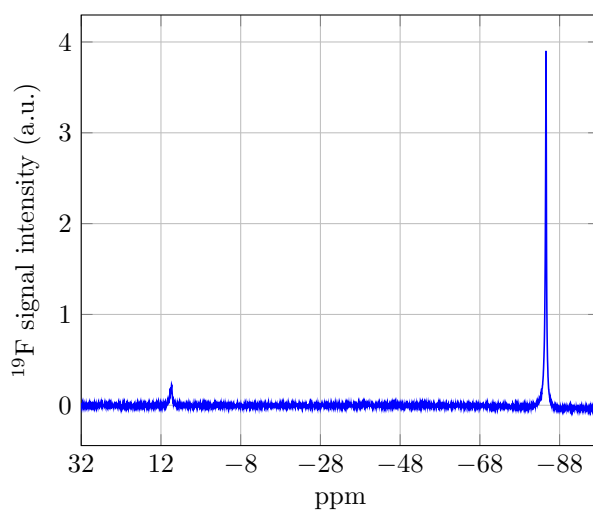
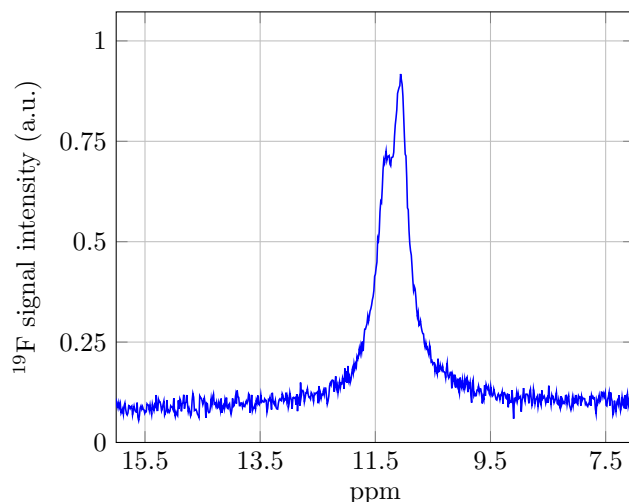


Figure 7.12:  $^{19}\text{F}$  DNP enhanced spectrum after dissolution. The  $^{19}\text{F}$  labelled protein peak appears at around 11 ppm, while the fluorouracil peak is at around  $-76$  ppm.  $\text{CFCl}_3$  has been used as reference compound.

and the enhanced fluorouracil signal, at  $\approx -80$  ppm. A line width corresponding to  $\approx 120$  Hz is observed. Figure 7.13 shows the zoomed protein signal. Of the six expected peaks, corresponding to the labelled amino acids, only two can be resolved. The sample just after dissolution is in fact subjected to formation

of bubbles that broaden the signal. However, for this experiment, the objective was to acquire the signal as soon as the sample fills the tube, to avoid loss of polarisation due to relaxation processes. To quantify the enhancement, a thermal



*Figure 7.13:*  $^{19}\text{F}$  DNP enhanced spectrum after dissolution in the region of the  $^{19}\text{F}$  labelled protein peak.

signal of the sample after dissolution has been acquired. 792 scans have been averaged to obtain a signal-to-noise ratio large enough to allow integration of the peak intensities. Enhanced and thermal NMR data have been processed by using the same parameters. The overall enhancement achieved with dissolution DNP was of a factor 1100 for  $^{19}\text{F}$  in fluorouracil, and a factor 330 for the labelled protein. This enhancement for  $^{19}\text{F}$  in protein, although lower than the enhancement achieved for fluorouracil, represents a significant result toward the development of a methodology to study  $^{19}\text{F}$  labelled proteins with dissolution DNP. However, the resolution does not allow to distinguish the six peaks corresponding to the labelled amino acid. This represents an issue only in the case in which the labelling concerns the same amino acids, whose NMR signals resonate close to the same chemical shift. If instead different amino acids are labelled, the enhanced signals should be visible in a much wider chemical range.

## 7.4 Conclusions

In this final Chapter, the feasibility of dissolution DNP experiments on fluorinated chemicals has been shown. Preliminary experiments have been performed on TFA,

showing that the best enhancement was achieved when using 40 mM free radical to polarise the sample in solid state. The highest registered enhancement on TFA was  $\approx 770$ .

Moreover, lysozyme has been identified as a model system to develop the methodology for studies of protein dynamics using  $^{19}\text{F}$  labels. A dissolution experiment was successfully performed, and hyperpolarised signal after dissolution was acquired in liquid state, showing an enhancement factor of  $\approx 330$ . This result proves the feasibility of this methodology, by showing that is possible to hyperpolarise  $^{19}\text{F}$  in the protein, and that the polarisation survives the dissolution process.

For future experiments, however, a few changes have to be adopted. First of all, during the acquisition, instead of acquiring a single FID with a  $\pi/2$  pulse, a series of consecutive FIDs should be acquired with a small flip angle pulse. If, on the one hand, the small flip angle pulse provides a smaller signal intensity, on the other hand, a large part of the hyperpolarisation is preserved. In this way, therefore, instead of a single spectrum with large intensity, many “smaller” spectra can be acquired consecutively, allowing to observe changes of the chemical shift of the peaks in the spectrum.

Secondly, instead of labelling the same amino acids in the protein, the labelling process should involve two or more amino acids. In such a way the NMR peaks, instead of being clustered around the same chemical shift, could be well resolved in the spectrum without any overlapping. This would compensate for the poor resolution in dissolution DNP experiments with the dual iso-centre magnet.

# Chapter 8

## Conclusions

### 8.1 Outlook

The work presented in this Thesis represents a step forward for the development of a new methodology to study protein dynamics. This methodology makes use of proteins labelled with  $^{19}\text{F}$  nuclei, in conjunction with dissolution DNP. On the one hand,  $^{19}\text{F}$  nuclei provide spectra with a large chemical shift dispersion and background-free NMR spectra. This presents a big advantage since conventionally used spin nuclei like  $^{13}\text{C}$  or  $^1\text{H}$  present a more complex scenario, where the relevant NMR signals have to be searched among other “less meaningful” NMR peaks. On the other hand, dissolution DNP provides the enhancement needed for achieving an otherwise poor signal-to-noise ratio, due to the small quantity of labels in the protein.

In this Thesis, the path to achieve this goal is shown. In Chapter 5 it was shown that it was possible to achieve a maximum DNP enhancement corresponding to  $\approx 40\%$  polarisation for  $^{19}\text{F}$  nuclei when the sample was deuterated and contained the least used amount of  $^{19}\text{F}$  nuclei.

Moreover, during the experiments for the optimisation of the  $^{19}\text{F}$  DNP enhancement, we discovered on an initially unexpected cross-relaxation process. It was observed that the  $^1\text{H}$  in the sample transferred their DNP polarisation to  $^{19}\text{F}$  nuclei. A strong dependence of this effect on the free radicals concentration and molecular structure was highlighted, and this phenomenon was studied as it could

be of interest for the scientific community. After analysing the experimental results, it was concluded that the cross-relaxation process is mediated by pairs of electrons, that facilitate the polarisation transfer between the two nuclear species, and the higher the concentration of the pairs of electrons, the more efficient the process.

The results obtained from the experiments presented in this chapter can only be qualitatively analysed, as the issues in temperature stability had an effect on the reproducibility of the numerical constants extracted by the data analysis. The difficulty in stabilising the temperature, that arises from the nature of the used cryostat, led to large errors in the obtained parameters. Many repetitions for the same experiment are therefore needed, and it could be of future interest to perform more experiments, obtain a larger data statistics and reduce the experimental errors. Nevertheless, the experiments presented clearly show a cross-relaxation behaviour that allowed us to draw the qualitative but meaningful conclusions as discussed above.

The role of the electrons in the polarisation transfer from  $^1\text{H}$  to  $^{19}\text{F}$  was better clarified in Chapter 6, where experiments performed on samples containing the free radical BDPA are presented. In these experiments it was shown that the efficiency of the cross-relaxation process depends on the first place on the characteristics of the used free radical, and it was confirmed that the cross-relaxation is mediated by pairs of electrons.

In the same Chapter evidences for the heteronuclear Cross Effect between of  $^{19}\text{F}$  and  $^1\text{H}$  were also shown. Such effect was predicted by Vega et al., but never directly observed. A sample containing  $^1\text{H}$  and  $^{19}\text{F}$  with BDPA presented an ideal scenario to study this phenomenon, as the heteronuclear Cross Effect enhancements manifested itself clearly in the spectra, allowing the study of this mechanism.

Finally, after clarifying the role of  $^1\text{H}$  and electrons in the  $^{19}\text{F}$  DNP hyperpolarisation, the attention was directed toward dissolution DNP experiments of fluorinated molecules. In chapter 7, an experiment showed that it is possible to perform dissolution DNP on fluorinated proteins. The NMR signal of labelled

lysozyme was successfully acquired after a dissolution DNP experiment. The achieved enhancement, corresponding to an overall factor of  $\approx 330$ , allowed us to acquire the  $^{19}\text{F}$  signal with a single scan.

## 8.2 Future works

The experiment performed on dissolution DNP for labelled protein shows the feasibility of the study. However this represents only a first step for a more complete definition of the methodology. A few problems, and possible solutions, can be identified. First of all, the decision of labelling the protein inserting  $\text{CF}_3$  groups is not ideal, as the  $^{19}\text{F}$  in this methyl-like structure relax quickly. In the first part of Chapter 7, it was in fact shown that  $^{19}\text{F}$  labels attached to aromatic rings have longer relaxation time constants. This would allow the nuclei to retain the hyperpolarisation for longer time after dissolution, increasing the overall enhancement for the detected NMR signal. Moreover, they provide a better chemical shift dispersion. In the analysed protein, the NMR peaks of the six labelled amino acid residues are within a range of 1 ppm and, due to the resolution of the spectrum after dissolution, it is not possible to resolve the different signals well.

Finally, a next set of experiments could consist in continuous acquisition of NMR signals after the dissolution with small flip angle pulses. In such a way, it is possible to monitor the evolution and dynamics of the NMR peaks as the protein interacts with a buffer solution in the NMR tube. The small flip angle pulse for each acquisition would entail a smaller NMR signals compared to the signal originated by the  $\pi/2$  pulse in the experiment performed in Chapter 7. However, a further optimisation of the  $^{19}\text{F}$  DNP process in solid-state could compensate the loss in signal intensity.

Improvements can also be achieved for the study of the heteronuclear Cross Effect. The results for the simulation in fact show a lack of symmetry for the optimal enhancements of  $^1\text{H}$  and  $^{19}\text{F}$ , showing that the maximum intensities can be achieved for different coupling constants of the interacting spins. It is therefore possible to change the deuteration of the sample to alter these interaction

constants, to better study the heteronuclear Cross Effect mechanism and to study how it works as the structure of the sample changes.

# Bibliography

- [1] J. H. Ardenkjaer-Larsen, B. Fridlund, A. Gram, G. Hansson, L. Hansson, M. H. Lerche, R. Servin, M. Thaning, and K. Golman, “Increase in signal-to-noise ratio of  $> 10,000$  times in liquid-state NMR.,” *Proc. Natl. Acad. Sci. U.S.A.*, vol. 100, no. 18, pp. 10158–10163, 2003.
- [2] D. Canet, *Nuclear Magnetic Resonance: Concepts and Methods*. Wiley, 1996.
- [3] M. H. Levitt, *Spin Dynamics: Basics of Nuclear Magnetic Resonance*. Wiley, 2001.
- [4] F. Bloch, “Nuclear induction,” *Phys. Rev.*, vol. 70, pp. 460–474, Oct 1946.
- [5] J. Ruiz-Cabello, B. P. Barnett, P. A. Bottomley, and J. W. Bulte, “Fluorine ( $^{19}\text{F}$ ) MRS and MRI in biomedicine,” *NMR Biomed.*, vol. 24, no. 2, pp. 114–129, 2011.
- [6] K. E. Arntson and W. C. K. Pomerantz, “Protein-Observed Fluorine NMR: A Bioorthogonal Approach for Small Molecule Discovery,” *J. Med. Chem.*, pp. 5158–5171, 2015.
- [7] J. L. Kitevski-LeBlanc and R. S. Prosser, “Current applications of  $^{19}\text{F}$  NMR to studies of protein structure and dynamics,” *Prog. Nuc. Mag. Res. Spec.*, vol. 62, pp. 1–33, 2012.
- [8] R. Ernst, G. Bodenhausen, and A. Wokaun, *Principles of Nuclear Magnetic Resonance in One and Two Dimensions*. International series of monographs on chemistry, Clarendon Press, 1987.

- [9] S. E. Day, M. I. Kettunen, F. a. Gallagher, D.-E. Hu, M. H. Lerche, J. Wolber, K. Golman, J. H. Ardenkjaer-Larsen, and K. M. Brindle, “Detecting tumor response to treatment using hyperpolarized  $^{13}\text{C}$  magnetic resonance imaging and spectroscopy.” *Nat. Med.*, vol. 13, no. 11, pp. 1382–1387, 2007.
- [10] A. Abragam and M. Goldman, “Principles of dynamic nuclear polarisation,” *Rep. Prog. Phys.*, vol. 41, no. 3, pp. 395–467, 1978.
- [11] F. Jähnig, G. Kwiatkowski, A. Däpp, A. Hunkeler, B. H. Meier, S. Kozerke, and M. Ernst, “Dissolution DNP using trityl radicals at 7 T field,” *Phys. Chem. Chem. Phys.*, vol. 19, pp. 19196–19204, 2017.
- [12] J. Ardenkjaer-Larsen, A. Leach, N. Clarke, J. Urbahn, D. Anderson, and T. Skloss, “Dynamic nuclear polarization polarizer for sterile use intent,” *NMR Biomed.*, vol. 24, pp. 927–32, 2011.
- [13] N. Chattergoon, F. Martínez-Santesteban, W. B. Handler, J. H. Ardenkjaer-Larsen, and T. J. Scholl, “Field dependence of T1 for hyperpolarized [1- $^{13}\text{C}$ ] pyruvate,” *Contrast Media Mol. Imaging*, vol. 8, no. 1, pp. 57–62, 2013.
- [14] S. R. Hartmann and E. L. Hahn, “Nuclear double resonance in the rotating frame,” *Phys. Rev.*, vol. 128, no. 5, pp. 2042–2053, 1962.
- [15] R. R. Ernst, G. Bodenhausen, A. Wokaun, and Others, *Principles of nuclear magnetic resonance in one and two dimensions*. Clarendon Press Oxford, 1987.
- [16] J. Leggett, R. Hunter, J. Granwehr, R. Panek, A. J. Perez Linde, A. J. Horsewill, J. McMaster, G. Smith, and W. Köckenberger, “A dedicated spectrometer for dissolution DNP NMR spectroscopy,” *Phys. Chem. Chem. Phys.*, vol. 12, no. 22, pp. 5883–5892, 2010.
- [17] C. Cudalbu, A. Comment, F. Kurdzesau, R. B. van Heeswijk, K. Uffmann, S. Jannin, V. Denisov, D. Kirik, and R. Gruetter, “Feasibility of in vivo  $^{15}\text{N}$  MRS detection of hyperpolarized  $^{15}\text{N}$  labeled choline in rats,” *Phys. Chem. Chem. Phys.*, vol. 12, pp. 5818–5823, 2010.

- [18] A. J. Perez Linde, A. Bornet, J. Milani, B. Vuichoud, R. Melzi, S. Jannin, and G. Bodenhausen, “Cross polarization from  $^1\text{H}$  to quadrupolar  $^6\text{Li}$  nuclei for dissolution DNP,” *Phys. Chem. Chem. Phys.*, vol. 16, pp. 24813–24817, 2014.
- [19] Y. Lee, H. Zeng, S. Ruedisser, A. D. Gossert, and C. Hilty, “Nuclear magnetic resonance of hyperpolarized fluorine for characterization of protein-ligand interactions,” *J. Am. Chem. Soc.*, vol. 134, no. 42, pp. 17448–17451, 2012.
- [20] Y. Kim and C. Hilty, “Affinity Screening Using Competitive Binding with Fluorine-19 Hyperpolarized Ligands,” *Angew. Chem. Int. Ed.*, vol. 54, no. 16, pp. 4941–4944, 2015.
- [21] S. Meiboom and D. Gill, “Modified Spin-Echo Method for Measuring Nuclear Relaxation Times,” *Rev. Sci. Instrum.*, vol. 29, no. 8, 1958.
- [22] N. Bloembergen, *Nuclear Magnetic Relaxation*. M. Nijhoff, 1948.
- [23] A. Abragam, *The Principles of Nuclear Magnetism*. Comparative Pathobiology - Studies in the Postmodern Theory of Education, Oxford University Press, 1961.
- [24] P. A. M. Dirac, “The Quantum Theory of the Emission and Absorption of Radiation,” *Proc. Royal Soc. Lond. A*, 1927.
- [25] T. C. Farrar and E. D. Becker, “Chapter 4 - relaxation mechanisms,” in *Pulse and Fourier Transform NMR*, pp. 46 – 65, San Diego: Academic Press, 1971.
- [26] J. J. Wittmann, M. Eckardt, W. Harneit, and B. Corzilius, “ $^1\text{H}$  electron-driven spin diffusion supports crossing the diffusion barrier in mas dnp,” *Phys. Chem. Chem. Phys.*, vol. 20, pp. 11418–11429, 2018.
- [27] A. Potapov, K. R. Thurber, W.-M. Yau, and R. Tycko, “ $^1\text{H}$  dynamic nuclear polarization-enhanced  $^1\text{H}$ - $^{13}\text{C}$  double resonance nmr in static samples below 20k,” *J. Magn. Reson.*, vol. 221, pp. 32 – 40, 2012.

- [28] B. M. Goodson, “Applications of optical pumping and polarization techniques in NMR: I. Optical Nuclear Polarization in Molecular Crystals,” vol. 55 of *Annu. Rep. NMR Spectro.*, pp. 299 – 323, Academic Press, 2005.
- [29] S. B. Duckett and R. E. Mewis, “Application of parahydrogen induced polarization techniques in NMR spectroscopy and imaging,” *Acc. Chem. Res.*, vol. 45, no. 8, pp. 1247–57, 2012.
- [30] N. Eshuis, R. L. Aspers, B. J. van Weerdenburg, M. C. Feiters, F. P. Rutjes, S. S. Wijmenga, and M. Tessari, “Determination of long-range scalar  $1\text{H}$ - $1\text{H}$  coupling constants responsible for polarization transfer in SABRE,” *J. Magn. Reson.*, vol. 265, pp. 59 – 66, 2016.
- [31] A. W. Overhauser, “Polarization of Nuclei in Metals,” *Phys. Rev.*, vol. 92, no. 2, pp. 411–415, 1953.
- [32] T. R. Carver and C. P. Slichter, “Polarization of Nuclear Spins in Metals,” *Phys. Rev.*, vol. 92, pp. 212–213, Oct. 1953.
- [33] L. R. Becerra, G. J. Gerfen, R. J. Temkin, D. J. Singel, and R. G. Griffin, “Dynamic nuclear polarization with a cyclotron resonance maser at 5 T,” *Phys. Rev. Lett.*, vol. 71, pp. 3561–3564, Nov 1993.
- [34] Y. Hovav, A. Feintuch, and S. Vega, “Theoretical aspects of dynamic nuclear polarization in the solid state – The solid effect,” *J. Magn. Reson.*, vol. 207, no. 2, pp. 176–189, 2010.
- [35] A. A. Smith, B. Corzilius, A. B. Barnes, T. Maly, and R. G. Griffin, “Solid effect dynamic nuclear polarization and polarization pathways,” *J. Chem. Phys.*, vol. 136, no. 1, p. 015101, 2012.
- [36] J. Ardenkjær-Larsen, I. Laursen, I. Leunbach, G. Ehnholm, L.-G. Wistrand, J. Petersson, and K. Golman, “EPR and DNP Properties of Certain Novel Single Electron Contrast Agents Intended for Oximetric Imaging,” *J. Magn. Reson.*, vol. 133, no. 1, pp. 1 – 12, 1998.
- [37] L. Becerra, G. Gerfen, B. Bellew, J. Bryant, D. Hall, S. Inati, R. Weber, S. Un, T. Prisner, A. McDermott, K. Fishbein, K. Kresicher, R. Temkin,

- D. Singel, and R. Griffin, “A Spectrometer for Dynamic Nuclear Polarization and Electron Paramagnetic Resonance at High Frequencies,” *J. Magn. Reson.*, vol. 117, pp. 28–40, 11 1995.
- [38] L. Lumata, Z. Kovacs, A. D. Sherry, C. Malloy, S. Hill, J. van Tol, L. Yu, L. Song, and M. E. Merritt, “Electron spin resonance studies of trityl OX063 at a concentration optimal for DNP,” *Phys. Chem. Chem. Phys.*, vol. 15, pp. 9800–9807, 2013.
- [39] J. Ardenkjær-Larsen, “On the present and future of dissolution-DNP,” *J. Magn. Reson.*, vol. 264, pp. 3–12, 2016.
- [40] Y. Hovav, A. Feintuch, and S. Vega, “Theoretical aspects of dynamic nuclear polarization in the solid state – The cross effect,” *J. Magn. Reson.*, vol. 214, pp. 29–41, 2012.
- [41] K. N. Hu, C. Song, H. H. Yu, T. M. Swager, and R. G. Griffin, “High-frequency dynamic nuclear polarization using biradicals: A multifrequency EPR lineshape analysis,” *J. Chem. Phys.*, vol. 128, no. 5, 2008.
- [42] K.-N. Hu, G. T. Debelouchina, A. A. Smith, and R. G. Griffin, “Quantum mechanical theory of dynamic nuclear polarization in solid dielectrics,” *J. Chem. Phys.*, vol. 134, no. 12, p. 125105, 2011.
- [43] Y. Hovav, D. Shimon, I. Kaminker, A. Feintuch, D. Goldfarb, and S. Vega, “Effects of the electron polarization on dynamic nuclear polarization in solids †,” *Phys. Chem. Chem. Phys.*, vol. 17, pp. 6053–6065, 2015.
- [44] T. A. Siaw, S. A. Walker, B. D. Armstrong, and S.-I. Han, “Inductively coupled nmr probe for versatile dynamic nuclear polarization operation at 7t: Observation of  $61 \pm 2\%$  1h polarization at 4k,” *J. Magn. Reson.*, vol. 221, pp. 5 – 10, 2012.
- [45] T. Maly, G. T. Debelouchina, V. S. Bajaj, K.-N. Hu, C.-G. Joo, M. L. Mak–Jurkauskas, J. R. Sirigiri, P. C. A. van der Wel, J. Herzfeld, R. J. Temkin, and R. G. Griffin, “Dynamic nuclear polarization at high magnetic fields,” *J. Chem. Phys.*, vol. 128, no. 5, p. 052211, 2008.

- [46] S. Jannin, A. Comment, and J. J. V. D. Klink, “Dynamic Nuclear Polarization by Thermal Mixing,” *Appl. Magn. Reson.*, vol. 43, pp. 59–68, 2012.
- [47] A. Karabanov, G. Kwiatkowski, C. U. Perotto, D. Wiśniewski, J. McMaster, I. Lesanovsky, and W. Köckenberger, “Dynamic nuclear polarisation by thermal mixing: quantum theory and macroscopic simulations,” *Phys. Chem. Chem. Phys.*, vol. 18, pp. 30093–30104, 2016.
- [48] M. Goldman, “Overview of Spin Temperature, Thermal Mixing and Dynamic Nuclear Polarization,” *Appl. Magn. Reson.*, vol. 34, no. 3, pp. 219–226, 2008.
- [49] V. A. Atsarkin, “Dynamic polarization of nuclei in solid dielectrics,” *Sov. Phys. Uspekhi*, vol. 21, no. 9, pp. 725–745, 1978.
- [50] L. L. Lumata, M. E. Merritt, C. R. Malloy, A. D. Sherry, J. van Tol, L. Song, and Z. Kovacs, “Dissolution dnp-nmr spectroscopy using galvinoxyl as a polarizing agent,” *J. Magn. Reson.*, vol. 227, pp. 14 – 19, 2013.
- [51] I. Solomon, “Relaxation processes in a system of two spins,” *Phys. Rev.*, vol. 99, no. 2, p. 559, 1955.
- [52] K. Hausser and D. Stehlik, “Dynamic Nuclear Polarization in Liquids,” in *Advances in Magnetic Resonance* (J. S. Waugh, ed.), vol. 3 of *Advances in Magnetic and Optical Resonance*, pp. 79 – 139, Academic Press, 1968.
- [53] J. Noggle and R. Schirmer, *The nuclear Overhauser effect: chemical applications*. Academic Press, 1971.
- [54] A. Comment, “Dissolution DNP for in vivo preclinical studies,” *J. Magn. Reson.*, vol. 264, pp. 39 – 48, 2016.
- [55] F. Jähnig, G. Kwiatkowski, and M. Ernst, “Conceptual and instrumental progress in dissolution DNP,” *J. Magn. Reson.*, vol. 264, pp. 22 – 29, 2016.
- [56] J. Milani, B. Vuichoud, A. Bornet, P. Miéville, R. Mottier, S. Jannin, and G. Bodenhausen, “A magnetic tunnel to shelter hyperpolarized fluids,” *Rev. Sci. Instr.*, vol. 86, no. 2, p. 024101, 2015.

- [57] B. P. McGeorge-Henderson, *Novel acquisition strategies for dissolution dynamic nuclear polarisation*. PhD thesis, University of Nottingham, 2016.
- [58] K. Wark, *Advanced Thermodynamics for Engineers*. McGraw-Hill, 1995.
- [59] J. Granwehr, R. Panek, J. Leggett, and W. Köckenberger, “Quantifying the transfer and settling in NMR experiments with sample shuttling,” *J. Chem. Phys.*, vol. 132, no. 24, p. 244507, 2010.
- [60] K. N. Hu, V. S. Bajaj, M. Rosay, and R. G. Griffin, “High-frequency dynamic nuclear polarization using mixtures of TEMPO and trityl radicals,” *J. Chem. Phys.*, vol. 126, no. 4, 2007.
- [61] D. Shimon, Y. Hovav, A. Feintuch, D. Goldfarb, and S. Vega, “Dynamic nuclear polarization in the solid state: a transition between the cross effect and the solid effect,” *Phys. Chem. Chem. Phys.*, vol. 14, no. 16, pp. 5729–5743, 2012.
- [62] J. T. Gerig, “Fluorine NMR,” *SelfPublished*, vol. 21, no. 1, pp. 1–35, 2001.
- [63] T.-C. Ong, M. L. Mak-Jurkauskas, J. J. Walsh, V. K. Michaelis, B. Corzilius, A. A. Smith, A. M. Clausen, J. C. Cheetham, T. M. Swager, and R. G. Griffin, “Solvent-Free Dynamic Nuclear Polarization of Amorphous and Crystalline ortho-Terphenyl,” *J. Phys. Chem. B*, vol. 117, no. 10, pp. 3040–3046, 2013.
- [64] Y. Matsuki, T. Maly, O. Ouari, F. Le Moigne, E. Rizzato, S. Lyubenova, J. Herzfeld, T. Prisner, P. Tordo, and R. G. Griffin, “Dynamic Nuclear Polarization using a Rigid Biradical,” *Angew. Chem. Int. Ed.*, vol. 48, no. 27, 2009.
- [65] B. T. Allen, “Zero-Field Splitting Parameter of the Mn Media,” *J. Chem. Phys.*, vol. 43, p. 3820, 1965.
- [66] A. Lesage, M. Lelli, D. Gajan, M. A. Caporini, V. Vitzthum, P. Miéville, J. Alauzun, A. Roussey, C. Thieuleux, A. Mehdi, G. Bodenhausen, C. Copret, and L. Emsley, “Surface Enhanced NMR Spectroscopy by Dynamic

- Nuclear Polarization,” *J. Am. Chem. Soc.*, vol. 132, no. 44, pp. 15459–15461, 2010.
- [67] A. Feintuch, D. Shimon, Y. Hovav, D. Banerjee, I. Kaminker, Y. Lipkin, K. Zibzener, B. Epel, S. Vega, and D. Goldfarb, “A Dynamic Nuclear Polarization spectrometer at 95GHz/144MHz with EPR and NMR excitation and detection capabilities,” *J. Magn. Reson.*, vol. 209, no. 2, pp. 136–141, 2011.
- [68] Q. Z. Ni, E. Daviso, T. V. Can, E. Markhasin, S. K. Jawla, T. M. Swager, R. J. Temkin, J. Herzfeld, and R. G. Griffin, “High Frequency Dynamic Nuclear Polarization,” *Acc. Chem. Res.*, vol. 46, no. 9, pp. 1933–1941, 2013.
- [69] H. Goff, E. Verespej, and D. Jermann, “Glass transitions in frozen sucrose solutions are influenced by solute inclusions within ice crystals,” *Thermochim. Acta*, vol. 399, no. 1, pp. 43 – 55, 2003.
- [70] L. Lumata, M. Merritt, and Z. Kovacs, “Influence of deuteration in the glassing matrix on  $^{13}\text{C}$  dynamic nuclear polarization,” *Phys. Chem. Chem. Phys.*, vol. 15, p. 7032, 2013.
- [71] A. Kiswandhi, B. Lama, P. Niedbalski, M. Goderya, J. Long, and L. Lumata, “The effect of glassing solvent deuteration and Gd  $3+$  doping on  $^{13}\text{C}$  DNP at 5 T,” *RSC Adv.*, vol. 6, no. 45, pp. 38855–38860, 2016.
- [72] F. Kurdzesau, B. van den Brandt, A. Comment, P. Hautle, S. Jannin, J. J. van der Klink, and J. a. Konter, “Dynamic nuclear polarization of small labelled molecules in frozen water–alcohol solutions,” *J. Phys. D*, vol. 41, no. 15, p. 155506, 2008.
- [73] L. Nygaards, I. Bojesen, T. Pedersen, and J. Rastrup-andersen, “Structure of fluorobenzene,” *J. Mol. Struct.*, vol. 2, pp. 209–215, 1968.
- [74] D. Shimon, A. Feintuch, D. Goldfarb, and S. Vega, “Static  $^1\text{H}$  dynamic nuclear polarization with the biradical TOTAPOL: a transition between the solid effect and the cross effect,” *Phys. Chem. Chem. Phys.*, vol. 16, no. 14, pp. 6687–6699, 2014.

- [75] K. R. Thurber and R. Tycko, “Theory for cross effect dynamic nuclear polarization under magic-angle spinning in solid state nuclear magnetic resonance: The importance of level crossings,” *J. Chem. Phys.*, vol. 137, p. 84508, 2012.
- [76] N. Bloembergen, S. Shapiro, P. S. Pershan, and J. O. Artman, “Cross-relaxation in spin systems,” *Phys. Rev.*, vol. 114, no. 2, pp. 445–459, 1959.
- [77] A. Woźniak-Braszak, “Methodology for solid state NMR study of cross relaxation and molecular dynamics in heteronuclear systems,” *Solid State Nucl. Magn. Reson.*, vol. 53, pp. 38–43, 2013.
- [78] C. Bengs, H. Schwalbe, and B. Corzilius, “Heteronuclear Cross-Relaxation under Solid-State Dynamic Nuclear Polarization,” *J. Am. Chem. Soc.*, vol. 138, pp. 16572–16575, 2016.
- [79] N. M. Loening, M. Rosay, V. Weis, and R. G. Griffin, “Solution-State Dynamic Nuclear Polarization at High Magnetic Field,” *J. Am. Chem. Soc.*, vol. 124, pp. 8808–8809, 2002.
- [80] O. Neudert, C. Mattea, H. W. Spiess, S. Stapf, and K. Münnemann, “A comparative study of  $^1\text{H}$  and  $^{19}\text{F}$  Overhauser DNP in fluorinated benzenes,” *Phys. Chem. Chem. Phys.*, vol. 15, no. 47, pp. 20717–26, 2013.
- [81] F. Kurdzesau, B. van den Brandt, a. Comment, P. Hautle, S. Jannin, J. J. van der Klink, and J. a. Konter, “Dynamic nuclear polarization of small labelled molecules in frozen water–alcohol solutions,” *J. Phys. D*, vol. 41, no. 15, p. 155506, 2008.
- [82] W. De Boer, M. Borghini, K. Morimoto, T. O. Niinikoski, and F. Udo, “Dynamic Polarization of Protons, Deuterons, and Carbon-13 Nuclei: Thermal Contact Between Nuclear Spins and an Electron Spin-Spin Interaction Reservoir,” *J. Low Temp. Phys.*, vol. 15, pp. 249–267, 1974.
- [83] W. De Boer, “Dynamic Orientation of Nuclei at Low Temperatures,” *J. Low Temp. Phys.*, vol. 22, pp. 185–212, 1976.

- [84] S. F. Cox, V. Bouffard, and M. Goldman, "The coupling of two nuclear Zeeman reservoirs by the electronic spin-spin reservoir," *J. Phys. C*, vol. 6, no. 5, 1973.
- [85] S. Reynolds and H. Patel, "Monitoring the Solid-State Polarization of  $^{13}\text{C}$ ,  $^{15}\text{N}$ ,  $^2\text{H}$ ,  $^{29}\text{Si}$  and  $^{31}\text{P}$ ," *Appl. Magn. Reson.*, vol. 34, pp. 495–508, 2008.
- [86] O. Lafon, A. S. L. Thankamony, M. Rosay, F. Aussenac, X. Lu, J. Trebosc, V. Bout-Roumazeilles, H. Vezin, and J. Amoureux, "Olivier Lafon and Hervé Vezin at the University of As featured in :," *Chem. Comm.*, vol. 49, pp. 2864–2866, 2013.
- [87] O. Lafon, M. Rosay, F. Aussenac, X. Lu, J. Trøbosc, O. Cristini, C. Kinowski, N. Touati, H. Vezin, and J.-p. Amoureux, "Beyond the Silica Surface by Direct Silicon-29 Dynamic Nuclear Zuschriften," *Angew. Chem.*, no. 1, pp. 8517–8520, 2011.
- [88] L. Sperrin, D. A. Je, S. Pawsey, M. Rosay, and C. P. Grey, "Dynamic Nuclear Polarization Enhanced Natural Abundance Spectroscopy," *J. Am. Chem. Soc.*, vol. 135, pp. 2975–2978, 2013.
- [89] I. J. Day, J. C. Mitchell, M. J. Snowden, and A. L. Davis, "Co-acquisition of hyperpolarised  $^{13}\text{C}$  and  $^{15}\text{N}$  NMR spectra," *Magn. Reson. Chem.*, vol. 45, pp. 1018–1021, 2007.
- [90] Ü. Akbey, F. Camponeschi, B.-j. V. Rossum, and H. Oschkinat, "Triple Resonance Cross-Polarization for More Sensitive  $^{13}\text{C}$  MAS NMR Spectroscopy of Deuterated Proteins," *ChemPhysChem*, vol. 12, no. 11, pp. 2092–2096, 2011.
- [91] L. Lumata, M. Merritt, C. Malloy, A. D. Sherry, and Z. Kovacs, "and Theoretical Considerations," *Appl. Magn. Reson.*, vol. 43, pp. 69–79, 2012.
- [92] L. Lumata, A. K. Jindal, M. E. Merritt, C. R. Malloy, A. D. Sherry, and Z. Kovacs, "DNP by Thermal Mixing under Optimized Conditions Yields > 60 000-fold Enhancement of  $^{89}\text{Y}$  NMR Signal," *J. Am. Chem. Soc.*, vol. 135, pp. 8673–8680, 2011.

- [93] M. Borghini and K. Scheffler, “Experimental Evidence for Dynamic Nuclear Polarization by Cooling of Electron Spin-Spin Interaction,” *Phys. Rev. Lett.*, vol. 26, no. 22, p. 1362, 1971.
- [94] V. A. Atsarkin and J. Nonetheless, “Experimental investigation of the manifestations of the spin-spin interaction reservoir in a system of epr lines connected with,” *Sov. Phys. JETP*, vol. 32, no. 3, pp. 421–425, 1971.
- [95] I. Kaminker, D. Shimon, Y. Hovav, A. Feintuch, and S. Vega, “Heteronuclear DNP of protons and deuterons with TEMPOL,” *Phys. Chem. Chem. Phys.*, vol. 18, no. 16, pp. 11017–11041, 2016.
- [96] D. Guarin, S. Marhabaie, A. Rosso, D. Abergel, G. Bodenhausen, K. L. Ivanov, and D. Kurzbach, “Characterizing Thermal Mixing Dynamic Nuclear Polarization via Cross-Talk between Spin Reservoirs,” *J. Phys. Chem. Lett.*, vol. 8, no. 22, pp. 5531–5536, 2017.
- [97] D. Shimon, Y. Hovav, I. Kaminker, A. Feintuch, D. Goldfarb, and S. Vega, “Simultaneous DNP enhancements of  $^1\text{H}$  and  $^{13}\text{C}$  nuclei: theory and experiments,” *Phys. Chem. Chem. Phys.*, vol. 17, no. 17, pp. 11868–11883, 2015.
- [98] D. T. Peat, M. L. Hirsch, D. G. Gadian, A. J. Horsewill, J. R. Owersbradley, and J. G. Kempf, “Low-field thermal mixing in  $[1-^{13}\text{C}]$  pyruvic acid for brute-force hyperpolarization,” *Phys. Chem. Chem. Phys.*, vol. 18, pp. 19173–19182, 2016.
- [99] A. Zagdoun, *Dynamic Nuclear Polarisation Surface Enhanced NMR Spectroscopy*. PhD thesis, School normale superieure de Lyon, 2014.
- [100] Y. Hovav, I. Kaminker, D. Shimon, A. Feintuch, D. Goldfarb, and S. Vega, “The electron depolarization during dynamic nuclear polarization: measurements and simulations,” *Phys. Chem. Chem. Phys.*, vol. 17, no. 1, pp. 226–244, 2015.
- [101] S. Blundell and K. Blundell, *Concepts in Thermal Physics*. OUP Oxford, 2010.

- [102] K. N. Hu, H. H. Yu, T. M. Swager, and R. G. Griffin, "Dynamic Nuclear Polarization with Biradicals," *J. Am. Chem. Soc.*, pp. 10844–10845, 2004.
- [103] C. M. Davis and K. A. Curran, "Manipulation of a schlenk line: Preparation of tetrahydrofuran complexes of transition-metal chlorides," *J. Chem. Educ.*, vol. 84, no. 11, p. 1822, 2007.
- [104] T. Sato, Y. Hamada, M. Sumikawa, S. Araki, and H. Yamamoto, "Solubility of Oxygen in Organic Solvents and Calculation of the Hansen Solubility Parameters of Oxygen," *Ind. Eng. Chem. Res.*, 2014.
- [105] S. Pylaeva, K. L. Ivanov, M. Baldus, D. Sebastiani, and H. Elgabarty, "Molecular Mechanism of Overhauser Dynamic Nuclear Polarization in Insulating Solids," *J. Phys. Chem. Lett.*, pp. 8–13, 2017.
- [106] Y. Hovav, A. Feintuch, and S. Vega, "Theoretical aspects of dynamic nuclear polarization in the solid state - Spin temperature and thermal mixing," *Phys. Chem. Chem. Phys.*, vol. 15, no. 1, pp. 188–203, 2013.
- [107] A. Kessenikh, A. Manenkov, and G. Pyatnitskii, "On explanation of experimental data on dynamic polarization of protons in irradiated polyethylenes," *Soviet Phys.-Solid State (English Transl.)*, vol. 6, 1964.
- [108] Y. Hovav, A. Feintuch, and S. Vega, "Dynamic nuclear polarization assisted spin diffusion for the solid effect case," *J. Chem. Phys.*, vol. 134, no. 7, p. 074509, 2011.
- [109] A. Karabanov, D. Wiśniewski, F. Raimondi, I. Lesanovsky, and W. Köckenberger, "Many-body kinetics of dynamic nuclear polarization by the cross effect," *Phys. Rev. A*, vol. 97, p. 031404, 2018.
- [110] D. M. Wilson, K. R. Keshari, P. E. Larson, A. P. Chen, S. Hu, M. V. Crieckinge, R. Bok, S. J. Nelson, J. M. Macdonald, D. B. Vigneron, and J. Kurhanewicz, "Multi-compound polarization by dnp allows simultaneous assessment of multiple enzymatic activities in vivo," *J. Magn. Reson.*, vol. 205, no. 1, pp. 141 – 147, 2010.

- [111] J. Granwehr, R. Panek, J. Leggett, and W. Köckenberger, “Quantifying the transfer and settling in NMR experiments with sample shuttling,” *J. Chem. Phys.*, vol. 132, no. 24, 2010.
- [112] J. Wolber, F. Ellner, B. Fridlund, A. Gram, H. Johannesson, G. Hansson, L. H. Hansson, M. H. Lerche, S. Mansson, R. Servin, M. Thaning, K. Goldman, and J. H. Ardenkjaer-Larsen, “Generating highly polarized nuclear spins in solution using dynamic nuclear polarization,” *Nucl. Instrum. Methods Phys. Res.*, vol. 526, no. 1-2 SPEC. ISS., pp. 173–181, 2004.
- [113] J. K. M. Sanders and B. K. Hunter, *Modern NMR spectroscopy: a guide for chemists*. Oxford University Press, 1987.
- [114] V. I. Bakhmutov, *Practical NMR Relaxation for Chemists*. Wiley, 2005.
- [115] K. N. Hu, C. Song, H. h. Yu, T. M. Swager, and R. G. Griffin, “High-frequency dynamic nuclear polarization using biradicals: A multifrequency epr lineshape analysis,” *J. Chem. Phys.*, vol. 128, no. 5, p. 052302, 2008.
- [116] F. Khan, I. Kuprov, T. D. Craggs, P. J. Hore, and S. E. Jackson, “<sup>19</sup>F NMR studies of the native and denatured states of green fluorescent protein,” *J. Am. Chem. Soc.*, vol. 128, no. 33, pp. 10729–10737, 2006.
- [117] P. J. Hore, S. L. Winder, C. H. Roberts, and C. M. Dobson, “Stopped-flow photo-cidnp observation of protein folding,” *J. Am. Chem. Soc.*, vol. 119, no. 21, pp. 5049–5050, 1997.
- [118] S. Venkataramani, J. Truntzer, and D. R. Coleman, “Thermal stability of high concentration lysozyme across varying pH: A Fourier Transform Infrared study,” *J. Pharm. Bioallied Sci.*, vol. 5, pp. 148–153, 2013.
- [119] T. Imoto, L. Johnson, A. North, D. Phillips, and J. Rupley, “21 vertebrate lysozymes,” vol. 7 of *The Enzymes*, pp. 665 – 868, Academic Press, 1972.
- [120] P. Adriaensens, M. E. Box, H. J. Martens, E. Onkelinx, J. Put, and J. Gelan, “Investigation of protein structure by means of fluorine-19 NMR. A study of hen egg-white lysozyme ,” *Eur. J. Biochem.*, vol. 177, pp. 383–394, 1988.